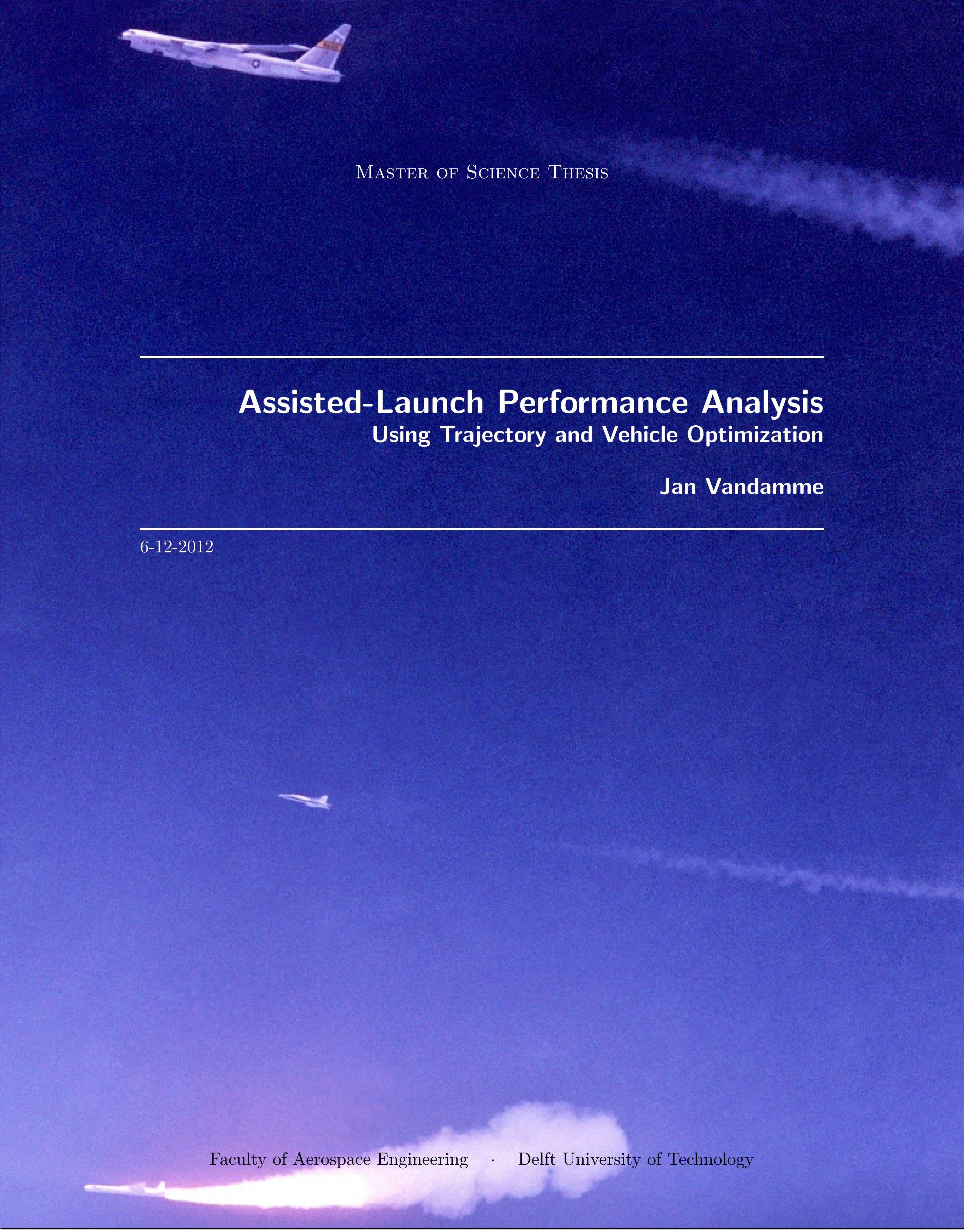

MASTER OF SCIENCE THESIS

Assisted-Launch Performance Analysis
Using Trajectory and Vehicle Optimization

Jan Vandamme

6-12-2012

Faculty of Aerospace Engineering · Delft University of Technology

Assisted-Launch Performance Analysis
Using Trajectory and Vehicle Optimization

Master of Science Thesis

For obtaining the degree of Master of Science in Aerospace Engineering at Delft University of Technology

Jan Vandamme

6-12-2012

Faculty of Aerospace Engineering · Delft University of Technology

Cover figure:
Pegasus Engine Ignites after Drop from B-52 Mothership (modified from [34])

TU Delft
Delft
University of
Technology

Delft University Of Technology
Department Of
Space Exploration

The undersigned hereby certify that they have read and recommend to the Faculty of Aerospace Engineering for acceptance a thesis entitled **"Assisted-Launch Performance Analysis"** by **Jan Vandamme** in partial fulfillment of the requirements for the degree of **Master of Science**.

Dated: 6-12-2012

Chairman of thesis comittee: ______________________
Prof. ir. B.A.C. Ambrosius

Thesis supervisor: ______________________
Dr. ir. E. Mooij

Member of thesis comittee: ______________________
Ir. B.T.C. Zandbergen

Member of thesis comittee: ______________________
Dr.-Dipl.Ing. S. Erb

Summary

At the time of writing 55 years have passed since the launch of Sputnik 1. While spaceflight has changed significantly in many ways since then, further improvement is still needed. This thesis study aims to provide an answer to the question if launch-assist systems could provide such an improvement and if so, how the launch vehicles should be designed.

Launch assists systems come in all shapes and sizes. They can be provided with an assist from the air with help of a fly-back booster, rocket plane, airplane, zeppelin or a balloon or from the ground with a rail or a gun. Most of the studies about the concept of assisted launch focus on the first leg, the assist itself and what is available for use on the market today or what could be built with current technology. However, most launch-assist platforms available today have been built for other purposes and are in no way optimal for launch assist. Therefore, it is interesting to investigate whether a launch-assist system purpose built for the job is needed and what performance requirements it should meet. There are two factors that come into play when answering this question. These factors are the cost of building and operating both the assist platform and the launch vehicle as well as the system's total performance. This thesis focuses on the performance of the entire system by assuming certain performance parameters of the assist platform. All of the concepts proposed have one thing in common. By giving the launch vehicle an initial velocity and/or an initial altitude (often referred to in this study as the launch-assist parameters), they bring the launcher closer to its destination, energetically speaking, and they might diminish atmospheric and gravitational losses. This thesis study's main objective is to shed some clarity onto the relationship between the launch-assist parameters, the launch-vehicle performance and the launch-vehicle parameters. Therefore, the research question for this work is formulated as follows:

How does a launch assist affect the performance and the design of a launch vehicle?

To answer the research question, extensive analysis is performed. Both a set of launch-vehicle parameters and a trajectory is optimized for a variety of given sets of launch-assist parameters. The simulation of the trajectory takes place by propagating the state vector by means of an integrator. This trajectory is dictated by the guidance program, which consists out of a pitch program that follows a 4^{th}-degree polynomial. The trajectory is subjected to several constraints, which are implemented with current-day technology in mind. The problem of optimizing all parameters of that trajectory as well as those of the launch vehicle is tackled by the use of a differential-evolution algorithm.

The results provide an overview for systems that could be used today with respect to the technology available. This means that no results are obtained from simulated launch assists that have a higher than 2,000 m/s assist speed or an assist altitude higher than 40,000 m. The results that were obtained showed that the launch-performance parameters have a large effect on the both the design and the performance of the vehicle. The payload-to-initial-mass ratio increased more than six-fold for hydrolox launchers and more than seven-fold for kerolox launchers between the no-assist case and the case of maximum assist. A high assist velocity affects the launch-vehicle performance more than a high-altitude assist almost to the extent that 1 m/s in velocity is as valuable as 100 m in altitude. Although the results widely vary from case to case, the hydrolox launchers outperform the kerolox launchers at every launch-assist combination. In general, small dimensions, low thrust-to-weight ratios, high chamber pressures and low exit pressures were often found to be the characteristics of an optimal launcher. In addition, there are also multiple cases where the optimal trajectory of the launcher is such that a non-negligible amount of lift is generated or that only a very low heat flux occurs so that no fairing protection is needed for the satellite.

The study is intended to be used as a tool in future concept studies and gives significant insight on important design considerations regarding both the launch-assist system as well as the launch vehicle itself. Through this work, it is my hope that the reader is convinced that current day launchers, which are often an update of an older launcher or designed around an engine that just so happens to be available, have room for improvement left by tackling the design process from a different angle. The main concepts that the study aims to support are the railed launch-assist concepts, the airplane/rocket plane launch-assist concepts and to some extent low ΔV flyback boosters.

Acknowledgements

This document represents the findings from a master thesis study on assisted launch performance conducted as a part of my Master of Science at the Delft University of Technology. The work focused on establishing a means to accurately model a wide array of launchers and analyze their performance given certain initial conditions. The work documents how this is modeled in a simulation program that optimizes the trajectory and the launch vehicle given certain required launch assist and vehicle parameters, in addition the work documents the results extensively and provides a detailed analysis.
I would like to take this moment to thank my supervisor Dr. Ir. Erwin Mooij, who has helped and assisted me during this year and has showed me many places where I should shift my attention to. I would also like to thank my friends of the 9^{th} floor both those who have stayed and those who have left for the help they offered me from time to time and more importantly, for the countless enjoyable massive music quiz sessions. When, not if, I will succeed in obtaining the mythical perfect score, I am sure that I will hear an echo of the 'perfect score' chants ringing in my memories. Last but not least, I would like to offer my sincere gratitude to my family and my close friends for helping me enjoying my life outside of work, they are the kind of people that one should never take for granted.

Delft, The Netherlands — Jan Vandamme
6-12-2012

Contents

List of Figures

List of Tables

Nomenclature

Latin symbols

a	Semi-major axis	[m]
C	Thrust-to-weight ratio	[-]
C_D	Drag coefficient	[-]
C_F	Thrust coefficient	[-]
C_L	Lift coefficient	[-]
C_S	Side force coefficient	[-]
c^*	Characteristic velocity	[m/s]
D	Drag	[N]
D	Diameter	[m]
E	Young's modulus	[Pa]
e	Eccentricity	[-]
$\mathbf{F}$	Force vector	[N]
G	Universal gravitational constant	$6.668 \cdot 10^{-11}$ [Nm^2/kg^2]
$\mathbf{g}$	Gravitational acceleration vector	[m/s^2]
$h*$	Geopotential height	[m']
h	Height	[m]
H_{abl}	Heat of ablation	[J/kg]
I_{sp}	Specific Impulse	[s]
i	Inclination	[rad]
$\hat{i}$, $\hat{j}$, $\hat{k}$	Cartesian unit vectors	[-]
j	Number of equality constraints	[-]
$J_{n,m}$	Gravitational scaling parameter	[-]
k	Boltzmann constant	$1.380622 \cdot 10^{-23}$ [Nm/K]
L	Lift	[N]
L	Length	[m]
L_M	Molecular scale temperature gradient	[K]
M	Molecular weight	[kg/kmol]
M	Mass	[kg]
M	Moment	[Nm]
$\dot{m}$	Mass flow	[kg/s]
n	Number of constraints	[-]

N_A	Avogadro constant	$6.022169 \cdot 10^{26}$ [kmol^{-1}]
p	Pressure	[Pa]
$P_{n,m}(x)$	Legendre function	[-]
$\dot{Q}$	Heat flux	[W/m^2]
$\bar{q}$	Dynamic pressure	[Pa]
R	Specific gas constant	[J/mol $\cdot$ K]
r	Distance	[m]
r	Radius	[m]
$R*$	Gas constant	$8.31432 \cdot 10^3$ [Nm/kmol $\cdot$ K]
R_N	Nose radius	[m]
S_{ref}	Aerodynamic reference surface	[m^2]
T	Thrust	[N]
t	Thickness	[m]
t	Time	[s]
T_M	Molecular scale temperature	[K]
T_{TOT}	Vacuum thrust	[kg]
u	Control variable	several
$\mathbf{V}$	Velocity vector	[m/s]
$\mathbf{V}(\mathbf{P})$	Gravitational potential vector	[J/kg]
v	Mean Anomaly	[-]
$\mathbf{x}$	n-vector of independent variables	several
x	State variable	[-]
x, y, z	Cartesian coordinates	[m]
Z	Geometric height	[m]

Greek symbols

α	Angle of attack	[rad]
β	Side-slip angle	[rad]
Γ	Vandekerckhove function	[-]
γ	Ratio of specific heats	[-]
γ	Flight-path angle	[rad]
ΔV	Change in velocity	[m/s]
δ	Latitude	[rad]
ϵ	Measure of the curvature of tan(θ) profile	[-]
ϵ	Correction factor	[-]
θ	Longitude	[rad]
θ	Pitch angle	[rad]
$\lambda_{n,m}$	Gravitational orientation parameter	[-]
λ	Slenderness ratio	[-]
μ	Standard gravitational parameter	[m^3/s^{-2}]
ρ	Density	[kg/m^3]
σ	Stress	[Pa]
σ	Bank angle	[rad]
τ_c	Time interval needed for vaporization	[s]
τ	Longitude	[rad]

υ	Poisson ratio	[-]
Υ	Vernal equinox or First point of Aries	[-]
Υ	Output	[-]
$\mathbf{\Phi}$	Increment function	[-]
$\mathbf{\Phi}$	Centrifugal potential vector	[J/kg]
ϕ	Latitude	[rad]
φ	Roll angle	[rad]
χ	Heading	[rad]
ψ	Yaw angle	[rad]
Ω	Longitude of the ascending node	[rad]
$\mathbf{\Omega}$	Rotational velocity vector	[rad/s]
ω	Argument of pericenter	[rad]

Acronyms and Abbreviations

AIAA	American Institute of Aeronautics and Astronautics
ASTOS	AeroSpace Trajectory Optimization Software
CEA	Chemical Equilibrium with Applications
DARPA	Defense Advanced Research Projects Agency
DE	Differential Evolution
DoF	Degrees of Freedom
GA	Genetic Algorithm
ESA	European Space Agency
ICAO	International civil aviation organization
ITAR	International Trade in Arms Regulation
LH2	Liquid Hydrogen
LOX	Liquid Oxygen
NASA	National Aeronautics and Space Administration
PaGMO	Parallel Global Multiobjective Optimizer
PSO	Partical Swarm Optimization
RK	Runge-Kutta
RP1	Refined Petroleum
Tudat	TUDelft Astrodynamics Toolbox

Indices

A	Aerodynamic force
A	Aerodynamic (air-path) reference frame
B	Body-fixed reference frame
b	Combustion efficiency
C	Earth-centered, Earth-fixed reference frame
E	Vehicle carried normal Earth reference frame
F	Thrus coefficient
G	Gravitational force
I	Inertial reference frame

i	Initial
p	Payload
T	Thrust force
T	Trajectory reference frame

Chapter 1

Introduction

This thesis is meant to lay the groundwork for future concept-design studies for launch-vehicle development with a focus on assisted-launch concepts. Major fields of interest include the study of optimal-ascent trajectories and launch-vehicle design. The thesis study is supposed to seek an answer to the following research question:

How does a launch assist affect the performance and the design of a launch vehicle?

How this question will be answered is explained in the scope of this introduction, which is discussed in section 1.1. In section 1.2 the layout of the report is presented.

1.1 Scope

During the 1950s and 1960s, the act of traveling into outer space by rocket was widely regarded as the epitome of human achievement. Just as it was for that other great invention of the aerospace world, the airplane, half a century before. At the dawn of the rocket age, flight by airplane had through constant innovation evolved into an every day activity for the average man. Using this as a precedent, the expectations of the general public with regard to spaceflight by the end of the century were quite high. In their minds, little of these expectations have actually come to fruition and space flight has become a disappointment.

Access to space is to this day not self-evident in current society. Not only are the risks far higher than those for an average airplane ride, a cost comparison of the two aerospace activities unveils perhaps an even greater discrepancy. One of the main reasons for the financial difference between the two is that space flight, 55 years after its first occurrence, still depends on expendable vehicles, whereas heavier than air flight relied on the usage of reusable vehicles from the very beginning. As if this fact on itself is not enough to constrain the industry from blossoming, the velocity needed to reach orbit is so high that a conventional launch vehicle exists of two or even more separate vehicles mounted on top of or next to each other while the actual payload contains only a small fraction of the total vehicle mass.

Arguably, spaceflight has seen very little innovation since the day it started. Launch vehicles still have the same shape, still use comparable propellants, are still launched the same way and are still mostly or fully expendable. If the past will be extrapolated into the future, it could take a long time before a threshold in efficiency, cost and safety will be reached that can significantly change the industry. For this very reason, other concepts of launch vehicles using different means of reaching orbit should be further investigated.

One of these alternatives is the adaptation of the strategy of giving an initial assist to the launch vehicle. Assisted launch is a technique that still uses a rocket vehicle as a means of transporting a payload into space, just as a conventional launch does, but its main difference is that it uses another method of transportation to give the launch vehicle a better orientation, position and velocity (launch-assist parameters) at the time of ignition of the launch vehicle. Not only brings this the rocket closer to its destination point both in a spatial sense as well as in an energetic sense, but it also creates an opportunity to further increase its efficiency by minimizing drag and gravity losses.

Most launch-assist platforms available today are designed for other purposes and are in no way optimal for launch assist. They consist out of either civil aviation planes built for long range flights, thus having significant extra structural mass due to the large fuel tanks, military fighter jets that traded in some speed and altitude capability for manoeuvreability and stealth or suborbital rocket planes that have added structural mass to house their passengers. Launch vehicles are then also not only designed to fit these sub-optimal assist platforms but are often designed around an already existing engine, in the hope to cut costs, or with the requirement of being manufactured in certain existing facilities, in the hope to provide work. Therefore, it is interesting to investigate whether a launch-assist system purpose built for the job is needed and what performance requirements it should meet. There are two factors that come into play when answering this question. These factors are the cost of building and operating both the assist platform and the launch vehicle as well as the system's total performance. This thesis focuses on the performance of the entire system by assuming certain performance parameters of the assist platform and it should be noted that the cost aspect is a significant restriction that should be incorporated in further studies.

Assisted launch unfortunately remains a topic that has not undergone a large amount of research and interest in the space community. With the exception of the Pegasus launcher no concept has found its way off the drawing board into space. In addition, the vast majority of the studies conducted so far focused on the feasibility of the concept at hand taking into account the technology and infrastructure of the day. Only a small number of studies has published a performance analysis of some kind and they generally followed the approach of only optimizing the trajectory for a given set of launch-assist parameters. In these studies, the launch vehicle remained mostly unchanged for all evaluated launch assists [6] or was just optimized for one set of launch-assist parameters. This particular set of parameters was determined by external factors, such as the performance of the airplane that the launch vehicle is supposed to be launched from.

To answer the research question posed at the start of this chapter, a number of launch simulations need to be performed. To this purpose, a program was coded in C++ that can simulate the launch of an array of vehicles with different values for the launch-vehicle parameters along different trajectories starting with different initial conditions.

The simulation of the trajectory takes place by propagating the state vector by means of an integrator. This trajectory is dictated by the guidance program. The guidance program is the model used to guide the launcher into the desired orbit. Because it is required that an optimal trajectory, starting out from a whole variety of launch-assist parameters, can be flown, the model needs to be very versatile. To provide this versatility, a 4^th-degree polynomial is used to describe the pitch angle through time. The guidance program is also subjected to a number of constraints, namely an altitude constraint, a bending load constraint, an axial acceleration constraint, an angle-of-attack constraint and a heat flux constraint.

There are a lot of combinations of the 4 degrees of the polynomial and the multiple launch-vehicle parameters that can be made that describes a launch vehicle and a trajectory that leads to insertion of a certain payload in the desired final orbit. To identify the combination that provides the highest initial payload-to-initial-mass ratio into the desired orbit, an optimization process is needed. The optimization algorithm used to fulfill this task is a differential evolution algorithm, which is a population based evolutionary algorithm that improves the solution by modifying the population throughout various generations.

Due to the exponential nature of the complexity of a launch vehicle versus the amount of ΔV required, a relatively small assist with small compounding effects of minimized losses can still open up the possibility of a significantly more simple launch vehicle. Perhaps to the extent that the vehicle only requires one stage to be competitive with respect to conventionally launched vehicles. Therefore the study focused on the optimization of single stage launch vehicles in order to give a clearer view at which assist parameters these types of vehicles could become competitive and by doing so the results also show continuous trends through the range of launch-assist parameters.

The results obtained from the optimizer are sets of optimal launch-vehicle design and trajectory parameters that represent a single stage vehicle and its trajectory that is supposed to be launched at a given set of launch-assist parameters. These results are subjected to an Extended Fourier Amplitude Sensitivity Test or EFAST sensitivity analysis in order to provide more insights into the trends that become apparent from the field of optimal vehicles generated. This is an analysis, described in [46] that quantifies the effect various parameters have on the total performance. These insights on why a certain combination of launch-assist parameters generates an interesting compounding effect of added assist energy, minimized losses and maximized vehicle efficiency can be important information for the design of a future launch system. Through this manner, the study purports to help future studies regarding both the launch-assist system as well as the launch vehicle itself. It does not give a detailed description of a specific launch system concept, although the conclusions and recommendations contain some information in that regard. For an overview of specific concepts and launch-assist methods already designed or proposed, the reader is referred to [56].

1.2 Layout of the thesis report

To find an answer to the research question, this body of work will begin in Chapter 2 with the basic theory used to propagate a vehicle, ranging from the reference frames and their relevant transformation matrices to the equations of motion. In Chapter 3 the atmospheric model, the gravitational model, the aerodynamic model, the launch-vehicle model, the thrust model, the guidance model and the trajectory constraint model will be introduced and discussed. A presentation of the numerical integrator is given in Chapter 4 followed by an introduction to the chosen optimization algorithm and its settings in Chapter 5. The assembly of the final simulation tool using external software components, such as PagMO (Parallel Global Multiobjective Optimizer), Tudat (TU Delft Astrodynamics Toolbox), CEA (Chemical Equilibrium with Applications) and Missile DATCOM, is documented in Chapter 6. Finally, the results of the study are presented in Chapter 7 followed by the conclusions and recommendations in Chapter 8.

Chapter 2

Flight Mechanics

This chapter will provide a formulation of the ascent trajectory problem beginning with a description of several reference frames that can be used to describe the motion and the dynamics of the system in section 2.1. This is followed by the definition of the state variables and an outline of the equations of motion in sections 2.2 and 2.3, respectively.

2.1 Reference frames

When a trajectory needs to be simulated, one needs to be able to define a motion or position and at least one frame of reference is therefore needed. The option of using multiple reference frames gives the added benefit that certain equations of motion are easier to be described in one type of reference frame and can then just be translated into another through transformation of vector coordinates from one frame to another. Another reason for using multiple reference frames is that certain definitions of vectors are more sensible in a certain reference frame, while they are not in others. For example, the thrust force vector is easily defined in the body fixed reference frame and a rocket's velocity vector with respect to the Earth's surface has a direct physical meaning. The following chapter will describe the reference frames used in the simulation program. All frames are right-handed orthogonal Cartesian frames:

- Inertial reference frame / Earth-centered inertial reference frame, F_I

  The first frame used is the Earth-centered inertial reference frame. The definition of an inertial reference frame can be derived from Newton's first law. An inertial reference frame is thus a reference frame w.r.t. which a particle remains at rest or in uniform rectilinear motion if no resultant force acts upon that particle. All reference frames that perform a uniform rectilinear translational (non-rotating) motion w.r.t. an inertial reference frame and in which the time differs only by a constant from the time in the inertial reference frame, are inertial.
  The Earth-centered inertial reference frame ($OX_IY_IZ_I$) is a pseudo inertial reference

frame that can only be used as an inertial one as long as the influence of the movement of the Earth around the Sun is very small on the flight of a rocket. Since this is considered to be the case in this study, the frame is approximated as an inertial one. It logically has its origin at the center of mass of the Earth and has its Z_I-axis directed North along the spin-axis of the Earth, which is assumed to be fixed. The X_I-axis passes through the equator at the line where the ecliptic and the equator intersect, it is directed toward the vernal equinox, which is also referred to as the First Point of Aries and denoted by Υ. The Y_I-axis is perpendicular to both the X_I and Z_I axes and completes the right-handed frame. This is the frame in which the state vector is propagated.

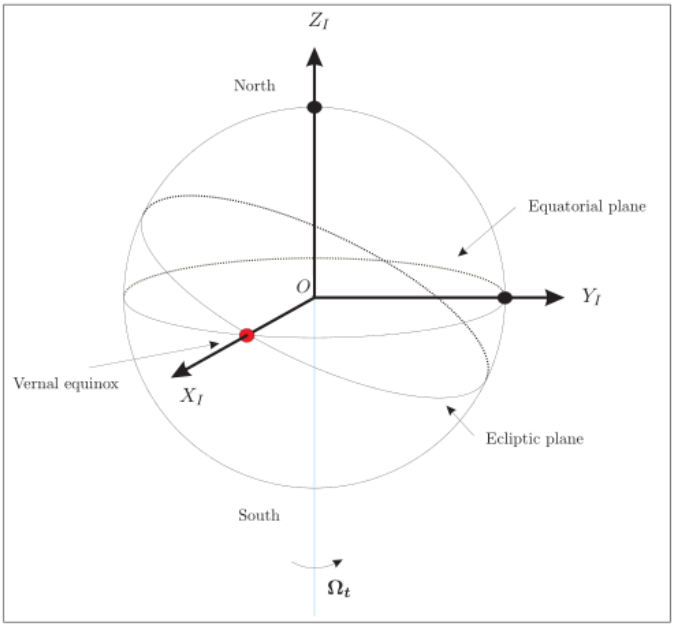

Figure 2.1: Representation of the Earth centered inertial reference frame [33]

- Earth-centered, Earth-fixed reference frame, F_C

  The second reference frame used is the Earth-centered, Earth-fixed reference frame ($OX_CY_CZ_C$). This frame is used to express the motion of the launch vehicle's center of mass w.r.t the Earth's surface. The frame is very similar to the Earth-centered inertial reference frame with equal definitions for both the origin as the Z-axis ($Z_C = Z_I$). The difference is the X-axis: the X_C-axis is defined to intersect the Greenwich meridian in the equatorial plane and not the vernal equinox, which makes it a frame rotating along with the Earth. The Y_C-axis is perpendicular to the X_C and Z_C axes.

- Vehicle-carried normal Earth reference frame, F_E

  The vehicle-carried normal Earth reference frame ($OX_EY_EZ_E$) is also known as the vertical reference frame and has its origin in the vehicle's center of mass. The frame is used as an intermediate reference frame to store the state vector in during state vector transformations. The X_EY_E plane is tangent to the Earth surface. For this the geoid is taken as a reference. The Z_E-axis is directed along the local gravity

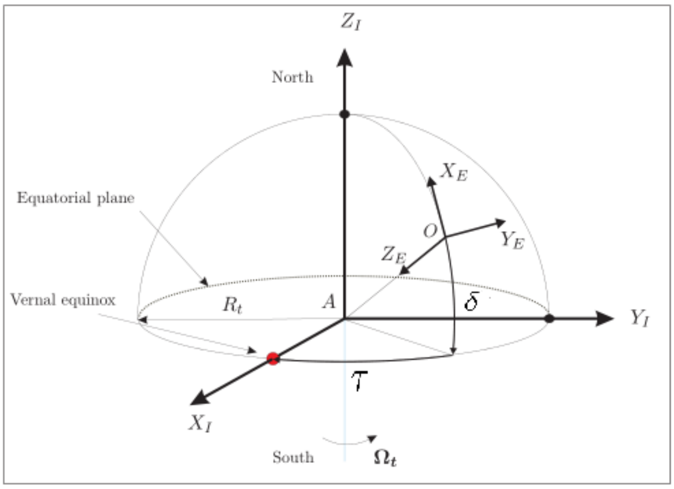

Figure 2.2: Representation of the vehicle-carried normal Earth reference frame for a spherical Earth. Adapted from [33]

vector as seen by the vehicle's center of gravity. The X_E-axis points to the direction of North and the Y_E-axis is perpendicular to the X_E-axis to the East. The frame is depicted in figure 2.2 where τ is the longitude, δ latitude and O is the center of the Earth, which is not the origin of the currently discussed reference frame.

- Body-fixed reference frame, F_B

  The Body-fixed reference frame ($OX_BY_BZ_B$) has a vehicle reference point as its origin and is used to define the orientation of the thrust vector, which is assumed to align with the X_B-axis at all times. The vehicle reference point is mostly the center of mass at t=0. The frame is fixed to the vehicle. The X_B-axis lies in the symmetry plane and points forward, the Z_B-axis also lies in the symmetry plane and points downwards. The Y_B-axis completes the right-handed system.

- Aerodynamic (air-path) reference frame, F_A

  Due to the absence of wind assumed in this study, the groundspeed-based and the airspeed-based aerodynamic reference frames ($OX_AY_AZ_A$) are one and the same. This frame is coupled to the aerodynamic velocity, which is defined as the velocity of the center of mass relative to the undisturbed air and is thus used in the study to define the direction of the drag vector. The origin of the frame is the same as the one of the Body-fixed reference frame and the X_A-axis is in the direction of the aerodynamic velocity. The Z_A-axis is collinear with the aerodynamic lift but opposite in direction and the Y_A-axis completes the right-handed system.

- Trajectory reference frame, F_T

  The origin of the trajectory reference frame ($OX_TY_TZ_T$) lies in the center of mass of the vehicle. The X_T-axis is directed along the velocity vector relative to the rotating Earth-centered, Earth-fixed reference frame. The Z_T-axis is in the vertical plane directed downwards and the Y_T-axis completes the right-handed system. Due to the assumption of no wind during this study, there is no distinction between a groundspeed-based and an airspeed-based trajectory reference frame.

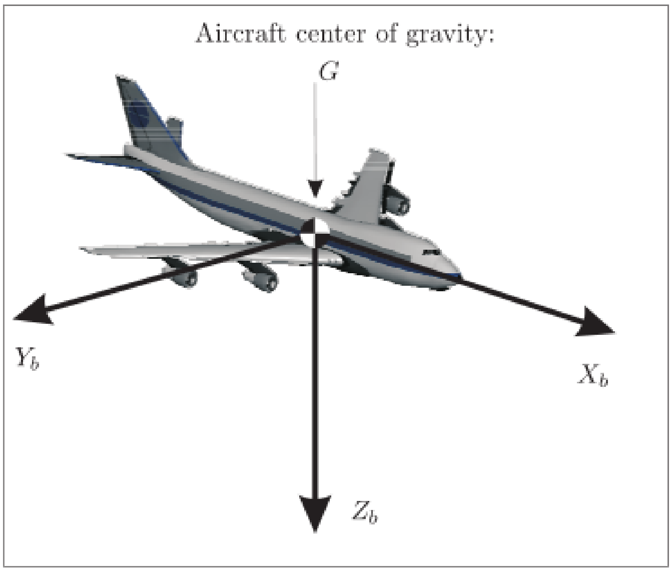

Figure 2.3: Body fixed reference frame for an aircraft [33]

2.2 State variables

In this section, the possible ways of expression of the position and velocity of an object will be discussed. The means presented here are orbital elements, Cartesian components and spherical components.

2.2.1 Orbital elements

Since the goal of a launch is reaching a certain target orbit, a description of the motion of a body around a planet in an elliptical orbit would be needed. Orbital elements are very useful for this purpose and consist out of the following state variables [32]:

- e: the eccentricity, defines the shape of the elliptical orbit. $(0 \leq e < 1)$
- a: the semi-major axis, defines the size of the orbit. $(a > R_e)$
- i: the inclination, defines the orientation of the orbit w.r.t. the Earth's equator. $(0° \leq i \leq 180°)$
- ω: argument of pericenter, defines where the perigee of the orbit is w.r.t. the Earth's surface. $(0° \leq \omega < 360°)$
- Ω: the longitude of the ascending node, defines the location of the ascending and descending orbit locations w.r.t. the Earth's equatorial plane. $(0° \leq \Omega < 360°)$
- θ: true anomaly, defines where the satellite is within the orbit $(0° \leq \theta < 360°)$

The state variables that denote the position and velocity of the object depend on the coordinate system used.

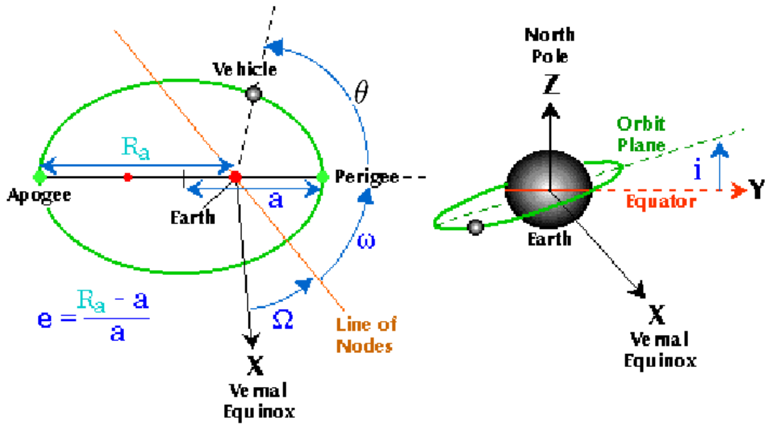

Figure 2.4: Orbital elements [38]

There are many types of coordinate systems, the two most common three dimensional coordinates are Cartesian coordinates and spherical coordinates. In a Cartesian coordinate system a point is specified by the coordinates x, y and z. These values are measured from the origin, which is dependent on the type of reference frame that is used. A vector at a certain point can be specified in terms of three unit vectors $\hat{\imath}$, $\hat{\jmath}$ and $\hat{k}$ that are all perpendicular to each other.
For the Cartesian system the following variables define position and velocity:

- Position: x, y, z
- Velocity: $\dot{x}, \dot{y}, \dot{z}$

In a spherical coordinate system a point is specified by the coordinates r, θ and ϕ. Where r is measured from the origin, τ is measured from the z-axis and δ is measured from the x-axis. A vector at a certain point can also be specified in terms of three unit vectors $\hat{r}$, $\hat{\tau}$ and $\hat{\delta}$ that are all perpendicular to each other. These unit vectors form a right handed set.
For the spherical coordinate system the following variables are used and are expressed w.r.t. the rotating Earth-centered reference frame:

- Position: distance r, longitude τ and latitude δ
- Velocity: speed V, flight-path angle γ and heading χ

The latitude is measured along the meridians and is zero at the equator. It is positive in the northern direction ($-90° \leq \delta < 90°$) The longitude is measured along the circles of latitude positive in the eastward direction ($-180° \leq \tau \leq 180°$). The distance, r, is the distance between the center of mass of the launcher and the center of mass of the Earth. V is the relative velocity (i.e., the modulus of the velocity vector V), γ is the angle between V and the local horizontal plane ($-90° \leq \gamma_G \leq 90°$) and the heading angle, χ, is the projection of V in the local horizontal plane w.r.t. the local North ($-180° \leq \chi_G < 180°$).

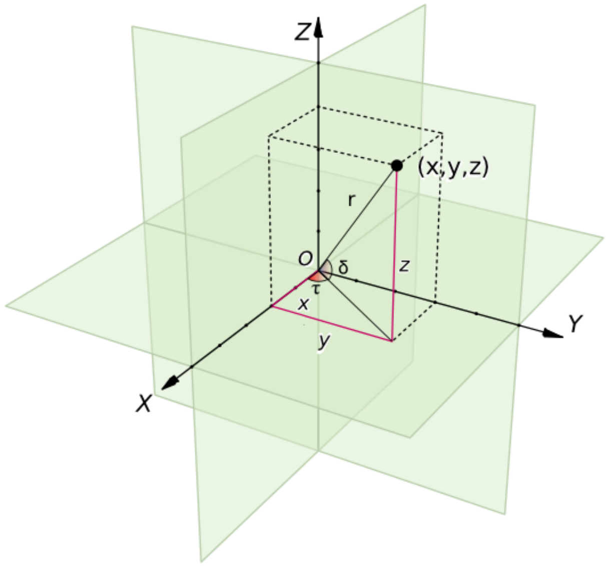

Figure 2.5: Cartesian and spherical coordinate systems [38]

At $\chi = 90°$, the vehicle is moving parallel to the equator to the East.
For simulation of a launch trajectory around a near spherical body, the use of a spherical coordinate system would give a better understanding to the problem. Unfortunately this coordinate system evokes singularities when defining the equations of motion, for instance when the flight-path angle is 90° and -90° [33]. Therefore, Cartesian coordinates will be used to express the equations of motion. Note that γ and χ depend on the velocity vector. Therefore, due to the difference in the flight-path angle between the one in the F_I frame and the one in the F_C frame, two spherical state vectors exist.

2.3 Equations of motion

The equations of motion are based on the three laws of Newton and do not incorporate relativistic effects. These laws are listed below [58]:

- Newton's 1^{st} law: Every particle continues in its state of rest or uniform motion in a straight line relative to an inertial reference frame, unless it is compelled to change that state by forces acting upon it.
- Newton's 2^{nd} law: The time rate of change of linear momentum of a particle relative to an inertial reference frame is proportional to the resultant of all forces acting upon that particle and is collinear with and in the direction of the resultant force.
- Newton's 3^{rd} law: If two particles exert forces on each other, these forces are equal in magnitude and opposite in direction (action = reaction).

It must be mentioned that the first two laws are only valid in an inertial reference frame. Normally inertial reference frames are based on stellar references, however for this study it will also be assumed that the frame in which the motion of the vehicle is propagated, the Earth centered inertial reference frame F_I, is, as the name implies, also an inertial frame and thus the absolute rotational velocity of F_I is assumed negligible. This assumption was made due to two reasons, first of all the study only concerns the launch, which has a small time frame in the order of minutes or hours compared to the time frame, a year, it takes for the Earth to orbit the Sun. Secondly, the fictitious forces in F_I are very small. Considering a non-inertial reference frame B that rotates with angular velocity ω and a particle, P, that has a relative position $\mathbf{r}_{rel}$ with a relative velocity $\mathbf{v}_{rel}$ and a relative acceleration $\mathbf{a}_{rel}$, the acceleration of a particle is described as follows:

$$\mathbf{a}_p = \mathbf{a}_B + (\dot{\omega} \times \mathbf{r}_{rel}) + \omega \times (\omega \times \mathbf{r}_{rel}) + 2(\omega \times \mathbf{v}_{rel}) + \mathbf{a}_{rel} \tag{2.1}$$

The second term involving $\dot{\omega}$, which is called the Euler acceleration, can in the case of F_I be disregarded since the angular velocity of the Earth around the sun is constant ($\omega \approx 1.991 \cdot 10^{-7}$ rad/s). Using a relative position of $6.5 \cdot 10^3$ km, the third term, the centrifugal acceleration becomes $2.57 \cdot 10^{-7}$ m/s^2. Using a relative velocity of 7.8 km/s, the fourth term, the acceleration due to the coriolis force becomes $3.1 \cdot 10^{-3}$ m/s^2. These low values are from hereon out deemed negligible during launch by assuming the Earth centered inertial reference frame to be truly inertial.
In the case of motion of a rigid body, the accompanying equations can be split up in translational and rotational equations. Whilst simulating a launch trajectory, the main interest is in the motion of the center of mass of the vehicle instead of its attitude motions. Neglecting the motion of the vehicle around this center of mass reduces the degrees of freedom to 3 (3 degrees of freedom or 3 DoF). In this study the vehicle is thus assumed to be a point mass because rotational dynamics would require precise knowledge of the launch vehicle configuration for which a launch trajectory is being developed. It would require detailed information about the geometry as well as the mass distribution of the vehicle throughout time. It is far beyond the scope of this study to accurately model this information since it is the objective of this study to not only analyze one single vehicle but a whole array of vehicles with different parameters. This leads to a choice of the 3 DoF simulation, which introduces the assumption that the control system can generate the required moments to change the attitude of the vehicle toward the on-coming flow. This means that all attitude changes are performed instantaneously, which is an oversimplification of reality. To diminish the effect of this oversimplification, the guidance program, which is dictated by the pitch attitude of the vehicle, is modeled as a smooth polynomial, see section 3.6.3.
The governing equation of motion for a rigid body with fixed-mass distribution is [32]:

$$\mathbf{F}_I = m \cdot \frac{d^2\mathbf{r_I}}{dt^2} = m \cdot \frac{d\mathbf{V_I}}{dt} \tag{2.2}$$

where,

- $\mathbf{F}_I$: Total of the external forces expressed in components of the inertial frame [N]
- $\mathbf{r_I}$: Position w.r.t. the inertial reference frame [m]

- $\mathbf{V_I}$: Velocity w.r.t. the inertial reference frame [m/s]

This is a dynamic equation that describes the motion of a body under the influence of external forces. The kinematic equation can be derived from it, which describes the rate of change of position of this body:

$$\frac{d\mathbf{r_I}}{dt} = \mathbf{V_I} \tag{2.3}$$

Using the definition of Cartesian position and velocity given in 2.2.1 the dynamic and kinematic equations of motion can be described as follows:

$$\frac{d\mathbf{V_I}}{dt} = \begin{pmatrix} \ddot{x}_I \\ \ddot{y}_I \\ \ddot{z}_I \end{pmatrix} = \frac{1}{m} \cdot [\mathbf{F}_{A,I} + \mathbf{F}_{G,I} + \mathbf{F}_{T,I}] \tag{2.4}$$

$$\frac{d\mathbf{r_I}}{dt} = \begin{pmatrix} \dot{x}_I \\ \dot{y}_I \\ \dot{z}_I \end{pmatrix} \tag{2.5}$$

where forces $\mathbf{F}$ with the indices A, G and T stand for the aerodynamic, gravitational and thrust force respectively, expressed in the Earth-centered inertial reference frame (index I). These forces are usually expressed in different reference frames. The aerodynamic force is often expressed in the body-fixed reference frame (index B) or the aerodynamic reference frame (index A), the gravitational force is often expressed in the vehicle carried normal Earth reference frame (index E) and the thrust force is also easily expressed in the body-fixed reference frame.
To this purpose the force vectors must be transformed by means of transformation matrices into vectors that apply to the correct reference frame. The required transformations are:

$$\mathbf{F}_{A,I} = \mathbf{C}_{I,B} \cdot \mathbf{F}_{A,B} \tag{2.6}$$

$$\mathbf{F}_{T,I} = \mathbf{C}_{I,B} \cdot \mathbf{F}_{T,B} \tag{2.7}$$

$$\mathbf{F}_{G,I} = \mathbf{C}_{I,E} \cdot \mathbf{F}_{G,E} \tag{2.8}$$

2.3.1 Euler Angles

The attitude of a vehicle relative to an inertial reference frame can be described by three successive rotations through three Euler angles[1]. Only the orientation of the reference frame is described by these Euler angles, no translation takes place through Euler angles.

[1] Named after Leonhard Euler (April 15, 1707 - September 18, 1783), a Swiss mathematician and physicist.

Each rotation should be around a different axis than the one before, resulting in 12 possible sets of Euler angles [33]. Six sets of 'symmetric' Euler angles which use two (non-consecutive) rotations about the same axis:

$$\begin{array}{lll} \alpha_x \to \alpha_y \to \alpha_x, & \alpha_y \to \alpha_x \to \alpha_y, & \alpha_z \to \alpha_x \to \alpha_z \\ \alpha_x \to \alpha_z \to \alpha_y, & \alpha_y \to \alpha_z \to \alpha_x, & \alpha_z \to \alpha_y \to \alpha_x \end{array} \tag{2.9}$$

And six sets of 'asymmetric' Euler angles, which use rotations around all axes:

$$\begin{array}{lll} \alpha_x \to \alpha_y \to \alpha_z, & \alpha_y \to \alpha_x \to \alpha_z, & \alpha_z \to \alpha_x \to \alpha_y \\ \alpha_x \to \alpha_z \to \alpha_x, & \alpha_y \to \alpha_z \to \alpha_y, & \alpha_z \to \alpha_y \to \alpha_z \end{array} \tag{2.10}$$

These sets are also often referred to as a combination of numbers, where 1 represents an Euler angle rotation around the X-axis, 2 an Euler angle rotation around the Y-axis and 3 an Euler angle rotation around the Z-axis

2.3.2 Frame transformations

The information of a single rotation through an Euler angle depends on the particular axis around which the rotation is performed. This information is transferred through the form of transformation matrix, which transforms the original definition of a vector in the original reference frame. In these transformation matrices the angle α, is the angle by which the reference frame is rotated around the X, Y or Z axes. The following matrices are transformation matrices for rotation around the X-axis, Y-axis and Z-axis respectively [33] [32].

$$\mathbf{C}_X(\alpha_x) = \begin{pmatrix} 1 & 0 & 0 \\ 0 & \cos\alpha_x & \sin\alpha_x \\ 0 & -\sin\alpha_x & \cos\alpha_x \end{pmatrix} \tag{2.11}$$

$$\mathbf{C}_Y(\alpha_y) = \begin{pmatrix} \cos\alpha_y & 0 & -\sin\alpha_y \\ 0 & 1 & 0 \\ \sin\alpha_y & 0 & \cos\alpha_y \end{pmatrix} \tag{2.12}$$

$$\mathbf{C}_Z(\alpha_z) = \begin{pmatrix} \cos\alpha_z & \sin\alpha_z & 0 \\ -\sin\alpha_z & \cos\alpha_z & 0 \\ 0 & 0 & 1 \end{pmatrix} \tag{2.13}$$

The transformation matrix $\mathbf{C}_{i,j}$ denotes a transformation from the j-frame to the i-frame. This matrix is equal to both the inverse as well as the transpose of the transformation matrix from the i-frame to the j-frame, see Eq. (2.14).

$$\mathbf{C}_{j,i} = \mathbf{C}_{i,j}^{-1} = \mathbf{C}_{i,j}^{T} \tag{2.14}$$

With this information the transformation matrix for an entire Euler angle set can be calculated. Consider the rotation sequence $\alpha_x \rightarrow \alpha_y \rightarrow \alpha_x$ also called a 3-2-1 transformation. The transformation for the entire rotation is described by [33]:

$$\begin{aligned}
\mathbf{v}_2 &= \mathbf{C}_X(\alpha_x)\cdot\mathbf{C}_Y(\alpha_y)\cdot\mathbf{C}_Z(\alpha_z)\\
&= \begin{pmatrix}1 & 0 & 0\\ 0 & \cos\alpha_x & \sin\alpha_x\\ 0 & -\sin\alpha_x & \cos\alpha_x\end{pmatrix}\cdot\begin{pmatrix}\cos\alpha_y & 0 & -\sin\alpha_y\\ 0 & 1 & 0\\ \sin\alpha_y & 0 & \cos\alpha_y\end{pmatrix}\cdot\begin{pmatrix}\cos\alpha_z & \sin\alpha_z & 0\\ -\sin\alpha_z & \cos\alpha_z & 0\\ 0 & 0 & 1\end{pmatrix}\\
&= \begin{pmatrix}\cos\alpha_y\cos\alpha_z & \cos\alpha_y\sin\alpha_z & -\sin\alpha_y\\ \sin\alpha_x\sin\alpha_y\cos\alpha_z-\cos\alpha_x\sin\alpha_z & \sin\alpha_x\sin\alpha_y\sin\alpha_z+\cos\alpha_x\cos\alpha_z & \sin\alpha_x\cos\alpha_y\\ \cos\alpha_x\sin\alpha_y\cos\alpha_z+\sin\alpha_x\sin\alpha_z & \cos\alpha_x\sin\alpha_y\sin\alpha_z-\sin\alpha_x\cos\alpha_z & \cos\alpha_x\cos\alpha_y\end{pmatrix}
\end{aligned} \tag{2.15}$$

Earth centered Inertial reference frame (F_I) to Earth-Centered, Earth-fixed reference frame (F_C).

The two frames are nearly identical to each other with the sole difference that the F_C-frame is rotating along with the central body. They are defined to coincide at $t = 0$.
The transformation matrix can be derived using the following variables,

- Ω_t = rotational rate of the Earth (rad/s)
- t = time from epoch (s)

$$\mathbf{C}_{C,I} = \mathbf{C}_Z(\Omega_t t) = \begin{pmatrix}\cos\Omega_t t & -\sin\Omega_t t & 0\\ \sin\Omega_t t & \cos\Omega_t t & 0\\ 0 & 0 & 1\end{pmatrix} \tag{2.16}$$

Earth centered Earth-fixed reference frame (F_C) to vehicle carried normal Earth reference frame (F_E)

For this transformation, two consecutive rotations are required.

- $-\tau$ about the Z_C-axis
- $\frac{\pi}{2} + \delta$ about the Y_E-axis

The transformation matrix then becomes [32]:

$$\mathbf{C}_{E,C} = \mathbf{C}_Y(\frac{\pi}{2}+\delta)\cdot\mathbf{C}_Z(-\tau) = \begin{pmatrix}-\sin\tau\sin\delta & -\sin\tau & -\cos\tau\cos\delta\\ -\sin\tau\sin\delta & \cos\tau & -\sin\tau\cos\delta\\ \cos\delta & 0 & -\sin\delta\end{pmatrix} \tag{2.17}$$

Vehicle carried normal Earth reference frame (F_E) to body-fixed reference frame (F_B)

For this transformation, three consecutive rotations are required.

- ψ Yaw angle about the Z_E-axis
- θ pitch about the Y_E'-axis[2]
- φ roll angle about the X_B-axis

The transformation matrix then becomes the same as in (2.15) [33]:

$$\begin{aligned}\mathbf{C}_{B,E} &= \mathbf{C}_X(\varphi)\cdot\mathbf{C}_Y(\theta)\cdot\mathbf{C}_Z(\psi)\\ &= \begin{pmatrix}\cos\theta\cos\psi & \cos\theta\sin\psi & -\sin\theta\\ \sin\varphi\sin\theta\cos\psi-\cos\varphi\sin\psi & \sin\varphi\sin\theta\sin\psi+\cos\varphi\cos\psi & \sin\varphi\cos\theta\\ \cos\varphi\sin\theta\cos\psi+\sin\varphi\sin\psi & \cos\varphi\sin\theta\sin\psi-\sin\varphi\cos\psi & \cos\varphi\cos\theta\end{pmatrix}\end{aligned} \tag{2.18}$$

Earth centered Inertial reference frame (F_I) to vehicle carried normal Earth reference frame (F_E)

This transformation matrix can be obtained by simply multiplying two of the previously found transformation matrices.

$$\mathbf{C}_{E,I} = \mathbf{C}_{E,C}\cdot\mathbf{C}_{C,I} \tag{2.19}$$

Earth centered Inertial reference frame (F_I) to body-fixed reference frame (F_B)

This transformation matrix can be obtained by simply multiplying two of the previously found transformation matrices.

$$\mathbf{C}_{B,I} = \mathbf{C}_{B,E}\cdot\mathbf{C}_{E,I} \tag{2.20}$$

Vehicle carried normal Earth reference frame (F_E) to trajectory reference frame (F_T)

To make a transformation between these two reference frames the following matrix needs to be used [38]:

$$\mathbf{C}_{T,E} = \mathbf{C}_Y(\gamma)\cdot\mathbf{C}_Z(\chi) = \begin{pmatrix}\cos\gamma\cos\chi & \cos\gamma\sin\chi & -\sin\gamma\\ -\sin\chi & \cos\chi & 0\\ \sin\gamma\cos\chi & \sin\gamma\sin\chi & \cos\gamma\end{pmatrix} \tag{2.21}$$

where γ is the flight-path angle and χ is the heading angle.

[2]The Y_E'-axis is the Y-axis after the first rotation.

Aerodynamic reference frame (F_A) to vehicle carried normal Earth reference frame (F_E)

To make a transformation between these two reference frames, three consecutive rotations are required.

- σ_A aerodynamic bank angle about the X_A-axis
- $-\gamma_A$ aerodynamic flight-path angle about the Y_A'-axis[3]
- $-\chi_A$ aerodynamic heading angle about the Z_E-axis

These rotations result in the following matrix [32]:

$$\begin{aligned}\mathbf{C}_{A,E} &= \mathbf{C}_Z(-\chi_A)\cdot\mathbf{C}_Y(-\gamma_A)\cdot\mathbf{C}_X(\sigma_A)\\ &= \begin{pmatrix}\cos\chi_A\cos\gamma_A & -\sin\chi_A\cos\sigma_A-\cos\chi_A\sin\gamma_A\sin\sigma_A & -\sin\chi_A\sin\sigma_A+\cos\chi_A\sin\gamma_A\cos\sigma_A\\ \sin\chi_A\cos\gamma_A & \cos\chi_A\cos\sigma_A-\sin\chi_A\sin\gamma_A\sin\sigma_A & \cos\chi_A\sin\sigma_A+\sin\chi_A\sin\gamma_A\cos\sigma_A\\ -\sin\gamma_A & -\cos\gamma_A\sin\sigma_A & \cos\gamma_A\cos\sigma_A\end{pmatrix}\end{aligned} \tag{2.22}$$

[3]The Y_A'-axis is the Y-axis after the first rotation.

Chapter 3

Models

This chapter provides an overview of all the different models that are used to simulate the conditions that occur during space launch. The chapter begins with an overview of the environment in section 3.1, which consists out of an atmospheric model (section 3.1.1) and the gravitational model (section 3.1.2). This is followed by the aerodynamic model in section 3.2 and an elaborate discussion of the launch vehicle model in section 3.3 where two sub models are presented, namely the launch vehicle performance model (section 3.3.1) and the launch vehicle mass model (section 3.3.2). The chapter is then completed with a description of the guidance model in section 3.6 and the trajectory constraint model in section 3.7.

3.1 Environment models

The environment in which the flight of the rocket is undertaken, has a significant impact on the performance of the launch system. For this reason it must be modeled accurately. In this section, both the atmospheric model and the gravitational model will be discussed.

3.1.1 Atmospheric model

Due to the influence of the atmosphere on the flight path of a vehicle, a thorough understanding of atmospheric properties is required and the atmosphere needs to be adequately modeled to provide realistic results and comparisons regarding different launch methods. The real atmosphere does not remain constant. At a different time, a change in temperature, density and pressure at any height and place on Earth will take place. In the real atmosphere, the actual performance of a vehicle does not provide a reliable basis in comparison with other vehicles. For these reasons, the need for standardization arises and a number of atmospheric models has been developed. These models can be put in either one of two groups. Either the model is a standard atmospheric model or it is a reference atmospheric model. The standard models only give atmospheric properties with changing position while the reference model can also take temporal, seasonal, geomagnetic and solar effects into account. Some simpler reference atmosphere models just involve a temperature or humidity offset from a standard atmosphere model and its standard day temperature gradient. This takes into account that the geometric height, Z, of the tropopause is increased on a hot day since increasing temperature causes the atmosphere to expand upwards. However, since this simulations aims to provide a comparison between multiple launches, they all are required to undergo the same circumstances. Therefore the simplicity of the models become a more important factor and the simplicity of the US 1976 standard atmosphere model was the reason why it was decided in [56] that it would be used in the simulations.

Standard atmospheric model, US 1976

One of the standard atmospheric models in common use is the US standard atmosphere of 1976, which will be shortly presented here [11]. This model is defined in terms of the International System (SI) of units and is identical to the standard atmosphere of the International Civil Aviation Organization (ICAO) below 32 km. The model presents values for atmospheric parameters from the Earth's surface up to an altitude of 1000 km at a latitude of 45° North. The temperature of this model is given by the following equation below 86 km geometric altitude [11]:

$$T_M = T_{M,b} + L_{M,b} \cdot (H - H_b) \tag{3.1}$$

where T_M is the molecular scale temperature with the value of subscript b ranging from 0 to 6 in accordance with each of the seven successive layers that are defined below 86 km, T_{M_0} is equal to T_0 and has the value of 288.15 K. L_M is the molecular scale temperature gradient and is given in Table 3.1. H_b stands for the geopotential height, which is an adjustment of geometric height using the variation of gravity with elevation.

Table 3.1: Defined reference levels and gradients [11]

Subscript b	Geopotential Height H_b [km']	Molecular scale temperature gradient $L_{M,b}$ [K/km']	Form of function relating T to H
0	0	-6.5	Linear
1	11	0	Linear
2	20	+1	Linear
3	32	+2.8	Linear
4	47	0	Linear
5	51	-2.8	Linear
6	71	-2.0	Linear
7	84.852	-6.5	Linear

The unit of measurement of geopotential altitude is the standard geopotential meter [m'], which represents the altitude over which the same work is done for lifting a unit mass as would be done when lifting that unit mass 1 geometric meter, through a region in which the acceleration of gravity is uniformly 9.80665 m/s^2.
A conversion from geopotential altitude and back can be made using the following formula [11]:

$$Z = \frac{r_0 \cdot H}{r_0 - H} \tag{3.2}$$

where Z is the geometric altitude and r_0 is the radius of the Earth and has the value of 6,356,766 m for the US 1976 standard atmosphere.
For higher altitudes Eq. (3.1) does not longer hold. From 86 to 91 km there is an isothermal layer modeled where the temperature stays at 186.8673 K. For the layer between 91 an 110 km Eq. (3.3) holds [11].

$$T = T_c + A \cdot \left(1 - \left(\frac{Z - Z_8}{a}\right)^2\right)^{(1/2)} \tag{3.3}$$

where A = -76.3232 K and a = -19.9429 km.
For the next layer between 110 and 120 km the temperature follows the following relationship [11]:

$$T = T_9 + L_{K,9} \cdot \ (Z - Z_9) \tag{3.4}$$

And finally for the layer between 120 and 1000 km [11]:

$$T = T_\infty - (T_\infty - T_{10}) \cdot \exp(-\lambda\xi) \tag{3.5}$$

where $\lambda = L_{K,9}/(T_\infty - T_{10})$ and $\xi = (Z - Z_{10}) \times (r_0 + Z_{10})/(r_0 + Z)$.
In the above expressions, T_∞ is the exospheric temperature defined at 1000 K.
The model has two different equations for computing pressure at various regions below an altitude of 86 km. The first of these equations is the following [11]:

$$P = P_b \cdot \left(\frac{T_{M,b}}{T_{M,b} + L_{M,b} \cdot (H - H_b)}\right)^{\left(\frac{g_0 \cdot M_0}{R^* \cdot L_{M,b}}\right)} \tag{3.6}$$

where R^* is the gas constant with the value 8.31432 $\cdot$ 10^3 Nm/kmol K. This equation is used when the molecular scale temperature lapse rate is not equal to zero [11].

$$P = P_b \cdot \exp\left(\frac{-g_0 \cdot M_0 \cdot (H - H_b)}{R^* \cdot T_{M,b}}\right) \tag{3.7}$$

In these equations g_0, M_0 and R^* are single valued constants, while $L_{M,b}$ and H_b are multi valued constants, meaning that they have a different value for each layer. M_0 is the

molecular weight of the atmosphere at sea level which stays constant throughout layers 0-6 up to a geometric altitude of 86 km and holds the value of 28.964 kg/kmol. The reference value for P_b for b = 0 is the defined sea level value, $P_0 = 101325$ N/m^2. Values for P_b with b = 1 through 6 can be obtained by applying these equations to find the value of the upper boundary of the previous layer.
For an altitude between 86 and 1000 km the pressure is computed as a function of geometric altitude and involves the altitude profile of kinetic temperature T rather than that of T_M [11]:

$$P = \sum P_i = \sum n_i \cdot k \cdot T = \frac{\sum n_i \cdot R^* \cdot T}{N_A} \tag{3.8}$$

where the Boltzmann constant, $k = 1.380622 \times 10^{-23}$ Nm/K, N_A is the Avogadro constant, $6.022169 \cdot 10^{26}$ kmol^{-1} and $\sum n_i$ = the sum of the number densities of the individual gas species comprising the atmosphere at an altitude above 86 km.
For all layers that make up the US 1976 model, the temperature and pressure are known by the aforementioned equations. The only relevant parameter concerning aerodynamic forces is the density. This can be solved by assuming the atmosphere to be a perfect gas where the ideal gas law holds:

$$\rho = \frac{P \cdot M}{R^* \cdot T} \tag{3.9}$$

The model that was used in the simulation and is based on these equations summarized above follows all equations up to a geometric height of 120 km. Above this altitude the atmosphere is assumed to be non-existent.

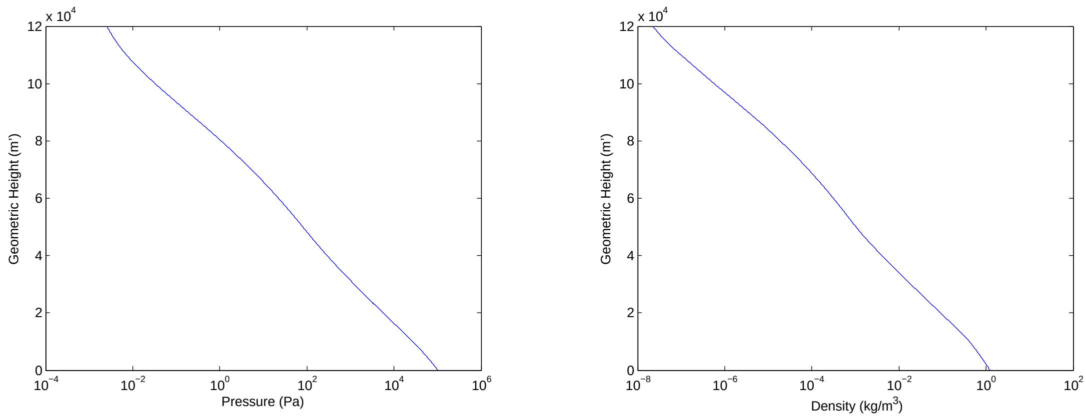

(a) (b)

Figure 3.1: Pressure (a) and density (b) to geometric height profiles generated by the model.

3.1.2 Gravitational model

Gravity is a very important force that acts on the vehicle. It is in most situations the main external force that determines the movement of a vehicle through space. This force

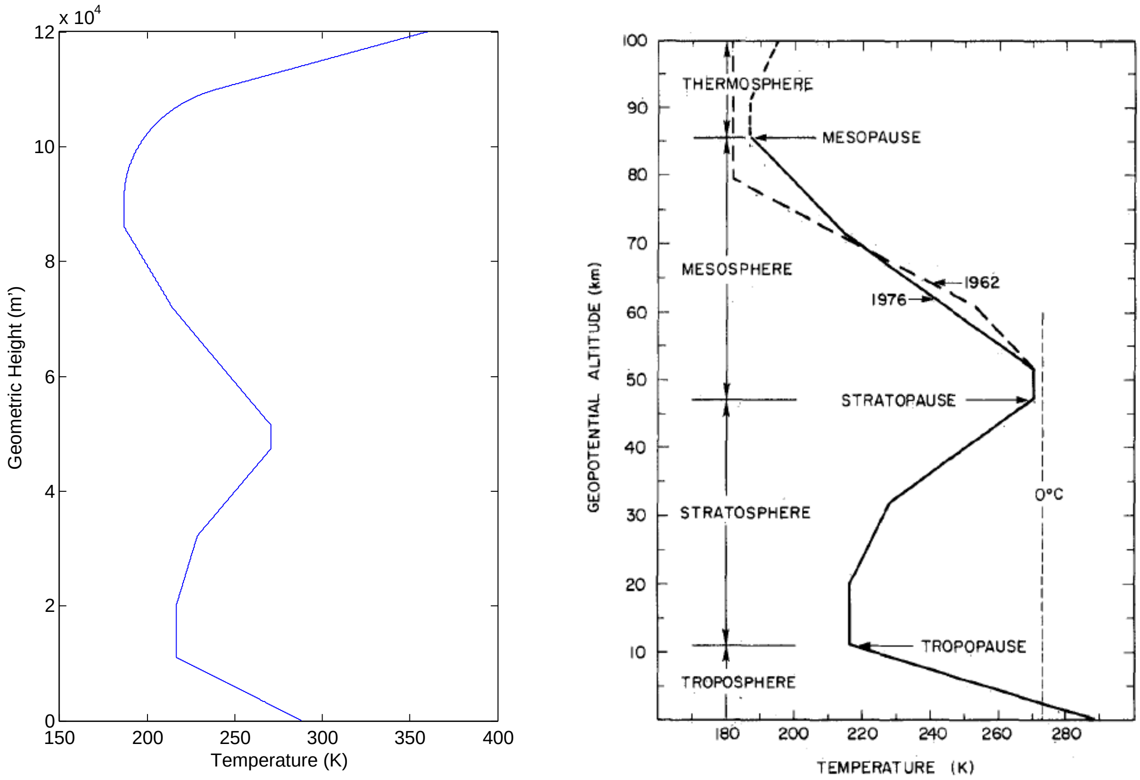

(a) (b)

Figure 3.2: A comparison of the temperature (in Kelvin) - geometric height profile of the model (a) and from literature (b) [8], which also shows the changes between US 1976 and US 1962.

can be written as follows:

$$\mathbf{F}_G = m \cdot \mathbf{g} \tag{3.10}$$

where m is the mass of the vehicle and $\mathbf{g}$ is the gravitational acceleration vector.
One can model this force by just assuming that the value of g is a constant (e.g., $g = g_0 = 9.80665$ m/s^2). This is a major oversimplification since in fact the value of g varies with position. Another way to model the gravitational acceleration vector is by assuming the Earth to be a point mass or homogeneous sphere with a mass of $5.9742 \cdot 10^{24}$ kg (M_E) [55]. In this case, the value of $\mathbf{g}$ would be governed by the gravitational force equation that Newton established in 1666 and describes the force of gravity between two point masses, A and B as follows:

$$\mathbf{F}_A = -G \frac{M_A \cdot M_B}{r_{AB}^2} \mathbf{e}_{AB} \tag{3.11}$$

where G stands for the Universal Gravitational Constant and has a value of $6.668 \cdot 10^{-11}$ Nm^2/kg^2, M_A and M_B are the masses of the two objects and r_{AB} is the distance between

the two objects that attract each other. [58]
In the case of attraction between the Earth and a man-made vehicle, the mass of the vehicle is negligible compared to the mass of the Earth and Eq. (3.11) becomes:

$$\mathbf{F}_G = -G\frac{M_E}{r^3}\mathbf{r} \tag{3.12}$$

This model is called the central gravity field model. It is incorrect to a certain extent because it does not take the heterogeneous distribution of mass of the Earth into account. Only a more complex model can take effects as the flattening of the Earth into account. Gravity can sometimes be defined as the sum of the gravitational acceleration with the centrifugal acceleration. In this definition gravity will be the force that is perceived by the observer The centrifugal acceleration is given by Eq. (3.13)

$$\nabla\Phi = -\omega \times (\omega \times \mathbf{r}) \tag{3.13}$$

This gives for the centrifugal potential written in rectangular coordinates:

$$\mathbf{\Phi} = \frac{\omega^2}{2}(x^2 + y^2) \tag{3.14}$$

The gravity potential is then defined as the sum of the gravitational potential and the centrifugal potential.
This gravitational potential can be written as following:

$$\mathbf{V}(\mathbf{P}) = G\int\int\int \frac{\rho(Q)}{\mathbf{l}_{PQ}}\mathrm{d}\sum_Q \tag{3.15}$$

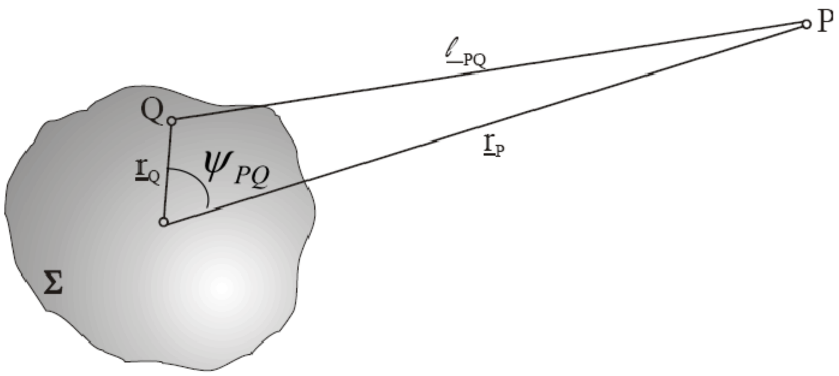

Figure 3.3: Location of P and Q [23]

This is an integration performed over the whole body (i.e. Earth) presented in figure 3.3. The vector $\mathbf{l}_{PQ}$ between the body with negligible mass in P and a random element at Q, part of the main body, can be rewritten in a series expansion with legendre polynomials and eventually a so-called harmonic expansion model arises where the satellite position is expressed in spherical coordinates w.r.t. the center of mass of the Earth: $\mathbf{r}$ (distance), ϕ (latitude) and θ (longitude): [37]

$$\mathbf{V}(\mathbf{P}) =$$
$$-\frac{\mu}{\mathbf{r}}\left(1-\sum_{n=2}^{\infty} J_n\left(\frac{\mathbf{R}_e}{\mathbf{r}}\right)^n P_n(\sin\phi)+\sum_{n=2}^{\infty}\sum_{m=1}^{n} J_{n,m}\left(\frac{\mathbf{R}_e}{\mathbf{r}}\right)^n P_{n,m}(\sin\phi)\cos\left(m(\theta-\theta_{n,m})\right)\right) \tag{3.16}$$

where

$$P_{n,m}(x) = (1-x^2)^{m/2}\frac{d^m P_n(x)}{dx^m} \tag{3.17}$$

and

$$P_n(x) = \frac{1}{(-2)^n n!}\frac{d^n}{dx^n}(1-x^2)^n \tag{3.18}$$

$P_{n,m}(x)$ is a Legendre function. When m is zero one speaks of legendre polynomials. The parameters n and m denote the degree and order of the expansion terms, respectively. The coefficients $J_{n,m}$ and $\lambda_{n,m}$ are scaling and orientation parameters.
It should be noted that the terms ($n = 1$, $m = 0$) and ($n = 1$, $m = 1$) are absent since the origin of the gravity field is assumed to coincide with the center of mass of the Earth. Based on measurements from satellite data, aerial data and terrain data, values for coefficients can be assigned. Since the function uses an infinite sum, the gravity field can be copied perfectly. Due to the accuracy of the measurements only values for a degree of around 3600 can be established, which provides a very high accuracy. In Table 3.2 the values of degree 2 and 3 are given.

Table 3.2: Numerical values of low degree gravitational coefficients of the Earth's gravity field [37]

n (degree)	m (order)	$J_{n,m}$ $[10^{-6}]$	$\lambda_{n,m}$ [deg]
2	0	1082.6267	0.0
2	1	0.0016	98.9
2	2	1.8154	-14.9
3	0	-2.5327	0.0
3	1	2.2090	7.0
3	2	0.3744	-17.2
3	3	0.2214	21.0

As one can see, $J_{2,0}$ is far larger than any of the other scaling coefficients. This is due to the fact that $J_{2,0}$ represents the effect of the flattening of the Earth due to the Earth's rotation. The $J_{3,0}$ coefficient, which is the second largest, gives the gravity field a pear shape which is predominantly due to the location of the continents on Earth.

Since $J_{3,0}$ already has a very small value, some models only use $J_{2,0}$ in their model. This leads to the following equation:

$$\mathbf{V}_{J_2} = -\frac{\mu}{\mathbf{r}}\left(1 - \left(\frac{\mathbf{R}_e}{\mathbf{r}}\right)\right)^n \cdot J_2 \cdot P_2 \sin\phi \tag{3.19}$$

Using the definition of the Legendre polynomial $P_2(t)$ [26],

$$P_2(t) = \frac{3t^2 - 1}{2} \tag{3.20}$$

one obtains

$$\mathbf{V}_{J_2} = -\frac{\mu}{\mathbf{r}}\left(1 + \frac{J_2\mathbf{R}_e^2}{2\mathbf{r}^2}[1 - 3\sin\phi^2]\right) \tag{3.21}$$

Replacing $sin\phi$ with z/r and adding centrifugal potential due to Earth rotation to V_{J_2}, one obtains the gravity potential.

$$\mathbf{U}_{J_2} = -\frac{\mu}{\mathbf{r}}\left(1 + \frac{J_2\mathbf{R}_e^2}{2\mathbf{r}^2}[1 - \frac{3z^2}{\mathbf{r}^2}]\right) + \frac{\boldsymbol{\omega}^2}{2}(x^2 + y^2) \tag{3.22}$$

The three components of the gravity vector are then the three partial derivatives of U_{J_2}:

$$\mathbf{g}_x = -\frac{x\mu}{\mathbf{r}^3}\left(1 + \frac{3J_2\mathbf{R}_e^2}{2\mathbf{r}^2} - \frac{15J_2\mathbf{R}_e^2 z^2}{2\mathbf{r}^4}\right) + x\boldsymbol{\omega}^2 \tag{3.23}$$

$$\mathbf{g}_y = -\frac{y\mu}{\mathbf{r}^3}\left(1 + \frac{3J_2\mathbf{R}_e^2}{2\mathbf{r}^2} - \frac{15J_2\mathbf{R}_e^2 z^2}{2\mathbf{r}^4}\right) + y\boldsymbol{\omega}^2 \tag{3.24}$$

$$\mathbf{g}_z = -\frac{z\mu}{\mathbf{r}^3}\left(1 + \frac{9J_2\mathbf{R}_e^2}{2\mathbf{r}^2} - \frac{15J_2\mathbf{R}_e^2 z^2}{2\mathbf{r}^4}\right) \tag{3.25}$$

It has been numerically determined that the difference due to the J_2 effect is less than 5 μg in all three components [26]. This means that in the event of a launch trajectory where the gravity loss amounts to 1000 m/s, the J_2 effect amounts to just 0.005 m/s in ΔV. The other coefficients are, as already pointed out, significantly smaller and not incorporating them in the model would only evoke a small discrepancy between the model and the actual Earth gravity field. The J_3 effect for instance, which is about one five hundredth of the J_2 effect, amounts to 0.00001 m/s and is thus totally negligible. For the same reason also the J_2 effect is discarded in favor for implementation of the central gravity field model.

3.2 Aerodynamic model

During launch, the vehicle penetrates the atmosphere to reach its goal: space orbit. Every vehicle that moves through the atmosphere is being influenced by aerodynamic forces that in turn have an effect on the trajectory of the vehicle. The magnitude of these forces are dependent on the velocity w.r.t. the atmosphere, the attitude and shape of the vehicle and the properties (temperature, density and pressure) of the atmosphere.

3.2.1 Aerodynamic forces

Aerodynamic forces arise due to the pressure and the skin friction of air when an object moves through it. A rocket mostly does this while having an incident angle. This so called angle of attack should be kept small in order to avoid high drag losses. The resultant force that the airflow implements upon the vehicle is in this model divided into three components: these are called the lift, the drag and the side force components. The side force component is during the model always equal to zero since there is no wind considered and the rocket is standard directed to fly at constant azimuth with a non-existent side slip angle. However, the model is capable to cope with the introduction of a side slip angle. The drag is defined parallel to the velocity vector, while the lift and the side force are defined perpendicular to it in the aerodynamic reference frame, F_A, as follows:

$$D = -F_{X,AA} \tag{3.26}$$

$$S = -F_{Y,AA} \tag{3.27}$$

$$L = -F_{Z,AA} \tag{3.28}$$

They satisfy the following relations:

$$D = C_D \frac{1}{2} \rho V^2 S_{ref} \tag{3.29}$$

$$S = C_S \frac{1}{2} \rho V^2 S_{ref} \tag{3.30}$$

$$L = C_L \frac{1}{2} \rho V^2 S_{ref} \tag{3.31}$$

where C_L is the lift coefficient ,C_D is the drag coefficient, C_S is the side force coefficient, ρ is the density of the atmosphere, V is the velocity relative to the atmosphere, and S_{ref} is the aerodynamic reference surface., which corresponds to the cross-sectional area of the body.

The three coefficients are dependent on the Mach number, the Reynolds number, the altitude, vehicle configuration, control surfaces, the side slip angle, β, and the angle of attack, α [44].

In order to obtain these coefficients, the off-the-shelf program code, Missile DATCOM is used for the simulations. The Missile DATCOM program is obtained as a supplement CD of the book "Design Methodologies for Space Transportation Systems", by Walter E. Hammond [24]. The program can be directly implemented in the larger simulation tool although it was quickly discovered that this severely increases the computational load. Therefore, it was chosen to construct a database of several launcher configurations. A configuration contained in that database (all are listed in table 3.3) is chosen to serve as the aerodynamic model when the estimated length and diameter of the stage are closest to values of the specific configuration. All these configurations were standard equipped

Table 3.3: Missile DATCOM database configuration matrix

L (m)	10	12.5	15	20	25	30	40	50	60	80	100
	0.5	0.625	0.75	1	1.25	1.5	2	2.5	3	4	5
	0.625	0.78125	0.9375	1.25	1.5625	1.875	2.5	3.125	3.75	5	6.25
	0.75	0.9375	1.125	1.5	1.875	2.25	3	3.75	4.5	6	7.5
	0.875	1.09375	1.3125	1.75	2.1875	2.625	3.5	4.375	5.25	7	8.75
	1	1.25	1.5	2	2.5	3	4	5	6	8	10
	1.25	1.5625	1.875	2.5	3.125	3.75	5	6.25	7.5	10	12.5
	1.5	1.875	2.25	3	3.75	4.5	6	7.5	9	12	15
D (m)	1.75	2.1875	2.625	3.5	4.375	5.25	7	8.75	10.5	14	17.5
	2	2.5	3	4	5	6	8	10	12	16	20
	2.5	3.125	3.75	5	6.25	7.5	10	12.5	15	20	25
	3	3.75	4.5	6	7.5	9	12	15	18	24	30
	3.5	4.375	5.25	7	8.75	10.5	14	17.5	21	28	35
	4	5	6	8	10	12	16	20	24	32	40
	4.7	5.9	7	9.5	12	14	19	23	28	37	47
	5.5	6.875	8.25	11	13.75	16.5	22	27.5	33	44	55

with a tangent ogive nosecone without any lifting surfaces and the sole difference between one and another are their respective lengths and diameters. This method of working with a database instead of working with a computationally intensive integrated Missile DATCOM program was validated by using both methods to run a simulation. The simulation performed had as assist conditions a velocity of 2,000 m/s and an altitude of 40 km. The simulation utilizing the Missile DATCOM database found after 1000 generations of 20 individuals a maximum payload to initial mass ratio injected into a circular 200 km high orbit of 0.18965 and a population average of 0.17535. The simulation with the integrated Missile DATCOM program found a maximum payload ratio of 0.18855 and a population average of 0.17534. These differences between these results fall within the noise of two different optimization runs and can therefore be assumed to be negligible. In section 6 the Missile DATCOM and its implementation in the simulation program is further discussed.

3.3 Launch-vehicle model

The computer simulation program is designed to perform multi disciplinary optimization. This means, in this case, that it optimizes both the launch trajectory as well as the launch vehicle model. This section gives an explanation of that launch-vehicle model, which subdivisions it has, and how these interact with each other and how the whole model interacts with the trajectory further on explained in the guidance model, see section 3.6. The launch vehicle model is subdivided into two smaller sections or models. These are identified as follows:

- The performance model

- The mass model

The main focus of the performance model is providing a decent assumption for the thrust of the launch vehicle. The mass model and the aerodynamic model evidently focus on an estimate of the mass and the aerodynamic characteristics of the vehicle, respectively. The vehicle model requires the following inputs:

- Choice of propellant between a refined petroleum oxygen mixture (RP1/LOX) and a hydrogen oxygen mixture (LH2/LOX), often referred to as kerolox and hydrolox.
- The oxidizer-to-fuel ratio
- The chamber pressure
- The combined length of the propellant tanks
- The diameter of the tanks
- The nozzle exit pressure
- The nozzle exit diameter

3.3.1 Performance Model

The choice of propellant in combination with a given oxidizer to fuel ratio and chamber pressure is enough to establish γ, the ratio of specific heats, the molar mass, M, and the chamber temperature, T_c. This is done effectively by linear interpolation of values stored in a data sheet. The data include values for all of these three variables for a total of 627[1] combinations of oxidizer-to-fuel ratios and chamber pressures for both propellant choices. These values were gathered from the NASA Glen Equilibrium Program also known as CEA [7]. Further explanation of this program is given in section 6. The chamber pressures used range with incremental steps of 8 bar from 8 up to 264 bar. Likewise, the oxidizer to fuel ratios range with incremental steps of 0.5 from 1 up to 10. The results from this program are published in Appendix A. Having this information in place, the rest of the performance model only exists of relations between change in pressure, temperature and thermal energy over the nozzle to the exhaust velocity, i.e., change in velocity of the gas flow using basic laws of mechanics and thermodynamics. These relations are also known as ideal rocket motor theory. The assumptions needed for this theory are quoted below [65]:

The exhaust gases are homogeneous and have a constant composition. As in many solid propellant rockets metal powder is added, which is expelled in solid or liquid state, the combustion gases are not always homogeneous. As the temperature decreases when the gases are expanded through the nozzle, the chemical equilibrium changes and thus the composition of the gases is not constant. - The gas or gas mixture expelled obeys the ideal gas law. The ideal gas law, or universal gas equation, is an equation of state of an

[1] 19 different oxidizer-to-fuel ratios for each of all 33 chamber pressures

ideal gas. It relates the pressure p of a gas with the volume V it occupies, the number to moles of the gas n, and the gas temperature1. The ideal gas law is valid for ideal gases only.Real gases obey this equation only approximately, but its validity increases as the density of the gas tends to zero. - The heat capacity of the gas or mixture of gases expelled is constant. In reality the heat capacity depends on the temperature and composition of the expelled matter and neither of them is constant. - The flow through the nozzle is one-dimensional, steady and isentropic. Only with a specially shaped nozzle, the flow can be made one-dimensional. During motor start-up and stop the gas flow is not steady. Though relatively small, there is some heat exchange with the surroundings causing the flow not to be isentropic."

What follows is a guide that follows ideal rocket motor theory through which thrust can be calculated with only the chamber pressure ρ_c, the nozzle exit pressure ρ_e, the ratio of specific heats γ, the molar mass M and the chamber temperature T_c. The relation between this ideal rocket motor theory and the actual behavior of a rocket motor will be accounted for by using correction factors in the design process. Two will be used, namely the combustion efficiency, ϵ_b, and the nozzle efficiency or nozzle quality, ϵ_F.
From the molar mass, the specific gas constant of the gas can be easily calculated with Eq. (3.32).

$$R = \frac{R_A}{M} \tag{3.32}$$

where R is the specific gas constant of a gas, R_A the universal gas constant which is equal to 8,314.5 m^3Pa/kgmolK. Similarly, a value for γ leads to a value for the Vandenkerckhove function given by:

$$\Gamma = \sqrt{\gamma} \cdot \left(\frac{2}{\gamma+1}\right)^{\left(\frac{\gamma+1}{2\cdot(\gamma-1)}\right)} \tag{3.33}$$

The ideal characteristic velocity can then be calculated with the following formula:

$$c^*_{id} = \frac{1}{\Gamma} \cdot \sqrt{R \cdot T_c} \tag{3.34}$$

However in the model, this ideal characteristic velocity is multiplied by a correction factor which accounts for some imperfections of the rocket motor. This factor is the combustion efficiency, ϵ_b, and has been allotted a value of 0.95. This correction factor will be subjected to further scrutiny in section 3.3.3. The chamber density can be calculated as follows:

$$\rho_c = \frac{P_c}{T_c \cdot R} \tag{3.35}$$

where P_c is the chamber pressure. The expansion will be assumed to be isentropic thus using the Poisson relation shown in Eq. (3.36) the exit density can be derived as shown in Eq. (3.37).

$$\frac{T_e}{T_c} = \left(\frac{P_e}{P_c}\right)^{\left(\frac{\gamma-1}{\gamma}\right)} = \left(\frac{\rho_e}{\rho_c}\right)^{(\gamma-1)} \tag{3.36}$$

$$\rho_e = \rho_c \cdot \left(\frac{P_e}{P_c}\right)^{\left(\frac{1}{\gamma}\right)} \tag{3.37}$$

The area ratio can be given as follows:

$$\frac{A_e}{A_t} = \frac{\Gamma}{\sqrt{\left(\frac{2\cdot\gamma}{\gamma-1}\right)\cdot\left(\frac{p_e}{p_c}\right)^{\left(\frac{2}{\gamma}\right)}\cdot\left(1-\frac{p_e}{p_c}\right)^{\left(\frac{\gamma-1}{\gamma}\right)}}} \tag{3.38}$$

While the equation for ideal thrust coefficient is given by Eq. (3.39):

$$C_{F_{id}} = \Gamma \cdot \sqrt{\frac{2\gamma}{\gamma-1}\cdot\left(1-\left(\frac{P_e}{P_c}\right)^{\left(\frac{\gamma-1}{\gamma}\right)}\right)} + \frac{P_e}{P_c}\cdot\frac{A_e}{A_t} \tag{3.39}$$

It must again be noted that in the model used, this ideal thrust coefficient is multiplied by a correction factor which accounts for some imperfections of the rocket motor. This thrust coefficient correction factor is the nozzle quality or nozzle efficiency, ϵ_F, and has been allotted a value of 0.97. Just as ϵ_b, ϵ_F will be subjected to further scrutiny in section 3.3.3. Another remark required to be made here is that the model does not address the effect of the ambient pressure on the thrust coefficient. This is done so because ambient pressure can only be determined in the launch trajectory model and information transfer between models is being minimized. For total clarity, the thrust force this model calculates is the maximum vacuum thrust force and the ambient pressure effect is accounted for outside this model, in the trajectory simulation without any loss of accuracy. From all the information acquired thus far, the exit velocity can be calculated as the product of the characteristic velocity and the thrust coefficient:

$$V_e = c^* \cdot C_F \tag{3.40}$$

The mass flow can also be calculated using the conditions found at the exit of the nozzle.

$$\dot{m} = \rho_e \cdot V_e \cdot A_e \tag{3.41}$$

where A_e is the exit area, which is one of the inputs required. Finally, all information is present to find the maximum vacuum thrust force the vehicle can produce according to this model, which is the product of the mass flow and the exit velocity.

$$F_{max} = \dot{m} \cdot V_e \tag{3.42}$$

3.3.2 Mass Model

The mass model consists out of several parametric formulas that can be used for mass estimation of several launch vehicle components. These components are the following:

- The engine
- The thrust structure
- The propellants
- The propellant tanks
- The nozzle
- The vehicle equipment bay
- The fairing
- The heat shield

As can be seen in various of the following subsections, many of the parametric formulas drastically depend on some of the values found in the performance model discussed earlier.

Engine mass

Several methods for estimating the engine mass were discussed in [56], finally the most simple method was selected, a small recap is given below. Two parametric formulas were found for each of the possible propellant choices in [68]. For a kerolox engine the following connection was found between engine mass and thrust delivered:

$$m = 0.0011 \cdot F^{0.9992} \tag{3.43}$$

This formula has a standard error of estimate (SEE) of 23.9%
For a hydrolox engine the following equation needs to be used:

$$m = 0.0114 \cdot F^{0.8573} \tag{3.44}$$

which has an SEE of 18.6%.

Thrust structure

For the thrust structure, a similar parametric formula was found in [31]:

$$m = C \cdot T_{TOT} \tag{3.45}$$

where C is the rocket engine thrust scaling coefficient, which depends on the material used, and T_{TOT} is the total vacuum thrust. C is 0.003 for aluminum and 0.0024 for composites. This formula was implemented in the model using the latter value, since the source of the formula is outdated and it is deemed that current technology would certainly be able to comply with the low requirement given.

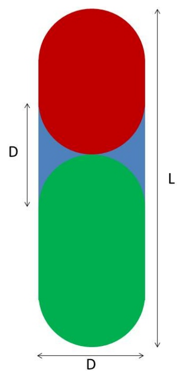

Figure 3.4: Propellant tanks depiction

Propellant mass

The propellant mass can be estimated using the tank dimensions, which are inputs for the model. The density of the propellants that the model needs to deal with are given by [66]:

- Liquid Oxygen: 1.141 kg/l
- Liquid Hydrogen 0.071 kg/l
- Dodecane (Kerosene) 0.749 kg/l

Using the oxidizer-to-fuel ratio, an average propellant density can be established according to the following formula:

$$\rho_{prop} = \frac{(O/F)_{ratio} + 1}{\frac{(O/F)_{ratio}}{\rho_{oxidizer}}} + \frac{1}{\rho_{fuel}} \tag{3.46}$$

Assuming that the propellant tanks have the shape of cylinders of which the ends are spherical caps and assuming that there is no space between the top of the spherical cap of the fuel tank and the bottom of the spherical cap of the oxidizer tank, it can be calculated how much volume the propellants can occupy.
Regarding the calculations of the tank mass, which will be shown in section 3.3.2, it would be more exact if the exact dimensions of both tanks were calculated with regard to thermal stresses. However, to keep it simple, it was opted to take a more general approach to the estimation methods.
The propellant volume available within the input for dimensions (length, L, and diameter, D) is thus not the entire volume of a spherically capped cylinder as can be seen in figure 3.4. Namely, the volume depicted in blue, needs to be accounted for. This volume can be calculated by subtracting a sphere of diameter D from a cylinder with length and diameter D. A calculation that is performed in Eq. (3.47).

$$V_{loss} = V_{cylinder} - V_{sphere} = \pi \cdot \frac{D^2}{4} \cdot D - \frac{4}{3} \cdot \pi \cdot \frac{D^3}{8} = \frac{1}{12} \cdot \pi \cdot D^3 \tag{3.47}$$

where $V_{cylinder}$ stands for the volume of a cylinder with both length and diameter equal to the tank's diameter, V_{sphere} stands for the volume taken in by a sphere with the diameter of the tank and V_{loss} stands for the resulting difference in volume between those two bodies. The total volume of the both propellant tanks with diameter, D, and sum of lengths, L, is then calculated as the volume of a cylinder with length $L - D$ and diameter D added with the volume of a sphere with diameter D, minus the difference in volume calculated in Eq. 3.47.

$$
\begin{aligned}
V_{total} &= V_{cylinder} + V_{sphere} - V_{loss} \\
&= \pi \cdot \frac{D^2}{4} \cdot (L - D) + \frac{4}{3} \cdot \pi \cdot \frac{D^3}{8} - \frac{1}{12} \cdot \pi \cdot D^3 \\
&= \frac{1}{4} \cdot \pi \cdot D^2 \cdot L - \frac{1}{6} \cdot \pi \cdot D^3
\end{aligned}
\tag{3.48}
$$

Having acquired values for both the average propellant density and the volume available in the tanks, the propellant mass can be calculated via a simple multiplication.

$$
m_{prop} = V_{total} \cdot \rho_{prop} \cdot 0.9 \tag{3.49}
$$

where the factor of 0.9 is a typical value for the fill ratio, the ratio between the propellant volume and the volume of the storage system, of liquid pump systems. This fill ratio accounts for the ullage[2] volume needed to keep some pressurant in the tank and also to allow for expansion of the liquids [69].

Tank Mass

One of the most often tank materials used is 6Al-4V titanium alloy [65]. Therefore, the tank mass will be estimated based on the properties this alloy. These properties are a tensile yield strength of 900 MPa, a density of 4428 kg/m^3, a modulus of elasticity of 110 GPa, a poisson ratio of 0.31 [65] and a coefficient of thermal expansion α of 8.8 $\frac{10^{-6}}{C}$. Two assumptions must be established. The first one is that the tank shell is part of the structure of the launcher and must be able to withstand the large compressive loads during launch. The second one is that the system is assumed to be pump fed due to the fact that this is normally used with large stages because the advantage of low tank mass increases significantly in that case [67]. This leads to the assumption that the tank is put under a maximum ullage pressure of 0.3 MPa.

There are basically two stresses that determine the thickness of the tank. First, there is the circumferential stress also known as the hoop stress, the other stress is the axial stress, which will be will be loaded under tension due to the assumption of a load carrying tank. The axial stress will thus be subjected to the critical buckling stress criterion.

There can also be a natural-frequency requirement, but this requires assumptions concerning the natural frequency and [62] notes that the driving requirements for the monocoque cylinder are bending rigidity and compressive stability.

[2]In liquid rockets, ullage is the space within a fuel tank above the liquid propellant.

Circumferential stress limit The hoop or circumferential stress must stay below the given tensile yield strength of 900 MPa and is given by the following formula [52]:

$$\sigma_y = \frac{P_c \cdot D}{2 \cdot t_{circum}} \tag{3.50}$$

In this equation, P_c is equal to the design burst pressure inside the tank times a safety factor, D is the diameter of the tank and t_{circum} is the wall thickness needed to keep the stress below the level required for the 6Al-4V titanium alloy. The design burst pressure is the pressure at which the shell is likely to fail catastrophically. It is likely to be 1.25 - 2 times (the burst safety factor) higher than the design pressure. The exact value depends on how conservative the design is chosen to be. For this study, the model was chosen to not be overly conservative, leading to the selection of a value of 1.5. The design pressure is set equal to the sum of the hydrostatic pressure given in Eq. (3.51) and the vapor pressure, which was assumed to be 0.3 MPa.
The hydrostatic pressure is calculated in Eq. (3.51)

$$P_{hydro} = \rho_{fluid} \cdot H \cdot a \tag{3.51}$$

where H is height of the fluid and a is the acceleration the fluid in the tank undergoes (this would be 9.81 m/s^2 on the surface of the Earth). Due to the fact that the propellant mass is not all the mass of the rocket, H will decrease faster than a will increase under constant thrust. Therefore, maximum hydrostatic pressure will occur at lift off. This means that the acceleration at this moment needs to be known. Unfortunately, at this moment, only the maximum thrust is known, which is given in Eq. (3.42). The total mass of the launcher is unknown, since this is the purpose of the calculations performed in the mass model. Therefore, the total vehicle mass used to obtain the acceleration at lift off is estimated in the model by using the assumption that the propellant mass, which is known, is 90 % of the total vehicle mass. This value is based on existing launch vehicles [15].

Critical buckling stress The equation for theoretical cylinder buckling stress, σ_{cr}, is:

$$\sigma_{cr} = \frac{\gamma \cdot E}{3 \cdot (1 - \upsilon)} \cdot \frac{t}{R} \tag{3.52}$$

where E is young's modulus, R is the cylinder radius, υ is the poisson ratio, t is the wall thickness and γ is a reduction factor used to correlate theory to test results and depends on a parametric parameter, ϕ, for cylinders [3] :

$$\phi = \frac{1}{16} \cdot \sqrt{\frac{R}{t}} \text{ (for } R/t < 1500 \text{ and } L/R < 5) \tag{3.53}$$

$$\gamma = 1 - 0.910 \cdot \left(1 - e^{-\phi}\right) \tag{3.54}$$

[3] No other formula was found for cylinders with an L/R ratio larger than 5 or a R/t ratio larger than 1500, so this formula holds through for all inputs in the model

with L as the length of the shell.
When this stress given by (3.52) becomes larger than the one due to thrust, bending moment and thermal stress for a given thickness, it means that this thickness is enough for the tank to withstand buckling. The stress given by the thrust is straightforwardly given by (3.55)

$$\sigma = \frac{F_{max}}{\pi \cdot D \cdot t} \tag{3.55}$$

Thermal stress is given by [65]:

$$\sigma = \frac{\lambda \cdot E \cdot \Delta T}{2 \cdot (1 - \upsilon)} \tag{3.56}$$

where λ is the coefficient of thermal expansion ($8.8 \cdot 10^{-6} \frac{1}{^\circ K}$ for 6AL-4V titanium) and E is the modulus of elasticity, 110 GPa and ΔT is the difference between the temperature of the propellant and the outside temperature. Since the model does not create a distinction between the fuel tank and the oxidizer tank two assumptions are made. Firstly, ΔT is set equal to $298.15 - 20.27 = 277.88$ and secondly, a factor is used to lessen the effect of thermal stress on the system using the non-cryogenic kerosene fuel. This factor was taken to be the proportion of the total propellant volume needed to contain oxygen. This is done in the following formula:

$$factor = \frac{\rho_{kerosene} \cdot (O/F)_{ratio}}{\rho_{liquidoxygen}} \cdot \frac{1}{1 + \frac{\rho_{kerosene} \cdot (O/F)_{ratio}}{\rho_{liquidoxygen}}} \tag{3.57}$$

The hull tank also has to deal with an additional stress given by the aerodynamic bending moment due to dynamic pressure.

$$m_{bending} = C_m \cdot \bar{q} \cdot S \cdot c = (C_{m_0} + C_{m_\alpha} \cdot \alpha) \cdot \bar{q} \cdot S \cdot c \tag{3.58}$$

where C_{m_0} is approximately zero, α is the angle of attack, $\bar{q}$ is the dynamic pressure, S is the surface area and c is the reference length. This additional load was not modeled into the mass model since knowledge about the maximum bending load is not known before optimization of the launch trajectory. Therefore it was assumed that the launchers would undergo the same order of stresses that conventional launch vehicles undergo and in section 3.3.3 the entire mass model was then scaled to correspond with current launchers. The model compares the two stresses for a thickness ranging from 0.0001 m incrementally increasing with 0.0001 m until the critical buckling stress becomes larger than the stress induced by thrust and thermal properties. Once this thickness is found, it is compared with the thickness found from the circumferential stress requirement and the largest value is selected. This thickness is assumed to be uniform along the outer hull of the tank. The two spherical caps that do not need to transfer any thrust loads or bending loads are therefore assumed to be significantly thinner (a thickness of 1 mm). The surface of the outer hull is modeled as a cylinder with length, L, and diameter, D, with two spherical caps at the end. This gives for the formula of the surface:

$$S_{hull} = (L - D) \cdot \pi \cdot D + \pi \cdot D^2 = L \cdot D \cdot \pi \tag{3.59}$$

This then gives for total tank mass:

$$m_{tank} = \rho_{titanium} \cdot (t \cdot (D \cdot L \cdot \pi) + \pi \cdot D^2 \cdot 0.001) \tag{3.60}$$

where $\rho_{titanium} = 4428$ kg/m^3.

Nozzle mass

The only dimensions obtained through the inputs and the performance model are values for both the exit area and the area ratio. The model uses these in combination with the chamber pressure through the following formula to estimate the mass of the nozzle [65] p415:

$$m_{nozzle} = \epsilon \cdot F_{max} \cdot \left(0.00225 + \frac{0.1475}{P_c}\right) \tag{3.61}$$

where ϵ is the area ratio, F_{max} is the maximum thrust and P_c is the chamber pressure. This formula is valid for regeneratively cooled nozzles.

Vehicle equipment bay

The vehicle equipment bay mass is modeled using the following method given by [67]:

$$m = 0.404 \cdot M_{dry}^{0.6814} \tag{3.62}$$

This formula has a SEE of 34%.

Fairing

In [56] the fairing estimation method was presented that will be used here. The formula for fairing mass is as follows

$$M_{Fairing} = C \cdot S_{Fairing} \tag{3.63}$$

where S is the wetted area in m^2, M is the mass in kg and C is the fairing unit weight. This method found very good values estimating various Ariane 5 ECA fairing configurations by assuming a value of 13.3 kg/m^2 for the fairing unit weight and by achieving wetted area estimates of the fairing by modeling the fairing as having a conical shape in the top halve and a cylindrical shape in the bottom half [56]. For this reason, the same value of 13.3 kg/m^2 was used in the model.
In addition, [56] also mentioned that the payload density within a fairing can be assumed

to be around 128.15 kg/m^3. This leads to the following equation for payload mass to fairing mass ratio:

$$\begin{aligned}\frac{M_{Payload}}{M_{Fairing}} &= \frac{128.15 \cdot V_{Fairing}}{13.3 \cdot S_{Fairing}} \\ &= \frac{128.15 \cdot \frac{2}{3} \cdot \pi \cdot r^2 \cdot h}{13.3 \cdot (\pi \cdot r \cdot \sqrt{r^2 + 0.25 \cdot h^2} + h \cdot r \cdot \pi)} = \frac{6.42 \cdot r \cdot h}{\sqrt{r^2 + 0.25 \cdot h^2} + h}\end{aligned} \tag{3.64}$$

Using the total launcher mass and an initial estimation of its payload mass ratio, a fairing mass estimate can be obtained.

Heat shield mass

The standard vehicle that will be modeled in this study is a non-reusable vehicle. This being the case, the logical choice for type of heat shield results in an ablative heat shield. In an ablative heat shield, the total heat transferred must be balanced with the total amount of material released:

$$Q = \rho \cdot r \cdot t \cdot S \cdot H_{abl} = M_{abl} \cdot H_{abl} \tag{3.65}$$

where H_{abl} is the heat of ablation of the ablative material. As a standard, a value of 2500 kJ/kg will be used [65].
The peak heat flux occurs at the stagnation point. Heat flux usually has two components, a radiative component and a convective component. Due to the fact that below orbital velocity the convective heat flux is far larger than the radiative component, only the convective component is taken into account. This convective heat flux can be calculated at the stagnation point (where the flow is laminar) with the following equation [51]:

$$\dot{Q} = C \cdot \left(\frac{\rho}{\rho_0}\right)^n \cdot \left(\frac{V}{1000}\right)^m \cdot \frac{1}{\sqrt{R_N}} \tag{3.66}$$

where for the free stream:

- C = 21,969 $\cdot$W/m$^{3/2}$
- n = 0.5
- m = 3.0
- ρ_0 = 1.225 kg/m^3

R_N is the nose radius of the launcher, which was set to 10% of the radius of the launcher. In [36] a maximum value in the order of 1 Btu/(ft$^2\cdot$ s) or 11,360 W/m^2 was found to occur during launch. This compares with the maximum heat flux allowed after fairing separation for the Vega launcher, which is 1,135 W/m^2 [3]. While the model used in

Missile DATCOM assumes an ogive nosecone, a spherical cap will be assumed to exist on top of the ogive, having a radius equal to 10% of the launcher's diameter.
In [2], C was modified with the factor $x_T^{-0.2}$ in order to find the heat flux downstream the turbulent boundary layer. Part of this heat flux can be emitted radiatively, the rest will need to be absorbed through ablation of the heat shield. In [51] the following maximal radiation heat loss was established for an aluminum tank:

$$\dot{Q} = \epsilon \cdot \sigma \cdot T^4 \tag{3.67}$$

where ϵ is the emissivity (0.8 for anodized aluminum), σ is the Stefan Boltzmann constant ($5.6704 \cdot 10^{-8}$ W/m^{2}K^4) and T is the melting temperature (aluminum (933.5 K)). Inserting the values for aluminum gives a maximal radiation heat loss of 6,075 W/m^2. The heat shield mass is modeled in a way that all surplus convective heat flux need to be absorbed by the ablative heat shield following Eq. (3.65).
Most positions along the launcher's nosecone have a far lower heat flux than what occurs at the stagnation point. This is shown via an analytical method and through experiments [13]. In this reference two spherically blunted cones with different semi-apex angles were investigated. As a rule of thumb, a doubling of the semi-apex angle resulted in a doubling of the heating rate ratio at identical chord positions. However, the stagnation point does not always occur at the tip of the nosecone due to different angles of attack that can occur during flight. Therefore, the mass of the heat shield was modeled as if the entire surface of the nosecone must be able to deal with the surplus convective heat flux in the stagnation points. In all but one simulation, the simulated heat shield mass was found to be lower than 0.1% of the total gross mass of the launcher.

3.3.3 Launch Vehicle Model Verification

In order to verify that this model accurately approaches reality its results will be matched with data from ESA Launch Vehicle Catalogue [15]. For this verification, six launcher stages, 3 kerolox and 3 hydrolox, were selected (based on the availability of the data) to compare the simulation with. These launcher stages are all first stages from the following launchers: the Atlas 5, the Zenit, The Delta IV, The Ariane V ECB, the Soyuz and the H2. The data of these stages and their simulated counterparts is displayed in Tables 3.4 and 3.5 and shows that there is already a close match between the real and simulated data points. However, this can be further improved by changing some values that were assumed throughout section 3.3. For example, the specific impulse of the simulations is fairly close to the actual values with a standard deviation of 7.5 seconds. Increasing the simulated values with 1.35% would however minimize the standard deviation to just 5.3 seconds. This can be done by increasing the nozzle efficiency from 0.97 to 0.983 while leaving the combustion efficiency at 0.95. More importantly, the dry mass of stages is consistently underestimated by the simulation. The same holds for the engine mass, where on average the engine mass is estimated to be 16.23% lower than in reality. Besides the fact that there is a very close match for liquid hydrogen propelled stages that use boosters for their assist there is no other remarkable connection to be distinguished. It was therefore chosen to optimize the parameters in Eq. (3.44) and (3.43) to minimize the standard deviation

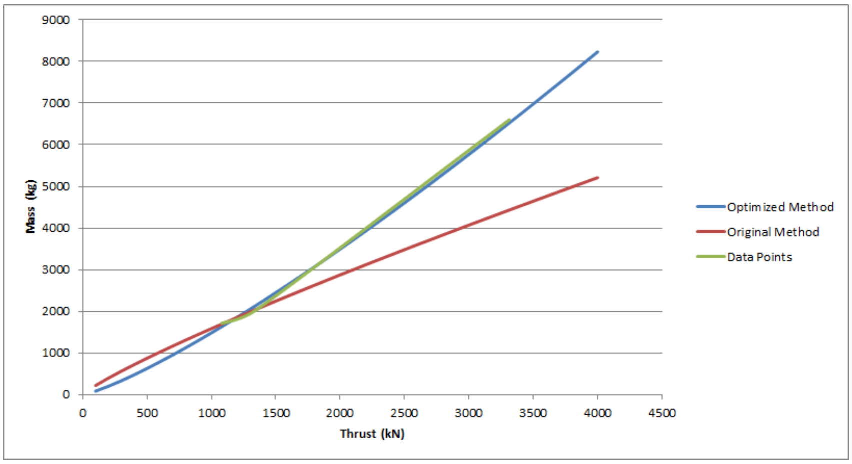

Figure 3.5: Hydrolox engine weight according to the original method (Eq. (3.44)), the optimized method (Eq. (3.68)) and the actual data points of the 3 hydrolox engines according to [15].

with the data of the six launchers.
This optimization showed that the following formula is optimal for hydrolox engines:

$$m = 0.00005755 \cdot F^{1.235275} \tag{3.68}$$

which has a standard deviation of 4.26%. Note that this formula now indicates an exponential growth in mass for a linear increase in thrust, which was not the case in the original Eq. (3.44). The following is then likewise found for kerolox engines:

$$m = 0.000345 \cdot F^{1.093032} \tag{3.69}$$

which has a standard deviation of 7.51%. The improvement with the original method for both types of engines is visualised in figures 3.5 and 3.6 where the data points, the actual engine weights of the six launchers according to [15], are also plotted for reference. Implementation of both the improvements in the mass estimation method as well as the thrust coefficient correction factor leads to tables 3.6 and 3.7. Here it can still be seen that the dry mass of the vehicles is still underestimated. It can not accurately be determined which factors weigh how much in this discrepancy. Therefore it was chosen to apply a certain factor to the dry mass in order to minimize the standard deviation between the simulated results and the actual vehicles. This minimization of the standard deviation requires a 30% increase of estimated dry mass resulting in a decrease of the standard deviation from 4.44% to 1.95%. At this point it is interesting to perform a preliminary opimization of a launcher stage with the objective of maximizing the ΔV and comparing the results with the actual launcher stages that have the maximum ΔV from the group of six. These are the Ariane V ECB for hydrolox stages and the Atlas V for kerolox stages. When optimizing the hydrolox launcher stage, the following values for the six parameters are found using a differential evolution algorithm from an external software package named PaGMO (Parallel Global Multiobjective Optimizer), which is further discussed in chapter 6. The results presented are those obtained after the algorithm has optimized

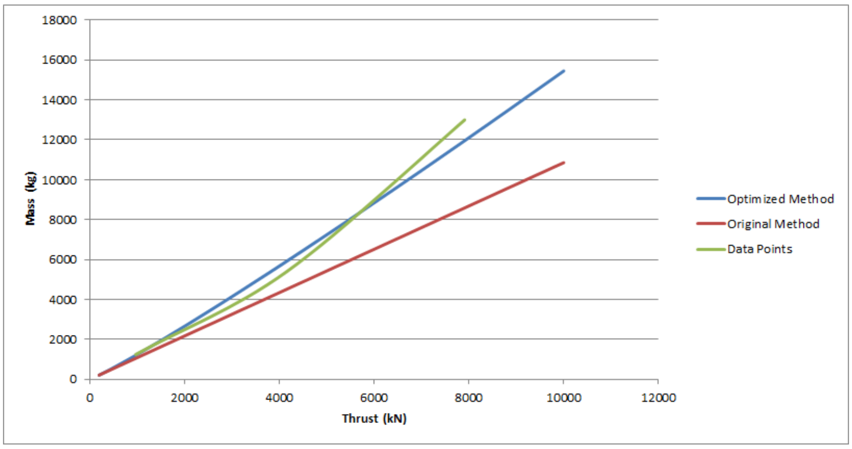

Figure 3.6: Kerolox engine weight according to the original method (Eq. (3.43)), the optimized method (Eq. (3.69)) and the actual data points of the 3 hydrolox engines according to [15].

a population of 20 individuals over 1000 generations. The reasoning behind the search spaces is presented in Chapter 7:

- Length = 100 m (search space: 10 - 100 m)
- Slenderness: 12.49 or a diameter of 8.01 m (search space: 1.82 - 20)
- Nozzle-to-tank-diameter ratio: ≈ 0 (search space: 0 - 1)
- Oxidizer to fuel ratio: 7 (search space: 1 - 10)
- Chamber pressure: 254.06 (search space: 8 - 264 bar)
- Exit pressure: ≈ 0 Pa (search space: 0 - 100,000 Pa)

These values give a maximum ΔV of 17,674 m/s, which is well in excess of the Ariane V's simulated ΔV of 10,761 m/s. Also interesting to note is that the optimal values approach the boundary of their respective search spaces on three occasions. Namely, the upper boundary for the length, the lower boundary for the nozzle-to-tank-diameter ratio and the lower boundary for the exit pressure.
The reason why the the nozzle-to-tank diameter is minimized is because this generates a positive effect for the engine mass (see Eq. (3.68)). Secondly, this also means that there is almost no thrust generated which leads to almost no hydrostatic pressure and thus a very small tank thickness.
The reason why the length is being maximized is due to two reasons. Due to the square-cube law, which dictates that when an object increases proportionally in size, the new volume is proportional with the cube of the multiplier while the surface area is proportional with its square. And this causes the construction mass ratio to drop in this case. Normally, this effect is counteracted by the fact that length influences the hydrostatic pressure by a 1 to 1 ratio due to the formula given in (3.51), which causes a thicker tank thickness for longer tanks, however in this case the hydrostatic pressure is non-existent

and there is no incentive to keep tank length low.
The reason why the exit pressure is minimized is due to the desired maximization of the specific impulse and it also helps to minimize the thrust.
The same was done with the kerolox launcher stage. The optimized values found can be seen below:

- Length = 100 m (search space: 10 - 100 m)
- Slenderness: 9.36 or a diameter of 10.69 m (search space: 1.82 - 20)
- Nozzle-to-tank-diameter ratio: ≈ 0 (search space: 0 - 1)
- Oxidizer-to-fuel ratio: 2.5 (search space: 1 - 10)
- Chamber pressure: 8 bar (search space: 8 - 264 bar)
- Exit pressure: ≈ 0 Pa (search space: 0 - 100,000 Pa)

The kerolox stage is found to have a maximum ΔV of 21,209 m/s. Again, this is way higher than the simulated Atlas V rocket stage, which has an estimated ΔV of just 9,092 m/s. A striking difference between the optimized kerolox launcher and the hydrolox launcher is that in addition to length, nozzle-to-tank-diameter ratio and exit pressure also the chamber pressure for the kerolox stage finds the lower boundary to be the most optimal solution. The chamber pressure is identified to have two effects on the model. These are an effect on the nozzle mass through Eq. (3.61) and an effect on the specific impulse through the pressure ratio as will be further explained in section 7.2.6. However both effects do not contribute in this optimization since the maximum thrust is near zero leading to a near zero nozzle mass. Since the exit pressure is also near zero, the pressure ratio is very large for all possible values for the chamber pressure and at very large pressure ratios, the change in specific impulse with further increase of the pressure ratio is almost non-existent. Therefore, it can be concluded that the chamber pressure does not influence the optimization process when the exit pressure and thrust are close to zero.
As mentioned, both optimizations leave a high ΔV but ineffective rocket stage with no thrust. For this reason a constraint was put in place that demanded the vacuum initial thrust-to-weight ratio to be higher than 1.15. This resulted in much closer matches of ΔV when comparing to the existing launchers. Putting the constraint in place generated a maximum ΔV for the hydrolox launcher of 10,618 m/s with the following characteristics:

- Length = 12.23 m (search space: 10 - 100 m)
- Slenderness: 6.17 or a diameter of 1.98 m (search space: 1.82 - 20)
- Nozzle-to-tank-diameter ratio: 0.46 (search space: 0 - 1)
- Oxidizer-to-fuel ratio: 6.95 (search space: 1 - 10)
- Chamber pressure: 243.36 bar (search space: 8 - 264 bar)
- Exit pressure: 9,416 Pa (search space: 0 - 100,000 Pa)

It should be pointed out that although the real Ariane V first stage has a larger ΔV, it does not have an adequate initial thrust to weight ratio and it needs to be assisted during the first phase of its launch by solid rocket boosters. The results obtained now are vastly different than when generated without the constraint. There are no parameters that approach a boundary of the search space because the requirement of high thrust leads to significant values of exit pressure and nozzle-to-tank-diameter ratio because if one of those two would be equal to zero so would the maximum thrust be. The thrust requirement also leads to significant hydrostatic pressure for launchers with a large length. This is the reason why the length of the launcher retreats from its maximum value of 100 m to only 12.23 m.
Also for the kerolox launcher a close match with the Atlas V ΔV of 9,092 m/s was found. The optimized kerolox launcher has a ΔV of 10,327 m/s with the following values:

- Length = 12.75 m (search space: 10 - 100 m)
- Slenderness: 7.58 or a diameter of 1.68 m (search space: 1.82 - 20)
- Nozzle exit-to-tank diameter ratio: 0.58754 (search space: 0 - 1)
- Oxidizer-to-fuel ratio: 2.5 (search space: 1 - 10)
- Chamber pressure: 255.57 bar (search space: 8 - 264 bar)
- Exit pressure: 15,557 Pa (search space: 0 - 100,000 Pa)

This result is also vastly different compared with the original when the thrust-to-mass constraint is put in place. It shows that just like in the case of the hydrolox launcher and for the same reason, none of the parameters approach any of their search space's boundaries.

Table 3.4: Comparison launch vehicle catalogue values and vehicle model for first stages

	Atlas 5 (Real) [15]	Atlas 5 (Simulated)	Zenit (Real) [15]	Zenit (Simulated)	Delta IV (Real) [15]	Delta IV (Simulated)
Type of Fuel	RP1	RP1	RP1	RP1	LH2	LH2
O/F Ratio	2.72	2.72 (+ 0.0%)	2.63	2.63 (+ 0.0%)	6	6 (+ 0.0%)
Vacuum Thrust (kN)	4,152	4,244 (+ 2.2%)	7,911	7,930 (+ 0.2%)	3,314	3,320 (+ 0.2%)
Expansion Ratio	36.87	36.87 (+ 0.0%)	37	36.97 (- 0.1%)	21.5	21.49 (+ 0.0%)
Chamber Pressure (bar)	257	257 (+ 0.0%)	250	250 (+ 0.0%)	97.2	97.2 (+ 0.0%)
Dry Mass (kg)	21,173	13,980 (- 34.0%)	28,080	21,402.5 (- 23.8%)	26,760	18,031 (- 32.6%)
Propellant Mass (kg)	284,089	284,405 (+ 0.1%)	318,800	318,427 (- 0.1%)	199,600	200,477 (+ 0.4%)
Engine Mass (kg)	5,390	4,611 (- 14.5%)	13,000	8,613 (- 33.8%)	6,600	4,441 (- 32.7%)
Length (m)	32.46	30.25 (- 6.8%)	33	32.3 (- 2.1%)	40.8	33.2 (- 18.6%)
Diameter (m)	3.81	3.81 (+ 0.0%)	3.9	3.9 (+ 0.0%)	5.13	5.13 (+ 0.0%)
Vacuum Isp (sec)	337.8	330 (- 2.3%)	337	330.9 (- 1.8%)	410	410 (+ 0.0%)
Nozzle to Tank Ratio	-	0.65	-	0.88	-	0.547
Exit Pressure (Pa)	-	51,000	-	49,300	-	35,800

Table 3.5: Comparison launch vehicle catalogue values and vehicle model for first stages

	Ariane 5 ECB (Real) [15]	Ariane 5 ECB (Simulated)	H2 (Real) [15]	H2 (Simulated)	Soyuz (Real) [15]	Soyuz (Simulated)
Type of Fuel	LH2	LH2	LH2	LH2	RP1	RP1
O/F Ratio	6.1	6.1 (+ 0.0%)	6	6 (+ 0.0%)	2.39	2.39 (+ 0.0%)
Vacuum Thrust (kN)	1,350	1,351 (+ 0.0%)	1,079	1,083 (+ 0.3%)	971	961 (- 1.0%)
Expansion Ratio	60	60.14 (+ 0.2%)	52	52.22 (+ 0.4%)	18.9[4]	18.88 (- 0.1%)
Chamber Pressure (bar)	116.2	116.2 (+ 0.0%)	127	127 (+ 0.0%)	51	51 (+ 0.0%)
Dry Mass (kg)	12,300	11,744 (- 4.5%)	11,900	7,138 (- 40.0%)	6,500	3,381 (- 48.0%)
Propellant Mass (kg)	173,000	173,228 (+ 0.1%)	86,200	86,086 (- 0.1%)	94,500	94,496 (+ 0.0%)
Engine Mass (kg)	2,040	2,055 (+ 0.7%)	1,714	1,700 (- 0.1%)	1,250	1,045 (- 16.4%)
Length (m)	30.5	26.6 (- 12.8%)	28	23.7 (- 15.4%)	27.8	22.5 (- 19.1%)
Diameter (m)	5.4	5.4 (+ 0.0%)	4	4 (+ 0.0%)	2.55[5]	2.55 (+ 0.0%)
Vacuum Isp (sec)	434	432.3 (- 0.4%)	446.1	430.7 (- 3.5%)	315	315 (+ 0.0%)
Nozzle to Tank Ratio	-	0.48	-	0.52	-	0.77
Exit Pressure (Pa)	-	13,200	-	16,900	-	21,700

[4] This was not taken from the ESA launch vehicle catalogue but rather from [42]

[5] Varying from 2.95 to 2.15

Table 3.6: Comparison launch vehicle catalogue values and vehicle model for first stages

	Atlas 5 (Real) [15]	Atlas 5 (Simulated)	Zenit (Real) [15]	Zenit (Simulated)	Delta IV (Real) [15]	Delta IV (Simulated)
Type of Fuel	RP1	RP1	RP1	RP1	LH2	LH2
O/F Ratio	2.72	2.72 (+ 0.0%)	2.63	2.63 (+ 0.0%)	6	6 (+ 0.0%)
Vacuum Thrust (kN)	4,152	4,225 (+ 1.8%)	7,911	7,887 (- 0.3%)	3,314	3,323 (+ 0.3%)
Expansion Ratio	36.87	36.87 (+ 0.0%)	37	36.97 (- 0.1%)	21.5	21.49 (+ 0.0%)
Chamber Pressure (bar)	257	257 (+ 0.0%)	250	250 (+ 0.0%)	97.2	97.2 (+ 0.0%)
Dry Mass (kg)	21,173	14,622 (- 30.9%)	28,080	24,790 (- 11.7%)	26,760	20,234 (- 24.4%)
Propellant Mass (kg)	284,089	284,405 (+ 0.1%)	318,800	318,427 (- 0.1%)	199,600	201,150 (+ 0.8%)
Engine Mass (kg)	5,390	6,026 (+ 11.2%)	13,000	11,923 (- 8.3%)	6,600	6,544 (- 0.8%)
Length (m)	32.46	30.25 (- 6.8%)	33	32.3 (- 2.1%)	40.8	33.2 (- 18.6%)
Diameter (m)	3.81	3.81 (+ 0.0%)	3.9	3.9 (+ 0.0%)	5.13	5.13 (+ 0.0%)
Vacuum Isp (sec)	337.8	334.5 (- 1.0%)	337	335.3 (- 0.5%)	410	415 (+ 1.2%)
Nozzle to Tank Ratio	-	0.64	-	0.866	-	0.54
Exit Pressure (Pa)	-	51,000	-	49,300	-	35,800

Table 3.7: Comparison launch vehicle catalogue values and vehicle model for first stages with updated engine

	Ariane 5 ECB (Real) [15]	Ariane 5 ECB (Simulated)	H2 (Real) [15]	H2 (Simulated)	Soyuz (Real) [15]	Soyuz (Simulated)
Type of Fuel	LH2	LH2	LH2	LH2	RP1	RP1
O/F Ratio	6.1	6.1 (+ 0.0%)	6	6 (+ 0.0%)	2.39	2.39 (+ 0.0%)
Vacuum Thrust (kN)	1,350	1,359 (+ 0.7%)	1,079	1,070 (- 0.8%)	971	961 (- 1.0%)
Expansion Ratio	60	60.14 (+ 0.2%)	52	52.22 (+ 0.1%)	18.9[6]	18.88 (- 0.1%)
Chamber Pressure (bar)	116.2	116.2 (+ 0.0%)	127	127 (+ 0.0%)	51	51 (+ 0.0%)
Dry Mass (kg)	12,300	11,866 (- 3.5%)	11,900	7,043 (- 40.8%)	6,500	3,538 (- 45.6%)
Propellant Mass (kg)	173,000	173,228 (+ 0.1%)	86,200	86,086 (- 0.1%)	94,500	94,496 (+ 0.0%)
Engine Mass (kg)	2,040	2,170 (+ 6.4%)	1,714	1,614 (- 5.8%)	1,250	1,194 (+ 4.5%)
Length (m)	30.5	26.6 (- 12.8%)	28	23.7 (- 15.4%)	27.8	22.5 (+ 19.1%)
Diameter (m)	5.4	5.4 (+ 0.0%)	4	4 (+ 0.0%)	2.55[7]	2.55 (+ 0.0%)
Vacuum Isp (sec)	434	438.1 (+ 0.9%)	446.1	436.4 (- 2.2%)	315	319 (+ 1.2%)
Nozzle to Tank Ratio	-	0.475	-	0.51	-	0.76
Exit Pressure (Pa)	-	13,200	-	16,900	-	21,700

[6] This was not taken from the ESA launch vehicle catalogue but rather from [42]
[7] Varying from 2.95 to 2.15

3.4 Thrust model

The actual launch vehicle that uses an assist will still need a propulsive force to reach Earth orbit. This propulsive force is considered to originate singularly from rocket propulsion and is provided according to Eq. (3.70), the momentum thrust, and Eq. (3.71), the pressure thrust.

$$T_{momentum} = \dot{m} \cdot U_e \tag{3.70}$$

$$T_{pressure} = A_e \cdot (p_e - p_a) \tag{3.71}$$

where $\dot{m}$ is the mass flow, U_e is the exhaust velocity, A_e is the nozzle exit area, p_e is the nozzle exit pressure and p_a is the ambient pressure. Rocket thrust for all stages of flight will be modeled as follows w.r.t the body fixed reference frame:

$$T = \begin{bmatrix} T_{momentum} + T_{pressure} \\ 0 \\ 0 \end{bmatrix} \tag{3.72}$$

The simulation model only provides the option to choose between two types of fuels in order to generate thrust. Both fuels, kerosene and liquid hydrogen, are liquid fuels. This makes the thrust model quite straightforward since liquid engines generally burn through their fuel at a steady rate due to the constant pressure in the combustion chamber. More advanced and expensive types of engines can be throttled as desired. Although in reality this cannot be done at full efficiency through the whole range of thrust from 0 N to maximum thrust, full efficiency and throttle ability is assumed in this study.
All forms of rocket propulsion operate according to the third law of Newton and accelerate mass and expel it, resulting in an equally great force in the opposite direction that propels the rocket. The speed to which the mass is accelerated out of the rocket is vitally important for the effectiveness of the rocket as was shown by Konstantin Tsiolkowski:

$$\Delta V = I_{sp} \cdot g_0 \cdot ln(\frac{m_i}{m_f}) \tag{3.73}$$

where I_{sp} is the specific impulse in seconds, g_0 is the gravity at sea level, namely 9.80655 m/s^2, m_i is the initial mass in kg and m_f is the final mass. The product of the specific impulse and the gravity at sea level is the exit velocity, which was given in Eq. (3.40) in section 3.3.1.

3.5 Analysis of the velocity budget

The main focus of this study is on the velocity or ΔV budget and how initial conditions that could be created by use of assisted launch techniques effect that budget. Therefore, a thorough study of this budget is definitely in order. The mission budget for space launch to a certain Earth orbit is often represented as follows:

$$\Delta V = \Delta V_{inj} + \Delta V_d + \Delta V_g + \Delta V_s \tag{3.74}$$

where ΔV_{inj} is the injection velocity required for the desired orbit, ΔV_d is the drag loss, ΔV_g is the gravity loss and ΔV_s is the steering loss up until the point of injection.
In section 3.4, Eq. (3.73) gave a definition of the launcher ΔV budget. This budget must always be larger or equal to the mission ΔV budget for the obvious reason that the desired payload would not be able to reach the desired orbit, and the mission would thus not be successful, if otherwise. This means that the mission ΔV budget needs to be as small as possible, and drag and gravity losses need to be minimized.
Drag loss can be defined by the following equation:

$$\Delta V_d = \int_{t=t_0}^{t=t_e} \frac{D}{m} dt \tag{3.75}$$

According to Eq. (3.29) the drag force, D, is positively correlated to the velocity, density, reference surface area and the aerodynamic coefficient. However, only the former two are related to the launch trajectory. The mass of the vehicle, m, depends on the dry mass and the thrust profile of the launcher but will continuously decrease. This means that to optimize Eq. (3.75) the velocity must be kept low and the mass high until the density severely decreases.
Another interesting aspect about drag loss can be derived from the drag force's linear dependence on the reference surface area and its independence on the length of the vehicle (assuming skin friction drag to be negligible[8]):

$$\Delta V_d \propto \frac{S_{ref}}{m_0} = \frac{S_{ref}}{S_{ref} \cdot l \cdot \rho_{rocket}} = \frac{1}{l \cdot \rho_{rocket}} \tag{3.76}$$

where m_0 is the take-off mass and obviously has a direct relationship with the instantaneous mass, which is a factor in Eq. (3.75). In words, imagine three launchers, launcher A, B and C that all have the same thrust-to-weight ratio. Launcher B is four times as tall as launcher A, while launcher C is twice as wide (i.e., the mass of each is four times the mass of launcher A). This means that launcher B and C both need four times as much thrust but only launcher C experiences a drag force four times as large. This implies that the drag loss does not increase with increasing diameter and decreases with increasing length. In addition, also average density of the launcher turns out to be inversely related to drag loss.
Unfortunately, rather than only have to optimize for the drag loss, the trajectory problem also needs to optimize for both the thrust loss and the gravity loss. This is quite complex so it might be beneficial to have a quick look at the equation of gravity loss separately [58]:

$$\Delta V_g = \int_{t=t_0}^{t=t_e} g \cdot \sin \gamma dt \tag{3.77}$$

[8] Varying length would result in varying skin friction drag and thus a different drag coefficient.

where g is the local acceleration due to gravity and γ is the local flight-path angle, which is defined from the triangle of velocities: $\tan\gamma = V_Z/V_X$ (where V_X and V_Z are the X- and Z-components of the total velocity V respectively). The local acceleration, g, only slightly changes with height during the propulsive phase of the launch, with the exception of an injection burn at geostationary altitude, which is done by some launch vehicles [59]. However, since both of the equations parameters are expressed in a non-inertial reference frame, the fictitious centrifugal force must be implemented in the formula, if not, eccentric orbits would have a periodical change in gravity loss. This equation is presented as follows:

$$\Delta V_g = \int_{t=t_0}^{t=t_e} (g - r\cdot\dot{\theta}^2)\cdot\sin\gamma dt \tag{3.78}$$

where r is the distance to the center of the Earth and $\dot{\theta}$ is the angular velocity.
The determining factor with regard to gravity loss is the flightpath angle. To keep gravity losses low, one must keep the flight-path angle low. In the ideal scenario the flight-path angle would be kept zero at all times (horizontal flight) and gravity losses would amount to zero. This scenario, which is not viable since it needs an impulsive shot in order to keep the vehicle from hitting the ground, quite clearly contradicts the scenario of low drag loss discussed before.
Another aspect of gravity loss is that it not only is a measure for efficiency of the launcher w.r.t. gravity, but it also incorporates the aspect of kinetic energy traded in for potential energy. Integrating for gravity loss along a non-disturbed elliptical orbit would result in a gravity loss between perigee and apogee and an equal gravity gain between apogee and perigee. In other words, a comparison between the gravity loss of a system that takes a payload to geostationary orbit and one that takes a payload to low Earth orbit is comparing apples with oranges.

3.6 Guidance model

In this section the guidance program as coded into the simulation will be discussed. As an introduction to guidance programs a trajectory breakdown of the most essential flight phases will be performed briefly. These flight phases occur at different times for each single vehicle and the occurrence of some even depend on the configuration and architecture of a launch vehicle (number of stages, number of boosters, etc.). Nonetheless almost all conventionally launched vehicles go through the most essential phases summarized below:

- Vertical lift-off
- Kick phase (Flight phase where the vehicle pitch angle is actively changed so the right conditions are met to insert into the gravity turn)
- Gravity turn (Flight phase with no angle of attack, flight-path angle is only disturbed by the force of gravity)
- Control law

- Coasting phase(s) and circularization

One problem with this approach is that the first phase (the vertical lift-off) already requires from the initial condition that the flight-path angle is 90°. This might be the case for most rocket launches but it is not for those that need to be simulated in this study. Optimization using the gravity turn and a certain control law was for this study dismissed in favor of pure optimized pitch control using polynomials. For further information on these flight phases the reader is referred to [56].

3.6.1 Initial conditions

After the vehicle is separated from its assist platform it will have a certain position, velocity, mass and attitude. These initial conditions are very important for the shape of the launch trajectory and need to be correctly inserted into the model that describes the entire trajectory ascent problem.

3.6.2 Coasting phase(s) and circularization

The coasting phase and circularization burn are the final phases of the guidance program. To circularize an orbit, a burn must be made at the apogee of the launch trajectory. There are no longer any gravitational or aerodynamic disturbing forces and the objective is simply to reach the necessary horizontal velocity and minimal eccentricity. For certain combinations of launch vehicles and desired orbits, the time it takes to reach the altitude of the required orbit is larger than the time the vehicle can burn. In these instances, the vehicle starts to coast to a higher altitude where it then provides a circularization burn. To do this, the guidance program must keep track of the apocenter given by the Keplerian elements of the vehicle state vector. When this apocenter equals the apocenter of the target orbit, the thrust should be deactivated so that the coasting phase begins. After some time, the launcher will reach its apogee and the circularization burn can begin. When the circularization burn is modeled as an impulsive shot, the right burn at apogee will lead to a circular orbit. However, due to the fact that this is not the case in the simulation it was chosen to initiate the burn when the launch vehicle altitude is higher than 98% of the apogee altitude. During this burn, the pitch angle of the vehicle is set equal to the flight-path angle. The burn ends when the orbit criteria are met. These are the final eccentricity and the apogee altitude. These can be defined as wished and correspond in this study with the values 0.01 or lower for final eccentricity and 250 km or higher for the apogee altitude. For fully optimized simulations (also with initial flight path angle optimization) the circularization burn can be assumed to be optimally very short. This due to the fact that it occurs at the highest altitude during the burn sequence which is the least favorite position to burn fuel in (gravity loss, gravity well, gravity assist).
From [58] we know that:

$$e = \frac{r_a - r_p}{r_a + r_p} \tag{3.79}$$

Due to the eccentricity requirement of 0.01 a minimum perigee of 120 km can only be insured if the apogee is higher than 250 km.

The optimization of the circularization process requires the simulation to be run for over one half of the orbital period. Therefore total launch simulation time is set to 3000 seconds.

3.6.3 Verification of the Pitch Polynomial

In order to avoid spiky pitch profiles that can be generated due to node optimization [38] and would imply instantaneous attitude changes, the pitch was modeled as a smooth continuous polynomial. Two pitch polynomials have been implemented during the optimization process. The first one presented is a third-degree polynomial of the following form:

$$\begin{aligned}\theta = \theta_{initial} \cdot (1 + (a - 0.5) \cdot w \cdot 0.00314 \cdot t - (b - 0.5) \cdot x \cdot 0.00000628 \cdot t^2 \\ + (c - 0.5) \cdot y \cdot 0.00000001256 \cdot t^3)\end{aligned} \tag{3.80}$$

where a, b and c are all optimized parameters with a search space between 0 and 1. Their weights are chosen so that each of the three parameters will exhibit an equal effect on the pitch angle when t is 500 s and can have at least a magnitude of 180 ° after 1000 seconds. The parameters w, x and y are values that are assigned to a specific optimization by means of trial and error so that none of the a, b and c parameters find an optimum value close to their boundaries.
The second polynomial has an added term, making it a fourth degree polynomial:

$$\begin{aligned}\theta = \theta_{initial} \cdot (1 + (a - 0.5) \cdot w \cdot 0.00314 \cdot t + (b - 0.5) \cdot x \cdot 0.00000628 \cdot t^2 \\ + (c - 0.5) \cdot y \cdot 0.00000001256 \cdot t^3 + (d - 0.5) \cdot z \cdot 0.00000000002512 \cdot t^4)\end{aligned} \tag{3.81}$$

In the three degree configuration, the search space was expanded by using the following values as the w, x and y parameters given in 3.80. $w = 3$, $x = 10$ and $y = 30$, the added fourth configuration has parameter z set to 180[9] . The average optimal value of 2 runs of 5000 generations with a population of 20 individuals was 0.200085 while the quadruple pitch parameter simulation found an average optimal value of 0.20111. Based on this result, fourth-order polynomials will be used as the method of choice to establish the pitch program. The resulting polynomials are shown in figure 3.7.

[9] These parameters were for the final results reset to $w = 8$, $x = 20$, $y = 60$ and $z = 180$ based on the experience that with using these search spaces very rarely a global optimum was found in the vicinity of one of the boundaries of the search spaces. It is however recommended for future research to use a more robust method to establish the search space of these variables.

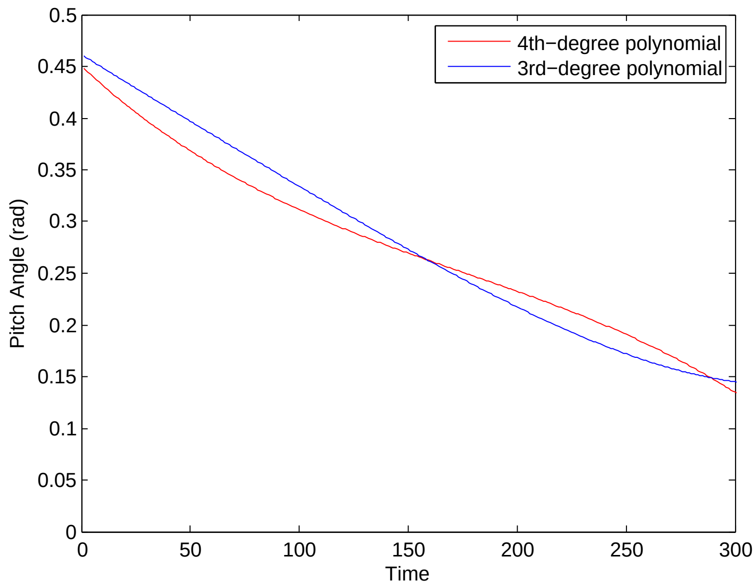

Figure 3.7: Comparison of the two polynomial types that obtained the best objective function value

3.7 Trajectory constraint model

3.7.1 Bending load

One of the requirements that should be enforced throughout all phases of flight is a structural constraint. Here we run into the problem that a structural study of each of the launch vehicles cannot be done within the scope of this study. To circumvent this problem a rule of thumb can be used known as the $\bar{q}\alpha$ limit, this rule originates from the bending load due to dynamic pressure given in Eq. (3.82).

$$M_{bending} = C_{m_0} + C_{m_\alpha} \cdot \alpha \cdot \bar{q} \cdot S \cdot c \tag{3.82}$$

where C_{m_0} is almost zero, α is the angle of attack, $\bar{q}$ is the dynamic pressure, S is the surface area and c is the chord length. The stability derivative C_{m_α} is the slope of the moment curve $C_m = C_m(\alpha)$ at the respective angle of attack at which $C_{m0} = 0$ [33]. Since, S, c and C_{m_α} are nearly constant, the $\bar{q}\alpha$ limit is linearly connected with the bending load. The multiplication of the dynamic pressure with the angle of attack is therefore an important structural constraint. Assigning a certain value for this limit will have a definite impact on the results of the optimization. As a guideline, from a study by both NASA and DARPA on horizontal launch systems that all used lifting surfaces it could be revealed that an assumption was used of a bending load limit of 5010 lbs $\cdot$ deg/ft^2 or 36.135 Pa $\cdot$ rad [35]. It should also be noted that the relevant angle of attack in Eq. (3.82) is the total angle of attack which can be calculated as follows [38]:

$$\alpha_t = \arccos(\cos\alpha \cdot \cos\beta) \tag{3.83}$$

However, since the side slip angle was during all simulations set to zero, the total angle of attack is nothing more than the normal angle of attack. The bending load constraint was not approached by any of the optimal simulations.

3.7.2 Axial acceleration

Another frequently used constraint in trajectory optimization is an axial acceleration constraint given in the following equation:

$$a_x = \frac{T(t) - D(t)}{m \cdot g_0} \tag{3.84}$$

During launch, fuel is drained from the launch vehicle reducing its weight significantly. All the while the engine can still perform at the same thrust causing the axial acceleration to increase. At some point, the thrust need to be throttled to prevent critical failure of either the launcher or the payload. During most simulations this constraint has been set at 50 m/s for all simulations. This value was based on 6 different launchers, which had an average maximum axial acceleration of 4.86 g [38]. Implementation of this constraint was due to the nature of the thrust-force model different than implementation of the other constraints. The thrust force model assumes constant thrust with adjustments due to air pressure unless the acceleration constraint would be violated. In case of violation, the thrust and mass flow is modified to its highest possible value without violating the acceleration constraint. In figure 3.8 all hydrolox axial-acceleration profiles can be viewed. The small peaks that violate the constraint are due to the fairing jettisoning event, where the thrust was still calculated based on the old mass (with fairing) while the mass was already decreased in that time step to the launcher mass without fairing.

3.7.3 Angle of attack

Normally the most meaningful way to implement an angle-of-attack constraint is how it is implicitly done in the bending moment constraint, see Eq. (3.82). However, due to the limits of the Missile DATCOM simulator the angle of attack has been hard constrained to 30 degrees or 0.5236 rad. Figure 3.9 displays several angle-of-attack profiles that are subjected to this constraint. It should be noted that the only cases that came close to the limit are the ones that do not utilize a velocity assist. All angle-of-attack profiles can be viewed in Appendix C. This constraint is implemented by discarding all solutions that violate it, which is different from the previously discussed implementation of the axial-acceleration constraint.

3.7.4 Heat Flux

The heat flux already has an effect on the launch vehicle mass model through the heat shield mass, which was discussed in section 3.3.2. Thus as long as the model is able to

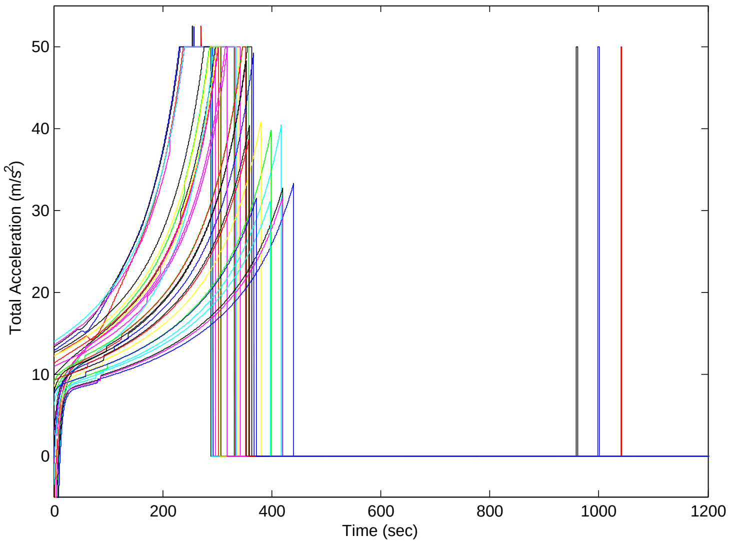

Figure 3.8: Example of how the axial-acceleration constraint is met for hydrolox vehicles.

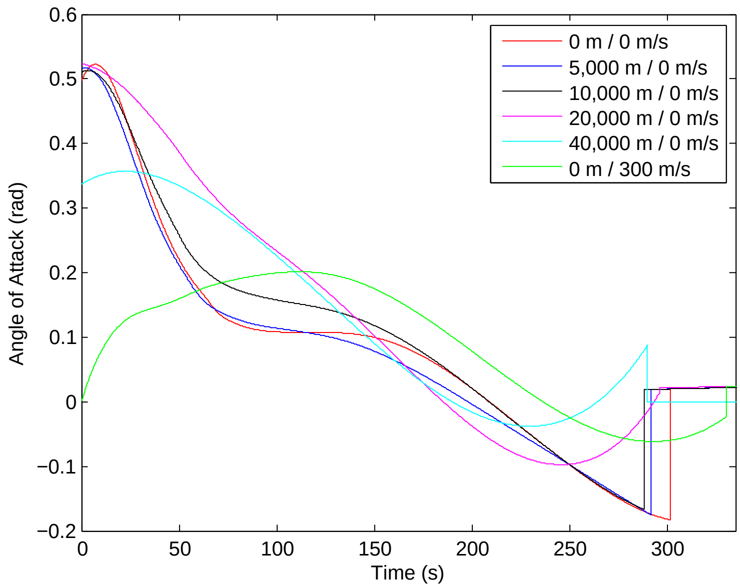

Figure 3.9: Example of how the angle-of-attack constraint is met for hydrolox vehicles. The legend contains case identifiers using the "h/V" notation.

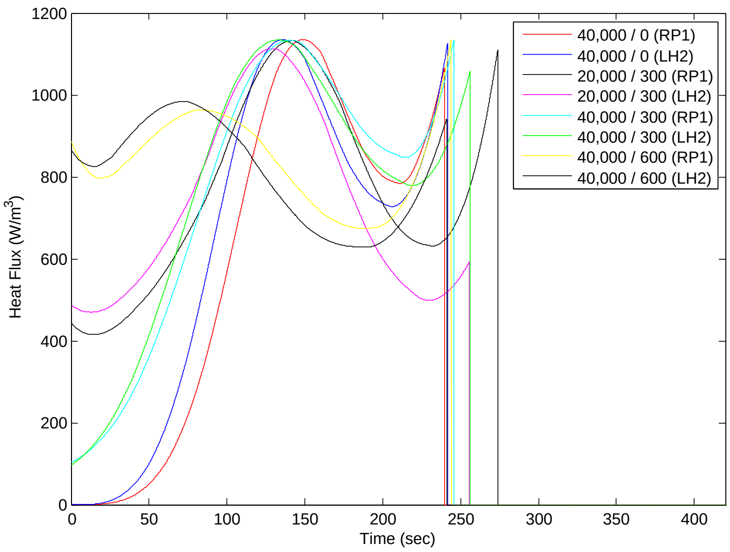

Figure 3.10: Example of how the heat-flux constraint is met. The legend contains case identifiers using the "h/V (type of fuel)" notation.

cope with the extra weight of the heat shield, the heat flux is essentially not constrained. The heat flux was only modeled as a hard constraint after fairing jettisoning. The value of this constraint was the same as the jettisoning criteria for the fairing, namely 1135 W/m^2. This resulted in a few interesting launch trajectory profiles further discussed in section 7.3. These trajectory profiles can also be seen in figure 3.10, where for some cases, the heat flux is clearly modeled to stay below the jettison criteria.

3.7.5 Altitude

The trajectory of the launcher is logically hard constrained to not go under the radius of the Earth. This constraint was not approached by any of the optimal simulations.

3.7.6 Sidenote

Other constraints that trajectory simulation software sometimes takes into account is staging re-entry locations and visibility for ground stations. In addition, a major requirement will be to not hit nor endanger the assist platform. This can be a quite significant constraint in the case of plane assist. These constraints require specific knowledge about the launch-vehicle geometry, type of assist and/or geography of the launch site. To reduce complexity of this study, it is decided to not incorporate this kind of info as inputs of the simulation nor will some consequences be taken into account. It is recommended to take these constraints into account in an advanced stage of a specific system design study. Another often used constraint is the dynamic pressure. While this was contemplated during the design process it was quickly found out that the maximum dynamic pressure of all optimized cases is the initial condition of the most extreme launch assist[10] . Therefore, it did not seem prudent to use dynamic pressure as a direct constraint but was it rather implemented indirectly through the bending moment, see Eq. (3.82).

[10]The most extreme launch assist in this case is meant to be the combination of an assist velocity of 2,000 m/s at an altitude of 0 m.

Chapter 4

Numerical Integration

The computation of the trajectory has to be done with a certain accuracy. To this purpose, a small overview was presented in [56] about the usage of numerical methods for the solution of the equations of motion. It was then decided that the main purpose of the integrator in this model was to maximize the speed and the single step fourth order Runge-Kutta (RK) method was then chosen since it outperforms multi-step methods on this criteria partially due to the fact of its stability at larger step sizes. This chapter will introduce the reader to the RK4 method in section 4.1 and will provide an explanation with regard to which step size was used for the simulations in section 4.2.

4.1 Runge-Kutta-4

During single step method numerical integration, no use is made of function values calculated in earlier steps to predict the value of the function at the next step. This means that all integration steps are completely independent of one another. To discuss the various single-step methods the following differential equation will be introduced.

$$\dot{\mathbf{y}} = \mathbf{f}\left(t, \mathbf{y}\right) \quad \text{with} \quad \mathbf{y}, \dot{\mathbf{y}}, \mathbf{f} \in \mathbb{R}^{\mathbf{n}} \tag{4.1}$$

Starting from initial values $\mathbf{y}_0 = \mathbf{y}(t_0)$ at time t_0 a numerical integration method seeks to approximate $\mathbf{y}$ at a later time ,t_0+h[1], as closely as possible by using an increment function, $\mathbf{\Phi}$, that closely approximates the slope of the secant through $(t_0, \mathbf{y}_0)$ and $(t_0+h, \mathbf{y}(t_0+h))$. In a mathematical notation this means:

$$\mathbf{y}(t_0 + h) \approx \mathbf{y}_0 + h \cdot \mathbf{\Phi} = \boldsymbol{\eta}(t_0 + h) \tag{4.2}$$

where $\boldsymbol{\eta}(t_0 + h)$ is thus the approximate solution. One of the most straightforward methods just equates the increment function $\mathbf{\Phi}$ to the slope of $\mathbf{y}$ at its initial point. This

[1] h is the time step

may deviate considerably from the real slope and needs a very small step size in order to guarantee great accuracy. This method is called the Euler forward method and is mathematically presented in Eq. (4.3)

$$\mathbf{y}(t_0 + h) \approx \mathbf{y}_0 + h \cdot \dot{\mathbf{y}}_0 = \mathbf{y}_0 + h \cdot \mathbf{f}(t_0, \mathbf{y}_0) \tag{4.3}$$

There are other variations from this method such as the Euler's backward method and the higher order modified Euler method. For more information the reader is referred to [57]. To further improve on the accuracy of numerical integration, a series of methods have been developed by mathematicians Carl Runge and Wilhelm Kutta. The method series, aptly named the Runge-Kutta methods, are based on the slopes at various points within the integration step. As opposed to just the slope at the initial point, the approach used in the Euler method, the RK4 method is based on slopes in four points and the increment function is calculated as a weighted mean of the four slopes, $\mathbf{k}_1, \mathbf{k}_2, \mathbf{k}_3$ and $\mathbf{k}_4$:

$$\mathbf{\Phi}_{RK4} = \frac{1}{6}(\mathbf{k}_1 + 2\mathbf{k}_2 + 2\mathbf{k}_3 + \mathbf{k}_4) \tag{4.4}$$

The four slopes are defined as follows:

$$\mathbf{k}_1 = \mathbf{f}(t_0, \mathbf{y}_0) \tag{4.5}$$

$$\mathbf{k}_2 = \mathbf{f}(t_0 + h/2, \mathbf{y}_0 + h\mathbf{k}_1/2) \tag{4.6}$$

$$\mathbf{k}_3 = \mathbf{f}(t_0 + h/2, \mathbf{y}_0 + h\mathbf{k}_2/2) \tag{4.7}$$

$$\mathbf{k}_4 = \mathbf{f}(t_0 + h, \mathbf{y}_0 + h\mathbf{k}_3) \tag{4.8}$$

The Runga-Kutta series all use the same build-up but can be extended with even more stages. The general formulation of an s-stage RK formula is as follows:

$$\mathbf{k}_1 = \mathbf{f}(t_0 + c_1, \mathbf{y}_0) \tag{4.9}$$

$$\mathbf{k}_i = \mathbf{f}(t_0 + c_i h, \mathbf{y}_0 + h\sum_{j=1}^{i-1} a_{ij}\mathbf{k}_j) \quad \text{with} \quad (i = 2, ..., s) \tag{4.10}$$

And the increment function is defined as follow:

$$\Phi = \sum_{i=1}^{s} b_i \mathbf{k}_i \tag{4.11}$$

The coefficients are usually determined such that they obey the following relations:

$$\sum_{i=1}^{s} b_i = 1; \quad c_1 = 0; \quad c_i = \sum_{j=1}^{i-1} \quad (i > 1) \tag{4.12}$$

As can be seen in Eq. (4.5) to Eq. (4.8), the order of h in k_i usually increases with every increase in i, there are however exceptions and the real order of each method needs to be determined through an elaborate mathematical examination. The local truncation error of RK4 is given as follows

$$e_{RK4} = |\mathbf{y}(t_0 + h) - \boldsymbol{\eta}(t_0 + h)| \leq const \cdot h^5 \tag{4.13}$$

The error is thus bound by a term of order h^5.
Now say that a certain s-stage RK formula will have an approximation of the exact solution up to terms of order h^s. This requires that $b_s \neq 0$. However, another Runge-Kutta method can have the same number of stages as the previous one but with $b_s = 0$. This RK method now has an approximation of the exact solution up to terms of order h^{s-1}. Two of these methods with the same number of stages but with a different order, p and $p+1$, give the following truncation errors:

$$e1 = |\mathbf{y}(t_0 + h) - \boldsymbol{\eta}_1(t_0 + h)| \leq const \cdot h^{p+1} \tag{4.14}$$

$$e2 = |\mathbf{y}(t_0 + h) - \boldsymbol{\eta}_2(t_0 + h)| \leq const \cdot h^{p+2} \tag{4.15}$$

Now it can be said that $e2$ is smaller than $e1$ by the order of h (a small value) it results in the following error estimation:

$$e1 = |\mathbf{y} - \boldsymbol{\eta}| \approx |\boldsymbol{\eta}_2 - \boldsymbol{\eta}_1| \tag{4.16}$$

This means that the estimate of the local truncation error is based on the difference of the two solutions. This estimate of error can in turn be used for step size control. Suppose that this error value is larger than a certain tolerance, ϵ. In this case the step needs to be repeated with a smaller step size, h^*, for the tolerance to be met. The new step size is found to be:

$$h^* = \sqrt[p+1]{\frac{\epsilon}{e(h)}} \cdot h \approx \sqrt[p+1]{\frac{\epsilon}{|\boldsymbol{\eta}_2 - \boldsymbol{\eta}_2|}} \cdot h \tag{4.17}$$

where $e(h)$ is the error due to the original step size. In practice about 0.9 times this value is commonly used. This still does require the user to define the initial step size but this choice might be directed by experience with earlier simulations of the same problem with the same integrator. Some of the more popular methods that use this technique are called the Runge-Kutta-Fehlberg methods.

4.2 Selection of the time step

To select the time step with which the model would be integrated, 100 randomly varying inputs were generated for the four variables of the pitch profile, see section 3.6.3. These inputs were varied around the found optimal values with a maximum deviation of -0.005% and 0.005% of their search spaces. All inputs were used to simulate the hydrolox case utilizing an assist velocity of 300 m/s and an assist altitude of 20 km. Each input was simulated with eight different time steps. The different time steps were 0.01, 0.02, 0.05, 0.1, 0.2, 0.5, 1.0 and 2.0 seconds. The results of the simulations with a time step of 0.01 seconds were used as a measure of approximate reality. These results had a mean altitude of 242,710 m with a standard deviation of 1,537 m and a payload ratio of 0.0534 with a standard deviation of $1.426 \cdot 10^{-5}$. The results of the other runs were tabulated in table 4.1 with the mean difference w.r.t the 0.01 second run and with the standard deviation around its own mean.

Table 4.1: Comparison of the results from different time step RK4 runs

Time Step	Mean altitude difference	Standard deviation altitude	Mean payload ratio difference	Standard deviation payload ratio
0.02	$1.1584 \cdot 10^3$	$1.3618 \cdot 10^3$	$-4.3841 \cdot 10^{-5}$	$2.7498 \cdot 10^{-5}$
0.05	$6.3627 \cdot 10^3$	$3.2122 \cdot 10^3$	$-2.0301 \cdot 10^{-4}$	$5.0271 \cdot 10^{-5}$
0.1	$1.3318 \cdot 10^4$	$1.0369 \cdot 10^4$	$-4.5621 \cdot 10^{-4}$	$1.5352 \cdot 10^{-4}$
0.2	$3.9164 \cdot 10^4$	$9.2364 \cdot 10^3$	-0.001	$1.6368 \cdot 10^{-4}$
0.5	$1.8296 \cdot 10^6$	$1.8468 \cdot 10^6$	-0.0271	0.0258
1.0	$1.5456 \cdot 10^6$	$1.3029 \cdot 10^6$	-0.0315	0.0247
2.0	$3.6826 \cdot 10^6$	$1.1369 \cdot 10^5$	-0.0534	$1.4188 \cdot 10^{-5}$

For time steps larger than or equal to 0.5 seconds the standard deviations are about the same magnitude as the mean values. This occurs because the orbit criteria, see section 3.6.2, are sometimes not met resulting in large discrepancies at the end of the simulation. The inability to meet the orbit criteria is due to the circularization burn, which is defined to start when the altitude is higher than 98% of the desired apogee altitude. This way, the burn is not modelled as an impulsive shot but as a realistic continuous burn. During this burn the pitch angle is set equal to the flight-path angle. In the case of circularization with an impulsive shot, it is optimal to burn exactly at the apogee. However since the modelled burn is not impulsive it does not exactly take place at the apogee and some variations of the optimal solution burn too long or too short, taking the vehicle over the desired apogee altitude causing a failure to insert into the desired orbit.
With a time step of 0.2 seconds or less, the orbit criteria are always met, as should be the case. Furthermore, the mean difference in the payload ratio decreases to less than one percent of its relative value of 0.0534 as soon as a time step equal to or shorter than 0.1 seconds is used. This difference is actually mainly caused by the more precise thrust cutoff when the launcher reaches the required orbit instead of being a consequence of the different trajectory generated by using a different trajectory. Decreasing the time step naturally causes computational time to increase. A decrease in the time step with a factor of ten translates to an increase in evaluation time of 5 to 6 for the entire optimization problem. This is due to some calculations that only need to be done once and not during every time step. The entire optimization was also run with different time steps and created an increase in optimized payload ratio of about the same magnitude of the observed increase in the single simulation. This indicates that the time step does not influence the optimization process. Therefore it was concluded that a time step of 0.1 seconds is sufficient for the purpose of this study.

Chapter 5

Optimization Techniques

The goal of this study is to compare the performance of various launchers utilizing various assist cases. To achieve this goal with a high degree of accuracy, the launch vehicle and the trajectory that this vehicle will follow in every case needs to be optimized. This chapter gives the reader an introduction to optimization and the optimization algorithm used.

5.1 General optimization problem

The general optimization problem is to find a set of independent variables that either minimize or maximize the outcome of a system characteristic that is dependent on these variables. The mathematical formulation of an optimization problem, in this case the minimization problem, can thus be written as follows:

$$\min f(\mathbf{x}) \tag{5.1}$$

$$\text{subject to}\, \mathbf{x} \in \boldsymbol{\Omega} \tag{5.2}$$

The vector $\mathbf{x}$ is an n-dimensional vector of independent variables, that is, $\mathbf{x} = (x_1, x_2, ..., x_n)^T \in \mathbb{R}^n$. The function $f : \mathbb{R}^n \to \mathbb{R}$ that we wish to minimize is called the objective function. The set $\boldsymbol{\Omega}$ is a subset of $\mathbb{R}^n$, called the constraint set [10]. The constraints of this set can be in the form of equality constraints, denoted by $\mathbf{h}(\mathbf{x})$ and inequality constraints, denoted by $\mathbf{g}(\mathbf{x})$:

$$\boldsymbol{\Omega} = \mathbf{x} : \mathbf{h}(\mathbf{x}), \mathbf{g}(\mathbf{x}) \tag{5.3}$$

where

$$\mathbf{h}(\mathbf{x}) = 0, \text{for}\; i = 1, 2, ..., j \tag{5.4}$$

$$\mathbf{g}(\mathbf{x}) \geq 0, \text{for } i = j+1, ..., n \tag{5.5}$$

where j is the number of equality constraints and $n - j$ is the number of inequality constraints. There is no limit to the number of inequality constraints whereas the number of equality constraints can not surpass the number of variables, since each equality constraint defines a variable and more equality constraints than variables would render the system redundant. An optimization problem can also require maximization of the objective function. These problems have the same representation as displayed above, since maximizing f is equivalent to minimizing $-f$. The above problem is the general form of a constrained optimization problem. If $\mathbf{\Omega} = \emptyset$, then the problem is referred to as an unconstrained optimization problem.
Optimization problems are often rather complex and therefore analytical techniques seldom suffice to obtain a solution to the problem. This is the reason that one generally has to rely on numerical methods to obtain solutions for the more difficult problems. Trajectory optimization definitely falls into that category.

5.1.1 Global optimization methods

There are two general types of optimization techniques that can be used to solve a complex problem. These are called global and local optimization techniques. When the problem is convex[1] i.e. when all the functions in the problem are convex, any local minimizer is global and local optimization techniques can be used as well as global optimization techniques. However, for problems that are not convex, such as the maximization of payload-to-weight-ratio that this study is dealing with, the local optimization technique can never be relied upon to find the global minimum. The difference between a global peak and a local peak can be explained using figure 5.1.

A local optimizer also needs an initial guess that acts as a starting point from which it can start the search to the local optimum in its vicinity. This requires a minimum knowledge about the problem at hand. Global optimizers do not need initial guesses since these are created randomly in the search space. Therefore the following discussion of numerical optimization techniques will be limited to global optimizers. For information about local optimizers the reader is referred to [56].

Evolutionary algorithms One type of evolutionary algorithms are the genetic algorithms, which were the first global optimization technique to be developed [20]. The algorithm has, just as the name reveals, its roots in genetics. The algorithm starts out with an initial set of points, called the initial population $P(0)$, within the constraint set $\mathbf{\Omega}$. The size of the population is usually taken to be twice to four times the number of design variables. The method then continues to iteratively perform operations of crossover and mutation on each population in order to produce a new population until a termination criterion is met.
Genetic algorithms do not work directly with points in the set $\mathbf{\Omega}$ but rather with an encoding. The set $\mathbf{\Omega}$ is mapped onto another set consisting of strings of symbols of equal length

[1] A real-valued function $f(x)$ is convex if the graph of the function lies below the line segment joining any two points of the graph.

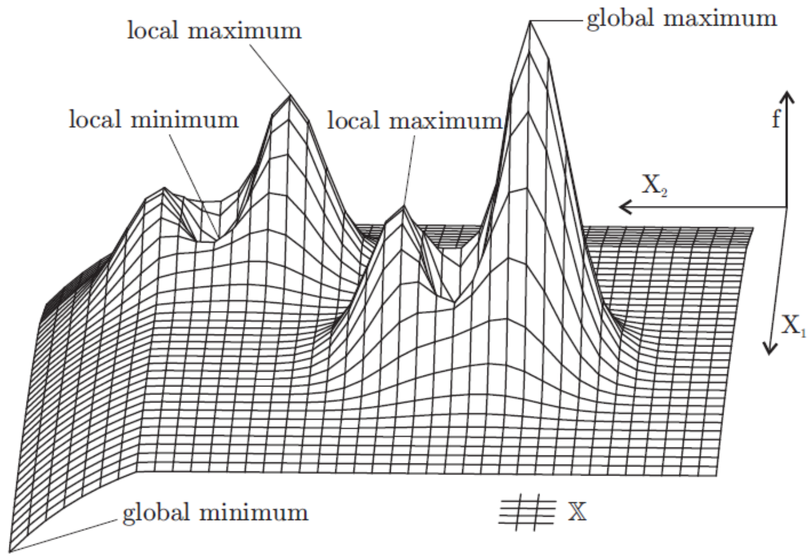

Figure 5.1: Global and local optima of a two-dimensional function [60].

(L). The strings are called chromosomes and the symbols form the so called alphabet. This can be done by transforming them into binary chromosomes, decimal chromosomes or into floating point representations. The latter is most promising for more complex problems like the one dealt with in this study. Each chromosome ($\mathbf{x}$) has a value of the objective function referred to as the fitness ($f(\mathbf{x})$) of the chromosome. After the choice of chromosome length, alphabet, encoding and initial population has been made, an operation called selection is applied. Different methods exist to perform this operation. One is called the tournament selection, another is the roulette wheel selection. The first one uses random selection of two individuals after which the best of the two goes to the next round. The second method uses a probability selection based on the fitness on all individuals The second stage is called evolution, where the crossover and mutation operations are performed. Crossover is when a pair of chromosomes are taken and replaced by a pair of offspring chromosomes. The operation involves exchanging substrings of in initial chromosomes. The initial chromosomes are chosen randomly.
The newer genetic algorithms also implement an idea called elitism. Elitism consists of the use of an external repository where the best solutions from every run are stored so they cannot disappear due to successive iterations. Because normally a good individual has a large probability to reproduce to do this the good individual is destroyed but reproduction does not always lead to the production of an even better individual. With elitism this cannot happen.

Differential Evolution The idea behind this algorithm is to simulate a population of solutions, that can produce offspring which replaces the original population in case it is better than its parent. The algorithm was first introduced by Storn and Price in 1996 [39]. Such a differential evolution (DE) algorithm uses a pair of vector populations that both contain Np D-dimensional vectors of real valued parameters. The current, $\mathbf{P}_x$, population is composed out of those vectors, $\mathbf{x}_{i,g}$ that are acceptable as initial points.

$$\mathbf{P}_x = \mathbf{x}_{i,g} \quad \text{with} \quad i = 0, 1, ..., Np - 1 \quad \text{and} \quad g = 0, 1, ..., g_{max} \tag{5.6}$$

$$\mathbf{x}_{i,g} = x_{j,i,g} \quad \text{with} \quad j = 0, 1, ..., D - 1 \tag{5.7}$$

where g indicates the generation or number of iteration and each vector is assigned a population index, i, and where parameters within vectors are indexed j. After initialization, DE mutates randomly chosen vectors to produce an intermediary population. Each vector in the current population is then recombined with a mutant of this intermediary population to produce a trial population. The trial vectors of the trial population overwrite the mutant vectors to reduce complexity. The initial value of the j^{th} parameter of the i^{th} vector can be written as follows:

$$x_{j,i,g} = r \cdot (b_{j,U} - b_{j,L}) + b_{j,L} \tag{5.8}$$

Here, r is a random number larger than zero and smaller or equal to one and $b_{j,U}$ and $b_{j,L}$ indicate the upper and lower boundary respectively for the parameter. The mutant vector can be created in many ways, one of them is given below:

$$\mathbf{v}_{i,g} = \mathbf{x}_{best} + F(\mathbf{x}_{r_1} - \mathbf{x}_{r_2}) \tag{5.9}$$

where F is the scale factor or weight, a real number that controls the rate of evolution that has no upper limit but seldom has a value greater than 1. Finally crossover into the trial vector only happens when the random number r is higher than the user defined value of the crossover probability. These two factors, the weight and the crossover probability, have a significant effect on the performance of the algorithm but their optimal values are problem specific. The trial vector is evaluated by the objective function and if a more optimized value is generated than that for the current population, the trial vector replaces the initial vector in the next generation. If not the initial vector remains in place [39].

Particle Swarm Optimization Particle swarm optimization (PSO) is a global optimization method that is based on the behavior of a swarm of insects, a flock of birds or a school of fish. The particle denotes the individual in the swarm, flock or school and the idea behind the optimization method is that each such individual behaves in a distributed way based on both its own and the swarm's intelligence. In the algorithm, each of these particles is assumed to have a certain position and a certain velocity. During its travel through the design space it remembers its best position it has discovered regarding the objective function. These positions are communicated between particles, which adjust the positions and velocities of the whole swarm during iterations. Initially, a certain number of particles, N, are defined. Normally, this number is taken equal to about 20 or 30 in order to have a high possibility of quick conversion without an astronomical amount of function evaluations that need to be performed. These particles are assigned a random position between the constraints. All of their initial velocities (the speed with which they are moving toward the supposed maximum of the objective function) is 0. The objective function is each iteration evaluated for all the particles. After the first iteration, the value of the objective function is memorized as that particle's personal best, $\mathbf{P}_{best}$, while the best value of all is denoted as the group's best, $\mathbf{G}_{best}$. The velocity of particle j in the ith iteration can be written down as follows [41]:

$$\begin{aligned} \mathbf{V}_j(i) =& \mathbf{V}_j(i-1) + c_1 \cdot r_1 \cdot [\mathbf{P}_{best,j} - \mathbf{X}_j(i-1)] + c_2 \cdot r_2 \cdot [\mathbf{G}_{best,j} - \mathbf{X}_j(i-1)] \\ & \text{with} \quad j = 1, 2, ..., N \end{aligned} \tag{5.10}$$

where $\mathbf{X}_j$ is the position of the particle and r_1 and r_2 are random variables between 0 and 1 that illustrate the importance of the personal best and the group best to the particle in order to change its velocity toward the target. c_1 and c_2 are so-called cognitive and social group learning rates, which denote the importance of the memory of the personal and group best. These values are often chosen to be equal to 2, so that the particle overflies the target about half of the time. The equation shows that a particle gets deflected from its previous direction toward the updated best values. The iterations are terminated once the whole population is converging toward the same values.

5.1.2 Comparison of algorithms in literature.

Genetic Algorithms, Particle Swarm Optimization and Differential Evolution are three of the most known global optimization techniques, but are by no means the only ones. Other global optimization methods include simulated annealing and ant colony optimization but these were rarely considered for trajectory optimization in the reviewed studies (only in [40] for simulated annealing). GA has been used for launch trajectory optimization [25] (sometimes in conjunction with the gradient method [64]) and for multidisciplinary optimization of both trajectory as well as vehicle design [5]. PSO is also frequently used for ascent trajectory optimization [9] [38] as is the case for DE [21]. GA was most often discussed in the literature but this might be the case because its the best known method of the three and the most available. In addition, the work of Tusar and Filipic [54] clearly shows that GA underperformed DE by a significant margin when trying to perform a multi objective optimization. It is also stated that it also underperformed DE for single objective optimization. This work compared the genetic algorithms NSGA-II, SPEA2 and IBEA with their differential evolution based variants DEMO^{NS-II}, DEMO^{SP2} and DEME^{IB} [54]. A comparison between DE and PSO was performed in [49]. Here it was demonstrated by means of optimization of a solar sail mission that DE also outperforms PSO significantly with 3.24%. The same was found in a similar orbit trajectory optimization study [27]. Since comparison of methods is problem specific, this does not imply that DE is better than PSO for multidisciplinary optimization of both trajectory and vehicle design and therefore these methods are compared by optimization of the problem at hand.

5.1.3 Problem formulation

The objective function that the algorithms need to minimize in the model is the following:

$$f[0] = -\frac{M_p}{M_i} \cdot 100,000,000,000 \tag{5.11}$$

where, M_p is the payload mass and the M_i is the initial launcher mass. However, this objection function is only evaluated when the eccentricity of the orbit gets below 0.01 while the apogee of the orbit is higher than an input value (in all simulations this value is 250 km unless indicated otherwise). If this is not the case the individual is evaluated with the following objective function in order to guide its evolution toward the first objective function:

$$f[0] = -a \tag{5.12}$$

where, a is the semi-major axis. If on the other hand any kind of constraint is violated during the simulation the objective function gets a penalty value assigned to it in order to make sure the algorithm discards solutions that violates constraints.

5.1.4 Comparison between Differential Evolution and Particle Swarm Optimization

This section compares data gathered by implementation of the DE algorithm with data from the PSO algorithm. At first, the PSO algorithm tends to outperform the DE algorithm but after a number of generations the DE starts to outperform the PSO while the PSO often mis converges in a local minimum. In addition, when the optimizers were given the task to optimize the no assist cases, which are the most difficult to find a solution for that does not violate any constraints, the PSO algorithm had more difficulty to find any set of parameters that leads to orbit insertion of a payload and in the case of the no assist kerolox case never did during its first 10,000 generations. The evolution of the fitness values using both techniques can be seen in figure 5.2, where for every tenth generation the fitness values of all the members of the population are plotted. Since DE did manage to optimize all problems and outperformed the PSO algorithm in general, the decision was made to use the DE algorithm for all cases.

5.1.5 Settings of the DE algorithm

In this section the selection of the weight coefficient, the crossover probability and the size of the population will be discussed.
The means to estimate good values for these parameters was deemed to be via comparison of how different values faired for when optimizing for certain launch conditions. The conditions evaluated were an altitude of 40,000 m and a speed of 2,000 m/s. The optimizer ran a population of 20 individuals over 5,000 generations in order to find the optimum for a hydrolox launcher. The decision was based on the sum of both the best and the worst fitness values in the final population. To start, a total of 25 simulations were run, which are depicted in table 5.1.

As can be seen in figure 5.3, the solutions form a convex curve. And there is a triangular area where a global optimum of the weight and crossover settings is likely to take place and where any setting is likely to have a stable and good performance. In this triangular area (governed by the points (0.5, 0.75), (0.75, 0.75) and (0.75, 0.99)) four additional runs were made. These were in the middle of the triangle (at (0.67 0.67)) and in the

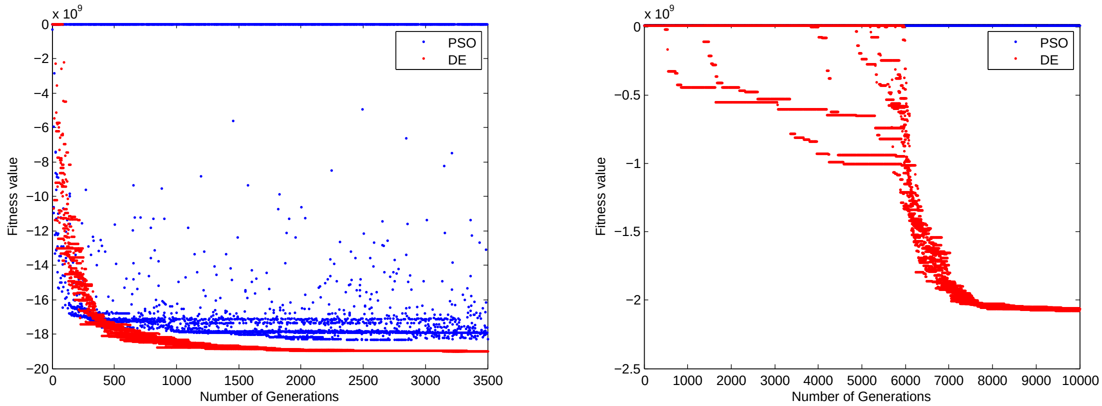

(a) (b)

Figure 5.2: Evolution of the objective value of the hydrolox maximum assist case (a), showing the early lead of the PSO algorithm being overtaken by the DE algorithm and the evolution of the most difficult case, the no assist kerolox case (b), where the PSO algorithm does not find a solution during 10,000 generations.

Table 5.1: Comparison of the results obtained from different weight and crossover probability DE algorithms

Weight \ Crossover Probability	0.01	0.25	0.5	0.75	0.99
0.01	0.1741	0.1709	0.1773	0.1429	0.0626
0.25	0.1913	0.1912	0.1977	0.1925	0.151
0.5	0.1852	0.1889	0.1968	0.2005	0.192
0.75	0.1787	0.1847	0.1972	0.1997	0.2004
0.99	0.1818	0.1844	0.1959	0.1969	0.1851

respective midway points between the middle of the triangle and the three corner points ((0.71, 0.71), (0.71, 0.83) and (0.58, 0.71)). The best result obtained by these four runs was 0.20132 achieved by using a weight of 0.71 and a crossover of 0.83. A second run confirmed this result by finding an optimum value of 0.2009.

Another setting that is important in evolutionary optimization is the size of the population. To investigate its effect 3 different population sizes were selected and each of these were run until the objective function was evaluated 100,000 times (e.g. 5,000 generations with a population of 20, 10,000 generations with a population of 10). Rarely improvements are found when larger populations than 40 individuals are generated. Therefore, the three population sizes of choice were 10, 20 and 40. The average optimized value of both runs for the different population sizes were 0.1976, 0.20111 and 0.19984. This confirms that the original setting, using 20 individuals as a population size, is an efficient setting.

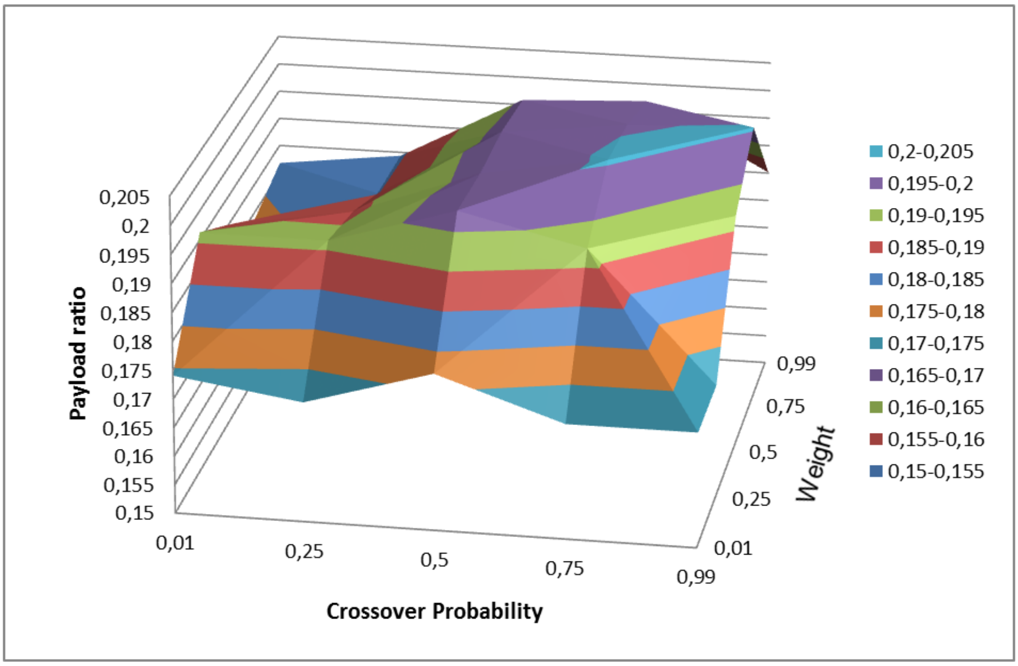

Figure 5.3: 3D visualization of the results obtained from different weight and crossover probability DE algorithms

Chapter 6

Tool Implementation and External Software

This chapter presents the reader a quick overview of the external software that was used to interact with the program code written in C++ by the author and how the overall tool works. The overview of the external software includes the aerodynamic prediction tool Missile DATCOM in 6.1, the astrodynamics toolbox Tudat in 6.2, the global optimization toolbox PaGMO 6.3 and the Chemical Equilibrium with Applications (CEA) tool 6.4. The chapter finishes with an overview of the code architecture of the simulation tool in section 6.5.

6.1 Missile DATCOM 97

Missile DATCOM is an aerodynamic prediction tool that predicts aerodynamic forces, moments and stability derivatives as a function of angle of attack and Mach number for missile configurations. It has been under continual development for more than 20 years. The code, which is written in FORTRAN, is also subject to ITAR (International Trade in Arms Regulations), but the 1997 version is available free of charge in a supplement CD of the book "Design Methodologies for Space Transportation Systems", by Walter E. Hammond [24]. Missile DATCOM can generate aerodynamic force coefficients for up to 20 different angles of attack and up to 20 different Mach numbers for a total of 400 coefficient sets per configuration. Missile DATCOM is software that was found to have some difficulty in predicting axial force error[1], but overall, it followed experimental data quite closely concerning normal force and center-of-pressure locations. Another downside of the code is that the method used to calculate the axial coefficient is only valid up to an angle of attack of 30°. Beyond this value the program switches to an empirically derived method with far greater uncertainty. For this study, the force components are

[1] In [14] the code was found to have a double "Mach" peak at about 1.7 Mach for the axial force coefficient, C_A, which is not expected to actually occur.

most important. The axial force is one of the most difficult aerodynamics forces to predict [48] and an angle of attack range of $\pm 30°$ is deemed large enough for the purpose of this study. Therefore, Missile DATCOM is chosen to be a sufficient basis for the aerodynamic model in the simulations presented in this thesis.
Implementation of the Missile DATCOM program was done through code provided by Frank Engelen, which was verified in [14]. This code block has as function to process the Missile DATCOM files. After reading in the input file, all coefficients are stored in a lookup table as a function of Mach number and angle of attack. The code does not allow to also use the aerodynamic coefficients dependent on the Reynolds number. Therefore the Reynolds number was assumed constant through the entire flight and a coefficient only depends on two variables. In order to estimate the dependency on these variables when their values fall between generated data points, bilinear interpolation is used. If a value of the independent variables is beyond the boundaries of the database the limit values are chosen and no extrapolation is performed.

6.2 Tudat

The TUDelft Astrodynamics Toolbox (Tudat) is an C++ library developed at the faculty of Aerospace Engineering of the TU Delft. The program is defined in the Tudat User Tutorial as follows [53]:

"Tudat (TU Delft Astrodynamics Toolbox) is a C++ library that provides functionality to perform astrodynamics simulations. Tudat is developed within the Astrodynamcis & Space missions chair at the Faculty of Aerospace Engineering, Delft Universtity of Technology, the Netherlands. Tudat is set up with particular focus on modularity and robustness of code."

The toolbox has a very wide range and can therefore be implemented in various applications such as interplanetary trajectories, launcher ascent trajectories, vehicle re-entry, etc. Information between the users and developers of Tudat is being exchanged through multiple venues. First there are the bi-weekly Working Group Meetings where all active developers and interested users discuss progress of the Tudat code and further development. Then there are also monthly management meetings meant to discuss the overall progress and longevity of Tudat. The internet is also used as a means of communication. The Tudat website can be accessed at tudat.tudelft.nl. The website hosts a forum with development discussions and also a wiki is available to explain the concept of Tudat to newcomers. The website is also used to create issues concerning the Tudat development and these can be created by all users. Minutes of meetings are also documented online. In addition, various external libraries such as Eigen, Boost and CMake are needed to use the functionality of Tudat.

6.3 PaGMO

PaGMO stands for Parallel Global Multiobjective Optimizer and is a C++ platform[2] with the intention to easily perform parallel computations of optimizations tasks. For

[2] PaGMO also has a python alter ego named PyGMO.

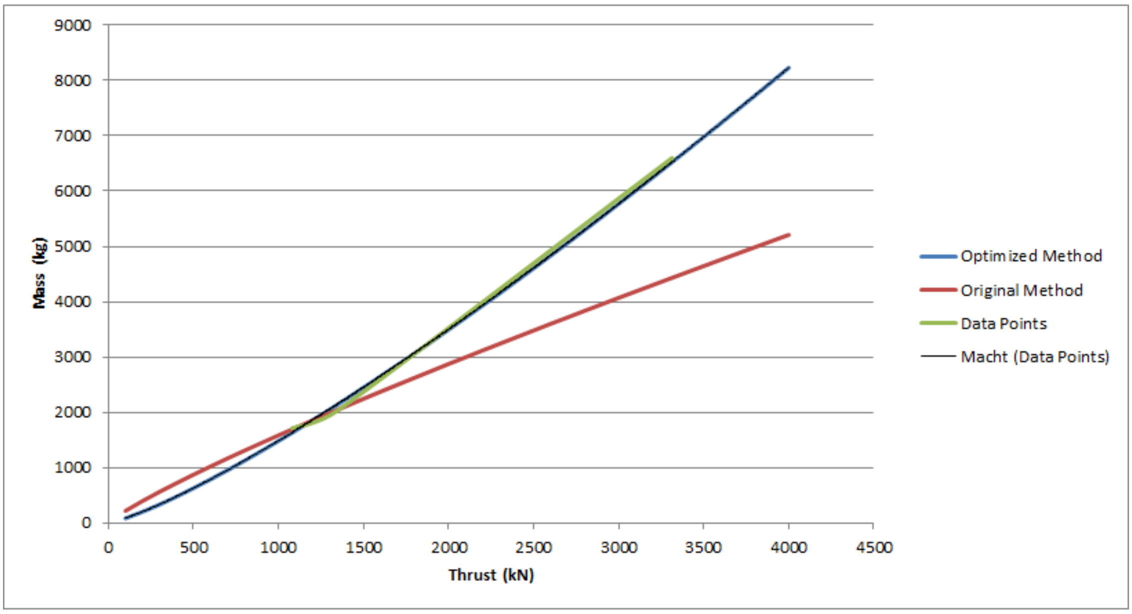

Figure 6.1: Hydrolox engine weight according to the original method (Eq. (3.44)), the optimized method obtained through PaGMO (Eq. (3.68)), the actual data points of the 3 hydrolox engines according to [15] and the "Macht" function from Microsoft Excel.

this purpose PaGMO contains many state of the art optimization algorithms, both global and local algorithms, and also includes an extended set of optimization problems. PaGMO can also interface with other optimization frameworks/algorithms such as NLOPT, SciPy, SNOPT, IPOPT, GSL. Developed within the European Space Agency, the code was initially coded for the automated design of interplanetary trajectories and spacecraft transfers in general. The user can implement his own problem and algorithm both in C++ and in Python. The reason that the decision was made to use PaGMO was driven by a couple of factors. First of all, PaGMO has been tested and validated for a number of space mission scenarios, secondly making use of such a platform leaves freedom to compare how different algorithms fare whilst trying to optimize the problem at hand. In addition, together with several members of the Tudat team it was decided that PaGMO was the most interesting optimization toolbox to interface with Tudat.
Verification of PaGMO was done by optimizing the standard deviation of the hydrolox engine data points as was done in section 3.3.3 and comparing this with the Microsoft Excel data-fit, which was shown in figure 3.5. Here it can be seen that the optimized method to minimize the standard deviation with PaGMO, depicted in blue, coincides with Microsoft Excel's internal function depicted in black. Another verification was by maximizing the area-to-circumference ratio of a rectangle, a problem where the solution has a maximal objective value if the rectangle is a square. This problem was made more difficult by extrapolating it to hyper rectangles. PaGMO's optimization algorithms found that the ratio between the hyper volume and the hyper circumference was always maximized when the hyper rectangle has the same size in all dimensions.

6.4 CEA

The program CEA, which stands for Chemical Equilibrium with Applications, is also known by the name of the NASA Glenn Equilibrium Program. The program is written in ANSI standard FORTRAN by Bonnie J. McBride and Sanford Gordon [7]. CEA calculates complex chemical equilibrium product concentrations from any set of reactants and determines thermodynamic and transport properties for the product mixture. It is used in this study to tabulate values for T_c, M and γ for both $RP1$ as well as $LH2$ fuel and a whole array of chamber pressures and area ratios. Assumptions made in the tool are one dimensional forms of the continuity, energy and momentum equations, zero velocity at the combustion chamber inlet, complete and adiabatic combustion, isentropic expansion in the nozzle, homogeneous mixing, ideal-gas law and zero temperature and velocity lags between condensed and gaseous species [22]. It is also used by the ASTOS (AeroSpace Trajectory Optimization Software) library as a 3rd party model [63] and it was also subjected to verification and comparison with another software industry standard and gave very similar results [61]. Therefore it was deemed to be useful as a means of obtaining the thermodynamic data needed for the vehicle model.
The CEA database used in the simulation program consists out of a total of 3648 data points. These were created at each increment of 0.5 in the oxidizer to fuel ratio, ranging from a value of 1 to a value of 10, and at each increment of 8 bar of chamber pressure, ranging from a value of 8 bar up until a value of 264 bar. These data points contain values of the ratio of specific heats, γ, the chamber temperature, T_c and the molar mass, R. The method that was used to interpolate linearly between these data points was extensively tested by Dominic Dirkx.

6.5 Code architecture

The code was developed in C++ in order to be compatible with Tudat. The flowchart is depicted in 6.2. The Input of the program, the launch simulator, consists out of two parts. First there is the individual generated by the differential evolution algorithm, which contains 11 to be optimized parameters and secondly there is a set of inputs defined by the user, which consists out of the fuel type and the initial state of the launcher. The inputs are given to the vehicle model in order to construct a configuration of the launcher and to the control block, which defines the settings of the thrust throttle and the orientation of the vehicle. The information from the vehicle model is transmitted into the launch simulator loop, depicted in blue, by passing it on to the body information, which also contains the state, and communicates the state vector with the environment model. After an update of the state vector, the body information code block transforms the state vector to different reference frames and coordinate systems. The other sub models can then also be updated. The Missile DATCOM Database provides new aerodynamic coefficients in the aerodynamic reference frame to the aerodynamic force code block, which has as output the aerodynamic force vector in the inertial frame. The same holds true for the rocket motor, which provides the magnitude of the thrust force to the thrust force code block, which converts it to a force vector in the inertial frame. Together with the gravitational force, these force models pass the force vectors on to the translational equations of motion from which the acceleration of the vehicle is derived. The propagator collects this acceleration and the integrator then computes a new state in the inertial frame which is then evaluated so that it does not violate any hard constraints, if it only violates for example the axial acceleration constraint this information is transmitted to the control block, which then alters the throttle setting. Other parts of the state can also influence the pitch control or the throttle. If no abort is made the state is resubmitted in the Body Information code block and the loop starts again. During optimization the objective function gets evaluated and the differential evolution algorithm minimizes its value by altering the optimizable parameters. If a constraint is violated the objective value gets a penalty value assigned to it during the function evaluation process. The output of the optimization process needs to be inputted in a copy of the launch simulator, which generates additional data on the launch in data files. Postprocessing of these data files is then done with Matlab.

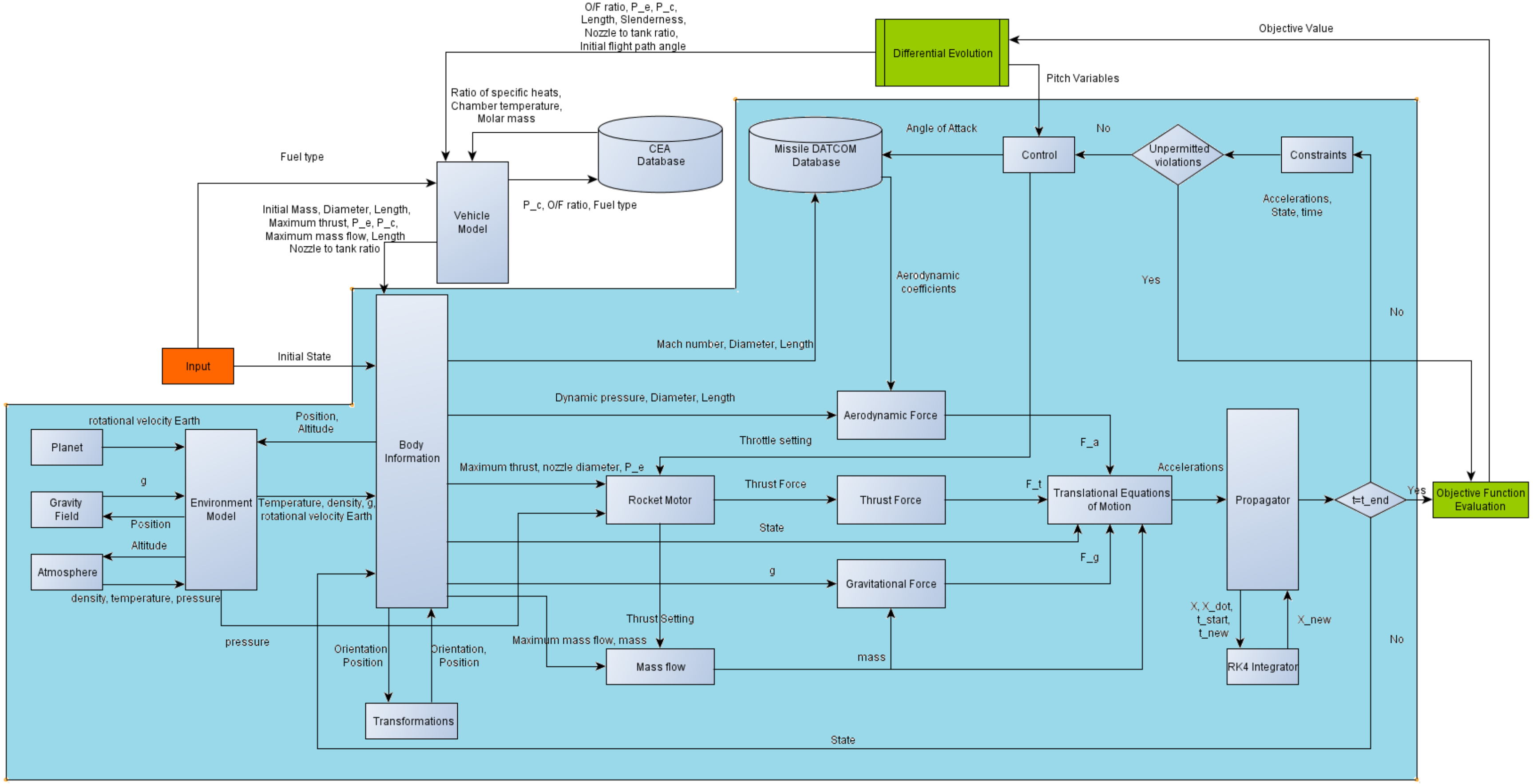

Figure 6.2: Flowchart of the simulation tool.

Chapter 7

Results

In this chapter the main results and a short introduction to how they were obtained are presented in section 7.1. This is followed by a thorough discussion of their implications in section 7.2 and finally, the model is subjected to a sensitivity analysis in section 7.4. The data on which most of the plots presented in this chapter are based, can be found in Appendix B.

7.1 Introduction to the results

The objective of the study is to optimize the performance of several launch vehicles that utilize the assisted-launch technique and draw conclusions on the effect that the launch-assist parameters have on the vehicle design and total system performance. For this reason, a launch simulation of these vehicles must be performed. This simulation is subjected to a number of constraints, which were discussed in section 3.7. These constraints are the bending-load limit, the axial-acceleration limit, the angle-of-attack limit, the heat-flux limit and the altitude limit. Each launch vehicle will be simulated with different input parameters. These inputs[1] are the propellant type (hydrolox or kerolox), the initial velocity and the initial altitude of the launcher, also referred to as the launch-assist parameters. During the optimization process a set of 11 parameters, consisting out of 5 trajectory parameters and 6 launch-vehicle parameters, is altered, generating a different flight path of the launch vehicle and a different launch vehicle performance and mass. The different flight path and launch-vehicle characteristics change the performance of the assist technique, which is defined as the ratio between the payload mass and the total launch-vehicle mass, from now on referred to as the payload mass ratio. For every unique set of inputs, a unique set of these 11 parameters will be found by the DE optimization algorithm that describe the optimal vehicle and trajectory required to get the maximum payload mass ratio into orbit considering the given inputs and applicable

[1]Another input needed for the model is an estimation of the optimized payload mass ratio, which is required for the estimation of the fairing mass.

constraints. The settings of this DE algorithm are a population of 20 with a crossover of 0.83 and a weight of 0.71 as discussed in section 5.1.5.
A total of 60 input sets were chosen, leading to a total of 60 sets of the aforementioned 11 parameters. Through this chapter, the author hopes to provide the reader with a thorough understanding of how the input parameters influence the launch-vehicle parameters, how the launch-vehicle parameters influence each other and how the input and launch-vehicle parameters influence the objective function, the payload mass ratio. The 60 sets of inputs consist out of the 30 combinations that can be made with the following launch-assist parameters for both the kerolox type of vehicle as well as the hydrolox type:

- Altitude: 0, 5000, 10000, 20000, 40000 [m]
- Velocity: 0, 300, 600, 1000, 1500, 2000 [m/s]

These parameters were chosen to have this range, because the outermost values roughly correspond with what is possible with current day technology for conceivable assist systems. The altitude limit of 40 km roughly corresponds with altitude records of high air balloons and air-breathing engines[2] while the speed limit was based on the record of the X-15 rocket plane[3]. The parameters also have increasing leaps between each other since it was expected beforehand that the further one gets from the no-assist case, the smaller the increments in the objective function will be, as can be seen in figures 7.2 and 7.3, where the surface is visibly steeper at the origin than at the outermost point[4]. This has several reasons, firstly it is in part due to the logarithmic nature of Tsiolkowski's equation, see Eq. (3.73), but it is also due to the nature of the sum of the drag and gravity losses, seen in figure 7.18, which are maximized at low altitudes and to a lesser extent at low velocities. To give a good overview of the objection function's impact by the parameters, more data points were deemed needed in the expected high gradient environments. The 11 trajectory and launch-vehicle parameters that need to be optimized are summarized below accompanied by their respective search spaces:

- The 4 Pitch variables (see section 3.6.3) (search space: 0 - 1)
- The length of the propellant tanks (search space: 10 - 100 m)
- The slenderness of the propellant tanks (search space: 1.82 - 20)
- The ratio between the exit diameter of the nozzle and the diameter of the propellant tanks (search space: 0 - 1)
- The ratio between the oxidizer and the fuel mass (search space: 1 - 10)
- The chamber pressure (search space: 8 - 264 bar)
- The nozzle exit pressure (search space: 0 - 100,000 Pa)

[2] The altitude record for balloons is pending verification at approximately 39,000 m and for aircraft it stands at 37,650 m [16]

[3] The fastest speed achieved by the X-15 was 2,020.62 m/s [43]

[4] This would be even more obvious when plotted logarithmically, which would indicate the relative increase in the payload mass ratio

- The initial flight-path angle[5] (search space: 0 - 1.5 rad)

For every set of input parameters the resulting launch-vehicle and trajectory parameters are tabulated in Appendix B together with other relevant information. Taking a look at the outermost left column of table B.1 reveals that for a launch of a kerolox launcher, ignited at an assist altitude of 0 m with an assist velocity of 0 m/s, the optimal length is 18.56 m. The optimal slenderness is 10.38, the optimal diameter is 1.79 m, the optimal nozzle diameter is 0.88 m, the optimal oxidizer-to-fuel ratio is 2.50, the optimal chamber pressure is 263.98, the optimal exit pressure is 45861 Pa and the optimal initial-flight-path angle is 84.81 deg. This optimal configuration leads to an injection of 859.9 kg into an orbit with an apogee larger than 250 km and an eccentricity smaller than 0.01. This results in an optimized payload mass ratio of 0.021. The table also reveals other information such as the maximum dynamic pressure, the maximum heat flux, the maximum bending load and the times of their occurrences, the gravity and drag losses, several masses, the initial and maximum acceleration, the moment when the fairing is jettisoned, the nozzle area ratio, the maximum thrust, and the maximum angle of attack.

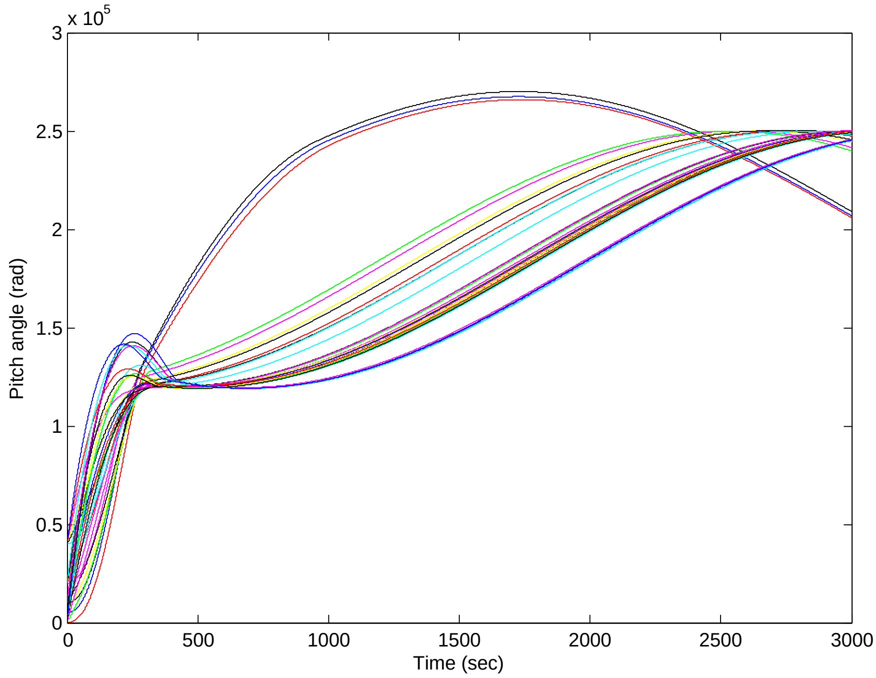

Figure 7.1: Altitude vs time plots of all optimized hydrolox simulations

In Appendix C a lot of additional information about all optimal launch trajectories is plotted. This includes the inertial velocity, the eccentricity, the altitude, the total acceleration, the pitch angle, the angle of attack, the dynamic pressure, the bending load, the heat flux, the position, the lift-to-weight ratio and altitude vs velocity. An example of this is given by the altitude plots of the 30 hydrolox vehicles, which is shown in figure 7.1.

[5]unless stated otherwise this is also the initial pitch angle since these were mostly set at the same values at t=0.

In this figure it can be seen that 3 particular cases deviate from the norm by performing a continual rise past the 120 km mark, while most follow a trajectory that stays in this region for an extended amount of time. This information is helpful to create a better understanding about the subject of assisted launch and some imperfections of the models used. This specific deviation is further explained in section 7.3.3. The color codes of the lines in the figure are only for enhanced visibility.
The evolution of the objective function, the payload mass ratio, is visualized in figure 7.2 for hydrolox launchers and 7.3 for kerolox launchers. In these figures the values of all 60 optimized payload mass ratios are interpolated with a cubic spline function and plotted in accordance to their respective launch-assist parameters. The importance of the assist altitude and velocity on the launcher's efficiency is quantified and it can be seen that the payload ratio increases both with increasing assist velocity as with increasing assist altitude. The optimized launcher for the no-assist case has a maximum payload mass ratio of only 0.021 for kerolox vehicles and 0.031 for hydrolox vehicles. This rises to values of 0.15 and 0.19 for kerolox and hydrolox vehicles for the highest assist case. To get a sense of the importance of both assist parameters with respect to each other, a comparison of the results utilizing the lowest assist altitude and those with the highest assist altitude shows the following. To get the same performance increase by adding velocity instead of altitude one should add a velocity of about 400 m/s for kerolox launchers and 540 m/s for hydrolox launchers for the entire performance increased caused by a change in assist altitude of 0 km to 40 km. The difference between the two types of launchers has to do with the drag losses, which will be discussed in section 7.2.12.

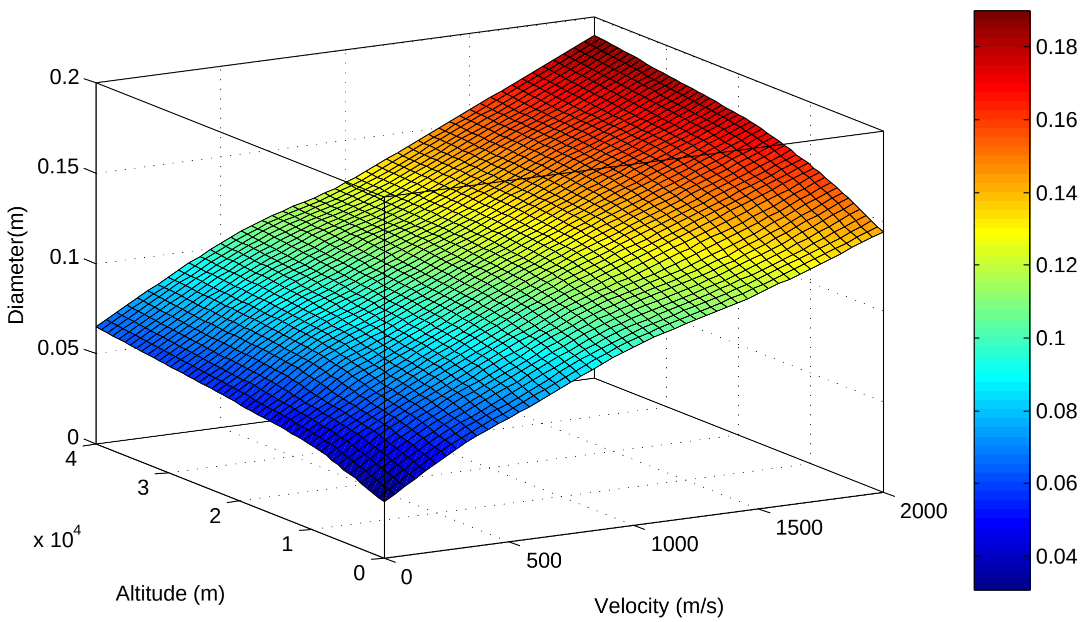

Figure 7.2: Cubic spline fit of the payload-mass to initial-mass ratio of optimized hydrolox launchers and launch trajectories for different combination of assist velocities and altitudes.

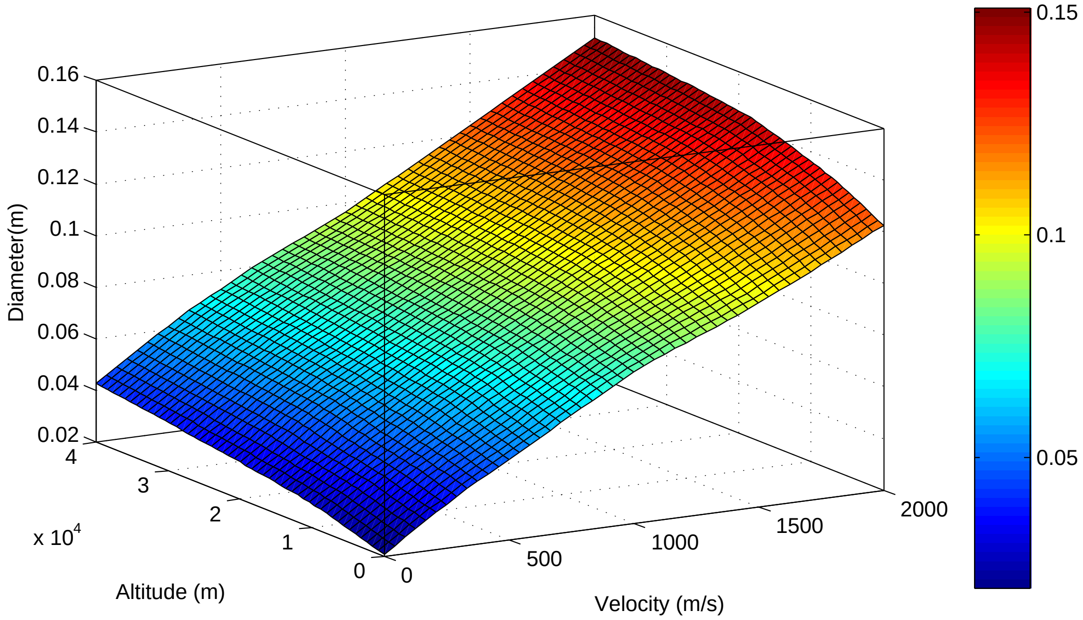

Figure 7.3: Cubic spline fit of the payload-mass to initial-mass ratio of optimized kerolox launchers and launch trajectories for different combination of assist velocities and altitudes.

7.2 Discussion of the launch-vehicle parameters

In this section all optimized launch-vehicle parameters and some extra parameters of the model will be discussed together with the trends that they follow, which will be analyzed and explained. All plots shown are cubic spline interpolations of 30 data points, meaning that the displayed 3-D surface intersects with all data points.

7.2.1 Fuel type

The model used two types of fuel, kerolox and hydrolox. This parameter is the sole parameter that was not optimized by the algorithm but was fixed. Therefore, the altitude-velocity plots of all parameters are presented in this chapter twice, once for the hydrolox launcher case (always depicted in the left subfigure) and once for the kerolox case (always presented in the right subfigure). As could already be seen in figures 7.2 and 7.3, all altitude-velocity combinations uniformly show that hydrolox vehicles provided a greater payload ratio than kerolox vehicles. Relatively speaking, the type of fuel gives a far smaller effect for high-assist systems. With no assist, the difference in the payload ratio is 0.01006 or in relative terms this means that a switch from a kerolox launcher to a hydrolox launcher gives a relative performance gain of 48.4 %. At an assist altitude of 40 km with a velocity of 2,000 m/s the difference in payload ratio is less than 0.039 corresponding to just a relative improvement of 25.7%. This effect is even greater when adjusting for residual propellant mass not accounted for in this study. The results of the vehicles published in Appendix B are also split up according to their fuel type. The tables B.1 to B.6 give the results for the kerolox vehicles while the results of the hydrolox vehicles are published in tables B.7 to B.12.

7.2.2 Length

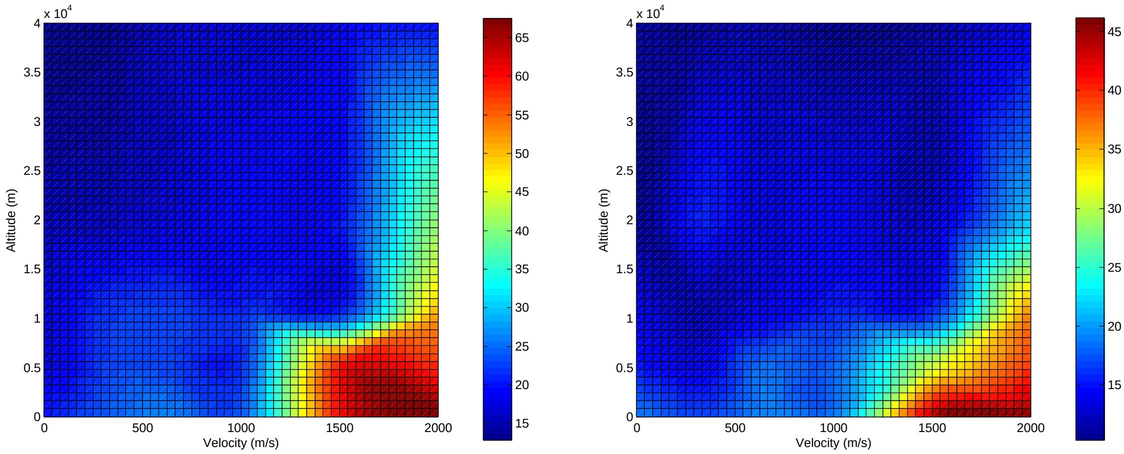

(a) (b)

Figure 7.4: Length (m) of the optimized hydrolox vehicles (a) and kerolox vehicles (b).

The search space of the length of the tank was taken to vary from 10 - 100 m. This is based on the dimensions of the six launchers, given in section 3.3.3, on which the model was based. These launchers are roughly 3 times longer than the lower boundary and 3 times shorter than the upper boundary of the search space used. The variation of length along the different vehicles optimized for different assist parameters shows a couple of clear trends. Looking at figure 7.4, the most attention is being grabbed by the high length peak in the high-velocity/low-altitude region. It appears at first glance that this happens to minimize drag losses. This square cube law effect of minimizing drag losses by increasing launcher dimensions was explained in section 3.5 and basically states that drag loss decreases with increasing length. However, when looking at the drag loss in figure 7.15 it can be seen that not one but two local peaks occur in drag loss while only one (the smaller one) translates in larger dimensions. Further discussion on this anomaly is provided in section 7.2.3.

Next to this global peak, the rest of the figure looks like irresponsive space. A look at the data presented throughout Appendix B reveals that there are the trends in this space of decreasing length with increasing altitude and decreasing length with decreasing velocity over the entire spectrum. This can be explained by a combination of the drag loss effect and by the results displayed in section 3.3.3. In this section, two vehicles were optimized for maximum ΔV. The first set with a thrust-to-weight ratio of zero had a maximum length of 100 m due to the tank surface-to-volume ratio that gets maximized with large tanks. The second set, had a thrust-to-weight ratio of 1.15 and found that the drive for a larger length to minimize the surface-to-volume ratio was counteracted by the drive to minimize the hydrostatic pressure, which causes a thicker tank thickness for longer tanks, and the drive for smaller mass to minimize the engine mass ratio (see Eqs. (3.69) and (3.68)) to the degree that the optimal length was found to be between 12 and 13 meter. This means that in the absence of severe drag loss, the thrust-to-weight ratio plays an important role in the optimization process of the length. With the launches that occur at

40 km, drag loss is almost negligible and the length is indeed observed to increase with decreasing thrust-to-weight ratios.

7.2.3 Slenderness and diameter

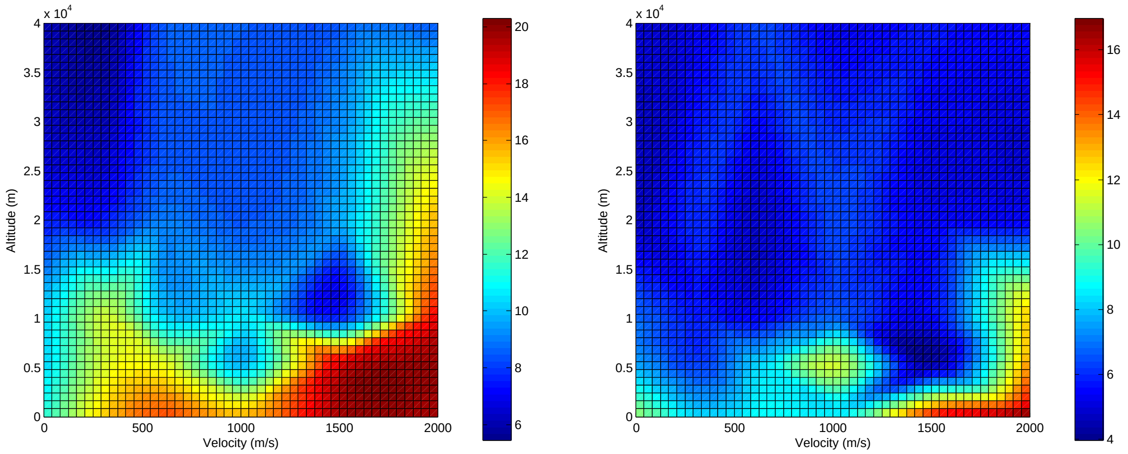

(a) (b)

Figure 7.5: Slenderness of the optimized hydrolox vehicles (a) and kerolox vehicles (b).

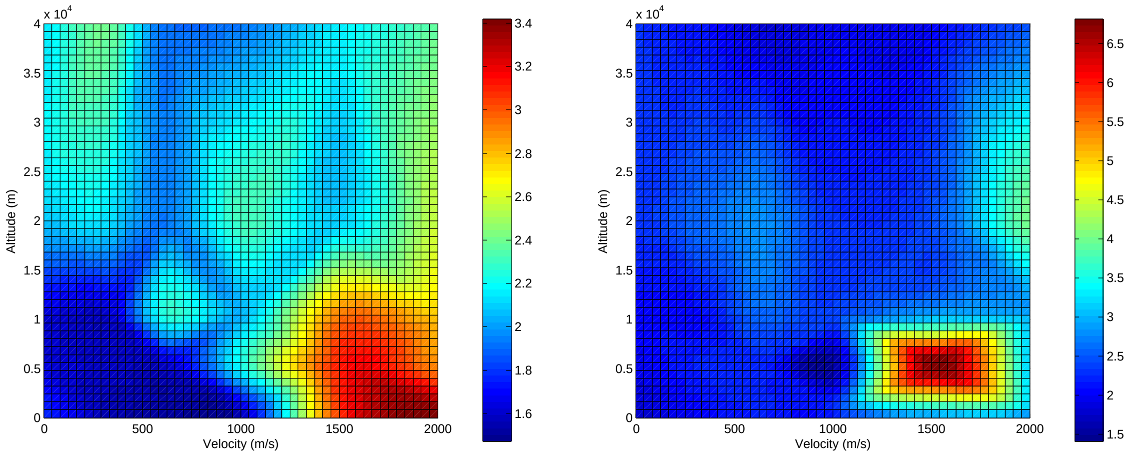

(a) (b)

Figure 7.6: Diameter (m) of the optimized hydrolox vehicles (a) and kerolox vehicles (b).

The search space of the slenderness, λ, ranges from 1.82 to 20. This was chosen based on data from [15] of several launch vehicles shown in table 7.1. In this table it can be seen that the maximum slenderness is 12.44 while the minimum slenderness is 2.73. It was deemed necessary to have at least a margin of 50% on both the minimum and the maximum value in the search space and due to programatic convenience the values of 1.82 and 20 were chosen. In figures 7.5 and 7.6, the optimal values of the slenderness

	ATLAS 5	Zenit	K1	Delta IV	Angara
Length Diameter Slenderness	32,46 3,81 8,52	33 3,9 8,46	18,3 6,7 2,73	40,8 5,13 7,95	25,14 2,9 8,67
	Long March CZ-5-200	Long March CZ-500	H2A	H2	Soyuz booster
Length Diameter Slenderness	28 2,25 12,44	31 5 6,2	37,2 4 9,3	28 4 7	19,6 2,68 7,31
	Soyuz	Energya strap on	Energya core	Delta 2	Ariane 5 ECB
Length Diameter Slenderness	27,8 2,55 10,9	38 4 9,5	59 8 7,38	26,08 2,44 10,67	30,5 5,4 5,65

Table 7.1: Length, diameter and slenderness of various first stage's [15]

and diameter can be seen over the launch parameter spectrum. The most noticeable trend of the slenderness parameter is that it maximizes in the high drag loss areas, which are located in the bottom corners of the plots as shown in figure 7.15, and that this is more the case for hydrolox launchers than for kerolox launchers. The explanation for the fact that kerolox launchers have less slender dimensions could be twofold. First of all, for kerolox vehicles, the nozzle-to-tank-diameter ratio is maximized for various simulations in the high velocity / low altitude spectrum implying that the only possible way to increase the nozzle exit diameter is to also increase the vehicle's tank diameter and thus have a slightly less slender body than desired. Secondly, the drag losses are significantly lower for the high-density kerolox vehicles than for the lower-density hydrolox vehicles. And as a final reason, hydrolox launchers have a greater performance than kerolox launchers and the higher the performance of the launcher, the more slenderness will tend to follow the drag-loss trend, which will be explained further on.
Another noticeable fact is that while the slenderness follows the drag loss it does this more so in the high velocity drag loss peak than in the low velocity drag-loss peak. To answer why this is the case one must take a look at Tsiolkowski's equation, see Eq. (3.73). Consider two launchers, both have a construction mass ratio of 7%. Launcher A is launched in the no-assist case and brings a payload to orbit of just 3%. Launcher B is launched with a high-assist velocity and brings a payload to orbit with a mass equal to 18% of the total launcher mass. Both launchers would be able to decrease their drag loss by 100 m/s by making the vehicle slender, which would result in a higher construction mass ratio of 7.5%. Assuming a specific impulse of 450 seconds this means that the ΔV of launcher A evolves as follows:

$$\Delta V = 450 \cdot 9.81 \cdot ln\left(\frac{1}{0.1}\right) = 10,165 \rightarrow \Delta V = 450 \cdot 9.81 \cdot ln\left(\frac{1}{0.105}\right) = 9,949 \qquad (7.1)$$

This formula shows that the performance increase due to the lower drag loss is more than canceled out by the performance decrease of 216 m/s due to the increased mass ratio.

For launcher B this performance decrease is only 88 m/s, see Eq. (7.2) causing its slender version to have a greater overall performance.

$$\Delta V = 450 \cdot 9.81 \cdot ln\left(\frac{1}{0.25}\right) = 6,120 \rightarrow \Delta V = 450 \cdot 9.81 \cdot ln\left(\frac{1}{0.255}\right) = 6,032 \qquad (7.2)$$

Furthermore, in the kerolox plots of slenderness and diameter there are two large anomalies identified at 5,000 m altitude with assist velocities of 1,000 m/s and 1,500 m/s. Combined with the large optimal length that was found at a velocity of 1,500 m/s and an altitude of 5,000 m, this leads to a very high global peak in the diameter plot. Since no physical explanation can be found for these anomalies, which are only observed with the kerolox launcher and not with its hydrolox counterpart, it might imply that the DE algorithm failed to converge at the true global optimum for this configuration resulting in an odd value for the slenderness. Furthermore, the simulation with an assist velocity of 1,000 m/s also has an anomaly regarding orbit insertion as can be seen in figure C.9, where it is displayed by the red graph having the highest altitude of all simulations from about 2,300 seconds into the simulation onwards. The fact that the slenderness parameter was identified by the sensitivity analysis as having a fairly small impact on the overall solution might be the reason why the algorithm failed to converge for the slenderness parameter on these two instances.
Other noticeable anomalies can be found in the hydrolox diameter plot. A region of high optimal diameters can be found for the high-altitude/low-velocity cases, this is mainly due to a region of local slenderness minima. Also at 2,000 m/s a large-diameter ridge is being displayed, which is a result of the large length tendency due to low optimal thrust-to-weight ratios found in this zone. This ridge would be even more pronounced if the slenderness at the data point utilizing an assist velocity of 2,000 m/s and an assist altitude of 20 km would not be so high. At this case, th hydrolox vehicle has a slenderness of 15.79 which compares with the kerolox vehicle that has a slenderness of just 5.33. The reason for this is because as was previously discussed, the slenderness of hydrolox launchers follows the drag loss trend more closely than kerolox launchers. And secondly, hydrolox launchers also have more drag loss than their kerolox counterparts.

7.2.4 Nozzle exit-to-tank ratio / Nozzle exit diameter

This ratio is optimized in a search space between 0 and 1, these values were chosen because this means that the nozzle never disrupts the airflow in a significant way by sticking out. This ratio scales the nozzle of the launcher and impacts the maximum thrust of the launcher (nozzle throat), the nozzle exit pressure (nozzle exit) and the nozzle mass. The ratio is displayed in figure 7.7 and shows that it gets influenced both by the length, see figure 7.4, and slightly by the exit pressure, see figure 7.12. The length effect can be recognized by the characteristic bottom-right global peak with an upward offshoot, while the exit pressure effect can be recognized by the distinct global minimum at the no-assist case.
The reason why it is influenced by the length is because an increase in length causes a cubic increase in mass and in order to keep the thrust-to-weight ratio to a decent level, the nozzle exit area, which has a great effect on the thrust, needs to be maximized. On

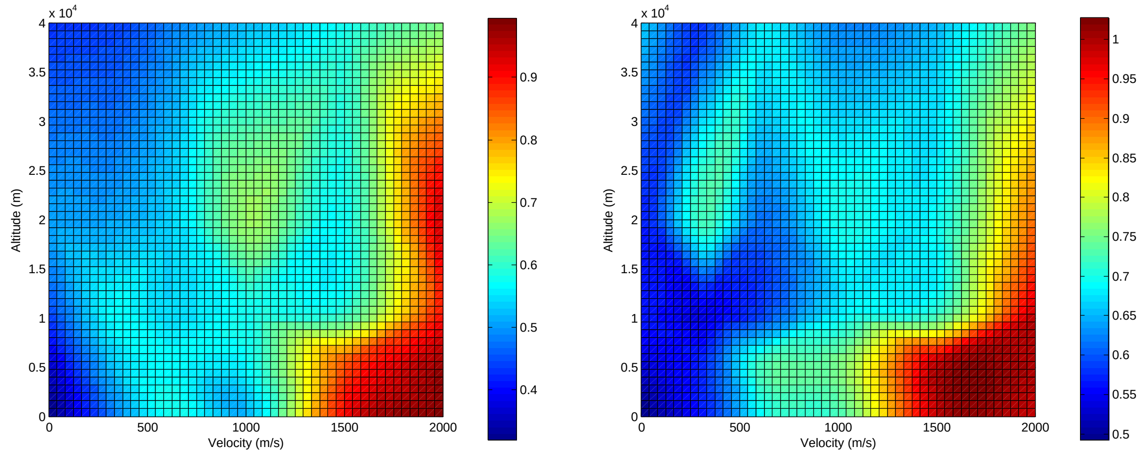

(a) (b)

Figure 7.7: Nozzle exhaust-to-tank diameter ratio of the optimized hydrolox vehicles (a) and kerolox vehicles (b).

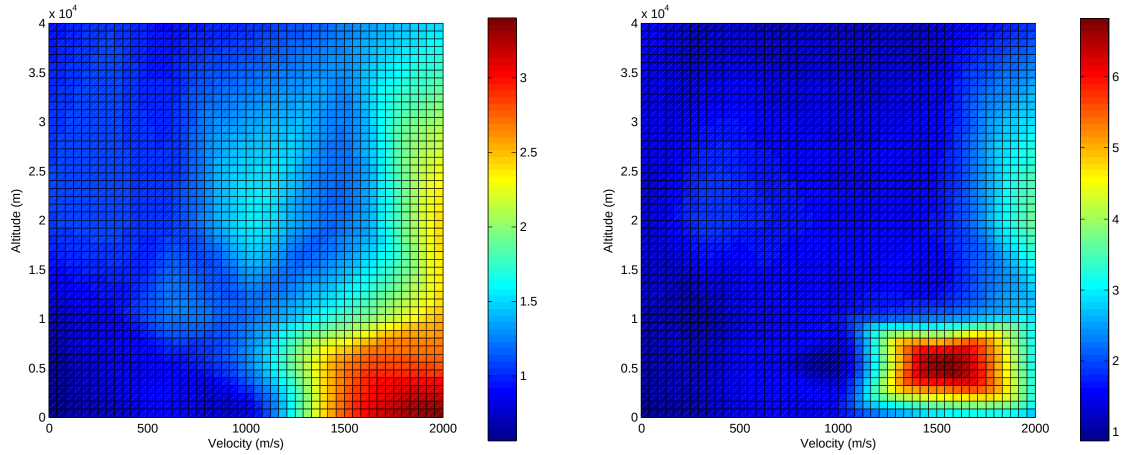

(a) (b)

Figure 7.8: Nozzle exhaust diameter (m) of the optimized hydrolox vehicles (a) and kerolox vehicles (b).

the other hand when the length is rather short the effect of the exit pressure can be seen. This is due to the fact that exit pressure peaks near the no-assist case implying the need for a small area ratio and together with a small thrust needed to propel the small vehicle, this translates into very small nozzle-to-tank ratios of 0.32 and 0.49 for the non-assisted hydrolox and kerolox cases respectively. Furthermore it was already noted that for the kerolox launcher the ratio approaches its upper boundary in a few assist cases (while that only happens in the most extreme hydrolox case) in these cases the ratio is deemed to interact with the slenderness of the launcher since they start to depend on each other but have opposite trends. The global maximum shown in the kerolox plot of the nozzle-exit diameter is due to the large optimal diameter found there, which was discussed in section

7.2.3.

7.2.5 Oxidizer-to-fuel ratio

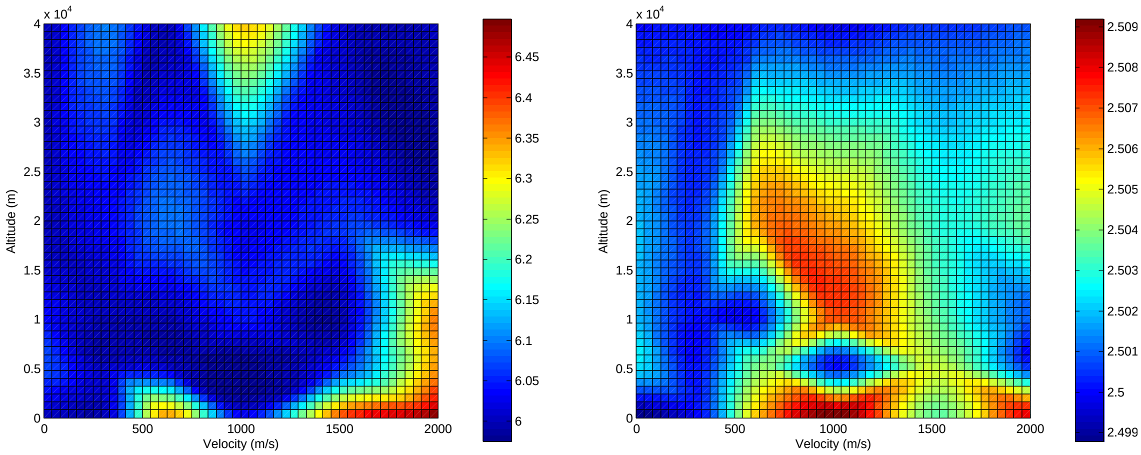

(a) (b)

Figure 7.9: Oxidizer-to-fuel ratio of the optimized hydrolox vehicles (a) and kerolox vehicles (b).

The search space of this parameter was set from 1 to 10 to have a large certainty that the optimum would be found for both types of fuels where the value tends to range from a low of 2.39 to 6.1, see tables 3.4 and 3.5. This parameter has two main influences on the performance of the rocket. Firstly, it will influence the specific impulse significantly and secondly it will influence the average propellant density and thus propellant tank volume and tank mass needed. The very minute variations shown in the plots, see figure 7.9 and note the legend, seem to indicate that not much of a trade off is performed by the model and that the value of the parameter is established independent of outside factors that change by choosing different assist parameters. The only real mentionable observation that can be made is about the hydrolox plot, where four of the six data points that have a value of 6.5 instead of 6 are grouped at the bottom right. The other two are regarded as noise from an imperfect model. The four data points coincide with the region where the drag loss and the dimension of the launcher is exceptionally high. This makes sense because higher oxidizer-to-fuel ratio leads to a higher density and lower drag loss, as shown by Eq. 3.76. No variation in the kerolox plot may indicate that either a higher resolution than 0,5 is needed in the CEA database or a more accurate interpolation method than the currently used linear interpolation method should be implemented.

7.2.6 Chamber Pressure

The search space for the chamber pressure was defined to lie between 8 and 264 bar. The effect of this parameter is twofold. First and foremost the chamber pressure has a significant impact on the specific impulse of the launcher. In [65] the effect of the

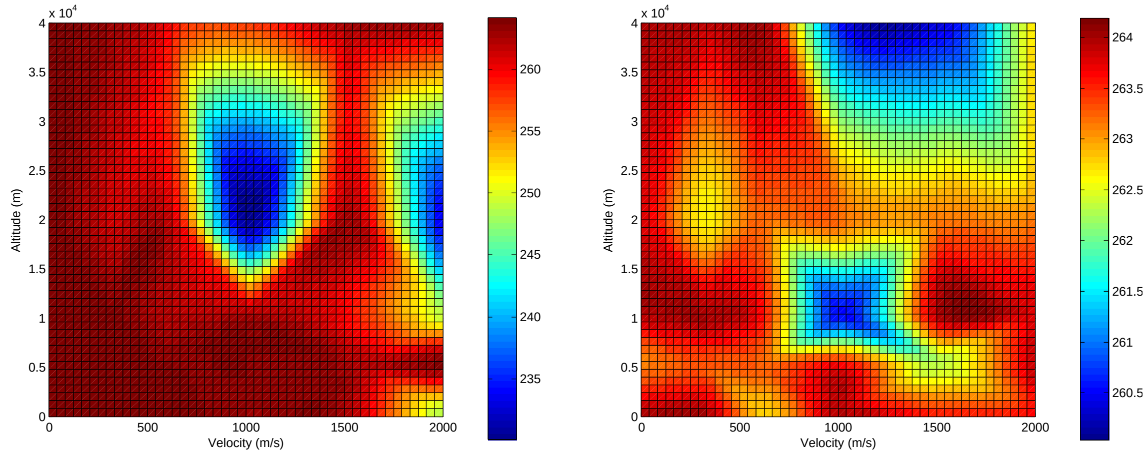

(a) (b)

Figure 7.10: Chamber pressure (bar) of the optimized hydrolox vehicles (a) and kerolox vehicles (b).

pressure ratio on the exhaust velocity is investigated by introducing the dimensionless exhaust velocity:

$$(U_e)_{dim} = \sqrt{2 \cdot \frac{\gamma}{\gamma - 1} \cdot \left(1 - \left(\frac{p_e}{p_c}\right)^{\left(\frac{\gamma-1}{\gamma}\right)}\right)} \tag{7.3}$$

The effect of Eq. (7.3) is plotted in 7.11 for various ratios of specific heats. As can be seen in this figure, the effect of the chamber pressure on the exhaust velocity almost flatlines at higher chamber pressures. For example, between a pressure ratio of 5,000 and one of 6,000 the advantage in specific impulse is only in the order of 0.5%. The other effect that the chamber pressure has on the model is on the nozzle mass, shown by Eq. (3.61). At very high pressure ratios the effect on the nozzle mass starts to contribute more to the optimization process than that of the specific impulse. This is why the low regions in the hydrolox chamber pressure plot, the left of figure 7.10, coincides with the low regions of the nozzle-exit pressure. Although this is not evident from figure 7.12 due to the high global peak at the no-assist case, careful examination of the data displayed in Appendix B led to the aforementioned conclusion that the local minima of the chamber pressure plots coincide with local minima found in the exit pressure data. In 2 of the 3 cases where exit pressure is modeled to be lower than 6,000 Pa, the chamber pressure is modeled to be lower than 240 bar (pressure ratios in excess of 4,000). But overall, the optimal chamber pressure is found to be around the maximum of the search space with few exceptions. This is an odd result since current engines, notably upper stage engines often operate at far lower chamber pressures. Examples are the Vulcain 2 (Ariane 5 first stage engine), which has a chamber pressure of 117.3 bar [4] and tests have been run for the Ariane 5 upper stage engine, Vinci, at around 55 bar [29]. The reason for this discrepancy with reality is up to speculation. It might be due to an underrepresentation of the chamber pressure in the mass model, since it would lead to a closer match with reality if the engine mass would be dependent on the chamber pressure. Another reason could be that for real engines, the additional small improvement might not be deemed important enough compared with regard to higher manufacturing costs. Whether or not the underrepresentation of the chamber pressure in the mass model has a genuine influence, the model should be expanded with a cost model to provide a definitive answer on the question whether or not current launchers utilize suboptimal chamber pressures.

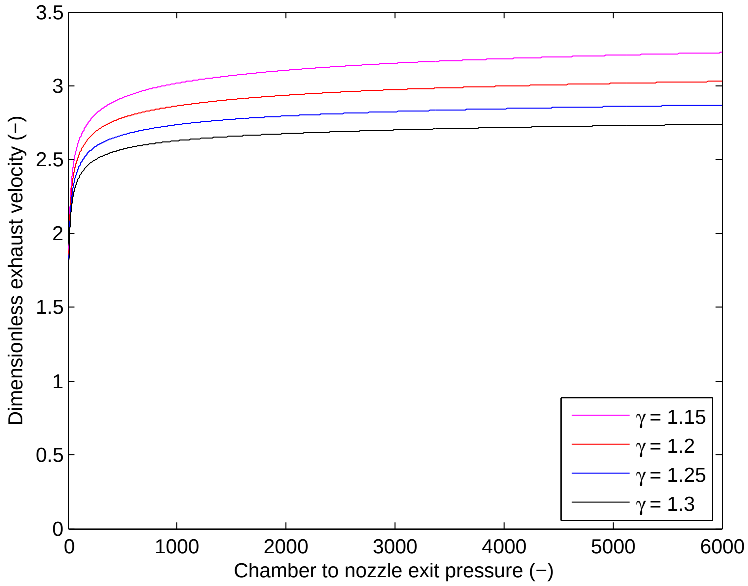

Figure 7.11: Dimensionless exhaust velocity as a function of pressure ratio

7.2.7 Exit Pressure

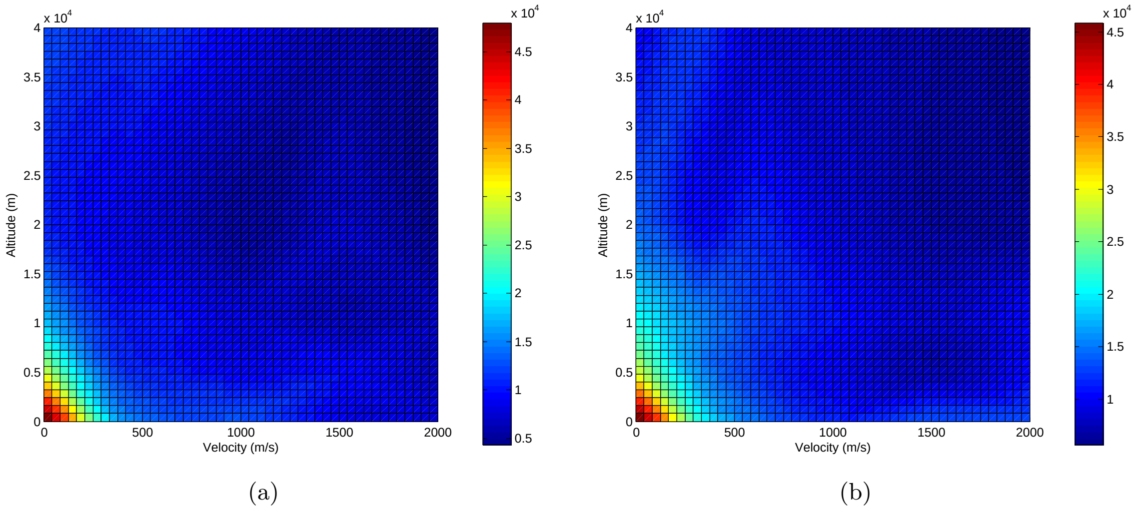

Figure 7.12: Exit pressure (Pa) of the optimized hydrolox vehicles (a) and kerolox vehicles (b).

The search space of the exit pressure was established to be between 0 and 100,000 Pa. The upper limit was established because an engine can not perform optimally from the Earth's surface all the way to space when the exit pressure is always higher than the ambient pressure, which decreases rapidly from its maximum value of 101,325 Pa. Therefore, it could be assumed beyond reasonable doubt that all optimal values lie within the region of the search space. An assumption that was rapidly confirmed as the first simulations were performed. This parameter also effects the exhaust velocity through the chamber-pressure-to-exit-pressure ratio depicted in figure 7.11. In addition, it also has an extra effect through the pressure thrust, see Eq. (3.71). In figure 7.12 it can be seen that this pressure thrust effect causes the optimal exit pressure to increase significantly in cases where the launcher spends a long period of time at low altitude, which happens for the low-assist cases. The reason why the optimal exit pressure decreases rapidly from its maximum even with the a relatively small increase in the assist parameters is due to the burn time in the densest parts of the atmosphere, which is rapidly diminished by even the smallest assist. The no-assist hydrolox launcher reaches 5 km after 58.6 seconds and 10 km after 79.5 seconds. For comparison, the optimal launcher launched at sea level with an initial velocity of 300 m/s reaches 5 km after 19.4 seconds and 10 km after 38.8 seconds. The launcher with assist altitude of 5 km and no assist velocity reaches the 10 km mark after 53.5 seconds without having to traverse the densest 5 km of the atmosphere. For a certain fixed assist velocity it is sometimes observed[6] that the optimized exit pressure achieves a minimum at 20,000 m altitude instead of 40,000 m altitude with cases at 10,000 m often optimizing about the same value as for cases at 40,000 m. Therefore it could be concluded that most if not all of the advantage of the pressure thrust component is already achieved at launch altitudes of 10,000 m.

7.2.8 Initial flight-path angle

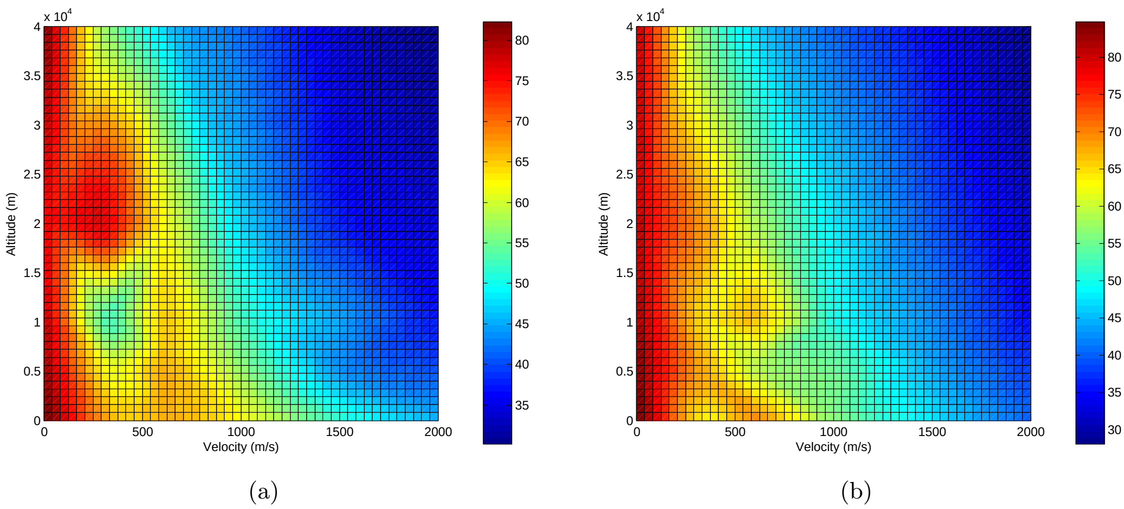

Figure 7.13: Initial flight-path angle (deg) of the optimized hydrolox vehicles (a) and kerolox vehicles (b).

[6] All for hydrolox but only at 300 and 1500 m/s for kerolox

The initial flight-path angle was chosen from a search space of 0 - 85.94° (0-1.5 radians) for convenience after it was established that even for the no-assist cases this angle was optimized to be lower than 85.94°. In the end, at burnout in a circular orbit, this parameter is desired to be 0. Also from the equation of gravity loss, Eq. (3.77), it can be seen that a large flight-path angle is detrimental to the launcher's performance. However, it must naturally be large enough to escape the atmosphere and with respect to drag losses and pressure thrust, the sooner the better. In figure 7.13 a clear trend can be seen where the flight-path angle decreases rapidly with increased assist velocity and also slightly decreases with increasing assist altitude. This smaller effect due to the altitude is higher at high-assist velocities than at low-assist velocities. For instance, the difference between the initial flight-path angle at 40,000 m and the one at 0 m is only 4.7° at no-assist velocity but more than 11.5° radians at an assist velocity of 2000 m/s[7]. There are some anomalies to be found in the plots and the data displayed in Appendix B. The initial flight-path angle turns out to be higher than expected with an assist velocity of 300 m/s at altitudes of 20 and 40 km for both fuel type vehicles. This is due to the fact that the optimizer found that it was better to gain altitude rapidly and keep the heat flux below the limit where a fairing would be needed. This is further explained in section 7.3.1. A couple of other flights also deviated slightly from the overall trend e.g. the case of 300 m/s at 0 m altitude for a kerolox vehicle where the initial flight-path is lower than its 600 m/s counterpart. This might be explained by the higher lift that gets produced at lower altitudes, as is discussed in section 7.3.2, but this explanation does not stay consistent with all high-lift cases. What can be noted about all other anomalies is that they take place in the low velocity part of the grid. This is also logical because the same deviation at a higher velocity has a greater impact due to the magnitude of velocity vector.

7.2.9 Thrust-to-weight ratio

The thrust-to-weight ratio is rather low for the whole range of vehicles ranging from a high of 1.372 to a low of 0.728. Considering the ΔV losses are mostly dominated by gravity loss, one would expect that a high thrust-to-weight ratio would be beneficial. In conventional vehicles gravity loss is larger than drag loss by a ratio of about ten to one [28]. This means that a higher thrust-to-weight ratio would shorten the time of flight and would be beneficial for gravity losses to a much greater degree that the increased velocity would be detrimental to drag losses. Even though the results show that the ratio of gravity losses to drag losses is considerably smaller than in conventional vehicles this is not believed to be the primary reason for the low results for thrust-to-weight ratios. There is namely another argument to be made in this discussion. While a higher thrust-to-weight ratio is mostly beneficial to the overall losses that occur during flight, an increase in this ratio can be achieved in two ways. The first is an increase in engine thrust, which increases engine mass according to Eq. (3.44) and (3.43), increases the thrust structure mass according to Eq. (3.45) and the tank thickness, Eq. (3.55). The second is to make the propellant tanks smaller for the same engine, which results in higher area to volume ratios for the propellant tanks and thus also higher construction mass ratios. In addition, in section 3.3.3 a general drive to minimize the thrust-to-weight ratio was discovered when only trying to maximize the ΔV of a launcher stage. This was caused due to a minimization

[7] This is for the kerolox types of vehicles, but the hydrolox vehicles share the same observations.

of the thrust structure mass and a low nozzle mass for a high specific impulse.
Even though costs are not taken into account, where the engines are usually the more costly component, the optimization model already hints at the use of small engines for the launch vehicle from a performance standpoint.
Another important influence that the thrust-to-weight ratio has is the impact on the optimal length of the vehicle. This was discussed in section 7.2.2 with the argument that when the thrust-to-weight ratio increases, the drive for a larger length to minimize the surface-to-volume ratio is increasingly counteracted by the drive to minimize the hydrostatic pressure and the drive to minimize the engine mass ratio.

7.2.10 Tank mass and engine mass

The tank-to-propellant mass ratio of the kerolox launchers are vastly superior to the mass ratios of the hydrolox launchers. For the optimized kerolox launchers the value ranges from 33.48 to 43.95 while for the hydrolox launchers the value stays a lot more constant in the range of 12.04 to 14.39. No significant trends could be established. The engine-to-propellant mass has peaks of 62.93 and 70.01 and lows of 44.64 and 48.02 for the hydrolox and kerolox vehicles respectively and also showed no significant trends. The only conclusion that can be drawn from this is that the mass ratios are clearly favorable for kerolox vehicles but eventually do not bridge the performance gap of the higher specific impulse of hydrolox vehicles.

7.2.11 Specific impulse

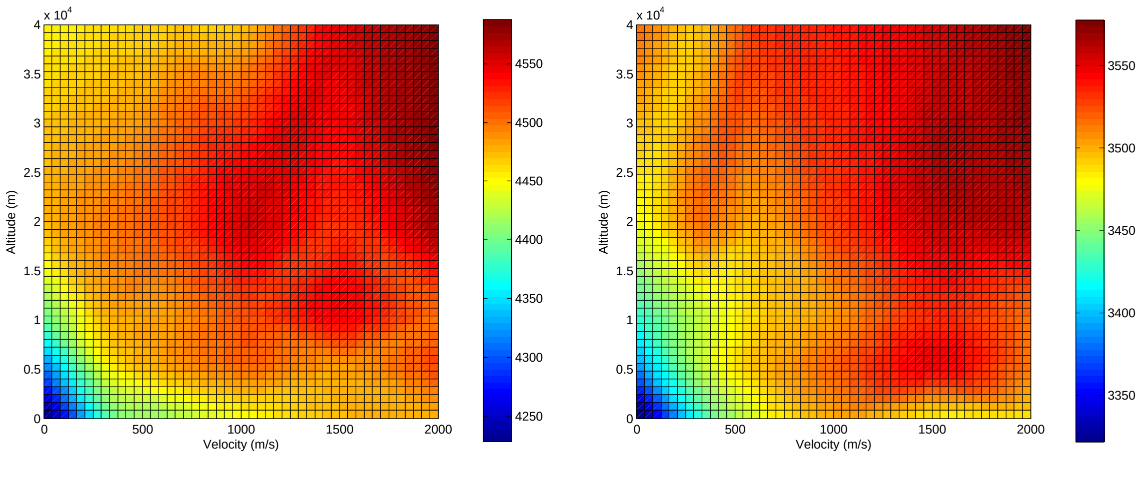

(a) (b)

Figure 7.14: Exhaust velocity of the optimized hydrolox vehicles (a) and kerolox vehicles (b).

The specific impulse depends on the exit velocity of the gas in the nozzle. This is given by Eq. (3.40) and from Eqs. (3.34), (3.38) and (3.39), from which it can be seen that the only parameters it influences are the exit pressure, the chamber pressure and the oxidizer-to-fuel ratio (through the ratio of specific heats γ, chamber temperature, T_c, and

molar mass, R). Since the variations in the chamber pressure and oxidizer-to-fuel ratio are rather low, the reflection of the exit pressure plots is most prevalent when looking at the chamber pressure plots. In the results given in Appendix B and plotted in figure 7.14, it can be seen that the exhaust velocity is often rather high. When no-assist was simulated, the exhaust velocities of the optimal solutions are the lowest for all assist combinations investigated. This is due to the fact that the launcher remains a longer time period in denser regions of the atmosphere. The lowest exhaust velocities found were 3,321.7 m/s for the kerolox launch vehicle and 4,228.2 m/s for the hydrolox launch vehicle, corresponding to a specific impulse of 338.6 and 431 s respectively[8].
Since these simulations were run without any assist the launch conditions are the same to those of other launchers. Therefore, these values could logically be compared with the values given for the 6 first stages presented in tables 3.4 and 3.5. The average first stage liquid hydrogen specific impulse is 430 seconds with a maximum of 446.1 swhile the first stage kerosene fueled engines achieve an average of 329.9 and a maximum of 337.8 s. The exhaust velocities are found to increase with the magnitude of the assist and reach a maximum when the assist consist out of an altitude of 40,000 m and a velocity of 2,000 m/s. Here the optimal vehicles had exhaust velocities of 4,587.4 and 3,578 m/s for hydrolox and kerolox stages respectively. This translates to specific impulses of 467.6 and 364.7 s. For the hydrolox launcher this compares well with the expected efficiency of the Vinci engine, which is 465 s. For the kerolox vehicle, the RD-0124 kerolox engine will be used as a benchmark, which is one of the most efficient kerolox engines in the world and reaches a specific impulse of 357 s [50]. All in all, the found optimal engine efficiencies are in correlation with the industry standard. However, a case could be made that the model slightly overestimates the efficiency of the kerolox launcher. On the other hand, other upper stage launch designs must take into account the larger interstage mass needed for a longer nozzle. This does not effect the optimization process of a single stage, which is performed in this study, resulting in large rocket nozzles with high area ratios. To have a sense of how important the specific impulse is, the thrust coefficient correction factor was lowered from 0.983 to 0.96 for the kerolox case of 1,000 m/s assist velocity and 10,000 m altitude. This leads to a reduction of the payload ratio of 0.384% or a relative decrease of 4.4%. In the case of just 300 m/s at 10,000 m it has a larger effect, namely a reduction of 0.505% or a relative decrease of 10.6%.

7.2.12 Drag Loss

The nature of drag loss was already discussed previously in section 3.5. From the results obtained and shown in figure 7.15, two main peaks can be established for both vehicle types. These peaks are located at the lowest altitude and at the outermost extremes of the velocity spectrum investigated. In addition, a valley of local minima can be seen at velocities between 500 and 1,000 m/s. This can be explained by examining Eq. (3.75), where drag loss is a function of three parameters: Drag(V^2), mass(t) and time itself. Therefore it is logical that to minimize drag loss a certain compromise must be reached between the velocity of traveling through the atmosphere and the time needed to escape it. In Eq. (3.76) it was also shown that drag loss is inversely related to the average density of the launcher and this can be seen when comparing the drag loss results of

[8] All specific impulses used in this section are acquired in vacuum conditions

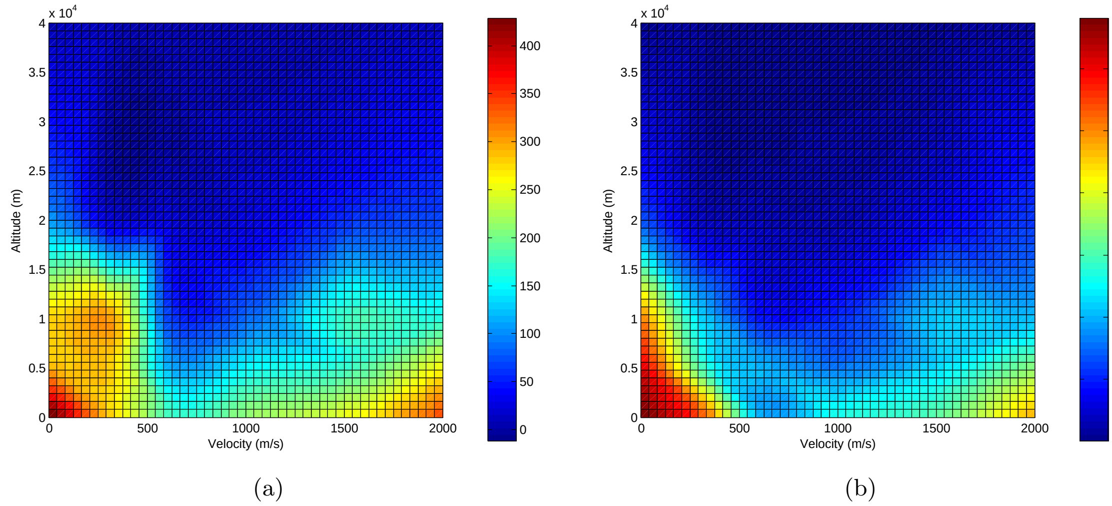

Figure 7.15: Drag loss (m/s) of the optimized hydrolox vehicles (a) and kerolox vehicles (b).

the set of hydrolox launchers with the set of kerolox launchers. The hydrolox launchers have an average drag loss of 143.6 m/s while the kerolox launchers have an average drag loss of just 99.8 m/s. Another anomaly in the drag loss results is that the drag loss is higher than expected at low-assist velocities. At the no-assist cases the drag loss reaches values as high as 340.8 m/s and 428.9 m/s for kerolox and hydrolox launchers respectively, which compares poorly with the values given for conventional launchers in [28] of 100 - 150 m/s. The reason for this anomaly is the high-lift trajectory that some of the low-assist simulations tend to follow. These lifting trajectories, which are further discussed section 7.3.2, would benefit smaller launchers more than larger launchers. This is again due to the square-cube law that relates the surface area that can provide lift with the volume/mass of the launcher. These trajectories also result in a flight profile where the launcher accumulates more velocity at lower velocities and thus accumulate more drag loss. In the altitude vs velocity plots displayed in figure 7.16, the 3 simulations with no assist velocity and the lowest assist altitudes can be seen to have significantly lower profiles. This is more so in the kerolox plot, displayed on the right than in the hydrolox plot. In the trade off between these high-lift trajectories vs low-drag loss trajectories, the pendulum swings more in the direction of high-lift trajectories for kerolox launchers than it does for hydrolox launchers. This is due to the fact that kerolox launchers are less sensitive to increased drag losses. This is also displayed by the comparison between figures C.24 and C.25 where it is displayed that the lift-to-weight is about the same magnitude for kerolox and hydrolox despite the severe density difference between both launcher configurations.

$$\frac{L}{M} \propto \frac{S}{V} \propto \frac{l \cdot d}{l \cdot d^2} = \frac{1}{d} = \frac{\lambda}{l} \tag{7.4}$$

Eq. (7.4) shows that the lift-to-mass ratio is dependent on the slenderness, λ, to length ratio. And while this is not the only driver for the slenderness and the length it might give an indication why the length anomaly of high drag and short length appears in the low assist corner of the assist spectrum provided.

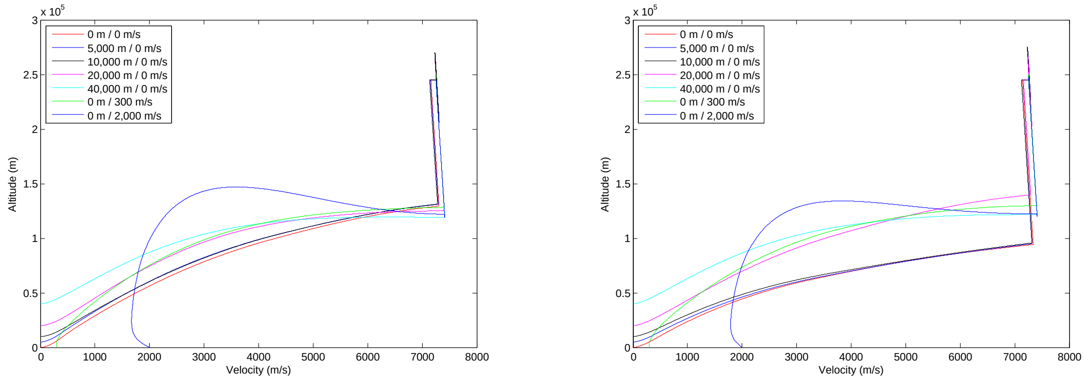

(a) (b)

Figure 7.16: Altitude vs Velocity plots of various launch cases for optimized hydrolox vehicles (a) and kerolox vehicles (b).

7.2.13 Gravity Loss

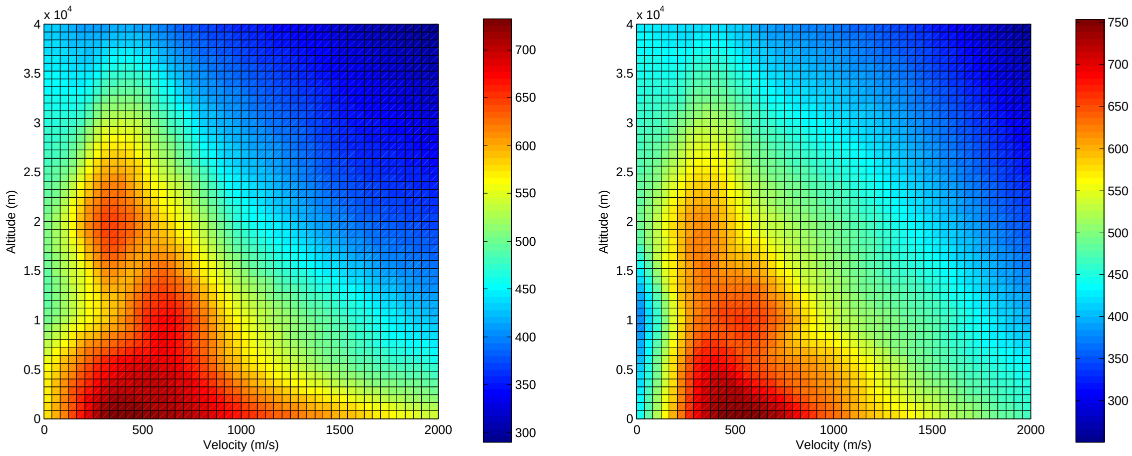

(a) (b)

Figure 7.17: Gravity loss (m/s) of the optimized hydrolox vehicles (a) and kerolox vehicles (b).

The gravity-loss difference between the different type of vehicles is almost negligible with an average of 482.2 m/s for hydrolox vehicles and 467 m/s for kerolox vehicles. However, when combining both types of losses, it can clearly be seen that kerolox launchers (566.8 m/s of average total losses) have an advantage to hydrolox launchers (625.8 m/s) of about 10%. Maxima of both launcher types are nearly the same with 721,5 m/s for the hydrolox launcher (at 0 altitude and 300 m/s) and 764.5 m/s for the kerolox launcher (at 0 altitude and 600 m/s). This compares with values of conventionally launched vehicles, which have gravity losses in the order of 1,000 - 1,500 m/s [28]. The trend in increasing gravity losses with decreasing assist velocity, which occurs from 2000 m/s all the way down to 600 m/s and in lesser extent 300 m/s is easy to explain. Furthermore if this trend would have materialized in the simulations with no-assist velocity, the gravity loss expected for the no-assist case would fall within or come close to the range of values of conventionally launched vehicles[9]. This trend can shortly be explained to be due to various causes. Firstly, there is the fact that at higher assist velocities, the duration of the flight can be shorter, since the difference between initial velocity and orbital velocity is smaller. Secondly, the initial flight-path angle and the flight-path profile in general can be significantly lower, since the initial vertical velocity component is already large at smaller flight-path angles and because the force against which the rocket must climb is smaller due to the centrifugal component. Looking at figure 7.18 a noticeable ridge is created at a velocity of 300 m/s indicating that at all altitudes with the exception of 40 km, the combined losses due to drag and gravity are highest at this assist velocity, an assist velocity often used in launch assist proposals. The reason for the anomaly encountered at low-assist velocities is more difficult to explain. This is most likely due to the major difference in the altitude profile these cases have when compared to other simulations. This altitude anomaly is further explained in section 7.3.3 and can be observed in figures C.8 and C.8. The gravity-loss anomaly is according to this hypothesis due to the higher thrust-to-weight ratio these launchers have, which results in a shorter burn time and causes them to burn more of their fuel at lower altitudes than the other launchers, which can be seen in the altitude-velocity plots 7.16.

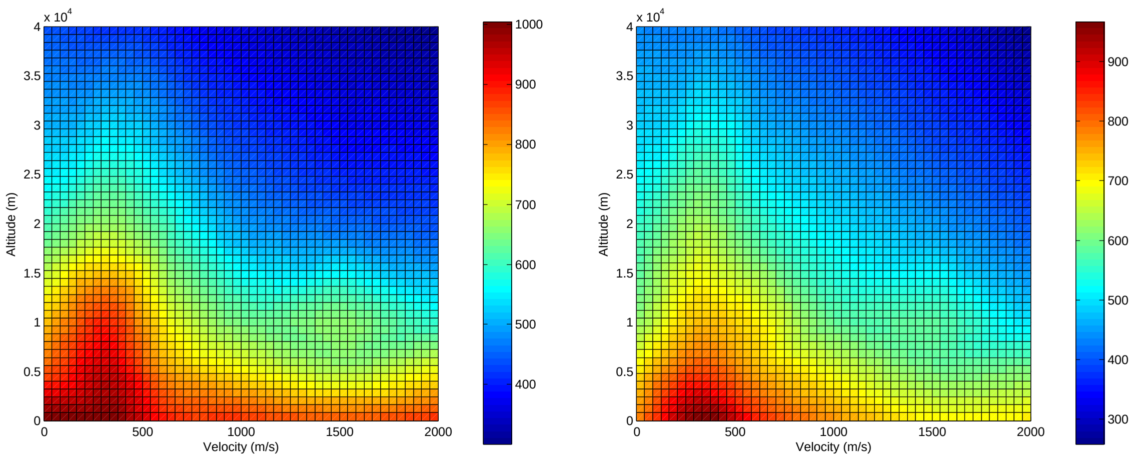

(a) (b)

Figure 7.18: Summation of the gravity and drag losses (m/s) of the optimized hydrolox vehicles (a) and kerolox vehicles (b).

[9]This with a launch to the fairly low target altitude of 250 km, which as explained in section 3.5 is also of influence on the gravity loss.

7.3 Notable flights

7.3.1 No fairing trajectories

There are eight flights[10] that have in common that the heat flux never surpasses the value of 1,135 W/m^2. As can be seen in figure 7.19a, this is partially due to the atmospheric model, which only assigns a density up to a geometric height of 120,000 m. In this figure all heat-flux profiles of these eight flights are plotted and it clearly shows that the optimizer optimized a second local maximum heat flux upon leaving the atmospheric model. This not only demonstrates the limits of the model and the inaccuracies that it brings forth, a more accurate atmospheric model would require some of the optimal trajectories to be slightly higher in order to keep the heat flux low. But the results plotted in 7.19a also demonstrates the capability and flexibility of the pitch program and the resultant flight profile. While figure 7.19a shows the lowest 8 heat flux profiles, figure 7.19b shows the runners up with peak heat fluxes in excess of 3,500 W/m^2 indicating that the limit of 1,135 W/m^2 is not trivial. The value for 1,135 W/m^2 was used as the constraint for fairing jettisoning. Modeling the trajectory in a way that does not surpass this low heat-flux limit has as a consequence that the fairing can be jettisoned before ignition and does not need to be accelerated along the way to orbit. To keep the heat flux below the aforementioned limit, the flight path needs to be different compared with other launch simulations that do not jettison the fairing before ignition. This can be seen in the form of a higher than usual optimal initial flight-path angle and a steeper trajectory in general, causing the launcher to travel sooner in less dense atmospheric conditions. This requirement of a steeper ascent profile is greater for the low altitude launch, since it is more difficult for this configuration to keep the heat flux below the limit. The fact that the lower the initial altitude, the quicker the trajectory guides the rocket to denser atmospheric conditions explains the counterintuitive decrease of optimal exhaust exit pressure with decreasing altitude, which is a trend opposite to the trend seen in all other configurations. The

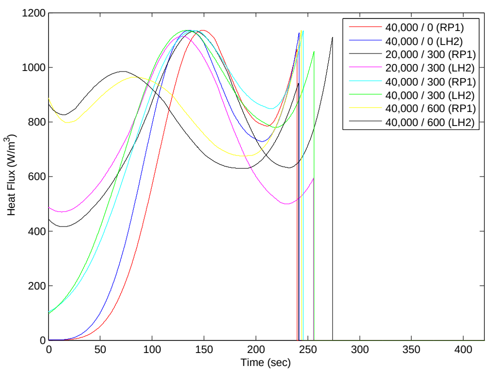

(a) Heat flux of eight optimized simulations with varying altitude and initial velocity demonstrating the model's ability to cope with the hard heat flux constraint after jettisoning.

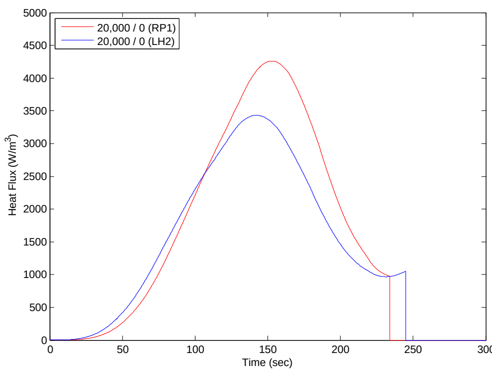

(b) Heat flux of 2 (LH2 and RP1) optimized simulations utilizing a launch assist of 20,000 m altitude with no velocity.

[10] Flights cases h-V of 40,000-300, 20,000-300, 40,000-600 and 40,000-0 for both fuel types.

steep trajectory also translates to a higher than usual gravity loss. This interesting trade-off between high gravity loss and no fairing mass has further less noticeable effects on additional parameters. The increased importance of gravity loss might cause the optimal T/W ratio to be higher, the decreased importance of drag loss might cause the slenderness to be lower, etc.
It can basically be said that the optimizer makes a trade-off between the optimal solution with jettisoning and the optimal solution without jettisoning. Looking at it in this manner explains why of the flights at 20,000 m only the flights with a velocity of 300 m/s found a low heat flux trajectory to be optimal. Logically one would assume that the optimum without jettisoning after an assist at 20,000 with 0 m/s initial velocity would deviate less from the optimum with jettisoning than would be the case of the 300 m/s counterpart. However the advantage gained, no fairing mass during acceleration, also depends naturally on the mass of the fairing, which is a lot lower in the case of no velocity assist.
The difference in heat flux by choosing to use a fairing is demonstrated in figure 7.19b. Also note that the final heat flux is around the heat flux constraint implying that at the edge of the atmospheric model, the heat flux of launchers traveling at near orbital velocities already tends to fall below the constraint. This means that with an atmospheric model extending to higher altitudes, similar optimal solutions regarding whether or not a fairing needs to be used, are likely to be found.

7.3.2 Low-assist flights

While the tendency for gravity loss is to get higher with lower assist flights this does not hold for the lowest of them all with low-assist altitudes and velocities. At low altitudes and velocities a reversal of the trend in gravity loss is seen and drag loss increases more than expected as was discussed in sections 7.2.13 and 7.2.12. In these cases, gravity losses are kept low by utilizing the lift of the vehicle as a means for keeping the flight-path angle low. This method does not occur anymore at higher velocities and altitudes as can be seen in figure 7.19, where a comparison of different lift-to-weight ratios is displayed and some of the higher assist cases are clearly identified of generating little to no lift. These high lift trajectories are not seen in current conventional launcher profiles but was already examined in other studies [18] [19], where a high lift trajectory with vertically launched axis-symmetric launch vehicles is deemed to be capable to enhance performance. The reason why modern launchers do not seem to fully utilize the lift generated by the launcher's body is up to speculation, perhaps excessive vibrations or bending loads lie at the cause. Other reasons could be a flawed assumption that a gravity turn is always optimal, aerodynamic instabilities or the fact that the vertical launch, which is always performed by modern launchers with exception of the MU-V, in combination with kick-rate constraints leads to a radically different ascent profile.

7.3.3 Altitude anomalies

In Appendix C a number of plots for all simulations is shown, one of these is the altitude vs time plot of a hydrolox vehicle and of a kerolox vehicle, which are shown in figure 7.20. A couple of anomalies are spotted in these plots. One of these, the kerolox case with an assist velocity of 1,000 m/s at an altitude of 5 km recognizable by having the highest

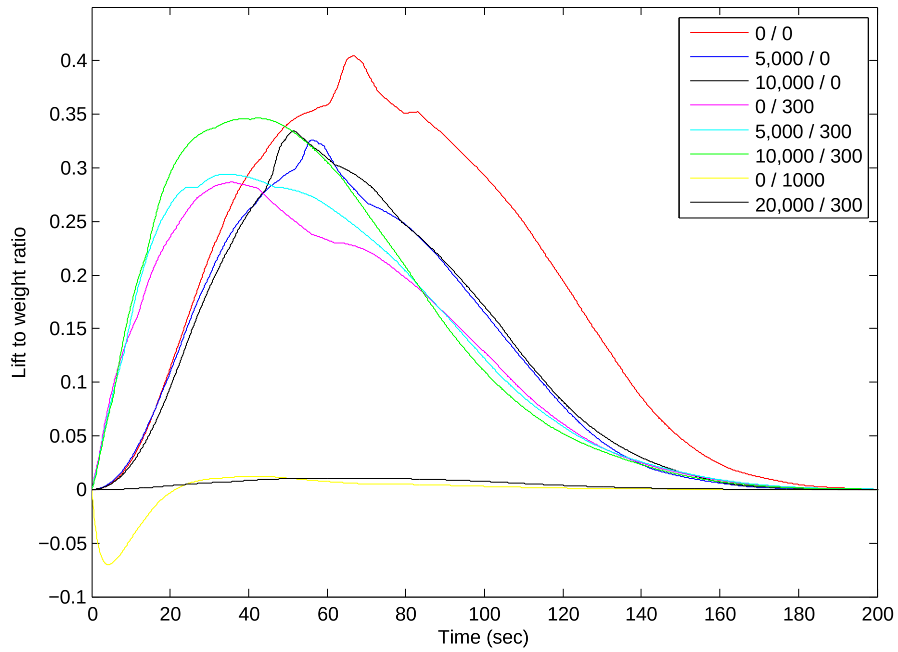

Figure 7.19: Lift-to-weight ratio of liquid hydrogen vehicles utilizing different launch assist altitudes and velocities. The legend identifies the specific simulations with their respective assist parameters documented in the following format: h [m] / V [m/s].

altitude after 3,000 seconds, was already discussed in section 7.2.3. The other anomalies tend to rise to apogee altitude, while most decreased their rate of climb significantly once they were higher than 120 km. These anomalies were identified to be cases with no-assist velocity at the four lowest altitudes[11] for kerolox launchers and the three lowest for hydrolox vehicles. These vehicles do not gain altitude rapidly due to their initial stationary position. In addition, these also have the highest thrust-to-weight ratios, resulting in the shortest times to orbit. This burn is in fact so short that these rockets cannot undertake the normal trajectory where launchers still provide thrust at perigee, which is slightly higher than the modeled atmosphere. This hypothesis is further strengthened by the observed difference in burnout times of the hydrolox and kerolox vehicles with an assist velocity of 0 m/s and an altitude of 20 km. The hydrolox launcher, which shows normal behaviour, has a burn time of 296.2 seconds while the kerolox launcher, which shows an anomaly, has a burn time of only 284.9 seconds.
Based on these cases the conclusion can be made that implementing a more intelligent thrust profile with perhaps even coasting arcs would further improve the objective function for these launchers.

[11]The four lowest altitudes are 0, 5, 10 and 20 km

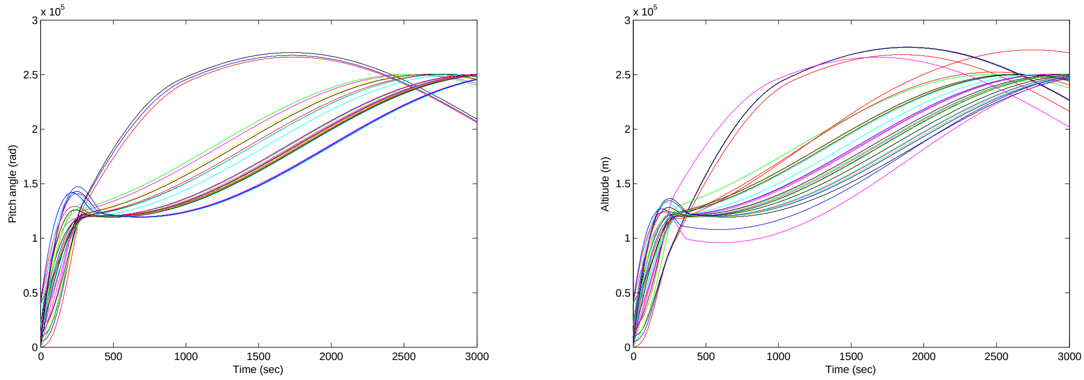

(a) (b)

Figure 7.20: Altitude vs Time plots of hydrolox vehicles (a) and kerolox vehicles (b), indicating some anomalies.

7.3.4 Effect of change in pitch angle

In this section the effects are discussed of having a pitch angle non-equal to the flight-path angle. To have a clear view on this effect 4 simulations are run with an initial flight-path angle of 0° for relatively low speed assists, since low speeds assist are most likely to be assisted by aircraft where the optimized initial flight-path angle would be difficult to achieve for most of the flights. These simulations were compared with their optimized flight-path angle counterparts. The 8 resulting pitch angle profiles are visualized in the top right of figure 7.21, showing an overcompensation in the second part of powered flight for the sub-optimal initial pitch angle setting. All results presented in this section were obtained by simulating hydrolox launchers. The results of these simulations show that the drag loss increases substantially with only a slight improvement in gravity loss, which can be seen in table 7.2. Although other factors play a role, this is deemed to be the main reason that causes the objective value, the payload ratio, to fall. This drop in payload ratio is lower than expected and can again be partially explained due to the fact that the launchers utilize a high lift-to-weight trajectory significantly higher than their optimized initial flight-path angle counterparts, which can be seen in the bottom right of figure 7.21. These high-lift trajectories are partially explained by the altitude vs velocity plot in the top left of figure 7.21, where it is shown that the cases with an initial flight-path angle of 0° have a much higher velocity at the same altitude, enabling them to generate more lift at comparable angles of attack. This causes the launcher to undergo higher bending loads due to high angles of attack and dynamic pressures, see bottom left of figure 7.21, but neither the bending load nor the angle of attack comes near any constraints.
To draw watertight conclusions from the high lift-to-weight benefit that sometimes seems to occur it is recommended to create a better structural mass model with regard to the high bending loads.

Case (Identified by assist parameters. Notation: V - h)	Drag loss (m/s)	Gravity loss (m/s)	Payload ratio (-)
300 m/s - 10,000 m, $\gamma = 0$	1089.2	522.3	0.0661
300 m/s - 10,000 m	295.5	585.2	0.0681
300 m/s - 20,000 m, $\gamma = 0$	1328.6	364.4	0.0738
300 m/s - 20,000 m	17.2	643.8	0.0789
600 m/s - 10,000 m, $\gamma = 0$	1112.9	509.1	0.077
600 m/s - 10,000 m	61.8	670.1	0.0883
600 m/s - 20,000 m, $\gamma = 0$	1035.6	387.9	0.0851
600 m/s - 20,000 m	19.2	575.6	0.0962

Table 7.2: Drag loss, gravity loss and performance comparison of various launcher cases with either an optimized initial flight-path angle or an initial flight-path angle of zero.

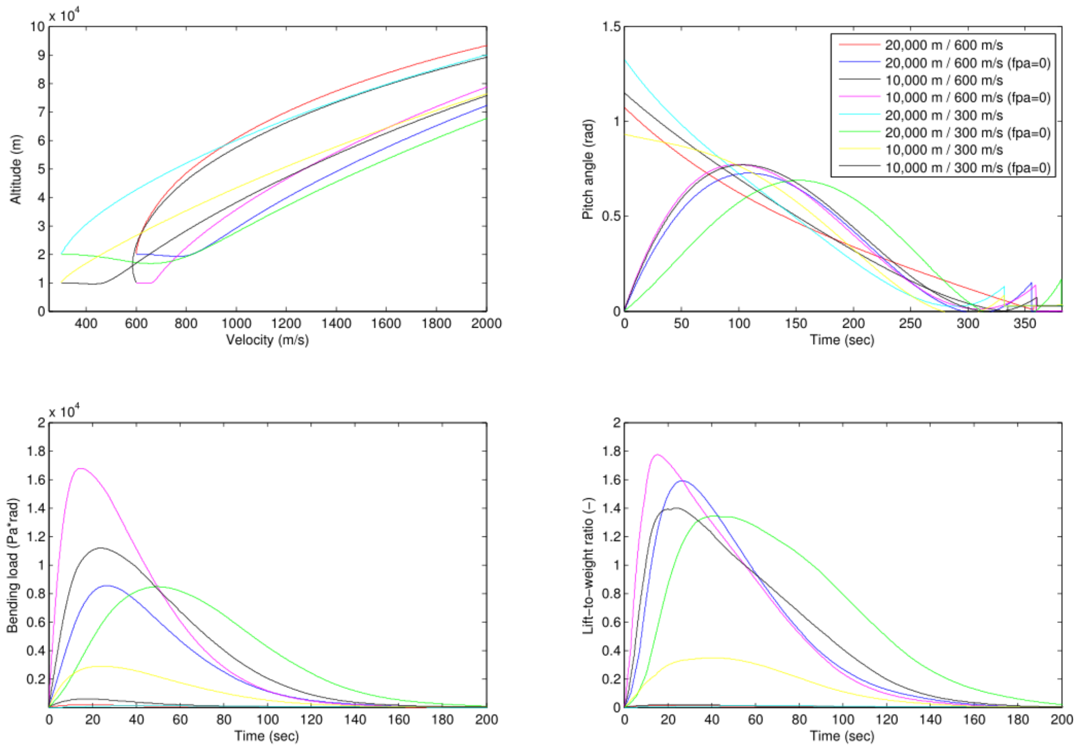

Figure 7.21: Comparison plots between optimal trajectories with an initial flight-path angle of zero and with optimized flight-path angle. Top left: Altitude-velocity plot, top right: Pitch angle - time plot, bottom left: Bending load - time plot and bottom right: lift-to-weight ratio - time plot.

7.4 Sensitivity Analysis

The results that were discussed so far in this chapter, were also subjected to a sensitivity analysis in order to know how sensitive the solution is to a change of one of the launch-vehicle parameters. The sensitivity analysis was performed with Matlab code [45] utilizing the extended Fourier amplitude sensitivity test (EFAST) method published in the paper of Saltelli, Tarantola and Chan [46]. This method is a variation on the FAST method, which was developed in the 1970s. FAST computes the effect of each input factor to the variance of the output. The variance of the output is generated by varying the parameters around their optimal values in the form of a latin hypercube. The calculation of the effect of each input parameter is then performed through Sobol sensitivity indices. There are two types of indices, the first one is sometimes called first-order sensitivity indices and is given by Eq. (7.5) and the second one is the total-effect sensitivity index given in Eq. (7.6).

$$S_i = \frac{V_i}{V(\Upsilon)} \qquad (7.5) \qquad\qquad S_{Ti} = 1 - \frac{V_{-i}}{V(\Upsilon)} \qquad (7.6)$$

where Υ is the output of the system and $V(\Upsilon)$ is the variance of the output. V_i is the fraction of $V(\Upsilon)$ due to factor x_i only while V_{-i} indicates the contribution to the variance due to all factors but x_i and all the higher-order effects in which it is involved [45]. This means that the sum of the total-effect sensitivity indices can be higher than 1 because the effect that the combination of parameter a and parameter b contributes to the variance is incorporated both in the total-effect sensitivity index of parameter a as well as in the total-effect sensitivity index of parameter b. The focus in this paper will lie on the total-effect sensitivity indices shown in figure 7.22. The first-order effect sensitivity indices are displayed in figure C.1. The sensitivity analysis is as discussed, performed with variations around the global optimum found by the differential evolution algorithm. When a constraint is met, the objective function is assigned a penalty value so that the differential evolution algorithm discards that solution. For the sensitivity analysis this penalty was slightly altered to a maximum of 10% per constraint compared with the expected result. The sensitivity analysis was performed in two parts. The first part analysed the sensitivity of the launch vehicle parameters and the second part analysed the launch trajectory components, namely the initial flight-path angle and the four pitch parameters. All optimal solutions were again simulated together with a total of 24,966 variations of these optimal solutions. This number was determined obtained by starting out with the minimum value for the amount of parameters as recommended in [46]. Several runs were made with several multitudes of this minimum value used as the number of data points within the hypercube. These results are shown in figure C.2. After this analysis, 24,966 variations was the chosen amount to conduct the sensitivity analysis. These 24,966 variations were spaced in a hypercube with a size of 1% of the search space in accordance to the EFAST algorithm. For each optimal solution, a different hypercube was generated, resulting in a total of 30 hypercubes[12]. The results of the overal importance (including combined effects) of the parameters on the model are given in figure 7.22. As can be seen from this figure, the two most important parameters are the length and the exit pressure. Two notable differences can be detected between the kerolox and hydrolox results. These are a smaller effect for kerolox vehicles due to the length of the vehicle as well as due to the oxidizer-to-fuel ratio. The second effect can be solely attributed to the fact that the variations performed during the sensitivity analysis were for all parameters and for all optimal points, scaled to be 1% of the initial search space of the parameter space. This results in smaller relative variations around the optimal oxidizer-to-fuel ratio of hydrolox vehicles, which have oxidizer-to-fuel ratios of 6 to 6.5,

[12]The same set of hypercubes were used to analyze both the hydrolox simulations and the kerolox simulations

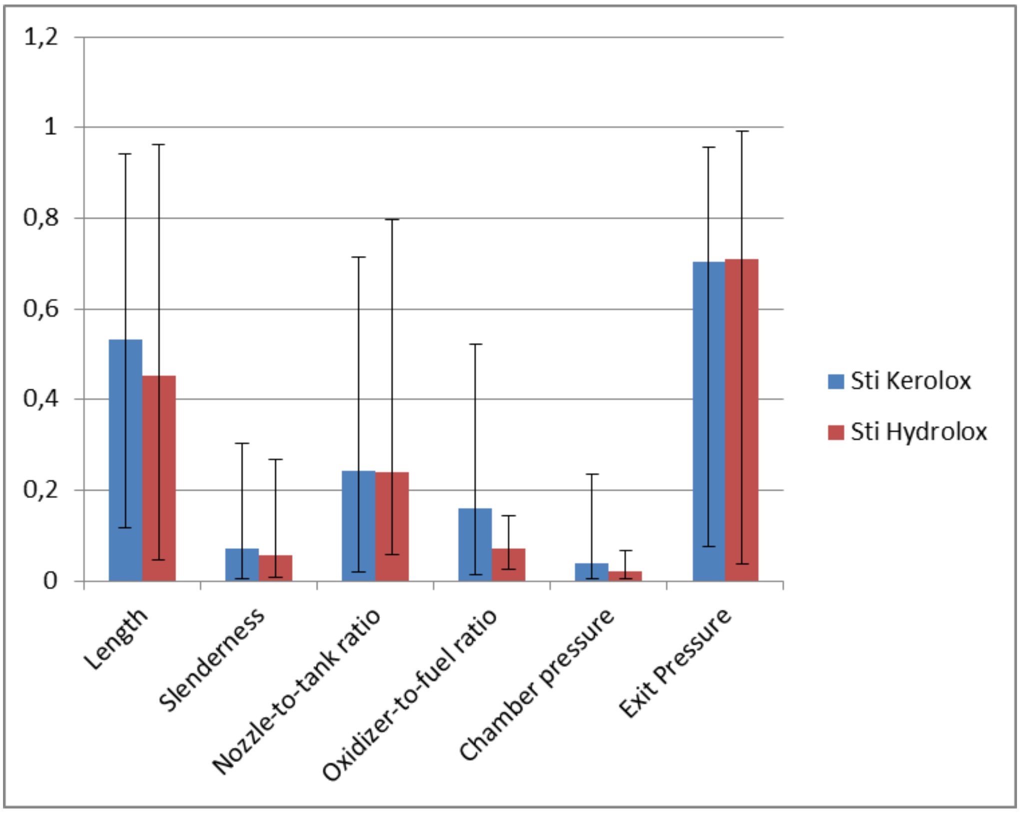

Figure 7.22: Mean of the total standardized effect of parameters on the variance of the model with indications of the maximum and minimum values

compared to the relative variations for the kerolox vehicles, which have oxidizer-to-fuel ratios of around 2.5 (about a relative difference of a factor of 2.5). In fact, when scaling the effect of the parameter to their relative sizes, one founds that both types of vehicles are about equally sensitive to the parameter. Total sensitivity to the oxidizer-to-fuel ratio was found to be 16.1% for the kerolox launcher, a comparable factor 2.3 larger than the 7.1% found for the hydrolox launcher. The difference in the effect that length has on launcher performance can basically be contributed to the same effect. Optimized values for the length of hydrolox vehicles are slightly larger than optimized values of kerolox vehicles. Therefore for a given variation the greater effect on the model will be given by the shorter launcher.

The overall results show that length has a bigger total effect than slenderness. While they are two comparable parameters, there are several reasons why this could be the case. These could have to do with accumulated drag loss and changes in the launcher's mass ratio, but the reason deemed most important for this effect is the thrust-to-weight ratio. With increased slenderness, the diameter increases, leading to an increase in mass, but so does the nozzle diameter and thrust thus the thrust-to-weight ratio stays the same. With an increase in length, both the length and the diameter[13] increase leading to a more rapid mass increase than thrust increase. The only other parameter whose sensitivity

[13] When slenderness remains the same value, the diameter of the vehicle will increase in correspondence with the length.

hinges greatly on the thrust-to-weight ratio effect is the nozzle-to-diameter ratio. This parameter's sensitivity, which is also effected by changes in the construction mass ratio due to a change in engine power, is the third greatest and thus further demonstrates the likely importance of the thrust-to-weight ratio on the model. The largest impact on the model is made by variations in the exit pressure. This parameter showed a clear trend of becoming increasingly important at high-assist simulations. This is because at this high assists the optimum exit pressure is rather low and the variation of 1% of the search space, a variation of 1000 Pa, has far greater effects when this occurs around an optimum value of 5,000 Pa w.r.t an optimal value of 50,000 Pa. This effect can be seen in figure C.3. This implies that the magnitude of the importance of the exit pressure mainly comes from the fact that the variation is relatively speaking quite large for this parameter. Nonetheless, even in the four cases with the largest optimal exit pressure ($>$ 15000 Pa) the average sensitivity of the model to the exit pressure was still close to 20%.

Chapter 8

Conclusions and Recommendations

This work began with the formulation of the research question:

How does a launch assist affect the performance and the design of a launch vehicle?

In section 8.1 the conclusions that were drawn during this thesis work are given. This is followed by section 8.2 where the recommendations are summarized for future work related to this research in 8.2.1 and for future launch-vehicle designs in section 8.2.2.

8.1 Conclusions

1. *The differential evolution algorithm was shown to be better suited to tackle this particular problem than the particle swarm optimization technique.*
   DE was found to be suited to find solutions for even the most difficult cases, while the PSO algorithm did not found any solution that obeyed the constraints. For the more easier cases the PSO method found better solutions faster but mis converged at local optima.

2. *Variations in the length and the exit pressure were found to have the largest impact on the sensitivity of the model.*
   Some of the conclusions concerning the sensitivity analysis were less transparent due to the fact that some parameters had more optimal solutions near the lower boundary of the search space than others, making the variations performed during the analysis larger in a relative sense. Nonetheless, the sensitivity analysis made clear that the model is more sensitive to the length and the exit pressure than the chamber pressure, the oxidizer-to-fuel ratio and the slenderness, which were found to have the least effect. The nozzle exit-to-tank diameter ratio was also found to have a significant effect due to its influence on the thrust-to-weight ratio.

3. *The overall effect of the chamber pressure on the performance is rather marginal but the effect of increased specific impulse with increased chamber pressure almost uniformly outweighs the construction-mass ratio increase.*
   The model was found to be the least sensitive to the chamber pressure and this was due to the fact that at large pressures, where the optimum was uniformly found, the chamber pressure exerts only very slight differences on the specific impulse. Only in a couple of cases this drive toward optimal high chamber pressures was to some extent counteracted by the negative effect the chamber pressure has on the mass ratio.

4. *The performance of the launcher measured by the payload mass-to-initial mass ratio increases both with increased altitude as well with increased velocity.*
   The payload ratios always increase with an increase in assist altitude as it does with an increase in assist velocity. The payload ratios rise from 3.1% and 2.1% for the no assist case to a maximum of 19% and 15.1% for the hydrolox and kerolox launchers respectively. The maxima both occur at the highest assist velocity and highest assist altitude simulated, which were 2,000 m/s and 40,000 m.

5. *Launchers with a low density hydrogen-oxygen propellant mixture were found to provide greater payload mass ratios to a low Earth orbit than launchers containing a high density kerosene-oxygen propellant mixture for all assist cases investigated.*
   The difference in performance ranged from a relative improvement of 25.7% at the maximum assist case to 48.4% at the no assist case.

6. *Combinations of a high-assist altitude and a low-assist velocity led to optimal launcher configurations without a fairing.* Eight out of the sixty trajectory simulations were found to perform better when a trajectory is flown that keeps the heat flux below the fairing jettisoning constraint for the entire flight profile. These flights, where the fairing is allowed to be jettisoned prior to launch, had assist altitudes of 40 km combined with assist velocities of 0, 300 and 600 m/s, the 7^{th} and the 8^{th} flight had assist altitudes of 20 km and assist velocities of 300 m/s.

7. *The assist velocity has a larger impact on the performance of the launcher than the assist altitude. This holds for both launcher types investigated but more so for kerolox launchers than hydrolox launchers.*
   The performance surplus generated by an assist altitude of 40 km compared with an assist altitude of 0 km roughly corresponds with the performance increase generated by having an assist velocity of 540 m/s instead of 0 m/s for hydrolox launchers. For a kerolox launcher this performance increase is already met at assist velocities of about 400 m/s. This implies that when given a fast assist platform, the trade-off between a kerolox launcher and a hydrolox launcher is more in favor of the kerolox launcher than it would be when a high assist platform would be used.

8. *The gravity loss and the optimal thrust-to-weight ratio decreases with larger launch-assist altitude and velocity.*
   Gravity loss and thus its negative effect on launcher performance gets smaller with increasing assist velocity and altitude. Smaller thrust-to-weight ratios cause a decrease in the construction mass ratio while it causes an increase in gravity loss. At

large launch-assist altitudes and velocities, the lower construction mass effect becomes more important compared with the gravity loss effect, leading to a reduction in the thrust-to-weight ratio.

9. *The overall tendency regarding the dimensions of the launchers is to minimize them.* The average length of all optimized launcher tanks is 22.9 m, while their diameter is on average 2.35 m and these values are mainly that high due to a few aberrancies, 36 of the 60 launchers have shorter tank lengths than 20 m. Optimal kerolox launchers are generally smaller than optimal Hydrolox launchers. A major driver to keep dimensions low is a high thrust-to-weight ratio, but this was found to be counteracted in high-drag-loss environments to minimize the drag loss.

10. *The importance of construction mass ratio is greater for low-performance systems than in their high-performance counterparts causing the slenderness to follow the drag loss trends more closely in high performance areas.*
    A certain increase in the construction mass leads to a higher increase in ΔV for low-performance systems than for high-performance systems. A more slender body improves on the system's drag loss regardless of performance. Therefore, optimization of the slenderness with the purpose of minimizing drag loss plays a greater role for high performance systems. This leads to a close match between the drag loss and the slenderness of the vehicle in the high-performance and high-drag-loss region of the launch-assist spectrum.

11. *At constant altitude, the drag loss reaches a minimum for assist velocities between 500 and 1,000 m/s.*
    Low assist velocities cause the launcher to spend large amount of times in the denser parts of the atmosphere. However, since drag force is proportional to the second power of the velocity, the velocity effect on the drag loss gets larger than the effect of the longer time spent in denser parts of the atmosphere and causes the drag loss to rise again with increased assist velocity.

12. *At constant altitude, the sum of gravity loss and drag loss reaches a maximum for assist velocities at about 300 m/s.*
    The sum of gravity and drag loss tends to get greater with decreasing velocity. However it reaches a maximum just before the no-assist velocity cases. This maximum is due to a combination of the high-lift trajectories that are being flow from no-assist velocity cases, which increase drag losses but decrease gravity losses, and from the higher thrust-to-weight the vehicles have when utilizing an assist without any initial velocity, which decreases gravity losses even further.

13. *Low assist flights and flights with a 0° initial flight-path angle prefer high-lift trajectory profiles*
    Several solutions for flights using assists at low altitudes and low velocities utilized the ability of the launcher to generate lift to its advantage. This entailed lower than normal flight profiles and higher than normal drag losses, bending loads and angles of attack. This phenomenon was even magnified when launch assist were simulated with 0° flight-path angles. While this might indeed be a better solution than the standard gravity turn, its validity is questioned due to the mass model's inability to cope with the influence of bending loads.

14. *The optimal initial flight-path angle decreases both with increasing assist altitude and even more so with increasing assist velocity.*
    At the no assist case the initial flight path angle is close to vertical with values of 85° and 82° for kerolox and hydrolox launchers respectively. This decreases both with increased assist altitude as with increased assist velocity. The decreasing effect with increasing assist altitude is quite small in general but gets more prominent with increased assist velocity. The optimal flight path angles for the highest assist cases are 28° and 30° for kerolox and hydrolox launchers respectively.

15. *The slenderness of the vehicle and the nozzle exit diameter have opposite trends, which conflict with launch assists that use high-assist velocities and low-assist altitudes.*
    The slenderness of the launcher increases with high-velocity and low-altitude assists, due to the higher drag losses that occur and the high payload ratio that causes a smaller effect of the construction mass ratio. In the same region, the optimal exit pressure is low and the mass is high for small tank diameters. To have adequate thrust-to-weight ratios and high specific impulses, the nozzle exit-to-tank diameter ratios reach the upper boundary of the search space, parity, in certain cases.

16. *The effect on the specific impulse is dominated by the optimal exit pressure.*
    Due to the fact that the oxidizer-to-fuel ratio and the chamber pressure show little to no variation across the assist spectrum, the exit pressure has the greatest influence on the specific impulse. The specific impulse is large when the exit pressure is low and vice versa. The exit pressure shows a singular peak around the no assist case since these are the cases where the propelled flight spends a more significant portion in a high density environment.

8.2 Recommendations

8.2.1 For further study on the subject:

- Include the mass and aerodynamic model of an attachable wing to investigate its effect. This is deemed to be the most important recommendation, since the results that were obtained, implied that aerodynamic lift can have an important effect on the trajectory and consequently on the overall performance.

- Include a more realistic mass model effect for the chamber pressure. Currently, it only has an almost negligible effect on the nozzle mass.

- Include a more realistic engine mass model. In this model, engine mass is dependent solely on the thrust. This implies that when a given engine increases its efficiency, it also increases its mass.

- Include a more realistic mass model effect for the bending load. Perhaps by modeling an exoskeleton that can carry the loads and can be jettisoned in a similar fashion as the fairing. This would save mass and was also proposed in the form of a strongback structure of a winged vehicle in [35].

- Estimate the residual propellant mass so that this can be subtracted from the final inert mass, where the payload mass was now based upon. It should be noted that an inclusion of the residual propellant mass model would only affect the trends display in the results if it would be influenced by launch-vehicle parameters. If it would be modeled as for instance a standard 1% of the initial mass, all optimized solutions would stay the same[1].

- Create either a higher resolution in the CEA database for the oxidizer-to-fuel ratio or a more accurate interpolation method. The results displayed a rather unrealistic picture that showed little to no variation in the parameter.

- Include a constraint concerning maximum pitch rate.

- Invent a more rigorous approach to define the search spaces of the pitch variables. It should be noted that further increases in these search space have been shown to lead to slower optimization times and higher chances for mis convergence.

- Adjust the thrust model so that the thrust does not have an immediate response.

- Implement a lower boundary constraint for the thrust throttle setting.

- Model the thrust as a series of optimizable nodes connected by a non-linear interpolation method instead of modeling it at constant thrust or constant axial acceleration.

- Include a staging event and either optimize the second stage in the same manner as was done in this study or simulate a standard upper stage.

- Include dependency on the Reynolds number on the model. This can be done by adding an extra dimension to the aerodynamic coefficient database, an extra dimension to the interpolation, and by using multiple Missile DATCOM input files. This will improve the accuracy of the aerodynamic coefficients.

- Interpolate, based on length and diameter, between the files generated by Missile DATCOM.

- Implement a different aerodynamic coefficient generator. It has been indicated that Missile DATCOM does not always estimate reality with great success. One of the most noticeable errors is the miscalculation of the axial coefficient, where double Mach peaks have been observed between 1 and 2 Mach [14]. Implementation of a newer version of the Missile DATCOM code would also be an improvement.

- Perform a sensitivity analysis on the vehicle model to identify the sensitivity of the model to certain assumptions such as fill ratio, ullage pressure, safety factors, efficiency factors, etc.

[1] It might have a slight influence if it was modeled as a more realistic 1% of the initial propellant mass.

8.2.2 For launch-vehicle design:

- Raising the altitude from sea level to 5,000 m altitude for the cases with 0 m/s assist velocity results in a relative increase of the payload ratio of 27% and 21% for hydrolox and kerolox respectively. Combined with the fact that the optimal vehicles for these cases are rather small, 12.1 and 39.8 tonnes, there might be a business case for an elevated launch site for small launchers.

- It should be further investigated if the requirement concerning heat flux for payloads of current and proposed assisted launch vehicles could not be raised to the extent that these vehicles would not need to provide a fairing during their ascent trajectory. A significant rise in the heat flux constraint will get rid of the need for a fairing for even lower and faster assisted vehicles and perhaps also horizontally launched vehicles.

- The results make the case for the use of relatively small engines from a performance point of view. Although it is advised to make a final decision on this topic after further investigation on the implementation of an optimized thrust profile.

- The results indicate several possibilities for launch-assist parameters that could lead to a launch-vehicle payload ratio greater than 10%. If this could be demonstrated the next logical step would be to trade some payload for reusability systems such as a heat shield, parachutes, de-orbit propellant mass, etc. Transforming the system into the first fully reusable space system, assuming reusability of the assist platform.

Appendix A

CEA Tables

In this appendix the tables generated with the online CEA tool are shown.

Table A.1: Molar mass of hydrogen-oxygen mixtures

O/F \ P_c	8	16	24	32	40	48	56	64
1	4,032	4,032	4,032	4,032	4,032	4,032	4,032	4,032
1,5	5,04	5,04	5,04	5,04	5,04	5,04	5,04	5,04
2	6,047	6,047	6,047	6,047	6,047	6,048	6,048	6,048
2,5	7,051	7,052	7,053	7,053	7,054	7,054	7,054	7,054
3	8,04	8,046	8,049	8,051	8,052	8,053	8,054	8,054
3,5	8,998	9,015	9,024	9,029	9,033	9,036	9,038	9,04
4	9,915	9,948	9,965	9,976	9,984	9,99	9,996	10
4,5	10,786	10,838	10,866	10,884	10,898	10,909	10,918	10,926
5	11,613	11,683	11,723	11,75	11,771	11,787	11,8	11,812
5,5	12,393	12,483	12,534	12,57	12,598	12,62	12,638	12,654
6	13,129	13,236	13,298	13,342	13,376	13,404	13,427	13,447
6,5	13,821	13,942	14,014	14,066	14,105	14,138	14,166	14,189
7	14,47	14,603	14,683	14,74	14,785	14,821	14,852	14,879
7,5	15,079	15,221	15,307	15,368	15,416	15,456	15,489	15,518
8	15,416	15,456	15,489	15,518	16,003	16,045	16,08	16,11
8,5	16,191	16,343	16,434	16,499	16,551	16,593	16,628	16,66
9	16,7	16,853	16,945	17,011	17,062	17,105	17,14	17,171
9,5	17,18	17,334	17,426	17,491	17,542	17,584	17,62	17,65
10	17,635	17,788	17,879	17,943	17,994	18,035	18,07	18,1

Table A.2: Molar mass of hydrogen-oxygen mixtures

O/F \ P_c	72	80	88	96	104	112	120	128
1	4,032	4,032	4,032	4,032	4,032	4,032	4,032	4,032
1,5	5,04	5,04	5,04	5,04	5,04	5,04	5,04	5,04
2	6,048	6,048	6,048	6,048	6,048	6,048	6,048	6,048
2,5	7,054	7,054	7,054	7,054	7,054	7,054	7,054	7,054
3	8,055	8,055	8,056	8,056	8,056	8,057	8,057	8,057
3,5	9,041	9,043	9,044	9,045	9,046	9,047	9,048	9,048
4	10,003	10,007	10,009	10,012	10,014	10,016	10,018	10,019
4,5	10,932	10,938	10,943	10,947	10,951	10,955	10,958	10,961
5	11,822	11,83	11,838	11,845	11,851	11,857	11,862	11,867
5,5	12,667	12,679	12,69	12,7	12,709	12,717	12,724	12,731
6	13,465	13,48	13,494	13,507	13,518	13,529	13,539	13,548
6,5	14,21	14,229	14,246	14,261	14,275	14,288	14,3	14,312
7	14,903	14,924	14,943	14,961	14,977	14,992	15,006	15,019
7,5	15,544	15,567	15,588	15,607	15,625	15,641	15,656	15,671
8	16,137	16,161	16,183	16,203	16,222	16,239	16,255	16,27
8,5	16,687	16,712	16,734	16,754	16,773	16,79	16,807	16,822
9	17,199	17,223	17,246	17,266	17,285	17,302	17,318	17,333
9,5	17,677	17,702	17,724	17,744	17,762	17,779	17,795	17,81
10	18,126	18,15	18,172	18,191	18,209	18,226	18,241	18,256

Table A.3: Molar mass of hydrogen-oxygen mixtures

O/F \ P_c	136	144	152	160	168	176	184	192
1	4,032	4,032	4,032	4,032	4,032	4,032	4,032	4,032
1,5	5,04	5,04	5,04	5,04	5,04	5,04	5,04	5,04
2	6,048	6,048	6,048	6,048	6,048	6,048	6,048	6,048
2,5	7,054	7,055	7,055	7,055	7,055	7,055	7,055	7,055
3	8,057	8,057	8,058	8,058	8,058	8,058	8,058	8,058
3,5	9,049	9,049	9,05	9,05	9,051	9,051	9,052	9,052
4	10,021	10,022	10,023	10,025	10,026	10,027	10,028	10,029
4,5	10,964	10,967	10,969	10,971	10,973	10,975	10,977	10,979
5	11,872	11,876	11,88	11,884	11,887	11,89	11,893	11,896
5,5	12,738	12,744	12,75	12,755	12,76	12,765	12,769	12,774
6	13,556	13,565	13,572	13,579	13,586	13,592	13,599	13,604
6,5	14,322	14,332	14,341	14,35	14,359	14,367	14,374	14,382
7	15,031	15,043	15,054	15,064	15,074	15,083	15,092	15,101
7,5	15,684	15,697	15,709	15,72	15,731	15,741	15,751	15,76
8	16,284	16,297	16,309	16,321	16,333	16,344	16,354	16,364
8,5	16,836	16,85	16,862	16,874	16,886	16,897	16,907	16,917
9	17,348	17,361	17,374	17,386	17,397	17,408	17,418	17,428
9,5	17,824	17,837	17,849	17,861	17,872	17,883	17,893	17,902
10	18,269	18,282	18,294	18,305	18,316	18,326	18,336	18,346

Table A.4: Molar mass of hydrogen-oxygen mixtures

O/F \ P_c	200	208	216	224	232	240	248	256	264
1	4,032	4,032	4,032	4,032	4,032	4,032	4,032	4,032	4,032
1,5	5,04	5,04	5,04	5,04	5,04	5,04	5,04	5,04	5,04
2	6,048	6,048	6,048	6,048	6,048	6,048	6,048	6,048	6,048
2,5	7,055	7,055	7,055	7,055	7,055	7,055	7,055	7,055	7,055
3	8,058	8,058	8,058	8,059	8,059	8,059	8,059	8,059	8,059
3,5	9,053	9,053	9,053	9,053	9,054	9,054	9,054	9,055	9,055
4	10,029	10,03	10,031	10,032	10,033	10,033	10,034	10,035	10,035
4,5	10,981	10,982	10,984	10,985	10,987	10,988	10,989	10,991	10,992
5	11,899	11,902	11,904	11,907	11,909	11,911	11,914	11,916	11,918
5,5	12,778	12,782	12,786	12,789	12,793	12,796	12,799	12,802	12,805
6	13,61	13,615	13,62	13,625	13,63	13,634	13,639	13,643	13,647
6,5	14,389	14,395	14,402	14,408	14414	14419	14425	14430	14435
7	15,109	15,117	15,124	15,131	15,138	15,145	15,152	15,158	15,164
7,5	15,769	15,778	15,786	15,794	15,802	15,81	15,817	15,824	15,831
8	16,373	16,382	16,391	16,4	16,408	16,416	16,423	16,431	16,438
8,5	16,927	16,936	16,945	16,954	16,962	16,97	16,977	16,985	16,992
9	17,438	17,447	17,455	17,464	17,472	17,48	17,488	17,495	17,502
9,5	17,912	17,921	17,929	17,937	17,945	17,953	17,96	17,968	17,975
10	18,354	18,363	18,371	18,379	18,387	18,394	18,402	18,409	18,415

Table A.5: Ratio of specific heats of hydrogen-oxygen mixtures

O/F \ P_c	8	16	24	32	40	48	56	64
1	1,3587	1,3587	1,3587	1,3587	1,3587	1,3587	1,3587	1,3587
1,5	1,3157	1,3157	1,3157	1,3157	1,3157	1,3157	1,3157	1,3157
2	1,2813	1,2817	1,2819	1,282	1,2821	1,2822	1,2822	1,2822
2,5	1,2504	1,2528	1,2538	1,2545	1,2549	1,2552	1,2555	1,2557
3	1,2183	1,2237	1,2263	1,228	1,2292	1,2301	1,2308	1,2313
3,5	1,1891	1,1963	1,2002	1,2027	1,2046	1,206	1,2072	1,2081
4	1,1668	1,1741	1,1782	1,1811	1,1832	1,1849	1,1863	1,1875
4,5	1,1508	1,1574	1,1613	1,164	1,1661	1,1678	1,1693	1,1705
5	1,1395	1,1452	1,1487	1,1511	1,1531	1,1547	1,156	1,1571
5,5	1,1317	1,1366	1,1395	1,1417	1,1434	1,1448	1,1459	1,147
6	1,1265	1,1307	1,1332	1,135	1,1365	1,1377	1,1387	1,1396
6,5	1,1232	1,1269	1,1291	1,1307	1,1319	1,133	1,1338	1,1346
7	1,1213	1,1247	1,1267	1,1281	1,1293	1,1302	1,1309	1,1316
7,5	1,1204	1,1236	1,1255	1,1269	1,1279	1,1287	1,1295	1,1301
8	1,12	1,1232	1,1251	1,1264	1,1274	1,1282	1,1289	1,1295
8,5	1,12	1,1232	1,1251	1,1264	1,1274	1,1283	1,129	1,1296
9	1,1202	1,1234	1,1253	1,1267	1,1277	1,1286	1,1293	1,1299
9,5	1,1205	1,1238	1,1258	1,1272	1,1282	1,1291	1,1299	1,1305
10	1,1209	1,1243	1,1263	1,1277	1,1288	1,1297	1,1305	1,1311

Table A.6: Ratio of specific heats of hydrogen-oxygen mixtures

O/F \ P_c	72	80	88	96	104	112	120	128
1	1,3587	1,3587	1,3587	1,3587	1,3587	1,3587	1,3587	1,3587
1,5	1,3157	1,3157	1,3157	1,3157	1,3157	1,3157	1,3157	1,3157
2	1,2823	1,2823	1,2823	1,2823	1,2823	1,2824	1,2824	1,2824
2,5	1,2559	1,256	1,2562	1,2563	1,2564	1,2565	1,2565	1,2566
3	1,2318	1,2322	1,2326	1,2329	1,2332	1,2334	1,2337	1,2339
3,5	1,209	1,2097	1,2103	1,2108	1,2113	1,2118	1,2122	1,2126
4	1,1885	1,1894	1,1902	1,1909	1,1916	1,1922	1,1927	1,1932
4,5	1,1716	1,1725	1,1734	1,1741	1,1748	1,1755	1,1761	1,1766
5	1,1582	1,1591	1,1599	1,1606	1,1613	1,1619	1,1625	1,1631
5,5	1,1479	1,1487	1,1494	1,1501	1,1507	1,1513	1,1518	1,1523
6	1,1403	1,1411	1,1417	1,1423	1,1428	1,1433	1,1438	1,1442
6,5	1,1352	1,1358	1,1364	1,1369	1,1373	1,1378	1,1382	1,1385
7	1,1322	1,1327	1,1332	1,1336	1,134	1,1343	1,1347	1,135
7,5	1,1306	1,1311	1,1315	1,1319	1,1323	1,1326	1,1329	1,1332
8	1,1301	1,1305	1,131	1,1313	1,1317	1,132	1,1323	1,1326
8,5	1,1301	1,1306	1,131	1,1314	1,1318	1,1321	1,1324	1,1327
9	1,1305	1,131	1,1314	1,1318	1,1322	1,1325	1,1328	1,1331
9,5	1,1311	1,1316	1,132	1,1324	1,1328	1,1331	1,1335	1,1338
10	1,1317	1,1322	1,1327	1,1331	1,1335	1,1339	1,1342	1,1345

Table A.7: Ratio of specific heats of hydrogen-oxygen mixtures

O/F \ P_c	136	144	152	160	168	176	184	192
1	1,3587	1,3587	1,3587	1,3587	1,3587	1,3587	1,3587	1,3587
1,5	1,3157	1,3157	1,3157	1,3157	1,3157	1,3157	1,3157	1,3157
2	1,2824	1,2824	1,2824	1,2824	1,2824	1,2824	1,2824	1,2825
2,5	1,2567	1,2567	1,2568	1,2568	1,2569	1,2569	1,257	1,257
3	1,2341	1,2342	1,2344	1,2346	1,2347	1,2348	1,2349	1,2351
3,5	1,2129	1,2132	1,2135	1,2138	1,214	1,2143	1,2145	1,2147
4	1,1937	1,1941	1,1945	1,1949	1,1952	1,1955	1,1959	1,1961
4,5	1,1771	1,1776	1,1781	1,1785	1,1789	1,1793	1,1796	1,18
5	1,1636	1,164	1,1645	1,1649	1,1653	1,1657	1,1661	1,1664
5,5	1,1528	1,1533	1,1537	1,1541	1,1544	1,1548	1,1551	1,1555
6	1,1446	1,145	1,1454	1,1457	1,1461	1,1464	1,1467	1,147
6,5	1,1389	1,1392	1,1395	1,1398	1,1401	1,1404	1,1406	1,1409
7	1,1353	1,1356	1,1359	1,1361	1,1363	1,1366	1,1368	1,137
7,5	1,1335	1,1337	1,134	1,1342	1,1344	1,1346	1,1348	1,135
8	1,1329	1,1331	1,1333	1,1336	1,1338	1,134	1,1342	1,1343
8,5	1,1329	1,1332	1,1334	1,1337	1,1339	1,1341	1,1343	1,1344
9	1,1334	1,1337	1,1339	1,1341	1,1343	1,1346	1,1348	1,1349
9,5	1,134	1,1343	1,1346	1,1348	1,135	1,1352	1,1354	1,1356
10	1,1348	1,1351	1,1353	1,1356	1,1358	1,136	1,1362	1,1364

Table A.8: Ratio of specific heats of hydrogen-oxygen mixtures

O/F \ P_c	200	208	216	224	232	240	248	256	264
1	1,3587	1,3587	1,3587	1,3587	1,3587	1,3587	1,3587	1,3587	1,3587
1,5	1,3157	1,3157	1,3157	1,3157	1,3157	1,3157	1,3157	1,3157	1,3157
2	1,2825	1,2825	1,2825	1,2825	1,2825	1,2825	1,2825	1,2825	1,2825
2,5	1,257	1,2571	1,2571	1,2571	1,2572	1,2572	1,2572	1,2573	1,2573
3	1,2352	1,2353	1,2354	1,2354	1,2355	1,2356	1,2357	1,2358	1,2358
3,5	1,2149	1,2151	1,2153	1,2155	1,2156	1,2158	1,2159	1,2161	1,2162
4	1,1964	1,1967	1,1969	1,1972	1,1974	1,1976	1,1979	1,1981	1,1982
4,5	1,1803	1,1806	1,1809	1,1812	1,1814	1,1817	1,1819	1,1822	1,1824
5	1,1667	1,1671	1,1674	1,1677	1,1679	1,1682	1,1685	1,1687	1,169
5,5	1,1558	1,1561	1,1564	1,1566	1,1569	1,1572	1,1574	1,1577	1,1579
6	1,1473	1,1475	1,1478	1,148	1,1483	1,1485	1,1487	1,1489	1,1491
6,5	1,1411	1,1413	1,1415	1,1418	1,142	1,1422	1,1423	1,1425	1,1427
7	1,1372	1,1374	1,1376	1,1377	1,1379	1,1381	1,1382	1,1384	1,1385
7,5	1,1352	1,1354	1,1355	1,1357	1,1358	1,136	1,1361	1,1363	1,1364
8	1,1345	1,1347	1,1348	1,135	1,1351	1,1353	1,1354	1,1355	1,1357
8,5	1,1346	1,1348	1,1349	1,1351	1,1352	1,1354	1,1355	1,1357	1,1358
9	1,1351	1,1353	1,1355	1,1356	1,1358	1,1359	1,1361	1,1362	1,1363
9,5	1,1358	1,136	1,1362	1,1363	1,1365	1,1366	1,1368	1,1369	1,1371
10	1,1366	1,1368	1,137	1,1371	1,1373	1,1375	1,1376	1,1378	1,1379

Table A.9: Chamber temperature of hydrogen-oxygen mixtures

O/F \ P_c	8	16	24	32	40	48	56	64
1	977,49	977,49	977,49	977,49	977,49	977,49	977,49	977,49
1,5	1411,9	1411,9	1411,9	1411,9	1411,9	1411,9	1411,9	1411,9
2	1797,3	1797,4	1797,5	1797,6	1797,6	1797,6	1797,7	1797,7
2,5	2138,5	2140,5	2141,4	2142	2142,3	2142,6	2142,8	2143
3	2430,9	2439,3	2443,2	2445,7	2447,4	2448,6	2449,6	2450,4
3,5	2668,3	2688,6	2698,7	2705	2709,5	2712,9	2715,6	2717,9
4	2853,8	2888,7	2906,9	2918,7	2927,3	2933,9	2939,3	2943,7
4,5	2995,7	3045,2	3072	3089,9	3103,1	3113,5	3122	3129,1
5	3102,2	3164,9	3199,7	3223,5	3241,4	3255,6	3267,3	3277,2
5,5	3179,6	3253,3	3295,2	3324,3	3346,4	3364,1	3378,9	3391,4
6	3233,1	3315,5	3363,1	3396,5	3422,2	3442,9	3460,2	3475,1
6,5	3267,7	3356	3407,7	3444,3	3472,6	3495,6	3514,9	3531,6
7	3287,3	3379,3	3433,5	3472,1	3502	3526,5	3547,1	3565
7,5	3295,7	3389,3	3444,7	3484,2	3514,9	3540	3561,2	3579,6
8	3295,7	3389,4	3444,9	3484,4	3515,2	3540,4	3561,7	3580,2
8,5	3289,7	3382,4	3437,2	3476,2	3506,6	3531,4	3552,4	3570,5
9	3279,2	3370,2	3423,8	3462	3491,6	3515,8	3536,2	3553,9
9,5	3265,6	3354,3	3406,5	3443,5	3472,2	3495,6	3515,4	3532,4
10	3249,6	3335,9	3386,4	3422,2	3449,9	3472,5	3491,4	3507,8

Table A.10: Chamber temperature of hydrogen-oxygen mixtures

O/F \ P_c	72	80	88	96	104	112	120	128
1	977,49	977,49	977,49	977,49	977,49	977,49	977,49	977,49
1,5	1411,9	1411,9	1411,9	1411,9	1411,9	1411,9	1411,9	1411,9
2	1797,7	1797,7	1797,7	1797,7	1797,7	1797,7	1797,7	1797,7
2,5	2143,1	2143,3	2143,4	2143,5	2143,5	2143,6	2143,7	2143,7
3	2451,1	2451,6	2452,1	2452,6	2452,9	2453,3	2453,6	2453,9
3,5	2719,8	2721,4	2722,8	2724	2725,1	2726,1	2726,9	2727,8
4	2947,5	2950,7	2953,6	2956,1	2958,4	2960,4	2962,3	2964
4,5	3135,2	3140,5	3145,2	3149,3	3153,1	3156,5	3159,6	3162,5
5	3285,7	3293,3	3299,9	3305,9	3311,3	3316,3	3320,8	3325
5,5	3402,4	3412	3420,6	3428,4	3435,5	3441,9	3447,9	3453,4
6	3488,1	3499,7	3510	3519,4	3528	3535,9	3543,1	3549,9
6,5	3546,3	3559,3	3571,1	3581,7	3591,5	3600,5	3608,9	3616,7
7	3580,7	3594,7	3607,4	3618,9	3629,5	3639,3	3648,4	3656,9
7,5	3595,9	3610,4	3623,5	3635,5	3646,5	3656,6	3666,1	3674,9
8	3596,5	3611	3624,2	3636,2	3647,3	3657,5	3667	3675,9
8,5	3586,6	3600,9	3613,8	3625,6	3636,5	3646,5	3655,8	3664,6
9	3569,4	3583,3	3595,9	3607,3	3617,8	3627,5	3636,6	3645
9,5	3547,4	3560,8	3572,9	3583,9	3594	3603,3	3612	3620
10	3522,2	3535,1	3546,6	3557,2	3566,8	3575,7	3584	3591,7

Table A.11: Chamber temperature of hydrogen-oxygen mixtures

O/F \ P_c	136	144	152	160	168	176	184	192
1	977,49	977,49	977,49	977,49	977,49	977,49	977,49	977,49
1,5	1411,9	1411,9	1411,9	1411,9	1411,9	1411,9	1411,9	1411,9
2	1797,8	1797,8	1797,8	1797,8	1797,8	1797,8	1797,8	1797,8
2,5	2143,8	2143,8	2143,9	2143,9	2144	2144	2144	2144,1
3	2454,1	2454,4	2454,6	2454,8	2455	2455,1	2455,3	2455,4
3,5	2728,5	2729,2	2729,8	2730,4	2730,9	2731,4	2731,9	2732,4
4	2965,5	2967	2968,3	2969,5	2970,7	2971,8	2972,8	2973,8
4,5	3165,1	3167,6	3169,9	3172	3174	3175,9	3177,7	3179,4
5	3328,8	3332,5	3335,8	3339	3342	3344,8	3347,4	3349,9
5,5	3458,6	3463,4	3467,9	3472,1	3476,1	3479,9	3483,5	3486,9
6	3556,2	3562,2	3567,7	3573	3577,9	3582,6	3587,1	3591,4
6,5	3624	3630,8	3637,3	3643,4	3649,2	3654,7	3659,9	3664,9
7	3664,9	3672,4	3679,4	3686,1	3692,5	3698,5	3704,3	3709,8
7,5	3683,2	3691	3698,4	3705,4	3712,1	3718,4	3724,4	3730,2
8	3684,2	3692	3699,5	3706,5	3713,2	3719,6	3725,6	3731,4
8,5	3672,7	3680,4	3687,7	3694,6	3701,2	3707,4	3713,3	3719
9	3652,9	3660,3	3667,4	3674	3680,3	3686,3	3692,1	3697,5
9,5	3627,6	3634,7	3641,5	3647,8	3653,9	3659,6	3665,1	3670,3
10	3598,9	3605,7	3612,1	3618,2	3623,9	3629,4	3634,6	3639,6

Table A.12: Chamber temperature of hydrogen-oxygen mixtures

O/F \ P_c	200	208	216	224	232	240	248	256	264
1	977,49	977,49	977,49	977,49	977,49	977,49	977,49	977,49	977,49
1,5	1411,9	1411,9	1411,9	1411,9	1411,9	1411,9	1411,9	1411,9	1411,9
2	1797,8	1797,8	1797,8	1797,8	1797,8	1797,8	1797,8	1797,8	1797,8
2,5	2144,1	2144,1	2144,1	2144,2	2144,2	2144,2	2144,2	2144,3	2144,3
3	2455,6	2455,7	2455,9	2456	2456,1	2456,2	2456,3	2456,4	2456,5
3,5	2732,8	2733,2	2733,6	2733,9	2734,3	2734,6	2734,9	2735,2	2735,5
4	2974,7	2975,6	2976,4	2977,2	2977,9	2978,6	2979,3	2979,9	2980,5
4,5	3180,9	3182,5	3183,9	3185,3	3186,6	3187,8	3189	3190,1	3191,2
5	3352,3	3354,6	3356,8	3358,8	3360,8	3362,7	3364,5	3366,3	3368
5,5	3490,1	3493,2	3496,1	3499	3501,7	3504,3	3506,8	3509,2	3511,5
6	3595,4	3599,3	3603	3606,6	3610	3613,3	3616,5	3619,6	3622,5
6,5	3669,7	3674,2	3678,6	3682,8	3686,9	3690,8	3694,5	3698,2	3701,7
7	3715,1	3720,1	3725	3729,7	3734,2	3738,5	3742,7	3746,8	3750,7
7,5	3735,7	3741,1	3746,2	3751,1	3755,8	3760,4	3764,8	3769,1	3773,2
8	3737	3742,4	3747,5	3752,5	3757,2	3761,8	3766,3	3770,6	3774,8
8,5	3724,5	3729,7	3734,7	3739,6	3744,3	3748,8	3753,1	3757,3	3761,4
9	3702,8	3707,8	3712,7	3717,3	3721,8	3726,1	3730,3	3734,3	3738,3
9,5	3675,3	3680,1	3684,7	3689,2	3693,4	3697,6	3701,5	3705,4	3709,1
10	3644,3	3648,9	3653,2	3657,5	3661,5	3665,4	3669,2	3672,8	3676,3

Table A.13: Molar mass of kerosene-oxygen mixtures

O/F \ P_c	8	16	24	32	40	48	56	64
1	15,329	15,461	15,563	15,646	15,718	15,782	15,839	15,891
1,5	17,645	17,657	17,663	17,667	17,669	17,671	17,672	17,674
2	20,506	20,62	20,682	20,725	20,757	20,783	20,804	20,821
2,5	22,506	22,701	22,817	22,9	22,965	23,019	23,064	23,103
3	23,984	24,209	24,345	24,444	24,522	24,586	24,641	24,689
3,5	25,166	25,4	25,542	25,645	25,727	25,794	25,852	25,902
4	26,145	26,379	26,522	26,624	26,706	26,773	26,83	26,88
4,5	26,971	27,201	27,339	27,44	27,519	27,584	27,639	27,687
5	27,674	27,897	28,03	28,126	28,202	28,264	28,316	28,362
5,5	28,278	28,491	28,617	28,708	28,779	28,838	28,887	28,93
6	28,799	29	29,119	29,204	29,27	29,324	29,369	29,409
6,5	29,249	29,437	29,547	29,626	29,686	29,736	29,778	29,814
7	29,638	29,812	29,914	29,985	30,04	30,085	30,123	30,155
7,5	29,975	30,134	30,227	30,291	30,34	30,38	30,414	30,443
8	30,266	30,41	30,493	30,55	30,594	30,629	30,659	30,684
8,5	30,516	30,646	30,719	30,769	30,807	30,838	30,863	30,885
9	30,731	30,846	30,909	30,953	30,986	31,012	31,034	31,052
9,5	30,914	31,014	31,069	31,107	31,135	31,157	31,175	31,19
10	31,07	31,156	31,203	31,234	31,258	31,276	31,291	31,304

Table A.14: Molar mass of kerosene-oxygen mixtures

O/F \ P_c	72	80	88	96	104	112	120	128
1	15,939	15,983	16,024	16,063	16,1	16,135	16,168	16,2
1,5	17,675	17,676	17,676	17,677	17,678	17,678	17,679	17,679
2	20,837	20,85	20,862	20,873	20,882	20,891	20,899	20,906
2,5	23,138	23,169	23,197	23,222	23,246	23,267	23,288	23,307
3	24,732	24,77	24,805	24,837	24,867	24,894	24,92	24,944
3,5	25,947	25,987	26,024	26,057	26,088	26,117	26,144	26,17
4	26,924	26,964	27,001	27,034	27,065	27,094	27,12	27,146
4,5	27,73	27,769	27,804	27,836	27,866	27,893	27,919	27,943
5	28,403	28,439	28,473	28,503	28,531	28,557	28,581	28,604
5,5	28,968	29,002	29,033	29,061	29,087	29,111	29,133	29,154
6	29,444	29,475	29,504	29,529	29,553	29,575	29,595	29,614
6,5	29,845	29,874	29,899	29,923	29,944	29,964	29,982	29,999
7	30,184	30,209	30,232	30,252	30,271	30,289	30,305	30,32
7,5	30,468	30,49	30,51	30,528	30,545	30,56	30,574	30,588
8	30,706	30,725	30,742	30,758	30,773	30,786	30,798	30,809
8,5	30,904	30,921	30,935	30,949	30,961	30,972	30,982	30,992
9	31,068	31,082	31,095	31,106	31,116	31,126	31,134	31,142
9,5	31,204	31,215	31,226	31,235	31,243	31,251	31,258	31,265
10	31,315	31,324	31,333	31,34	31,347	31,354	31,359	31,365

Table A.15: Molar mass of kerosene-oxygen mixtures

O/F \ P_c	136	144	152	160	168	176	184	192
1	16,23	16,259	16,287	16,314	16,34	16,365	16,389	16,412
1,5	17,68	17,68	17,68	17,681	17,681	17,681	17,682	17,682
2	20,913	20,92	20,926	20,931	20,936	20,941	20,946	20,95
2,5	23,324	23,341	23,357	23,372	23,386	23,4	23,413	23,425
3	24,967	24,988	25,008	25,028	25,046	25,064	25,081	25,097
3,5	26,194	26,216	26,238	26,258	26,278	26,297	26,315	26,332
4	27,169	27,192	27,213	27,233	27,253	27,271	27,289	27,306
4,5	27,966	27,987	28,008	28,027	28,046	28,063	28,08	28,096
5	28,625	28,645	28,664	28,682	28,7	28,716	28,732	28,747
5,5	29,174	29,193	29,21	29,227	29,243	29,258	29,272	29,286
6	29,632	29,649	29,665	29,68	29,695	29,708	29,721	29,734
6,5	30,015	30,03	30,044	30,058	30,071	30,083	30,094	30,106
7	30,334	30,348	30,36	30,372	30,383	30,394	30,404	30,414
7,5	30,6	30,611	30,622	30,633	30,642	30,651	30,66	30,669
8	30,82	30,83	30,839	30,848	30,856	30,864	30,871	30,878
8,5	31,001	31,009	31,017	31,024	31,031	31,038	31,044	31,05
9	31,15	31,156	31,163	31,169	31,175	31,18	31,185	31,19
9,5	31,271	31,277	31,282	31,287	31,292	31,296	31,3	31,304
10	31,37	31,374	31,378	31,382	31,386	31,39	31,393	31,396

Table A.16: Molar mass of kerosene-oxygen mixtures

O/F \ P_c	200	208	216	224	232	240	248	256	264
1	16,435	16,457	16,479	16,5	16,52	16,54	16,559	16,578	16,596
1,5	17,682	17,683	17,683	17,683	17,684	17,684	17,684	17,684	17,685
2	20,955	20,959	20,962	20,966	20,97	20,973	20,976	20,979	20,982
2,5	23,437	23,448	23,459	23,47	23,48	23,49	23,499	23,508	23,517
3	25,113	25,128	25,142	25,156	25,17	25,183	25,195	25,208	25,22
3,5	26,348	26,364	26,379	26,394	26,408	26,422	26,436	26,449	26,461
4	27,322	27,338	27,353	27,367	27,381	27,395	27,408	27,421	27,433
4,5	28,112	28,127	28,141	28,155	28,169	28,182	28,194	28,206	28,218
5	28,762	28,775	28,789	28,802	28,814	28,826	28,838	28,849	28,86
5,5	29,299	29,312	29,324	29,336	29,348	29,359	29,369	29,38	29,39
6	29,746	29,757	29,768	29,779	29,789	29,799	29,809	29,818	29,827
6,5	30,116	30,126	30,136	30,146	30,155	30,163	30,172	30,18	30,188
7	30,423	30,432	30,44	30,449	30,457	30,464	30,471	30,479	30,485
7,5	30,677	30,684	30,691	30,699	30,705	30,712	30,718	30,724	30,73
8	30,885	30,891	30,898	30,904	30,909	30,915	30,92	30,925	30,93
8,5	31,056	31,061	31,066	31,071	31,076	31,081	31,085	31,089	31,093
9	31,195	31,199	31,204	31,208	31,212	31,215	31,219	31,222	31,226
9,5	31,308	31,312	31,315	31,318	31,321	31,324	31,327	31,33	31,333
10	31,399	31,402	31,405	31,408	31,41	31,413	31,415	31,417	31,419

Table A.17: Ratio of specific heats of kerosene-oxygen mixtures

O/F \ P_c	8	16	24	32	40	48	56	64
1	1,2724	1,2597	1,2528	1,2484	1,2451	1,2426	1,2406	1,239
1,5	1,2405	1,2464	1,2493	1,2511	1,2524	1,2533	1,2541	1,2547
2	1,1526	1,1598	1,1642	1,1673	1,1698	1,1718	1,1734	1,1749
2,5	1,1271	1,1311	1,1335	1,1352	1,1365	1,1376	1,1386	1,1394
3	1,1214	1,1247	1,1266	1,128	1,129	1,1299	1,1306	1,1312
3,5	1,1195	1,1226	1,1245	1,1257	1,1267	1,1275	1,1282	1,1288
4	1,1188	1,1219	1,1237	1,125	1,126	1,1268	1,1275	1,128
4,5	1,1187	1,1219	1,1237	1,1251	1,1261	1,1269	1,1276	1,1282
5	1,1192	1,1224	1,1244	1,1257	1,1268	1,1276	1,1284	1,129
5,5	1,1201	1,1235	1,1255	1,1269	1,1281	1,129	1,1298	1,1304
6	1,1214	1,125	1,1272	1,1287	1,1299	1,1309	1,1317	1,1324
6,5	1,1233	1,1271	1,1294	1,131	1,1323	1,1334	1,1343	1,135
7	1,1256	1,1297	1,1321	1,1339	1,1353	1,1364	1,1374	1,1382
7,5	1,1284	1,1328	1,1355	1,1374	1,1389	1,1401	1,1412	1,1421
8	1,1318	1,1365	1,1394	1,1415	1,1431	1,1444	1,1455	1,1465
8,5	1,1357	1,1409	1,1439	1,1461	1,1479	1,1493	1,1505	1,1515
9	1,1402	1,1458	1,149	1,1514	1,1532	1,1547	1,1559	1,157
9,5	1,1454	1,1512	1,1547	1,1571	1,159	1,1606	1,1618	1,1629
10	1,1511	1,1572	1,1608	1,1633	1,1653	1,1668	1,1681	1,1692

Table A.18: Ratio of specific heats of kerosene-oxygen mixtures

O/F \ P_c	72	80	88	96	104	112	120	128
1	1,2376	1,2363	1,2352	1,2342	1,2333	1,2325	1,2318	1,2311
1,5	1,2552	1,2557	1,2561	1,2564	1,2567	1,257	1,2572	1,2574
2	1,1762	1,1773	1,1783	1,1793	1,1801	1,1809	1,1816	1,1823
2,5	1,1401	1,1408	1,1414	1,1419	1,1424	1,1429	1,1433	1,1437
3	1,1317	1,1322	1,1326	1,133	1,1334	1,1337	1,134	1,1343
3,5	1,1293	1,1297	1,1301	1,1305	1,1308	1,1312	1,1314	1,1317
4	1,1286	1,129	1,1294	1,1298	1,1301	1,1304	1,1307	1,131
4,5	1,1287	1,1292	1,1296	1,13	1,1303	1,1307	1,131	1,1313
5	1,1296	1,1301	1,1305	1,1309	1,1313	1,1316	1,1319	1,1322
5,5	1,131	1,1315	1,132	1,1325	1,1329	1,1332	1,1336	1,1339
6	1,1331	1,1336	1,1341	1,1346	1,135	1,1354	1,1358	1,1362
6,5	1,1357	1,1363	1,1369	1,1374	1,1379	1,1383	1,1387	1,1391
7	1,139	1,1396	1,1402	1,1408	1,1413	1,1418	1,1422	1,1426
7,5	1,1429	1,1436	1,1442	1,1448	1,1454	1,1459	1,1463	1,1468
8	1,1473	1,1481	1,1488	1,1494	1,15	1,1505	1,151	1,1515
8,5	1,1524	1,1532	1,1539	1,1546	1,1552	1,1558	1,1563	1,1568
9	1,1579	1,1588	1,1595	1,1602	1,1608	1,1614	1,162	1,1625
9,5	1,1639	1,1648	1,1655	1,1662	1,1669	1,1674	1,168	1,1685
10	1,1702	1,171	1,1718	1,1725	1,1731	1,1737	1,1742	1,1747

Table A.19: Ratio of specific heats of kerosene-oxygen mixtures

O/F \ P_c	136	144	152	160	168	176	184	192
1	1,2304	1,2298	1,2292	1,2287	1,2282	1,2277	1,2272	1,2268
1,5	1,2576	1,2578	1,258	1,2581	1,2583	1,2584	1,2585	1,2586
2	1,1829	1,1835	1,1841	1,1846	1,1851	1,1856	1,186	1,1865
2,5	1,1441	1,1445	1,1448	1,1452	1,1455	1,1458	1,1461	1,1463
3	1,1346	1,1348	1,1351	1,1353	1,1355	1,1357	1,1359	1,1361
3,5	1,132	1,1322	1,1324	1,1326	1,1328	1,133	1,1332	1,1334
4	1,1313	1,1315	1,1317	1,1319	1,1321	1,1323	1,1325	1,1327
4,5	1,1315	1,1318	1,132	1,1322	1,1324	1,1326	1,1328	1,133
5	1,1325	1,1328	1,133	1,1333	1,1335	1,1337	1,1339	1,1341
5,5	1,1342	1,1345	1,1347	1,135	1,1352	1,1355	1,1357	1,1359
6	1,1365	1,1368	1,1371	1,1374	1,1376	1,1379	1,1381	1,1383
6,5	1,1394	1,1398	1,1401	1,1404	1,1407	1,1409	1,1412	1,1414
7	1,143	1,1434	1,1437	1,144	1,1443	1,1446	1,1449	1,1452
7,5	1,1472	1,1476	1,1479	1,1483	1,1486	1,1489	1,1492	1,1495
8	1,1519	1,1524	1,1527	1,1531	1,1535	1,1538	1,1541	1,1544
8,5	1,1572	1,1576	1,1581	1,1584	1,1588	1,1591	1,1595	1,1598
9	1,1629	1,1634	1,1638	1,1642	1,1645	1,1649	1,1652	1,1655
9,5	1,1689	1,1694	1,1698	1,1702	1,1706	1,1709	1,1712	1,1716
10	1,1752	1,1756	1,176	1,1764	1,1767	1,1771	1,1774	1,1777

Table A.20: Ratio of specific heats of kerosene-oxygen mixtures

O/F \ P_c	200	208	216	224	232	240	248	256	264
1	1,2263	1,2259	1,2255	1,2251	1,2248	1,2244	1,2241	1,2237	1,2234
1,5	1,2588	1,2589	1,259	1,259	1,2591	1,2592	1,2593	1,2594	1,2594
2	1,1869	1,1872	1,1876	1,188	1,1883	1,1886	1,189	1,1893	1,1896
2,5	1,1466	1,1468	1,1471	1,1473	1,1475	1,1478	1,148	1,1482	1,1484
3	1,1363	1,1364	1,1366	1,1367	1,1369	1,137	1,1372	1,1373	1,1374
3,5	1,1335	1,1337	1,1338	1,134	1,1341	1,1342	1,1344	1,1345	1,1346
4	1,1328	1,133	1,1331	1,1333	1,1334	1,1336	1,1337	1,1338	1,1339
4,5	1,1332	1,1333	1,1335	1,1337	1,1338	1,1339	1,1341	1,1342	1,1343
5	1,1343	1,1345	1,1346	1,1348	1,135	1,1351	1,1353	1,1354	1,1355
5,5	1,1361	1,1363	1,1365	1,1367	1,1368	1,137	1,1372	1,1373	1,1375
6	1,1386	1,1388	1,139	1,1392	1,1394	1,1395	1,1397	1,1399	1,14
6,5	1,1417	1,1419	1,1421	1,1423	1,1425	1,1427	1,1429	1,1431	1,1433
7	1,1454	1,1457	1,1459	1,1461	1,1464	1,1466	1,1468	1,147	1,1472
7,5	1,1498	1,15	1,1503	1,1505	1,1508	1,151	1,1512	1,1514	1,1516
8	1,1547	1,155	1,1552	1,1555	1,1557	1,156	1,1562	1,1564	1,1566
8,5	1,1601	1,1604	1,1606	1,1609	1,1612	1,1614	1,1616	1,1619	1,1621
9	1,1658	1,1661	1,1664	1,1667	1,1669	1,1672	1,1674	1,1676	1,1679
9,5	1,1719	1,1721	1,1724	1,1727	1,1729	1,1732	1,1734	1,1736	1,1739
10	1,178	1,1783	1,1785	1,1788	1,179	1,1793	1,1795	1,1797	1,1799

Table A.21: Chamber temperature of kerosene-oxygen mixtures

O/F \ P_c	8	16	24	32	40	48	56	64
1	1451,14	1478,37	1498,59	1514,89	1528,64	1540,58	1551,16	1560,68
1,5	2479,39	2487,63	2491,48	2493,84	2495,47	2496,7	2497,66	2498,44
2	3160,42	3222,46	3256,67	3279,86	3297,17	3310,86	3322,1	3331,58
2,5	3352,22	3446,76	3502,57	3542,28	3573,1	3598,27	3619,52	3637,9
3	3377,63	3478,45	3538,77	3582,12	3616,06	3643,97	3667,69	3688,33
3,5	3357,55	3457,06	3516,67	3559,55	3593,14	3620,8	3644,31	3664,78
4	3321,78	3417,66	3474,97	3516,15	3548,36	3574,85	3597,37	3616,95
4,5	3279,4	3370,74	3425,15	3464,14	3494,58	3519,58	3540,79	3559,22
5	3233,78	3320,16	3371,38	3407,97	3436,46	3459,81	3479,59	3496,74
5,5	3186,35	3267,53	3315,4	3349,48	3375,93	3397,56	3415,83	3431,65
6	3137,72	3213,55	3257,99	3289,48	3313,86	3333,72	3350,46	3364,93
6,5	3088,15	3158,53	3199,49	3228,37	3250,63	3268,72	3283,92	3297,02
7	3037,74	3102,61	3140,05	3166,31	3186,47	3202,78	3216,46	3228,21
7,5	2986,51	3045,82	3079,76	3103,41	3121,48	3136,05	3148,22	3158,64
8	2934,43	2988,19	3018,65	3039,74	3055,76	3068,63	3079,34	3088,48
8,5	2881,5	2929,75	2956,79	2975,38	2989,43	3000,66	3009,97	3017,89
9	2827,7	2870,54	2894,28	2910,47	2922,63	2932,31	2940,3	2947,08
9,5	2773,07	2810,67	2831,24	2845,16	2855,56	2863,79	2870,56	2876,29
10	2717,68	2750,26	2767,86	2779,68	2788,45	2795,36	2801,03	2805,8

Table A.22: Chamber temperatures of kerosene-oxygen mixtures

O/F \ P_c	72	80	88	96	104	112	120	128
1	1569,35	1577,32	1584,69	1591,57	1598,01	1604,07	1609,8	1615,23
1,5	2499,09	2499,65	2500,13	2500,55	2500,93	2501,26	2501,57	2501,84
2	3339,74	3346,88	3353,21	3358,88	3364	3368,65	3372,92	3376,85
2,5	3654,09	3668,54	3681,58	3693,47	3704,38	3714,45	3723,81	3732,55
3	3706,6	3722,99	3737,86	3751,46	3764	3775,63	3786,48	3796,64
3,5	3682,92	3699,19	3713,97	3727,49	3739,96	3751,53	3762,32	3772,44
4	3634,29	3649,84	3663,94	3676,85	3688,75	3699,78	3710,07	3719,7
4,5	3575,51	3590,11	3603,34	3615,44	3626,58	3636,9	3646,51	3655,52
5	3511,88	3525,44	3537,7	3548,9	3559,2	3568,74	3577,62	3585,92
5,5	3445,6	3458,06	3469,32	3479,58	3489,01	3497,74	3505,85	3513,42
6	3377,65	3388,99	3399,23	3408,55	3417,1	3425	3432,33	3439,17
6,5	3308,52	3318,76	3327,98	3336,35	3344,03	3351,1	3357,66	3363,78
7	3238,49	3247,63	3255,84	3263,29	3270,11	3276,38	3282,18	3287,59
7,5	3167,75	3175,81	3183,05	3189,6	3195,58	3201,07	3206,15	3210,87
8	3096,44	3103,48	3109,78	3115,47	3120,65	3125,41	3129,79	3133,86
8,5	3024,77	3030,84	3036,25	3041,13	3045,57	3049,63	3053,37	3056,84
9	2952,95	2958,11	2962,7	2966,84	2970,58	2974,01	2977,16	2980,08
9,5	2881,23	2885,56	2889,41	2892,87	2896	2898,85	2901,47	2903,89
10	2809,91	2813,5	2816,68	2819,54	2822,12	2824,47	2826,62	2828,61

Table A.23: Chamber temperatures of kerosene-oxygen mixtures

O/F \ P_c	136	144	152	160	168	176	184	192
1	1620,4	1625,32	1630,03	1634,54	1638,87	1643,04	1647,05	1650,92
1,5	2502,1	2502,33	2502,55	2502,75	2502,93	2503,11	2503,28	2503,43
2	3380,48	3383,86	3387,02	3389,97	3392,74	3395,35	3397,82	3400,16
2,5	3740,74	3748,44	3755,71	3762,6	3769,13	3775,34	3781,27	3786,93
3	3806,2	3815,22	3823,76	3831,87	3839,59	3846,96	3854,01	3860,76
3,5	3781,95	3790,94	3799,45	3807,54	3815,24	3822,59	3829,63	3836,37
4	3728,77	3737,32	3745,42	3753,12	3760,44	3767,43	3774,11	3780,52
4,5	3663,98	3671,96	3679,51	3686,68	3693,5	3700,01	3706,22	3712,18
5	3593,72	3601,07	3608,02	3614,61	3620,87	3626,85	3632,55	3638,01
5,5	3520,53	3527,22	3533,54	3539,54	3545,23	3550,64	3555,82	3560,76
6	3445,59	3451,62	3457,31	3462,7	3467,81	3472,67	3477,31	3481,74
6,5	3369,5	3374,87	3379,94	3384,73	3389,28	3393,59	3397,71	3401,63
7	3292,64	3297,37	3301,83	3306,05	3310,03	3313,82	3317,43	3320,86
7,5	3215,27	3219,39	3223,27	3226,93	3230,39	3233,68	3236,8	3239,77
8	3137,66	3141,2	3144,54	3147,67	3150,64	3153,45	3156,12	3158,65
8,5	3060,06	3063,08	3065,9	3068,56	3071,07	3073,44	3075,69	3077,83
9	2982,79	2985,31	2987,68	2989,9	2992	2993,98	2995,85	2997,63
9,5	2906,14	2908,23	2910,19	2912,02	2913,75	2915,38	2916,93	2918,39
10	2830,44	2832,16	2833,76	2835,26	2836,67	2838	2839,25	2840,45

Table A.24: Chamber temperatures of kerosene-oxygen mixtures

O/F \ P_c	200	208	216	224	232	240	248	256
1	1654,66	1658,27	1661,78	1665,17	1668,47	1671,67	1674,78	1677,81
1,5	2503,58	2503,72	2503,85	2503,98	2504,1	2504,22	2504,34	2504,44
2	3402,37	3404,48	3406,48	3408,39	3410,22	3411,97	3413,65	3415,26
2,5	3792,35	3797,55	3802,54	3807,33	3811,95	3816,41	3820,71	3824,86
3	3867,24	3873,47	3879,47	3885,25	3890,83	3896,23	3901,45	3906,51
3,5	3842,84	3849,06	3855,05	3860,83	3866,41	3871,8	3877,03	3882,08
4	3786,66	3792,57	3798,26	3803,75	3809,04	3814,16	3819,11	3823,91
4,5	3717,89	3723,38	3728,66	3733,75	3738,66	3743,4	3747,99	3752,43
5	3643,24	3648,26	3653,09	3657,75	3662,24	3666,57	3670,76	3674,81
5,5	3565,5	3570,04	3574,41	3578,62	3582,67	3586,58	3590,36	3594,01
6	3485,98	3490,05	3493,95	3497,71	3501,33	3504,81	3508,18	3511,43
6,5	3405,38	3408,98	3412,43	3415,75	3418,94	3422,01	3424,98	3427,84
7	3324,15	3327,29	3330,3	3333,19	3335,97	3338,65	3341,23	3343,72
7,5	3242,6	3245,32	3247,91	3250,41	3252,8	3255,1	3257,32	3259,46
8	3161,07	3163,38	3165,6	3167,72	3169,75	3171,7	3173,59	3175,4
8,5	3079,87	3081,81	3083,67	3085,45	3087,16	3088,8	3090,38	3091,89
9	2999,33	3000,94	3002,49	3003,96	3005,38	3006,74	3008,04	3009,3
9,5	2919,79	2921,11	2922,38	2923,59	2924,75	2925,86	2926,93	2927,95
10	2841,58	2842,66	2843,68	2844,67	2845,6	2846,5	2847,37	2848,2

Table A.25: Chamber temperatures of kerosene-oxygen mixtures

O/F \ P_c	264
1	1680,76
1,5	2504,55
2	3416,8
2,5	3828,88
3	3911,41
3,5	3886,99
4	3828,56
4,5	3756,74
5	3678,74
5,5	3597,55
6	3514,58
6,5	3430,61
7	3346,13
7,5	3261,52
8	3177,15
8,5	3093,36
9	3010,5
9,5	2928,94
10	2849

Appendix B

Main Results

In this appendix the main results generated with the program are tabulated. As a side note, the maximum thrust is always presented without the exit pressure term, thus denotes maximum thrust at design altitude. And the thrust-to-mass ratio is calculated with included fairing mass even for the solutions that jettison the fairing before ignition

Table B.1: Optimized launch vehicle parameters and characteristics using kerolox propellants

Velocity (m/s)	0	0	0	0	0
Altitude (m)	0	5000	10000	20000	40000
Pitch 1	0,1013	0,0792	0,084	0,2187	0,3183
Pitch 2	0,7251	0,7144	0,6867	0,6723	0,3612
Pitch 3	0,347	0,4241	0,4838	0,3022	0,4957
Pitch 4	0,5604	0,5239	0,497	0,573	0,5482
Length (m)	18,558	14,823	13,667	10,816	11,094
Slenderness	10,38	7,5495	6,686	4,7284	4,8734
Diameter (m)	1,7879	1,9635	2,0441	2,2875	2,2764
Nozzle diameter (m)	0,8804	1,0507	1,1559	1,3034	1,5026
Oxidizer to fuel ratio	2,4988	2,5023	2,5018	2,5019	2,5
Chamber Pressure (bar)	263,98	263,13	263,95	263,77	263,99
Exit Pressure (Pa)	45861	27546	20978	14089	9975,6
Initial Flight path angle (Deg)	84,814	83,553	81,791	80,401	80,083
Optimized payload Ratio	0,0208	0,0251	0,0292	0,3427	0,0429
Estimated payload Ratio	0,021	0,028	0,032	0,035	0,04
Target Altitude (m)	250000	250000	250000	250000	250000
Gravity Loss (m/s)	445,1	410,1	380,4	490,9	428,4
Drag Loss (m/s)	340,8	297,9	242,4	61,2	3,4
Maximum Dynamic Pressure (Pa)	48940	26584	14211	2513	134,4
Time max dynamic Pressure (s)	85,7	78	78	87,6	88,3
Initial Acceleration (m/s^2)	11,7	12,05	12,33	12,5	12,5
Maximum Acceleration (m/s^2)	50	50	50	50	50
Initial Mass (kg)	41351	38902	38431	36380	37231
Final Mass (kg)	3039,5	3040,6	3161,5	3184	3625,1
Jettisoning (s)	365	352,2	350,9	222,8	0
Fairing mass (kg)	224,6	281,2	317,1	328,1	0
Maximum Bending load (Pa $\cdot$ rad)	8120	5958	3746,5	950	48,1
Time max Bending (s)	63,8	61	60,8	89,8	75,7
Heat shield Mass (kg)	9	8,7	8	0	0
mass flow (kg/s)	155,5	145	139,9	127,6	127
Payload Mass (kg)	859,9	978,3	1123	1246,9	1596,2
Max thrust (N)	516546	491948	479830	443686	446702
Exhaust Velocity (m/s)	3321,7	3392,8	3428,9	3477,9	3518,1
Maximum Angle of Attack (rad)	0,515	0,502	0,517	0,52	0,523
Delta V (m/s)	8652,8	8623,6	8536,4	8440,2	8158,1
Area Ratio	41,1	63,9	81,2	114,9	155,3
Mass Engine (kg)	787,67	746,85	726,7	667,16	672,1
Mass Nozzle (kg)	77,48	114,92	142,35	186,16	253,24
Mass Tank (kg)	957,84	859,3	833,43	765,83	778,83
Max Heat flux (W/m^2)	37426	35523	32303	4260	1135
Time max heat flux (s)	212,5	215	78	152,8	99,1
T/M (N/kg)	12,492	12,646	12,486	12,196	11,998

Table B.2: Optimized launch vehicle parameters and characteristics using kerolox propellants

Velocity (m/s)	300	300	300	300	300
Altitude (m)	0	5000	10000	20000	40000
Pitch 1	0,40141	0,37675	0,40895	0,42489	0,42309
Pitch 2	0,607	0,58421	0,50483	0,32181	0,42187
Pitch 3	0,2543	0,25299	0,3067	0,51772	0,4512
Pitch 4	0,59075	0,60361	0,59393	0,52871	0,53997
Length (m)	16,4992	13,527	11,7915	15,4315	10,8795
Slenderness	8,12269	6,18082	5,76523	5,99709	5,21521
Diameter (m)	2,03125	2,18855	2,04527	2,57316	2,08611
Nozzle diameter (m)	1,15298	1,25848	1,10898	1,86945	1,21478
Oxidizer to fuel ratio	2,5	2,50012	2,50011	2,50057	2,50003
Chamber Pressure (bar)	263,998	263,32	264	262,631	263,941
Exit Pressure (Pa)	21249,6	16043,4	15680,6	10209,3	12260,1
Initial Flight path angle (Deg)	64,635	68,4453	65,4663	69,19	56,3973
Optimized payload Ratio	0,03983	0,04412	0,04751	0,05431	0,0617
Estimated payload Ratio	0,04	0,045	0,05	0,055	0,06
Target Altitude (m)	250000	250000	250000	250000	250000
Gravity Loss (m/s)	703,4	678,4	630,8	613,7	415
Drag Loss (m/s)	262,1	138,4	106,3	16,5	3,9
Maximum Dynamic Pressure (Pa)	55081,5	33118	18583	3965	173,7
Time max dynamic Pressure (s)	0	0	0	0	0
Initial Acceleration (m/s^2)	7,7	8,79	9,775	10,4	11,6
Maximum Acceleration (m/s^2)	50	50	50	50	50
Initial Mass (kg)	46524,4	43140,1	32601,7	68070,8	31013,1
Final Mass (kg)	4056,5	3989,3	3126,7	7089,1	3477,7
Jettisoning (s)	240,4	221,9	211,4	0	0
Fairing mass (kg)	478,9	498,9	418,4	0	0
Maximum Bending load ($Pa \cdot rad$)	6244	3046	1934	362	50,7
Time max Bending (s)	28,3	25,8	27	27,6	51,7
Heat shield Mass (kg)	0	0	0	0	0
mass flow (kg/s)	140,7	132,6	101	200,2	98,7
Payload Mass (kg)	1853,2	1903,3	1549	3696,7	1913,4
Max thrust (N)	482411	458940	350092	703796	344754
Exhaust Velocity (m/s)	3427,5	3462,1	3465,3	3514,6	3494,5
Maximum Angle of Attack (rad)	0,274	0,289	0,3157	0,341	0,4148
Delta V (m/s)	8326,4	8202,5	8079,3	7900,2	7592
Area Ratio	80,4	102,4	104,7	151,5	129,7
Mass Engine (kg)	730,99	692,25	514,93	1104,61	506,35
Mass Nozzle (kg)	141,57	171,73	133,9	389,61	163,28
Mass Tank (kg)	983,71	889,72	664,43	1412,32	632,84
Max Heat flux (W/m^2)	1859	2918	2632	1132,6	1134
Time max heat flux (s)	0	150	143	142	140,8
T/M (N/kg)	10,369	10,6384	10,7385	10,3392	11,1164

Table B.3: Optimized launch vehicle parameters and characteristics using kerolox propellants

Velocity (m/s)	600	600	600	600	600
Altitude (m)	0	5000	10000	20000	40000
Pitch 1	0,38633	0,43518	0,28762	0,33299	0,47947
Pitch 2	0,32955	0,44634	0,59118	0,54415	0,35633
Pitch 3	0,59578	0,41728	0,44257	0,4784	0,5138
Pitch 4	0,49037	0,54802	0,51713	0,50516	0,52504
Length (m)	19,0521	18,0421	13,609	13,4834	11,2983
Slenderness	8,74287	8,12332	5,31686	4,81443	6,26334
Diameter (m)	2,17916	2,22102	2,5596	2,80063	1,80387
Nozzle diameter (m)	1,51719	1,61023	1,51041	1,72514	1,22024
Oxidizer to fuel ratio	2,50588	2,50382	2,50011	2,50623	2,49999
Chamber Pressure (bar)	262,78	263,262	263,58	263,25	264
Exit Pressure (Pa)	14294,7	12074,8	12654,1	11461,6	8808,88
Initial Flight path angle (Deg)	68,8358	58,9612	66,0217	58,1154	45,923
Optimized payload Ratio	0,05639	0,06093	0,06543	0,07044	0,07806
Estimated payload Ratio	0,055	0,065	0,07	0,075	0,08
Target Altitude (m)	250000	250000	250000	250000	250000
Gravity Loss (m/s)	746,5	646,3	654,5	539,6	387,3
Drag Loss (m/s)	97,3	98,1	42,4	14,6	3,5
Maximum Dynamic Pressure (Pa)	219979	132358	74218	15851,1	694
Time max dynamic Pressure (s)	0	0	0	0	0
Initial Acceleration (m/s^2)	2,1	5,2	6,2	9,22	11
Maximum Acceleration (m/s^2)	50	50	50	50	50
Initial Mass (kg)	62477,3	61267,4	58396,9	68437	24822
Final Mass (kg)	6470,1	6654,7	6462,2	8007,7	3205
Jettisoning (s)	175,4	180,6	77,9	52,8	0
Fairing mass (kg)	880,8	1018,2	1043,8	1309	0
Maximum Bending load (Pa $\cdot$ rad)	3091	4319	585	343,5	53
Time max Bending (s)	15,5	12,5	17,9	14,8	23,3
Heat shield Mass (kg)	0,4	0,3	0	0	0
mass flow (kg/s)	174,8	171	156,6	187,9	75,4
Payload Mass (kg)	3522,9	3732,8	3821,1	4820,4	1937,5
Max thrust (N)	607596	597900	546555	657957	266435
Exhaust Velocity (m/s)	3475,2	3495,6	3490,6	3501,4	3531,9
Maximum Angle of Attack (rad)	0,211	0,302	0,2596	0,293	0,3515
Delta V (m/s)	7831,2	7701,3	7620,8	7444,6	7157
Area Ratio	113,1	131,2	126	137,3	173
Mass Engine (kg)	940,68	924,3	837,85	1026,22	382,07
Mass Nozzle (kg)	251,03	286,52	251,55	329,94	168,35
Mass Tank (kg)	1324,7	1284,92	1157,91	1371,11	501,15
Max Heat flux (W/m^2)	14325	11020,5	7688	3401	963
Time max heat flux (s)	0	0	0	0	86,5
T/M (N/kg)	9,72507	9,75886	9,35932	9,61405	10,7338

Table B.4: Optimized launch vehicle parameters and characteristics using kerolox propellants

Velocity (m/s)	1000	1000	1000	1000	1000
Altitude (m)	0	5000	10000	20000	40000
Pitch 1	0,35945	0,34764	0,38198	0,35717	0,45402
Pitch 2	0,50485	0,51959	0,42348	0,59188	0,46149
Pitch 3	0,49209	0,49963	0,57817	0,41108	0,46954
Pitch 4	0,50727	0,50282	0,48242	0,52992	0,52141
Length (m)	19,0725	18,1594	15,7677	14,3292	10,3185
Slenderness	8,47571	11,2901	6,57739	6,3481	5,25643
Diameter (m)	2,25025	1,60844	2,39726	2,25725	1,96302
Nozzle diameter (m)	1,64924	1,21861	1,64386	1,57863	1,22087
Oxidizer to fuel ratio	2,5092	2,5	2,50713	2,50594	2,49958
Chamber Pressure (bar)	263,944	263,598	260,514	263,214	260,426
Exit Pressure (Pa)	11334,3	9758,82	10770,4	8856,84	8057,48
Initial Flight path angle (Deg)	55,6807	54,3499	49,9696	47,507	39,6175
Optimized payload Ratio	0,07837	0,08262	0,08655	0,09138	0,09645
Estimated payload Ratio	0,075	0,085	0,09	0,095	0,1
Target Altitude (m)	250000	250000	250000	250000	250000
Gravity Loss (m/s)	629,3	593,5	529,9	482,7	361,3
Drag Loss (m/s)	133,2	77,6	52,2	13,7	2,2
Maximum Dynamic Pressure (Pa)	610791	367453	206199	44024,7	1926,9
Time max dynamic Pressure (s)	0	0	0	0	0
Initial Acceleration (m/s^2)	-5,84	-0,25	3,8	8,05	9,69
Maximum Acceleration (m/s^2)	50	50	50	50	50
Initial Mass (kg)	66754,8	33237,8	61363	49307,2	26261,1
Final Mass (kg)	8258,8	4227	8123	6769,2	3769,8
Jettisoning (s)	130,1	119,1	112,6	89,7	58,1
Fairing mass (kg)	1276,8	718,7	1403	1188,5	665,485
Maximum Bending load (Pa $\cdot$ rad)	3915	2166	1874	415	52,2
Time max Bending (s)	11,4	8,5	8,4	9,7	14,1
Heat shield Mass (kg)	7,5	5,4	3,7	0,9	0
mass flow (kg/s)	170,2	82	161,7	126,7	69,9
Payload Mass (kg)	5231,4	2723,1	5310,7	4505,9	2532,8
Max thrust (N)	596123	288571	567022	447431	247528
Exhaust Velocity (m/s)	3502,8	3520,3	3506,8	3530,4	3539,4
Maximum Angle of Attack (rad)	0,225	0,229	0,1975	0,2411	0,3
Delta V (m/s)	7252,3	7182,5	7010	6924	6779,4
Area Ratio	139	158	143,6	171,8	184,8
Mass Engine (kg)	921,31	416,91	872,17	673,27	352,56
Mass Nozzle (kg)	302,51	166,53	298,09	280,93	167,44
Mass Tank (kg)	1372,15	680,68	1231,88	969,54	509,21
Max Heat flux (W/m^2)	65221,4	59904,1	36790,4	17534,9	3935,9
Time max heat flux (s)	0	0	0	0	0
T/M (N/kg)	8,93004	8,68201	9,24045	9,07435	9,42565

Table B.5: Optimized launch vehicle parameters and characteristics using kerolox propellants

Velocity (m/s)	1500	1500	1500	1500	1500
Altitude (m)	0	5000	10000	20000	40000
Pitch 1	0,30391	0,30399	0,39171	0,37522	0,41225
Pitch 2	0,66193	0,69279	0,45214	0,57429	0,49043
Pitch 3	0,43878	0,4096	0,5638	0,46067	0,5573
Pitch 4	0,50729	0,51477	0,48501	0,50979	0,47704
Length (m)	44,1592	30,6699	16,5618	12,9515	11,203
Slenderness	14,6486	4,4899	5,61482	5,29576	5,65653
Diameter (m)	3,01456	6,83086	2,94965	2,44564	1,98054
Nozzle diameter (m)	3,00448	6,82098	2,13671	1,7007	1,29488
Oxidizer to fuel ratio	2,5036	2,5046	2,50368	2,50308	2,50035
Chamber Pressure (bar)	263,515	262,317	263,994	263,122	260,322
Exit Pressure (Pa)	13105,3	7556,54	8579,93	6781,5	6899,27
Initial Flight path angle (Deg)	47,0941	44,0082	42,2663	39,0715	34,0136
Optimized payload Ratio	0,09871	0,10537	0,11115	0,11828	0,12363
Estimated payload Ratio	0,1	0,105	0,11	0,115	0,12
Target Altitude (m)	250000	250000	250000	250000	250000
Gravity Loss (m/s)	537,7	485,2	469,6	413,2	317,4
Drag Loss (m/s)	156,1	112,7	107,2	34,4	2,4
Maximum Dynamic Pressure (Pa)	1374140	826421	463360	99003	4334,1
Time max dynamic Pressure (s)	0	0	0	0	0
Initial Acceleration (m/s^2)	-14,5	-8,67	-8,5	3,39	8,45
Maximum Acceleration (m/s^2)	50	50	50	50	50
Initial Mass (kg)	289399	923909	96002,9	51255,9	29391,3
Final Mass (kg)	41854,1	141590	14897,5	8316,7	4937,5
Jettisoning (s)	99,6	87,5	92	83,6	61,9
Fairing mass (kg)	7333,7	24552,4	2669,3	8316,7	889,3
Maximum Bending load (Pa $\cdot$ rad)	1703	586	1916	419	41
Time max Bending (s)	4,2	3,5	6,6	7,5	10,2
Heat shield Mass (kg)	91,9	61,8	17,9	5,9	0,4
mass flow (kg/s)	637,9	2069,7	226,2	117,5	69
Payload Mass (kg)	28567,2	97356,5	10671,1	6062,7	3633,7
Max thrust (N)	2223760	7341460	799493	418323	245475
Exhaust Velocity (m/s)	3486,2	3547,2	3534,5	3559,3	3556,11
Maximum Angle of Attack (rad)	0,263	0,2535	0,174	0,22	0,267
Delta V (m/s)	6651,4	6557,9	6485,7	6367,9	6234,25
Area Ratio	122,2	196,7	177,1	216,7	211,5
Mass Engine (kg)	3884,53	14331,2	1269,84	625,56	349,31
Mass Nozzle (kg)	992,94	5279,69	516,88	331,24	190,06
Mass Tank (kg)	7025,33	20734,5	1880,06	967,33	552,5
Max Heat flux (W/m^2)	190152	98044	111726	56810	13219
Time max heat flux (s)	0	0	0	0	0
T/M (N/kg)	7,68406	7,94609	8,3278	8,16146	8,35196

Table B.6: Optimized launch vehicle parameters and characteristics using kerolox propellants

Velocity (m/s)	2000	2000	2000	2000	2000
Altitude (m)	0	5000	10000	20000	40000
Pitch 1	0,3255	0,33417	0,36363	0,4223	0,34945
Pitch 2	0,63251	0,68485	0,64775	0,47284	0,7104
Pitch 3	0,46093	0,39942	0,41382	0,54445	0,37438
Pitch 4	0,5033	0,52014	0,51836	0,48891	0,52691
Length (m)	45,8342	39,9775	37,6945	21,8635	13,3736
Slenderness	16,9713	13,8723	12,9079	5,32786	5,49624
Diameter (m)	2,70068	2,88182	2,92026	4,10361	2,43322
Nozzle diameter (m)	2,66964	2,88159	2,91504	3,72837	1,84071
Oxidizer to fuel ratio	2,50802	2,5	2,50074	2,50371	2,50078
Chamber Pressure (bar)	263,725	264	263,801	263,167	262,892
Exit Pressure (Pa)	13104	10508,9	10108,6	6380,98	5663,47
Initial Flight path angle (Deg)	39,8954	37,4962	34,6504	31,692	28,0966
Optimized payload Ratio	0,12255	0,13022	0,13626	0,14485	0,15115
Estimated payload Ratio	0,125	0,13	0,135	0,14	0,19
Target Altitude (m)	250000	250000	250000	250000	250000
Gravity Loss (m/s)	464,5	432,2	391,6	337,1	251
Drag Loss (m/s)	237,9	167,9	101,1	58	7,3
Maximum Dynamic Pressure (Pa)	2440970	1468370	824127	175941	7704
Time max dynamic Pressure (s)	0	0	0	0	0
Initial Acceleration (m/s^2)	-30,6	-20,25	-10	-1,27	7,4
Maximum Acceleration (m/s^2)	44,9	42,7	42,2	42,5	41,7
Initial Mass (kg)	243845	240024	231939	245677	53696,3
Final Mass (kg)	40651,7	41685	41783,5	46611,6	10468,8
Jettisoning (s)	95,3	92,2	92,7	82,6	66,7
Fairing mass (kg)	7675,5	7847,6	7865	8628,6	2527,7
Maximum Bending load (Pa $\cdot$rad)	4174	1475	768	718,4	9,24
Time max Bending (s)	4,7	4	9	6,3	17,6
Heat shield Mass (kg)	246,7	178,2	134,6	40	11,8
mass flow (kg/s)	503,5	487,9	483,2	536,6	118,3
Payload Mass (kg)	29884,3	31255,1	31604	35585,7	8116,2
Max thrust (N)	1755290	1713450	1699020	1913420	423276
Exhaust Velocity (m/s)	3485,9	3512,2	3516,4	3565,6	3578
Maximum Angle of Attack (rad)	0,239	0,2365	0,2255	0,1908	0,229
Delta V (m/s)	6133,5	6031,7	5905,7	5799,2	5677,3
Area Ratio	122,4	148,4	153,4	228,6	253,3
Mass Engine (kg)	2999,36	2921,36	2894,45	3296,02	633,62
Mass Nozzle (kg)	784,42	928,2	951,73	1597,83	391,82
Mass Tank (kg)	5840,12	5462,99	5230,42	4928,69	989,82
Max Heat flux (W/m^2)	475633	357501	266343	103914	28263
Time max heat flux (s)	0	0	0	0	0
T/M (N/kg)	7,19838	7,13866	7,32529	7,78836	7,88278

Table B.7: Optimized launch vehicle parameters and characteristics using hydrolox propellants

Velocity (m/s)	0	0	0	0	0
Altitude (m)	0	5000	10000	20000	40000
Pitch 1	0,07812	0,32335	0,06294	0,26318	0,18037
Pitch 2	0,97471	0,5423	0,99274	0,6158	0,59087
Pitch 3	0,162	0,42165	0,16668	0,29534	0,40533
Pitch 4	0,58484	0,5356	0,58168	0,59142	0,55579
Length (m)	20,431	17,0035	16,8899	15,3777	12,894
Slenderness	11,5255	10,4661	10,4019	7,35343	5,95251
Diameter (m)	1,77268	1,62462	1,62374	2,09122	2,16615
Nozzle Diameter (m)	0,56763	0,60583	0,72687	1,05332	0,93048
Oxidizer to fuel	6,00637	6,07103	6,03563	6	6
Chamber Pressure (bar)	263,871	263,945	263,758	264	263,961
Exit Pressure (Pa)	47986,6	27294,7	17255,4	10705,4	12573,6
Initial flight path angle	0,95786	0,92411	0,90566	0,88745	0,94210
Optimized payload Ratio	0,03086	0,07408	0,04632	0,05341	0,06527
Estimated payload Ratio	0,035	0,077	0,041	0,055	0,055
Target Altitude (m)	250000	250000	250000	250000	250000
Gravity Loss (m/s)	576,1	714	500,8	504,6	429,1
Drag Loss (m/s)	428,9	176,7	275,9	98,5	5,1
Maximum Dynamic Pressure (Pa)	36112	219780	11985	2461	138
Time of dynamic pressure (s)	81,8	0	66,5	64,7	76,7
Initial Acceleration (m/s^2)	12,15	-0,8	13,3	13,5	13,9
Maximum Acceleration (m/s^2)	50	50	50	50	50
Initial Mass (kg)	17237,5	17300	11978,1	17610,4	15465,1
Final Mass (kg)	2131,2	2842,5	1708,6	2659,6	2513,4
Jettisoning (s)	270,5	196,5	253,7	213,7	0
Fairing mass (kg)	155,5	339,5	126,3	248,3	0
Maximum Bending load (Pa $\cdot$ rad)	5042	2500	1644	850	41
Time max Bending (s)	62,5	89,6	49	56	66,8
Heat shield Mass (kg)	0,6	0,3	0,2	0	0
mass flow (kg/s)	52,7	43	37	52,1	46,5
Payload Mass (kg)	531,9	1281,6	554,9	940,6	1009,4
Max thrust (N)	222945	190011	162636	233168	207099
Exhaust Velocity (m/s)	4228,2	4419	4401,1	4476,4	4452,8
Maximum Angle of Attack (rad)	0,523	0,2026	0,513	0,524	0,357
Delta V (m/s)	8800,4	7893,3	8524,2	8398,2	8027,3
Area Ratio	39,5	125,1	96,1	145,6	126,6
Mass Engine (kg)	302,38	204,62	204,75	319,54	275,99
Mass Nozzle (kg)	32,11	38,35	57,07	124,02	95,68
Mass Tank (kg)	1039,22	722,15	717,21	1038,7	918,32
Max Heat flux (W/m^2)	11502	17104,8	9349	3432	1135
Time max Heat flux (s)	174,6	0	156,4	142,5	135,9
T/W (N/kg)	12,9337	10,9833	13,5778	13,2404	13,3914

Table B.8: Optimized launch vehicle parameters and characteristics using hydrolox propellants

Velocity (m/s)	300	300	300	300	300
Altitude (m)	0	5000	10000	20000	40000
Pitch 1	0,39105	0,39673	0,44301	0,16242	0,32132
Pitch 2	0,47397	0,57324	0,58853	0,81901	0,66486
Pitch 3	0,42892	0,32393	0,26956	0,24882	0,3023
Pitch 4	0,53736	0,56674	0,58656	0,57511	0,56941
Length (m)	23,9634	22,4141	21,9255	15,8012	13,3072
Slenderness	15,4058	14,1052	13,7668	7,39214	5,52631
Diameter (m)	1,55548	1,58907	1,59263	2,13757	2,40797
Nozzle Diameter (m)	0,74068	0,84203	0,89999	1,08414	1,05158
Oxidizer to fuel	6,00284	6,0029	5,99981	6,03337	6,10186
Chamber Pressure (bar)	263,715	263,809	263,795	261,293	262,941
Exit Pressure (Pa)	18914,1	12853,3	10812,7	9072,29	11141,4
Initial flight path angle	0,77484	0,71766	0,62157	0,88618	0,65645
Optimized payload Ratio	0,05572	0,06284	0,06805	0,07886	0,08787
Estimated payload Ratio	0,055	0,06	0,065	0,07	0,075
Target Altitude (m)	250000	250000	250000	250000	250000
Gravity Loss (m/s)	721,5	666,5	585,15	643,8	405,5
Drag Loss (m/s)	278,9	279,9	295,5	17,2	6,9
Maximum Dynamic Pressure (Pa)	55067,3	33122	18596	3966	174
Time of dynamic pressure (s)	0	0	0	0	0
Initial Acceleration (m/s^2)	7,5	8,45	9,82	11,3	12,5
Maximum Acceleration (m/s^2)	50	50	50	50	50
Initial Mass (kg)	15867,2	15445,2	15192,5	18941	19753
Final Mass (kg)	2334,2	2380,9	2437	3238,4	3582,6
Jettisoning (s)	240,6	236,2	233,4	0	0
Fairing mass (kg)	223,7	237,2	252,5	0	0
Maximum Bending load (Pa $\cdot$ rad)	3973	3332	2882,5	115	47,2
Time max Bending (s)	23	24,2	24,3	42,7	51,1
Heat shield Mass (kg)	0	0	0	0	0
mass flow (kg/s)	41,4	38,8	38,3	47,9	53,5
Payload Mass (kg)	884,1	970,6	1033,9	1493,7	1735,7
Max thrust (N)	181934	172583	171576	215405	238836
Exhaust Velocity (m/s)	4389,7	4449,2	4474,8	4495	4460,6
Maximum Angle of Attack (rad)	0,201	0,2583	0,303	0,232	0,3644
Delta V (m/s)	8350,9	8250,3	8113,9	7858,3	7529
Area Ratio	88,7	124,1	144,3	166,9	140,6
Mass Engine (kg)	235,17	220,35	218,79	289,77	329,16
Mass Nozzle (kg)	58,89	78,26	90,35	131,56	122,72
Mass Tank (kg)	953,81	915,2	898,43	1090,44	1147,9
Max Heat flux (W/m^2)	4124	3520,5	3802	1113	1134
Time max Heat flux (s)	153,2	149,8	141,5	129,6	133,4
T/W (N/kg)	11,466	11,1739	11,2935	11,3724	12,0911

Table B.9: Optimized launch vehicle parameters and characteristics using hydrolox propellants

Velocity (m/s)	600	600	600	600	600
Altitude (m)	0	5000	10000	20000	40000
Pitch 1	0,32335	0,33016	0,37681	0,26812	0,41944
Pitch 2	0,5423	0,44484	0,3587	0,62903	0,36403
Pitch 3	0,42165	0,55244	0,62475	0,45641	0,61293
Pitch 4	0,5356	0,49294	0,47275	0,50601	0,47329
Length (m)	26,105	22,5873	22,6798	17,1344	15,9576
Slenderness	17,1263	14,1067	10,0785	8,86207	8,38882
Diameter (m)	1,52426	1,60117	2,25032	1,93345	1,90224
Nozzle Diameter (m)	0,88808	0,90924	1,22481	1,04277	0,91027
Oxidizer to fuel	6,34116	6,00449	6,0005	6,09309	6,00419
Chamber Pressure (bar)	263,937	263,607	262,097	261,069	260,032
Exit Pressure (Pa)	12899,4	10357,7	10073,2	7611,77	11315,1
Initial flight path angle (deg)	0,77171	0,76686	0,75405	0,71724	0,54241
Optimized payload Ratio	0,07408	0,0823	0,08834	0,09617	0,10833
Estimated payload Ratio	0,077	0,085	0,1	0,1	0,11
Target Altitude (m)	250000	250000	250000	250000	250000
Gravity Loss (m/s)	714	686,8	670,1	575,6	386,9
Drag Loss (m/s)	176,7	110,5	61,8	19,2	4,5
Maximum Dynamic Pressure (Pa)	219780	132226	74204	15849	695
Time of dynamic pressure (s)	0	0	0	0	0
Initial Acceleration (m/s^2)	-0,8	2,73	5,51495	9,1	12,2
Maximum Acceleration (m/s^2)	50	50	50	50	50
Initial Mass (kg)	17300	15896,6	30892,6	17238,9	15446
Final Mass (kg)	2842,5	2741,9	5402	3170,7	3087,3
Jettisoning (s)	196,5	171,5	82,6	57	0
Fairing mass (kg)	339,5	343,7	782,9	436,9	0
Maximum Bending load ($Pa \cdot rad$)	2500	1448	1080	171	44
Time max Bending (s)	89,6	12,3	12	17	21
Heat shield Mass (kg)	0,3	0,2	0	0	0
Mass flow (kg/s)	43	37,7	66,9	38,2	40,7
Payload Mass (kg)	1281,6	1308,3	2729	1657,9	1673,3
Max thrust (N)	190011	169102	299750	172432	181515
Exhaust Velocity (m/s)	4419	4480,4	4483,7	4513,8	4465,1
Maximum Angle of Attack (rad)	0,2026	0,202	0,2593	0,268	0,278
Delta V (m/s)	7893,3	7776,1	7703,4	7527	7063,2
Area Ratio	125,1	149,7	152,6	194,7	137
Mass Engine (kg)	248,17	214,89	435,76	220,09	234,52
Mass Nozzle (kg)	86,71	92,43	167,18	122,85	91
Mass Tank (kg)	1013,48	929,37	1752,92	966,29	888,81
Max Heat flux (W/m^2)	17104,8	12960,2	8197,5	4093	984
Time max Heat flux (s)	0	0	0	0	72
T/W (N/kg)	10,9833	10,6376	9,70297	10,0025	11,7516

Table B.10: Optimized launch vehicle parameters and characteristics using hydrolox propellants

Velocity (m/s)	1000	1000	1000	1000	1000
Altitude (m)	0	5000	10000	20000	40000
Pitch 1	0,23955	0,23968	0,28056	0,33391	0,31838
Pitch 2	0,64456	0,68503	0,71886	0,56343	0,60287
Pitch 3	0,47257	0,44593	0,36922	0,5122	0,50763
Pitch 4	0,49862	0,50291	0,52882	0,48932	0,48299
Length (m)	24,834	22,314	21,7038	19,4735	16,2907
Slenderness	15,5514	9,93228	10,4793	8,40724	8,47795
Diameter (m)	1,59689	2,24661	2,07111	2,31627	1,92154
Nozzle Diameter (m)	0,84521	1,28746	1,20377	1,55823	0,99838
Oxidizer to fuel	6,02932	5,97869	6,04586	6,03333	6,33393
Chamber Pressure (bar)	263,069	263,609	262,369	230,059	258,877
Exit Pressure (Pa)	12465,1	8944,39	8005,56	5183,71	8834,2
Initial flight path angle (deg)	0,71886	0,65456	0,60851	0,54487	0,47909
Optimized payload Ratio	0,09854	0,10687	0,11327	0,12032	0,12638
Estimated payload Ratio	0,1	0,115	0,125	0,13	0,135
Target Altitude (m)	250000	250000	250000	250000	250000
Gravity Loss (m/s)	659,7	583,4	551,9	462,1	351,5
Drag Loss (m/s)	213,1	145,6	81,9	24,3	2
Maximum Dynamic Pressure (Pa)	609491	366899	206023	44022	1927
Time of dynamic pressure (s)	0	0	0	0	0
Initial Acceleration (m/s^2)	-15,9	-7,6	-0,26	7,6	10,9
Maximum Acceleration (m/s^2)	50	50	49,2	48,3	50
Initial Mass (kg)	17503,8	30368,4	25381,1	28114	16649,6
Final Mass (kg)	3235,7	5912,3	5057,8	5891,2	3557,5
Jettisoning (s)	136,1	124,6	111,3	96,7	58,3
Fairing mass (kg)	443,6	881,7	798,9	919,2	564,6
Maximum Bending load (Pa $\cdot$ rad)	1843	710	494	339	1927
Time max Bending (s)	4,3	4	14,3	9,8	23
Heat shield Mass (kg)	3,6	3,2	2,4	0,7	14,6
mass flow (kg/s)	38,1	67	53,2	60,4	39,4
Payload Mass (kg)	1724,9	3245,5	2875	3382,7	2104,1
Max thrust (N)	169385	301628	240073	274940	176271
Exhaust Velocity (m/s)	4450,8	4502,3	4512	4554,6	4471,1
Maximum Angle of Attack (rad)	0,215	0,214	0,255	0,243	0,224
Delta V (m/s)	7399,4	7234,9	7133,8	6966,6	6746,2
Area Ratio	127,3	169,9	186,8	243,9	171,1
Mass Engine (kg)	215,28	439,14	331,24	391,69	226,2
Mass Nozzle (kg)	78,78	187,07	163,93	252,07	110,5
Mass Tank (kg)	1014,26	1723,15	1418,82	1565,33	915,98
Max Heat flux (W/m^2)	77175,5	50572	39530,5	17308,3	3979,3
Time max Heat flux (s)	0	0	0	0	0
T/W (N/kg)	9,67704	9,9323	9,45873	9,77947	10,5871

Table B.11: Optimized launch vehicle parameters and characteristics using hydrolox propellants

Velocity (m/s)	1500	1500	1500	1500	1500
Altitude (m)	0	5000	10000	20000	40000
Pitch 1	0,26315	0,4355	0,31794	0,45157	0,38607
Pitch 2	0,7496	0,37634	0,59079	0,31079	0,60365
Pitch 3	0,37443	0,61196	0,50277	0,68332	0,43963
Pitch 4	0,52318	0,47439	0,49226	0,4535	0,51314
Length (m)	61,2933	59,409	22,1837	20,5464	18,2075
Slenderness	19,7046	18,9321	7,54095	9,76108	8,42877
Diameter (m)	3,11061	3,13801	2,94177	2,10493	2,16016
Nozzle Diameter (m)	2,86134	2,69587	1,79433	1,22462	1,24882
Oxidizer to fuel	6,38482	6,05353	5,99883	6,05638	6,01475
Chamber Pressure (bar)	262,489	262,701	259,439	262,669	263,257
Exit Pressure (Pa)	8524,06	9587,98	6494,75	7191,78	6137,07
Initial flight path angle (deg)	0,59427	0,50780	0,51512	0,43410	0,39219
Optimized payload Ratio	0,11903	0,12749	0,13879	0,15009	0,1581
Estimated payload Ratio	0,12	0,14	0,15	0,155	0,16
Target Altitude (m)	250000	250000	250000	250000	250000
Gravity Loss (m/s)	593,7	504	478,1	393,9	319,3
Drag Loss (m/s)	250,1	170	175,8	57	3,5
Maximum Dynamic Pressure (Pa)	1371020	825636	462483	98984	4334,5
Time of dynamic pressure (s)	0	0	0	0	0
Initial Acceleration (m/s^2)	-31	-15,8	-22,5	1,7	9,12
Maximum Acceleration (m/s^2)	40,4	39,8	40,8	40,4	38,7
Initial Mass (kg)	172799	166164	51029,7	24892,4	22919,8
Final Mass (kg)	36154,9	36384,3	11434,7	5848,5	5584,9
Jettisoning (s)	90,9	98,8	90,4	92,7	62,5
Fairing mass (kg)	5228,2	5835,9	1915,5	964,3	915,4
Maximum Bending load ($Pa \cdot rad$)	5150	6294	264,2	867	36,7
Time max Bending (s)	5	6,4	13,8	6,8	11
Heat shield Mass (kg)	51,2	50,2	11,2	5,2	0,3
Mass flow (kg/s)	314,5	310,5	99,1	50,3	45,9
Payload Mass (kg)	20568	21184,9	7082,3	3736,1	3623,6
Max thrust (N)	1407250	1393060	450163	227735	208672
Exhaust Velocity (m/s)	4474,6	4486,3	4542,5	4525,9	4551,1
Maximum Angle of Attack (rad)	0,275	0,2384	0,2341	0,204	0,246
Delta V (m/s)	6862,3	6653,6	6620,6	6376,4	6240,4
Area Ratio	179	159,9	221,5	205,4	235,9
Mass Engine (kg)	2943,85	2907,19	720,2	310,44	278,59
Mass Nozzle (kg)	920,66	813,93	365,43	170,95	179,79
Mass Tank (kg)	10518,8	10292,2	2811,9	1370,59	1258,01
Max Heat flux (W/m^2)	186557	144448	111558	61217,7	12659
Time max Heat flux (s)	0	0	0	0	0
T/W (N/kg)	8,14385	8,38365	8,82159	9,14878	9,10444

Table B.12: Optimized launch vehicle parameters and characteristics using hydrolox propellants

Velocity (m/s)	2000	2000	2000	2000	2000
Altitude (m)	0	5000	10000	20000	40000
Pitch 1	0,2675	0,36671	0,32329	0,30479	0,29821
Pitch 2	0,72366	0,52829	0,69758	0,73082	0,80278
Pitch 3	0,41177	0,5273	0,4058	0,3908	0,32293
Pitch 4	0,5131	0,49081	0,51628	0,51882	0,53671
Length (m)	67,5273	57,5372	52,6081	40,9385	19,5537
Slenderness	19,7418	19,9974	18,8752	15,7936	8,20976
Diameter (m)	3,42053	2,87723	2,78716	2,59209	2,38177
Nozzle Diameter (m)	3,40298	2,81383	2,55416	2,47068	1,52727
Oxidizer to fuel	6,49743	6,37116	6,37712	6,01009	5,99978
Chamber Pressure (bar)	248,023	263,836	247,8	232,32	263,95
Exit Pressure (Pa)	7381,21	6363,49	6681,1	4502,45	4688,85
Initial flight path angle (deg)	0,52247	0,46303	0,43010	0,39687	0,35130
Optimized payload Ratio	0,14426	0,15582	0,16523	0,17767	0,19006
Estimated payload Ratio	0,15	0,16	0,17	0,18	0,2
Target Altitude (m)	250000	250000	250000	250000	250000
Gravity Loss (m/s)	536,1	466,7	420	364,6	290,2
Drag Loss (m/s)	341	257,6	161,6	67,3	10,3
Maximum Dynamic Pressure (Pa)	2434590	1465530	823028	175911	7703,9
Time of dynamic pressure (s)	0	0	0	0	0
Initial Acceleration (m/s^2)	-56,1	-39,3	-23	-3,5	7,4
Maximum Acceleration (m/s^2)	33,2	32,7	31,4	31,1	31,5
Initial Mass (kg)	233855	139794	119739	77701,4	30019,1
Final Mass (kg)	54268,5	34017,5	29960,4	20574,4	8241,1
Jettisoning (s)	81,2	86,4	85,7	77,6	58,7
Fairing mass (kg)	8778	5583,2	5068,4	3473,9	1413,1
Maximum Bending load ($Pa \cdot rad$)	11228	1005,3	1084	389	22
Time max Bending (s)	4,8	8,9	3,9	4,8	6
Heat shield Mass (kg)	158,5	111	82,6	31	2,3
Mass flow (kg/s)	387,8	238	201,6	135,1	54,7
Payload Mass (kg)	33735,2	21782,7	19785	13805,1	5705,3
Max thrust (N)	1737760	1074770	907988	618107	250971
Exhaust Velocity (m/s)	4481,6	4516,8	4503	4576,3	4587,4
Maximum Angle of Attack (rad)	0,2725	0,2575	0,261	0,2365	0,222
Delta V (m/s)	6375,1	6199,4	6044	5871,7	5709
Area Ratio	194,4	232	211	277,8	298,6
Mass Engine (kg)	3820,31	2110,16	1713,4	1065,48	349,96
Mass Nozzle (kg)	1249,56	910,52	708,5	644,02	273,65
Mass Tank (kg)	13995,9	8233,03	6902,09	4439,37	1618,63
Max Heat flux (W/m^2)	420977	356748	272084	130696	28565,7
Time max Heat flux (s)	0	0	0	0	0
T/W (N/kg)	7,43093	7,68824	7,58306	9,10444	8,36038

Appendix C

Figures

This appendix contains all figures that were deemed to add information to the study discussed in the main text. The first three figures contain sensitivity indices. The other figures displayed contain information about all launch trajectories. Every page contains two plots, the upper contains the hydrolox cases while the bottom one contains the kerolox cases. Various colours are used to display the cases, which only has as purpose to help the reader follow a case of interest.

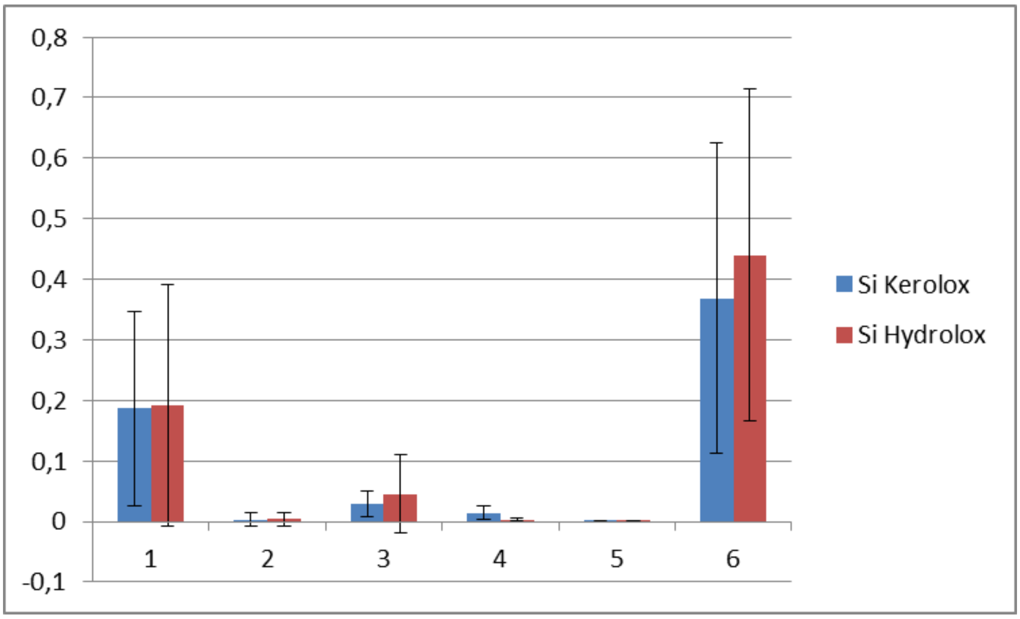

Figure C.1: Mean of the first-order standardized effect of the launch-vehicle parameters on the variance of the model with indications of the maximum and minimum values

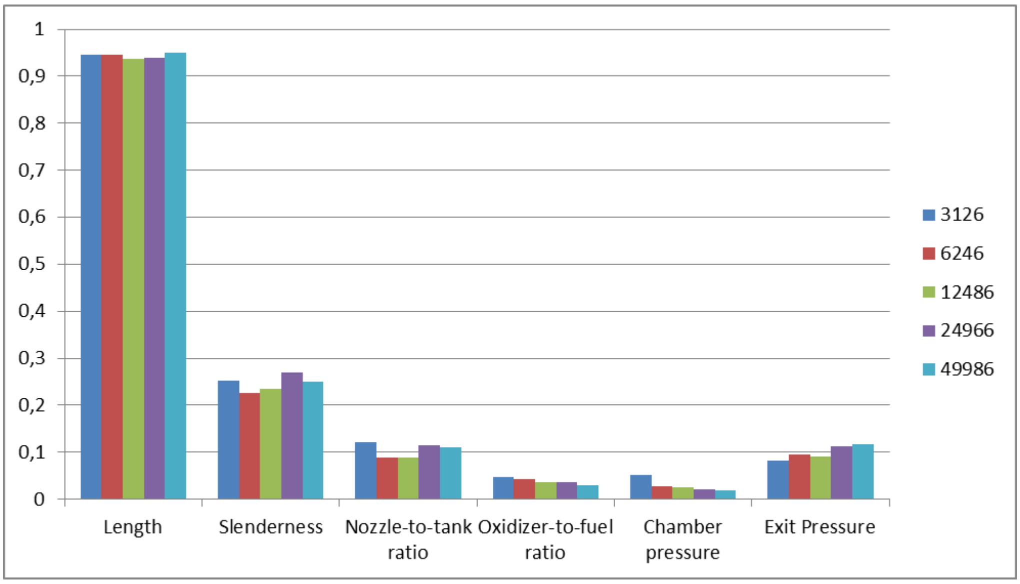

Figure C.2: Total standardized effect of parameters on the variance of the model with various hypercube sample sizes.

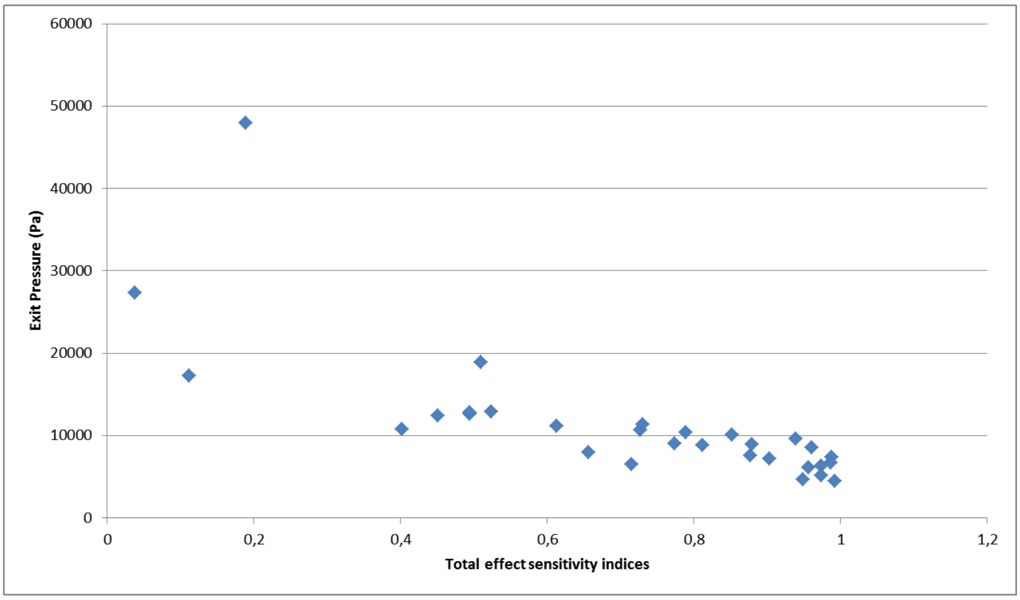

Figure C.3: Total effect sensitivity indices of exit pressure parameter at various values of optimized exit pressure.

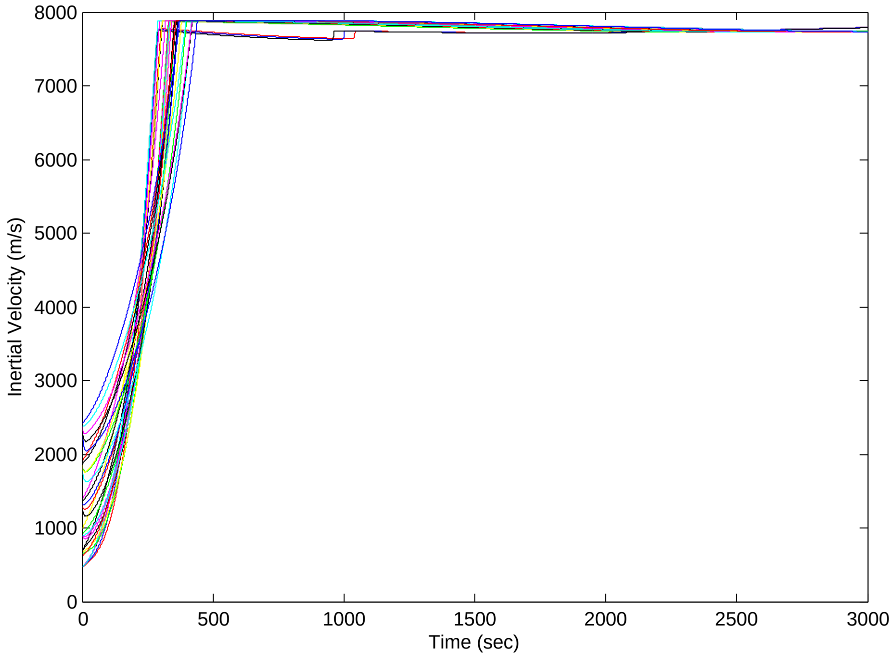

Figure C.4: Inertial velocity plots of all optimized hydrolox simulations

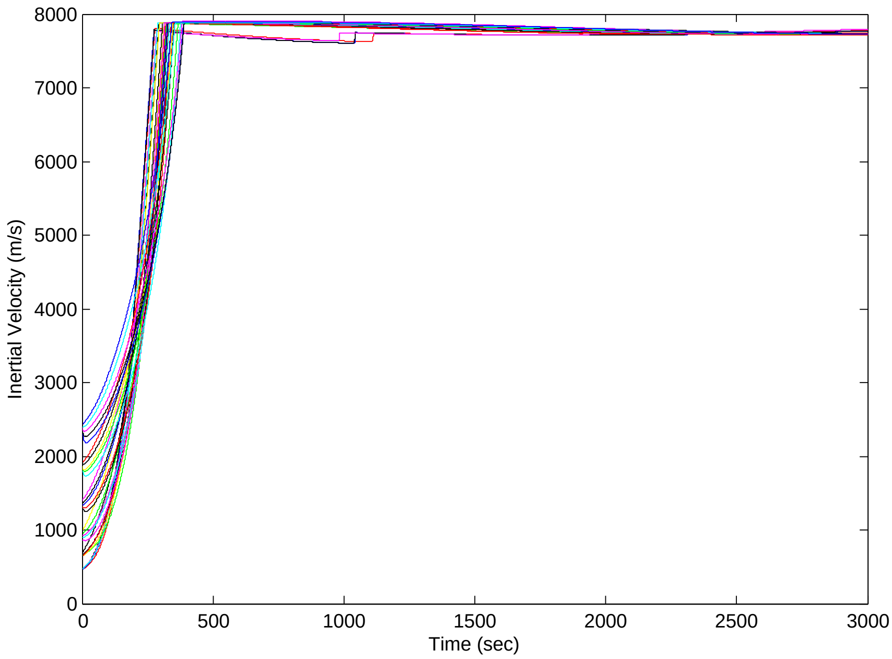

Figure C.5: Inertial velocity plots of all optimized kerolox simulations

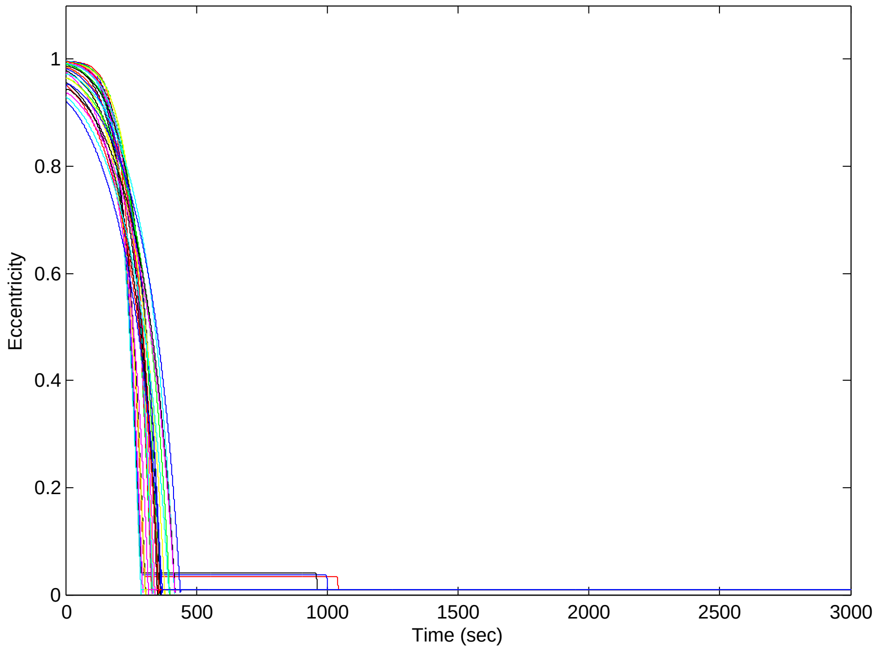

Figure C.6: Eccentricity plots of all optimized hydrolox simulations

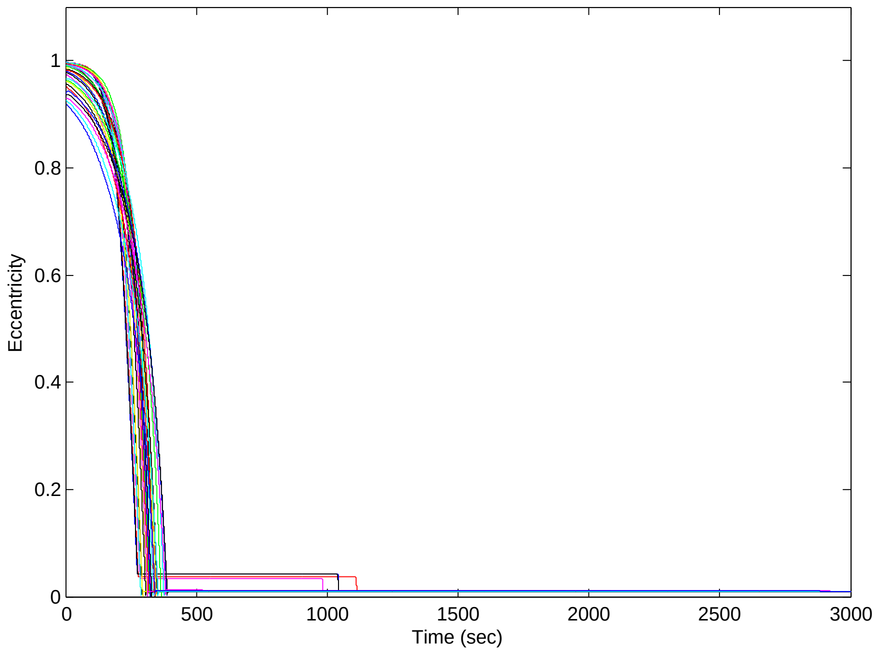

Figure C.7: Eccentricity plots of all optimized kerolox simulations

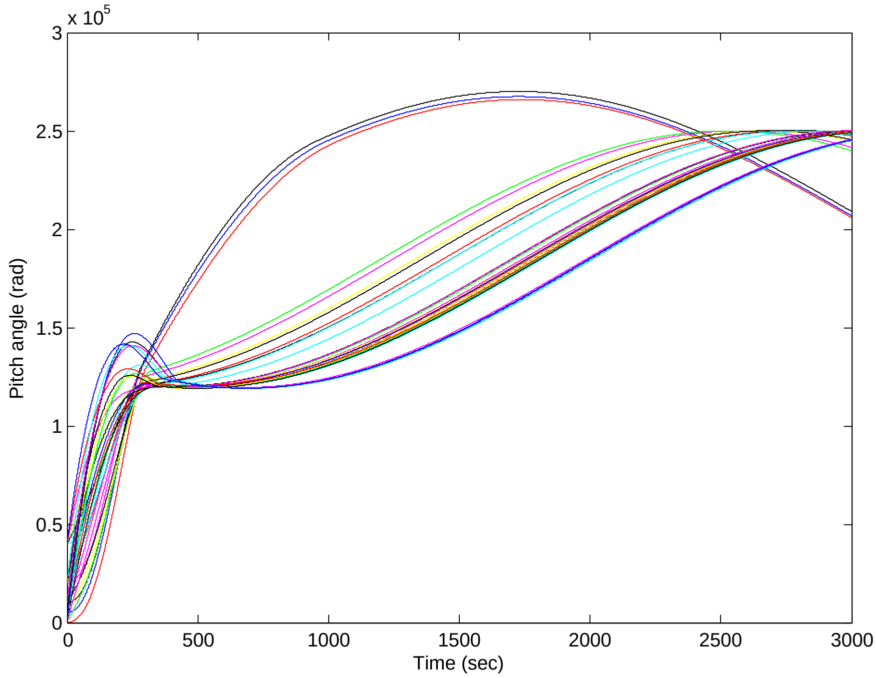

Figure C.8: Altitude plots of all optimized hydrolox simulations

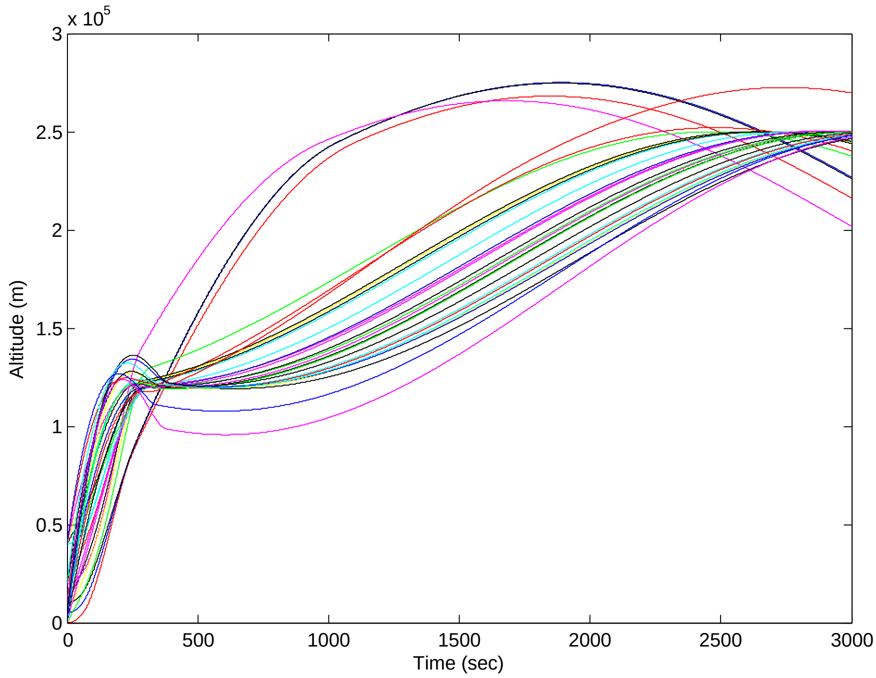

Figure C.9: Altitude plots of all optimized kerolox simulations

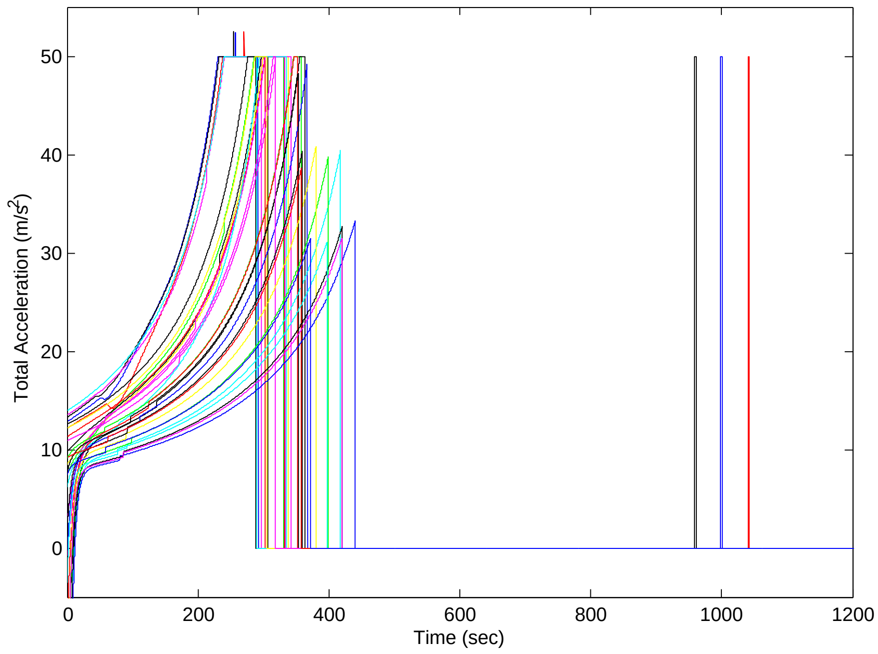

Figure C.10: Total acceleration plots of all optimized hydrolox simulations

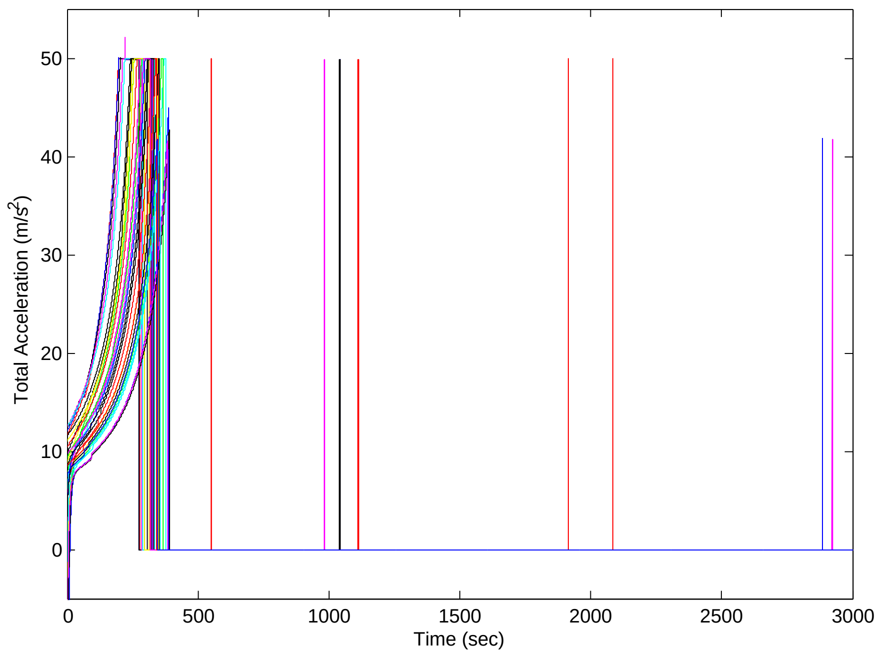

Figure C.11: Total acceleration plots of all optimized kerolox simulations

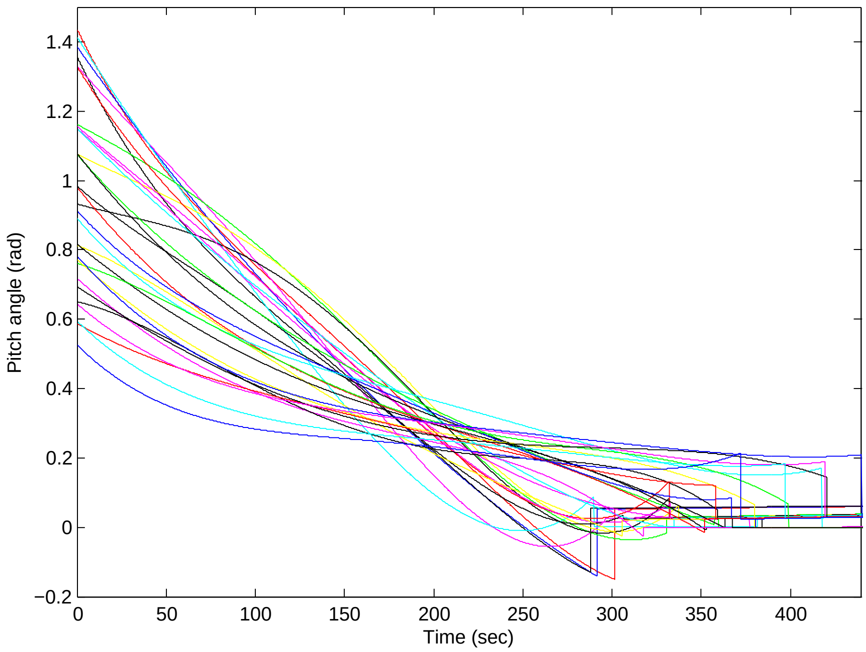

Figure C.12: Pitch angle plots of all optimized hydrolox simulations

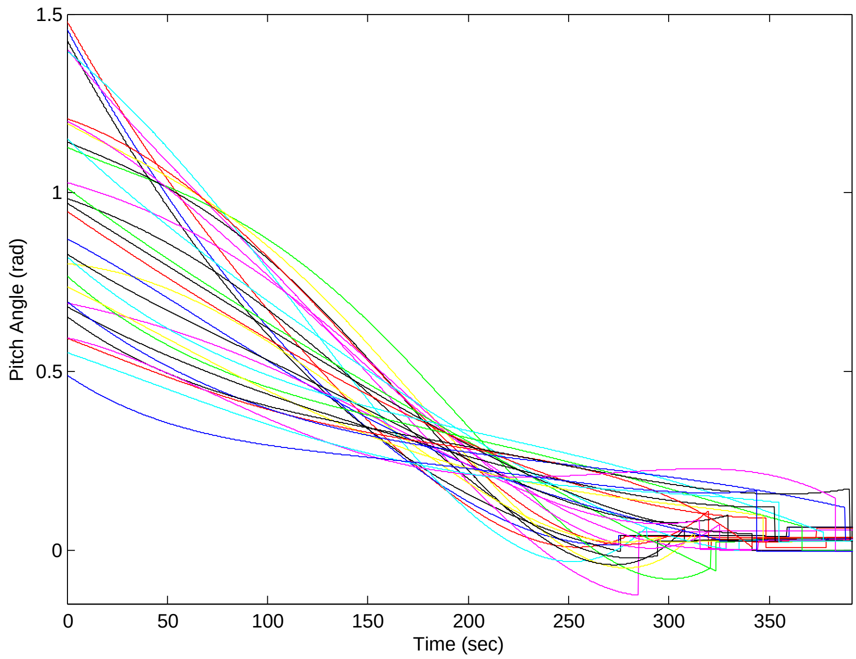

Figure C.13: Pitch angle plots of all optimized kerolox simulations

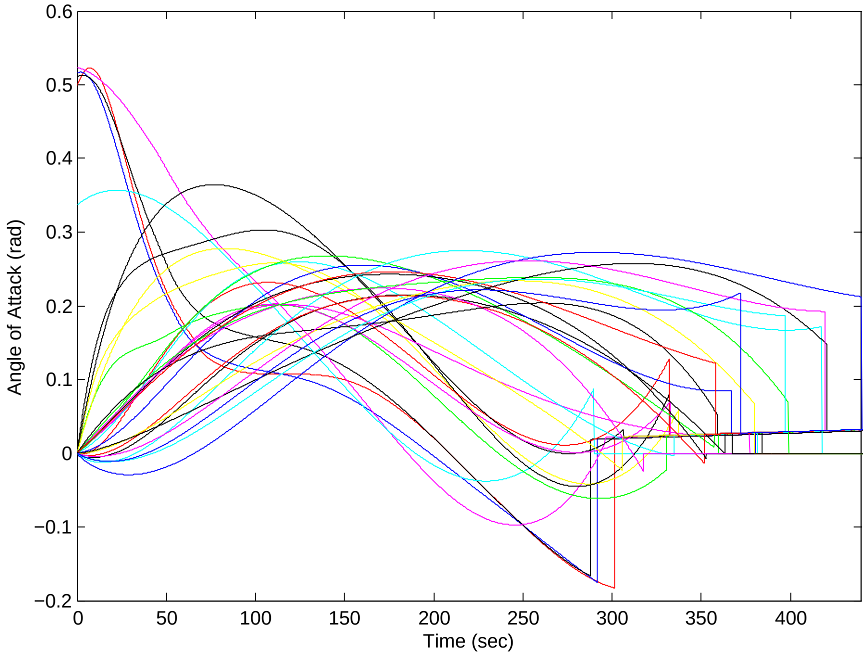

Figure C.14: Angle of attack plots of all optimized hydrolox simulations

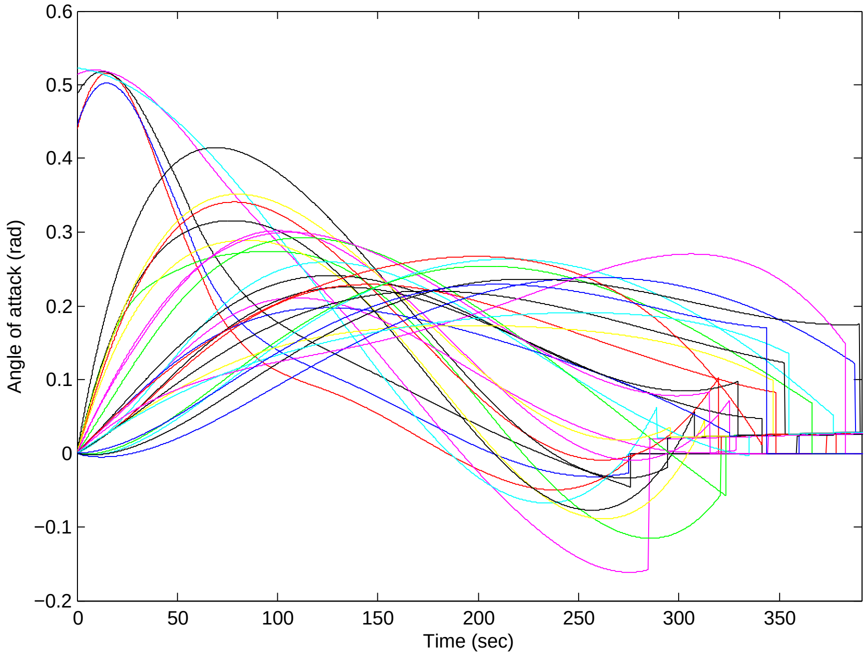

Figure C.15: Angle of attack plots of all optimized kerolox simulations

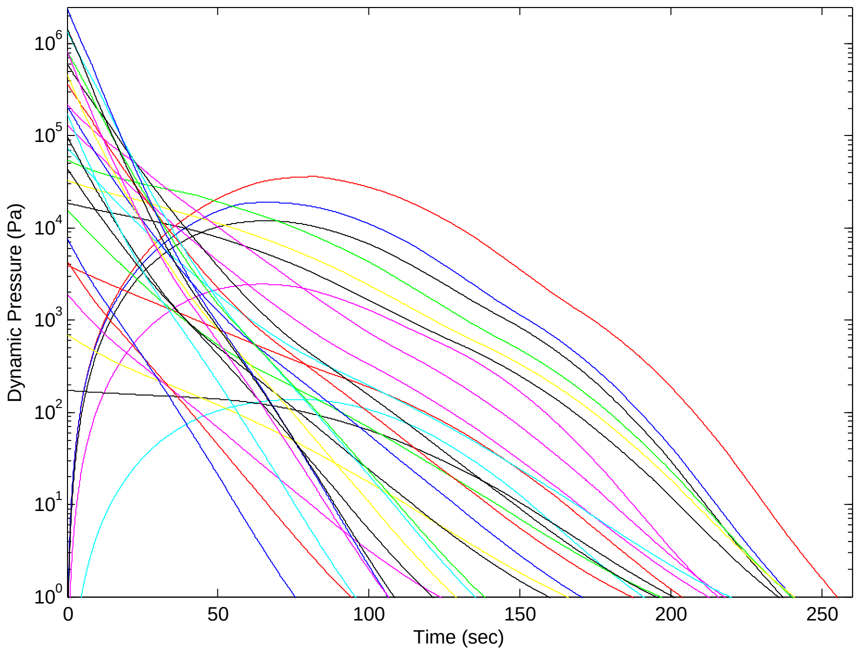

Figure C.16: Logarithmic dynamic pressure plots of all optimized hydrolox simulations

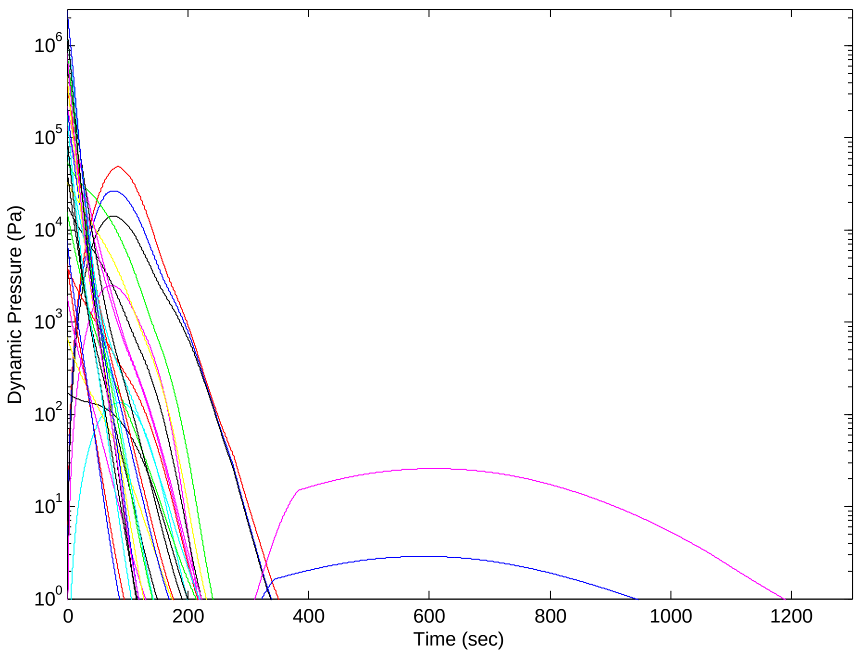

Figure C.17: Logarithmic dynamic pressure plots of all optimized kerolox simulations

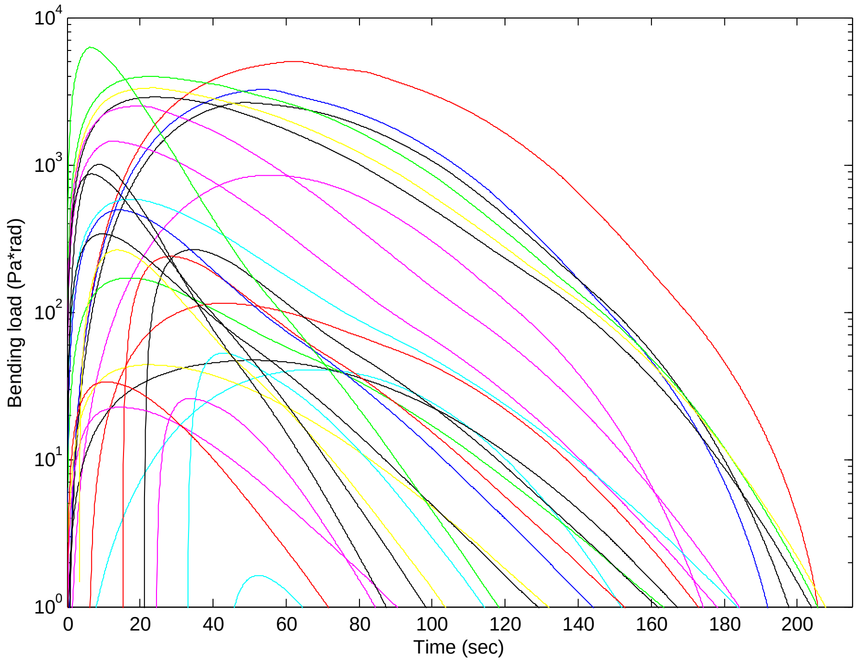

Figure C.18: Logarithmic bending load plots of all optimized hydrolox simulations

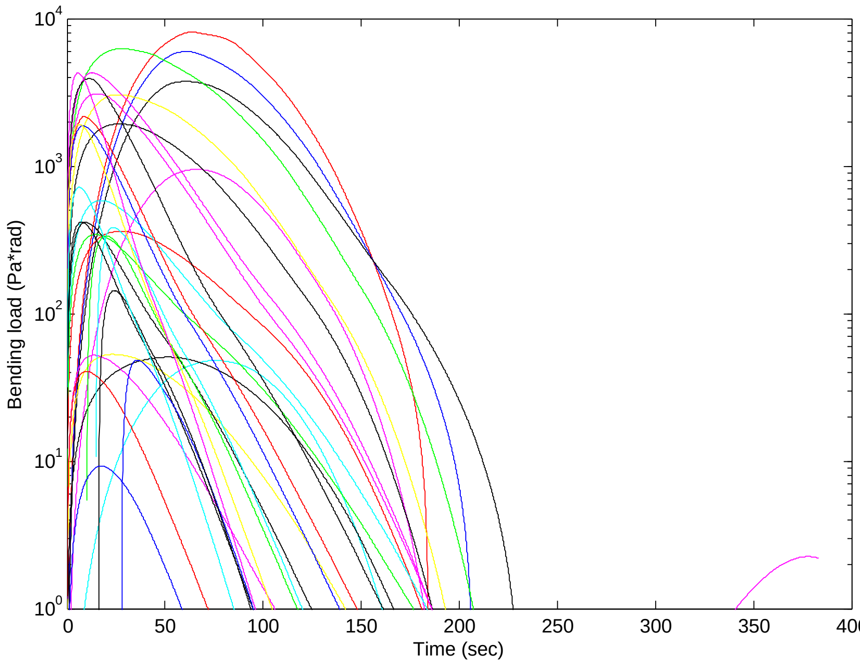

Figure C.19: Logarithmic bending load plots of all optimized kerolox simulations

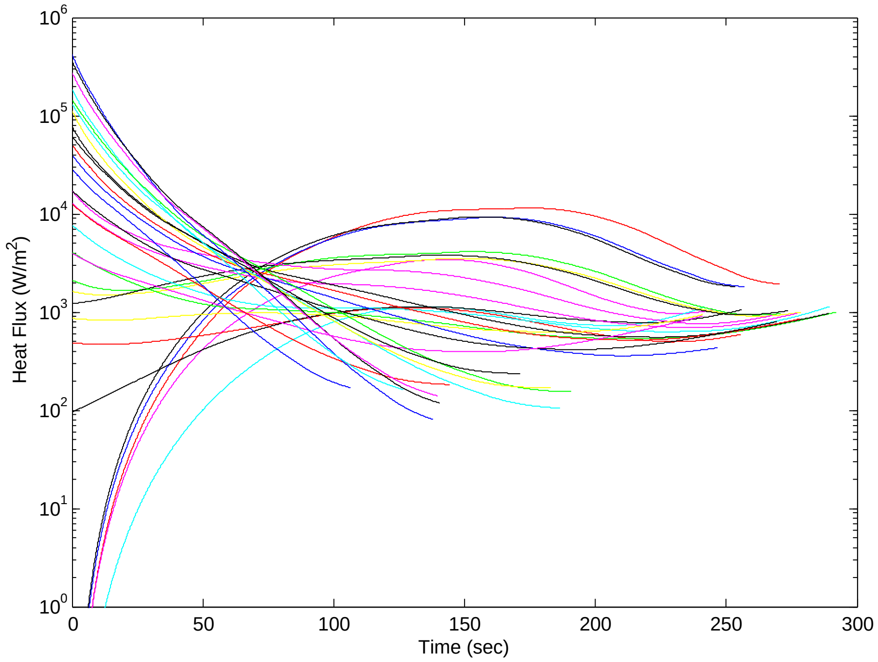

Figure C.20: Logarithmic heat flux plots of all optimized hydrolox simulations

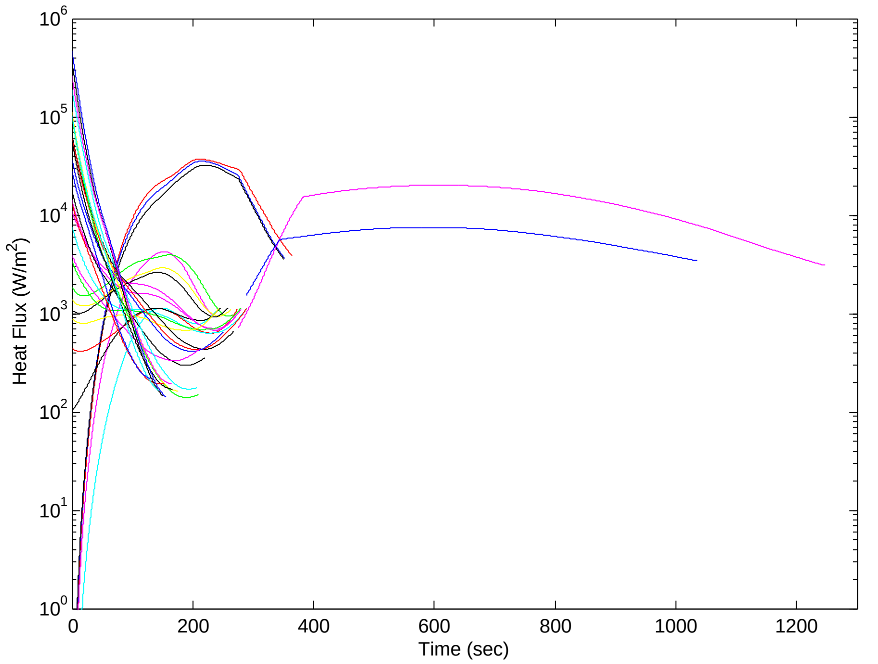

Figure C.21: Logarithmic heat flux plots of all optimized kerolox simulations

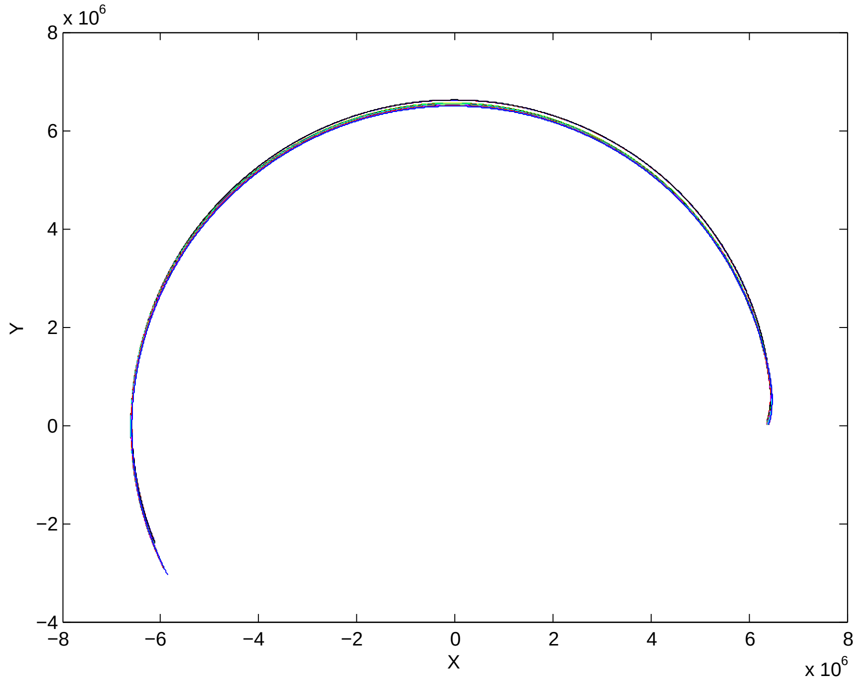

Figure C.22: Position plots in Cartesian coordinates of all optimized hydrolox simulations in the equatorial plane

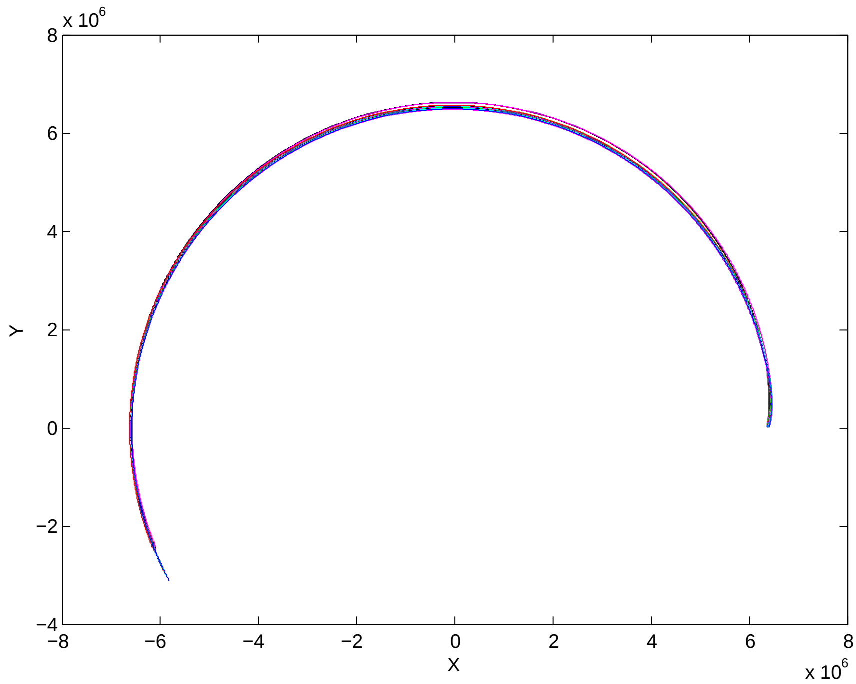

Figure C.23: Position plots in Cartesian coordinates of all optimized kerolox simulations in the equatorial plane

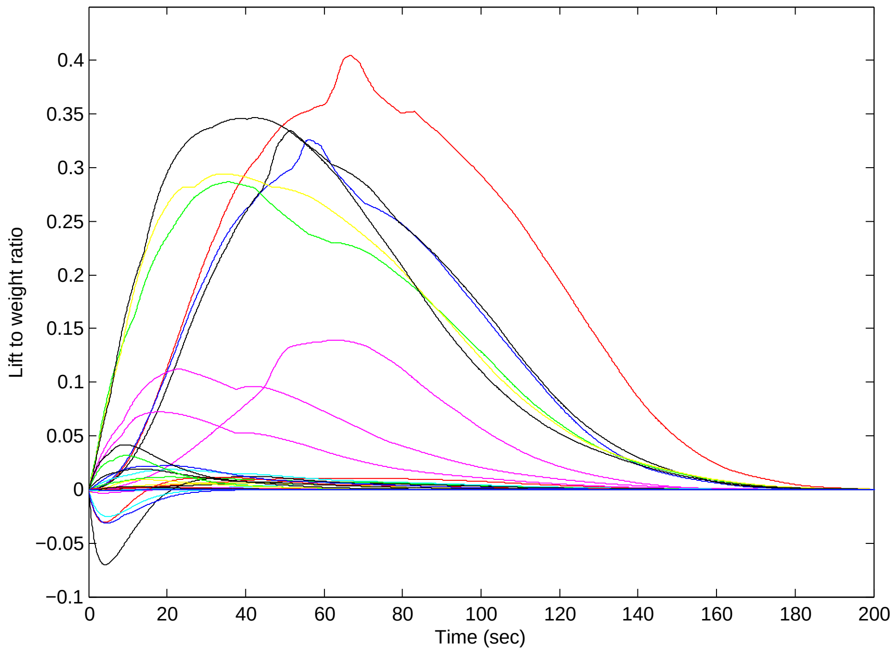

Figure C.24: Lift to weight plots of all optimized hydrolox simulations.

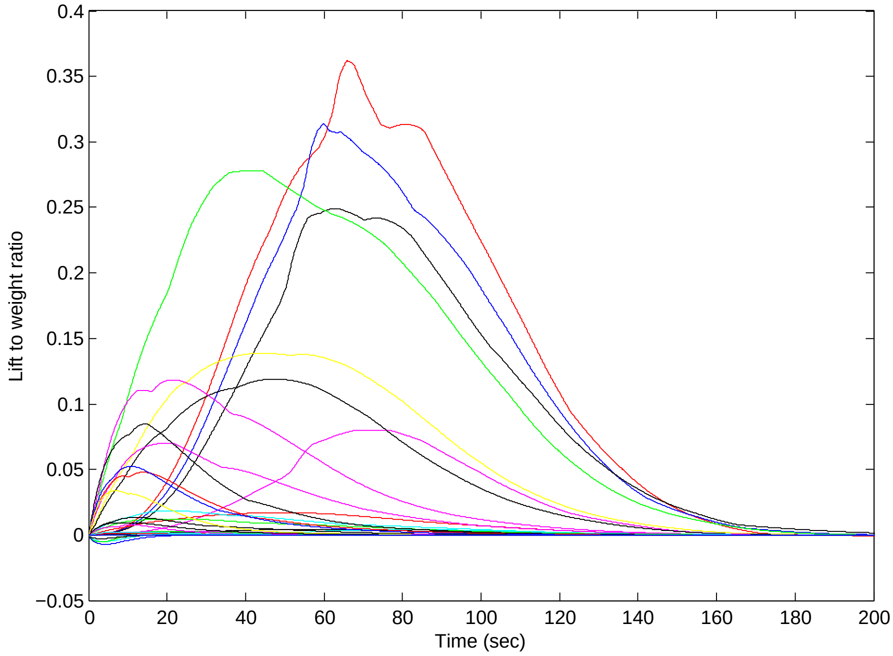

Figure C.25: Lift to weight plots of all optimized kerolox simulations.

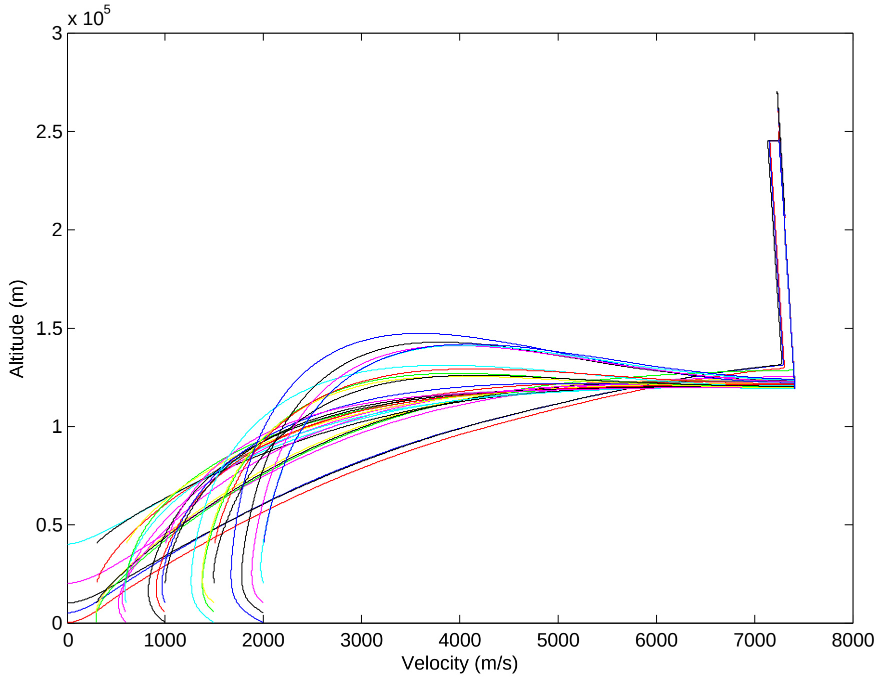

Figure C.26: Altitude vs velocity plots of all optimized hydrolox simulations.

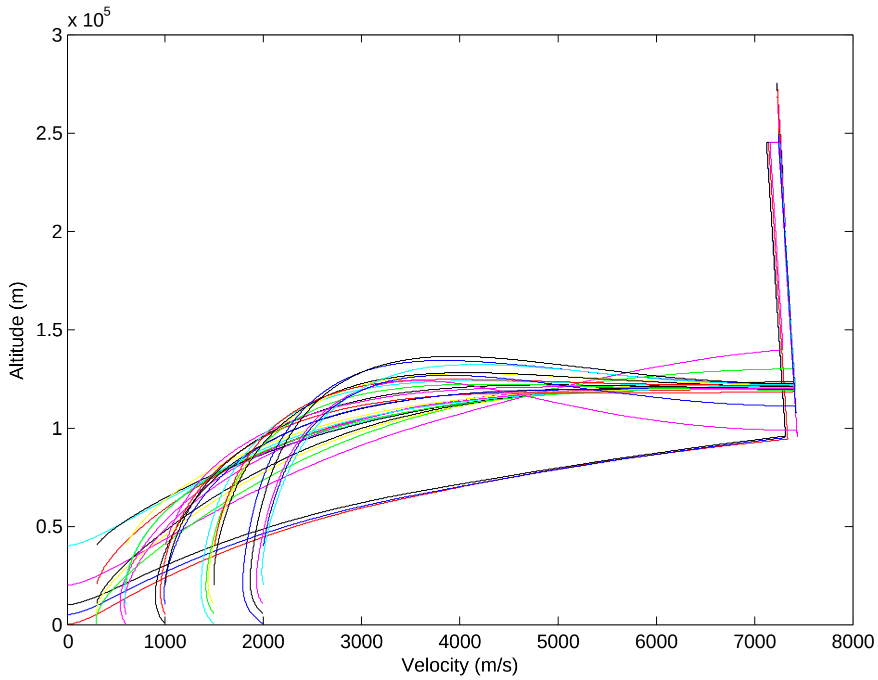

Figure C.27: Altitude vs velocity plots of all optimized kerolox simulations.

Bibliography

[1] American National Standards Institute, *Guide to Reference and Standard Atmosphere Models*, ANSI/AIAA Paper G-003C-2009, Feb. 3. 2003.

[2] Anderson, J. D., *Hypersonic and high temperature gas dynamics*, 2001. Reprint. New York: McGraw-Hill, 1989. Print.

[3] ARIANESPACE, *Vega User's Manual*, Issue 3 / Revision 0, March, 2006. 188 pp.

[4] ASTRIUM Space Transportation, *VULCAIN 2: Thrust Chamber*, 4pp.

[5] Bayley, D.J., *Design Optimization of Space Launch Vehicles Using a Genetic Algorithm*, Auburn, Alabama, Aug. 2007.

[6] Carter, P., Owen, B., Eremenko, P., Hudson, J., Lynch, R., *Design Trade Space Analysis for Air-Launched Spacelift Vehicles*, 2nd Responsive Space Conference, Los Angeles, CA, Apr. 2004.

[7] NASA, *Chemical Equilibrium with Applications (CEA).*, NASA N.p., n.d. Web. 11 Oct. 2012. **http://www.grc.nasa.gov/WWW/CEAWeb/**

[8] Champion, K.S.W., Cole, A.E., Kantor, A.J., *Standard and Reference Atmospheres*, Handbook of Geophysics and the Space Environment, pp. 14-1 - 14-43. Air Force Geophys. Lab., Bedford, Massachussets, 1985. retrieved from: **http://www.cnofs.org/Handbook_of_Geophysics_1985/Chptr14.pdf**

[9] Chenglong, H., Xin, C., Leni, W. *Optimizing RLV Ascent Trajectory Using PSO Algorithms* College of Automation Engineering, NanJing University of Aeronautics and Astronautics, Nanjing, China, 2008.

[10] Chong, K.P., Zak, H.S., *An Introduction to Optimization*, New York: Wiley, 1996. Print.

[11] COESA, *1976: U.S. Standard Atmosphere*, 1976. NOAA, 227 pp.

[12] Cornelisse, J.W., Schyer, H.F.R., Wakker, K.F., *Rocket Propulsion and Spaceflight Dynamics*, Pitman, London. 1979.

[13] DeJarnette, F.R., Davis, R.M., *A simplified method for calculating laminar heat transfer over bodies at an angle of attack*, Langley Research Center, NASA TN D-4720, Washington D.C., Aug. 1968.

[14] Engelen, F.M. *Quantitative risk analysis of unguided rocket trajectories*, Master of Science Thesis, Delft University of Technology. 2012.

[15] ESA, *Esa Launch Vehicle Catalogue*, European Space Agency, Paris.

[16] FAI *RECORDS.* FAI portal. N.p., n.d. Web. 10 Oct. 2012. **http://www.fai.org/records**

[17] Ferguson, F., Corbett, T., Lindsay, H., *The development of waveriders using an axisymmetric flowfield*, Center for Aerospace Research, North Carolina A&T State University.

[18] Filatyev, A.S, Golikov, A.A., *New Possibilities of Significant Improvement of Aerospace Launcher Efficiency by Rigorous Optimization of Atmospheric Flight.*, Central Aerohydrodynamic Institute (TsAGI), 24^{th} International Congress of The Aeronautical Sciences, 2004.

[19] Filatyev, A.S, Golikov, A.A., *Aerospace Trajectory Optimization: Novel view on a role of atmospheric flight*, Central Aerohydrodynamic Institute (TsAGI), 26^{th} International Congress of The Aeronautical Sciences, 2008.

[20] Gen, M., Cheng, R., *Genetic Algorithms & Engineering Optimization*, John Wiley & Sons, Inc. 2000. Print.

[21] Giri, R., Ghose, D., *Differential Evolution Based Ascent Phase Trajectory Optimization for a Hypersonic Vehicle*, Springer-Verlag Berlin Heidelberg, 2010.

[22] Gordon, S., McBride, B.J., *Computer Program for Calculation of Complex Chemical Equilibrium Compositions and Applications - I. Analysis*, NASA, Reference Publication 1311, Oct. 1994.

[23] Gunter, B., Hanssen, R., Simons, D., *Introduction to Earth Observation: Lecture 5, Gravity field - Physics*, TU Delft, Delft. 2008. Lecture.

[24] Hammond, W. E., *Design methodologies for space transportation systems*, Reston, VA: AIAA, 2001. Print.

[25] Hartfield, R.J., Ahuja, F., Albarado, K.M., Walsh, T., *A Method for Optimizing Launch Vehicle Aero-Assist Including Path Optimization*, Auburn University, AIAA 2011-6566, Aug. 2011.

[26] Hsu, D.Y., *Comparison of Four Gravity Models*, IEEE, Litton Guidance & Control Systems. 1996

[27] Izzo, D., Becerra, V. M., Myatt, D. R., Nasuto, S. J., and M., B. J., *Search Space Pruning and Global Optimisation of Multiple Gravity Assist Spacecraft Trajectories*, Journal of Global Optimization, 38:283296. 2007.

[28] Kirk, D.R., *MAE 4262: Rockets and Mission Analysis - Rocket Equation and Losses*, Mechanical and Aerospace Engineering Department, Florida Institute of Technology, Jan. 22, Lecture. retrieved from: **http://www.docstoc.com/docs/123207503/Rocket-Equation-and-Losses**

[29] Krhsel, G., Schfer, K., Kronmller, H., Zimmermann, H., *P4.1 Test Facility for Altitude Simulation of Vinci Engine - Bench Development*, Institute of Space Propulsion, European Conference for Aero-Space Sciences (EUCASS), German Aerospace Center (DLR), Germany.

[30] Mendenhall, M.R., Chou, H.S.Y., Love, J.F., *Computational Aerodynamic Design and Analysis of Launch Vehicles*, Nielsen Engineering & Research, Inc, AIAA Paper 2000-0385, Jan. 2000.

[31] Merkl, A., *Mass Model for TSTO Vehicle Concepts*, ESA Reference: FESTIP-SS-50, 31 Jan. 1995.

[32] Mooij, E., *The Motion of a Vehicle in a Planetary Atmosphere*, Delft University Press, 1997. retrieved from: **http://repository.tudelft.nl/view/ir/uuid%3Ae5fce5a0-7bce-4d8e-8249-e23293edbb55/**

[33] Mulder, J.A, van Staveren, W.H.J.J., van der Vaart, J.C., de Weerdt, E., *Flight Dynamics - Lecture Notes*, February 5, 2007, Delft

[34] NASA, *NASA Photo: EC91-348-4*, NASA Dryden Flight Research Center Photo Collection, N.p, n.d. Web. date last accessed: 15 Nov. 2012. **http://www1.dfrc.nasa.gov/Gallery/Photo/Pegasus/Small/EC91-348-4.jpg**.

[35] NASA, DARPA, *Report of the Horizontal Launch Study - Interim Report*, June 2011

[36] Noffz, G.K., Curry, R.E., *Summary of Aerothermal Test Results from the First Flight of the Pegasus Air-Launched Space Booster*, AIAA paper 91-5046, NASA Dryden Flight Research Facility, AIAA Third International Aerospace Planes Conference, Orlando, FL, 3-5 Dec. 1991

[37] Noomen, R., Chu, Q.P., Kamp, A., *Space Engineering and Technology III - AE3-803 Version 2.0* Lecture Notes, TU Delft, June, 2007, Delft

[38] Pagano, A., *Global Launcher Trajectory Optimization for Lunar Base Settlement*, Master of Science Thesis, Delft University of Technology. 2010 retrieved from: **http://repository.tudelft.nl/view/ir/uuid%3Afa96b280-af15-4520-b528-f93b07752e8d/**

[39] Price, K.V., Storn, R.M., Lampinen, J.A., *Differential Evolution - A Practical Approach to Global Optimization*, Springer-Verlag Berlin Heidelberg, 2005. Print.

[40] Rafique, A.F., He, L.S., Zeeshan, Q., Kamran, A., Nisar, K., *Multidisciplinary design and optimization of an air launched satellite launch vehicle using a hybrid heuristic search algorithm*, Engineering Optimization, 43:3, 305-328, Taylor & Francis, Informa Ltd. 2011. **http://dx.doi.org/10.1080/0305215X.2010.489608**

[41] Rao, S.S., *Engineering Optimization - Theory and Practice*, Fourth edition, Johm Wiley & Sons, Inc., 2009. Print.

[42] *RD-108-8D75K.* Encyclopedia Astronautica. N.p., n.d. Web. 11 Oct. 2012. **http://www.astronautix.com/engines/rd18d75k.htm**

[43] Resnick, B., *North American X-15: Record Breaking Vehicles*, Popular Mechanics, Popular Mechanics. N.p., n.d. Web. 10 Oct. 2012. **http://www.popularmechanics.com/technology/engineering/extreme-machines/worlds-top-12-fastest-vehicles-north-american-x-15#slide-5**

[44] de Ridder, S., *Study on Optimal Trajectories and Energy Management Capabilities of a Winged Re-Entry Vehicle during the Terminal Area*, Master of Science Thesis, Delft University of Technology. July 2009.

[45] Ridolfi, G., Mooij, E., Corpino, S., *Complex-Systems Design Methodology for Systems-Engineering Collaborative Environment*, Systems Engineering - Practice and Theory, Boris Cogan (Ed.), ISBN: 978-953-51-0322-6, InTech, **http://www.intechopen.com/books/systems-engineering-practice-and-theory/complex-systems-design-methodology-for-systems-engineering-collaborative-environment**

[46] Saltelli, A., Tarantola, S., Chan, K.P.S., *A Quantitative Model-Independent Method for Global Sensitivity Analysis of Model Output*, Joint Research Centre of the European Comission, Italy, 1999.

[47] Shaughnessy, J.D., Pinvknry, S.Z., McMinn, J.D., Cruz, C.I., Kelly. M. *Hypersonic Vehicle Simulation Model: Winged-Cone Configuration*, NASA Technical Memorandum 102610, November. 1990.

[48] Sooy, T.J., Schmidt, R.Z. *Aerodynamic Predictions, Comparisons, and Validation using Missile DATCOM (97) and Aeroprediction 98 (AP98)* Journal of Spacecraft and Rockets, Vol.42, No.2, March-April 2005.

[49] Spaans, J., *Improving Global Optimization Methods for Low Thrust Trajectories*, Delft University of Technology, Delft, The Netherlands, Aug. 2009.

[50] Starsem, *RD-0124 An Optimized Propulsion System for Soyuz/ST*, Versailles, May 14, 2002, Lecture.

[51] Stern, R.G., *Aerothermal Heating for Satellite Reentry Conditions*, The Aerospace Corporation, Aerospace Report No. TR-2004(8506)-2, El Segundo, California, 22^{nd} Sept. 2004.

[52] *Thin-Walled Pressure Vessels.*, eFunda: The Ultimate Online Reference for Engineers. N.p., n.d. Web. 11 Oct. 2012. **www.efunda.com/formulae/solid_mechanics/mat_mechanics/pressure_vessel.cfm**

[53] Tudat Working Group, *Tudat User Tutorial*, Aug. 25, 2011.

[54] Tusar, T., Filipic B., *Differential Evolution versus Genetic Algorithms in Multiobjective Optimization*, Springer-Verlag Berlin Heidelberg, Jozef Stefan Institute, Ljubljana, Slovenia, 2007.

[55] Vallado, D.A., McClain, W.D., *Fundamentals of astrodynamics and applications*, Dordrecht: Kluwer Academic Publishers, 2001. Print.

[56] Vandamme, J., *Study on the Effect of Asssisted Launch on Launch Vehicle Performance*, Literature Study, TU Delft, Delft, Feb. 2^{nd} 2012.

[57] Vuik, C., van Beek, P., Vermolen, F., van Kan, J., *Numerical Methods for Ordinary Differential Equations*, Delft, VSSD, 2007. Print.

[58] Wakker, K.F., *Astrodynamics - I - AE4-874, Part 1*, Lecture Notes, TU Delft, August, 2007, Delft

[59] Wakker, K.F., *Astrodynamics - II - AE4-874, Part II*, Lecture Notes, TU Delft, August, 2007, Delft

[60] Weise, T., *Global Optimization Algorithms: Theory and Application.* 2008.

[61] Werley, B. L., *A Comparison of CEA and HSC Software for Oxidant Safety Thermo/Equilibrium Analysis*, Self-published opinion, BWOpinion Website, **www.enter.net/ bwerley**, 2010, 31 pages.

[62] Wertz, J. R., Larson, W.J., *Space mission analysis and design.* 3^{rd} edition. Torrance, CA, Microcosm, 1999. Print.

[63] Wiegand, A., *Practical Problem Solving on Fast Trajectory Optimization* 3rd International Workshop on Astrodynamics tools and Techniques. Lecture. 2006.

[64] Yokoyama, N., *Flight Trajectory Optimization Using Genetic Algorithm Combined with Gradient Method*, University of Tokyo, Japan, 2001.

[65] Zandbergen, B.T.C., *Thermal Rocket Propulsion (version 2.04) - AE4S01*, Lecture Notes, TU Delft, February, 2010, Delft

[66] Zandbergen, B.T.C., *Storage tanks for liquids and gases - AE4S01*, TU Delft, Delft, 1 May 2004, Lecture.

[67] Zandbergen, B.T.C., *Aerospace Design & Systems Engineering Elements I - AE1-201, Part: Launcher design and sizing*, Lecture Notes, TU Delft, Delft

[68] Zandbergen, B.T.C., *TU Delft: Thruster mass estimation.*, TU Delft: LR. N.p., n.d. Web. 31 Aug. 2011. **http://lr.tudelft.nl/en/organisation/departments-and-chairs/space-engineering/space-systems-engineering/expertise-areas/space-propulsion/system-design/analyze-candidates/dry-mass-estimation/powered-systems/thruster-mass/**.

[69] Zandbergen, B.T.C., *TU Delft: Data for rocket propulsion system size estimation* ., TU Delft: LR. N.p., n.d. Web. 10 Oct. 2012. **http://www.lr.tudelft.nl/en/organisation/departments-and-chairs/space-engineering/space-systems-engineering/expertise-areas/space-propulsion/design-data/size-estimation/**.